Nano-Engineered Electrochemical Aptasensors for Label-free Detection of *Cryptosporidium*, Cadmium and Arsenic in Water

---

By

Indiphile Nompetsheni

Submitted in accordance with the requirements
for the degree of

MASTERS

in the subject

CHEMISTRY

at the

UNIVERSITY OF SOUTH AFRICA

Supervisor: Prof. X Fuku

Co-supervisor: Prof. N Palaniyandy

Co-supervisor: Dr. N.W Hlongwa

Declaration

Name: Indiphile Nompetsheni

Student number: 21068046

Degree: Master of Chemistry

Exact wording of the title of the dissertation as appearing on the electronic copy submitted for examination:

Nano-Engineered Electrochemical Aptasensors for Label-free Detection of *Cryptosporidium*, Cadmium and Arsenic in Water

I declare that the above dissertation is my own work and that all the sources that I have used or quoted have been indicated and acknowledged by means of complete references.

I further declare that I submitted the dissertation to originality checking software and that it falls within the accepted requirements for originality.

I further declare that I have not previously submitted this work, or part of it, for examination at Unisa for another qualification or at any other higher education institution.

SIGNATURE

22/10/2025

DATE

Acknowledgements

I would like to express my sincere gratitude to my supervisor, Prof. Xolile Fuku, for his unwavering support, patience, encouragement, guidance, and mentorship throughout this journey. I am also grateful to my co-supervisors, Dr Ntuthuko Hlongwa and Prof. Palaniyandy Nithyadharseni, for their unwavering support and guidance. This work would not have been possible without their guidance and motivation. I would like to acknowledge Dr Idris Balarabe Mustapha and Dr Ndebele Nobuhle for their love and support. Special thanks to the staff members and students in the Applied Electrochemistry (AEC) thematic area for their contributions during AEC meetings. I extend my gratitude to the iNanoWs technical team for their assistance. I would like to acknowledge the iNanoWs for funding this project, as well as CSIR and NMISA for supplying the necessary instrumentation.

Finally, I would like to show my heartfelt gratitude to my family, especially my mother, Nomzwabantu Nompetsheni, and my siblings, Samkele, Pamela, Zintle, Awanele, and Othembele Nompetsheni, for their love and support during difficult times. To my lifeline, I greatly appreciate your support, love, patience, and understanding.

Dedication

This work is dedicated to my late father, Zwelixolile Ace Nompetsheni

Publications

1. Indiphile Nompetsheni, Ntuthuko W. Hlongwa, Nithydharseni, Palaniyandy Xolile Fuku, Journal of Applied Electrochemistry,2025, 55, 2679-2700.

2. Indiphile Nompetsheni, Ntuthuko W. Hlongwa, Nithydharseni, Palaniyandy Xolile Fuku, Journal of Microchimica Acta Journal, 2025,192,1-26

3. Indiphile Nompetsheni, Ntuthuko W. Hlongwa, Nithydharseni, Palaniyandy Xolile Fuku, Ternary MnO_2-CQD-TiO_2 Nanocomposite- Enabled Aptasensor for Rapid and Sensitive Detection of *Cryptosporidiosis,* Journal of *Electroanalysis,* 2026, 38, e70092.

4. Indiphile Nompetsheni, Nobuhle Ndebele, Xolile Fuku, Engineering a High-Performance Mil101(Fe)-CQD-TiO_2 Aptasensor Platform for Trace-Level Quantification of Hazardous Ions in Real Water Systems, Journal of Environmental Chemical Engineering, 2026, 14,121634.

5. Indiphile Nompetsheni, Ntuthuko W. Hlongwa, Nithydharseni, Palaniyandy Xolile Fuku, Bridging Porosity and Conductivity: Comparative Study of Mil101(Fe)-CQD-TiO_2 and CQD-TiO_2-MnO_2 Electrocatalysts for Detection of *Cryptosporidium,* Journal of the Indian Chemical Society, 2026, 103, 102488.

6. Indiphile Nompetsheni, Ntuthuko W. Hlongwa, Nithydharseni, Palaniyandy Xolile Fuku, Real-Time Monitoring of *Crytosporidium* in water Using CQD-TiO_2 Aptasensor: Benchmarking Electrochemical and Spectroscopic Detection Pathways, Accepted by ChemistrySelect Journal.

7. Indiphile Nompetsheni, Xolile Fuku, Synergistic CQD–TiO_2–MnO_2 Ternary Nanoengineered Electrochemical Aptasensor for Ultrasensitive Escherichia coli Monitoring in Environmental Waters, Under review on Discover Electrochemistry Journal.

Presentations

Oral presentations

1. Indiphile Nompetsheni, Ntuthuko W. Hlongwa, Nithydharseni, Palaniyandy Xolile Fuku, Carbon-based-Electrochemical aptasensor for the detection of *Cryptosporidium* in water, 7th International Symposium on Electrochemistry Conference, from 13th to 16th of April 2025, KwaZulu-Natal.

2. Indiphile Nompetsheni, Ntuthuko W. Hlongwa, Nithydharseni, Palaniyandy Xolile Fuku, Fabrication of CQD-TiO_2 nanocomposite as a potential electrode modifier for aptasensor applications, Institute for Nanotechnology Water Sustainability 1st Symposium Conference, 3rd April 2025, Thamsanqa Nkambule Auditorium, University of South Africa, Florida campus.

3. Indiphile Nompetsheni, Ntuthuko W. Hlongwa, Nithydharseni, Palaniyandy Xolile Fuku, CQD-TiO_2 composite as a potential for crypto-electrode modifier for high-performance aptasensing with ultra-low detection limits, 45th National Conversion of South African Chemical Institute (SACI-45) conference, from 30th November -5th December 2025, at the University of Witwatersrand, Johannesburg, South Africa.

Poster presentations

1. Indiphile Nompetsheni, Ntuthuko W. Hlongwa, Nithydharseni, Palaniyandy Xolile Fuku, Fabrication of carbon quantum dots modified electrodes for potential aptasensor application, 9th NanoAfrica, 20th – 24th October 2024, Northwest Province.
2. Indiphile Nompetsheni, Ntuthuko W. Hlongwa, Nithydharseni, Palaniyandy Xolile Fuku, Ternary composite of Mil101(Fe)-CQD-TiO_2 for Electrochemical sensing of *Cryptosporidium*, Innovation Festival, Proudly African, Globally Relevant,18th November 2025, UNISA Florida campus.

Awards

1. Nominated for the **Best Researcher Award (International Analytical Chemistry Awards):** Indiphile et al. 2025, 55, 2679-2700.
2. Awarded the SACI Postgraduate conference bursary sponsored by the **Electrochemistry Division.**
3. Awarded Best Overall Poster Presentation, 5th Prize, **Innovation Festival, Proudly African, Globally Relevant.**

Abstract

Nano-Engineered Electrochemical Aptasensors for Label-free Detection of *Cryptosporidium*, Cadmium and Arsenic in Water

Indiphile Nompetsheni

Water is an essential resource for human survival, agriculture, and livestock. However, over the past thirty years, the World Health Organization has reported growing concerns about the impact of environmental pollution on water quality. Water quality is deteriorating due to contamination from microbes and heavy metals. Among the major microbial and potential heavy metals in water are *Cryptosporidium (Crypto)*, cadmium (Cd^{2+}) and arsenic. *Crypto* is an intestinal protozoan parasite that has become a significant cause of cryptosporidiosis, a gastrointestinal disease that can affect healthy adults and may be fatal for children and individuals with weakened immune systems. In contrast, Cd^{2+} and arsenic are amongst the most toxic and harmful metal ions found in the environment. These metals are highly mobile and can accumulate and spread throughout ecosystems. When ingested, they cause various health issues, including cardiovascular diseases, acute poisoning and cancer. These contaminants pose serious risks to aquatic species and the ecosystem at large. Early diagnostic methods for detecting Crypto, Cd^{2+}, and arsenic were developed using microscopy, molecular, and spectroscopic techniques. However, these methods often yield false-negative results, are time-consuming, lack sensitivity and specificity, and have low detection limits. *Crypto,* arsenic, and Cd^{2+} pose a challenge to delivering safe drinking water due to their low concentrations in large volumes. Consequently, there is a need to develop portable, sensitive, and selective methods for detecting *Crypto*, arsenic, and Cd^{2+} at trace levels. This work develops a novel carbon quantum dot

titanium dioxide (CQD-TiO_2), Mil101(Fe)-CQD-TiO_2 based-aptasensor platform capable of label-free simultaneous detection of *Crypto* and heavy metals at trace levels in phosphate buffer solutions and real water samples. The electrocatalysts used in this work were synthesized using precipitation and hydrothermal methods. Various characterization techniques, such as High-resolution transmission electron microscopy (HR-TEM), X-ray diffraction (XRD), and X-ray photoelectron spectroscopy (XPS), were employed to confirm the structural and morphological properties of the synthesized materials. The electrochemical properties of the modified electrodes were studied using cyclic voltammetry (CV), Electrochemical impedance spectroscopy (EIS), square-wave voltammetry (SWV), and Chronopotentiometry (CP), revealing enhanced reaction kinetics and improved stability. The use of various electrocatalysts as aptamer vehicles on the electrode surface has significantly improved the performance of aptasensors, resulting in greater selectivity, higher accuracy, and lower detection limits. As a result, a CQD-TiO_2-based aptasensor platform was developed for detecting *Crypto*, achieving a detection limit of 0.0024 ng L^{-1}, and a sensitivity of 0.27 mA μM^{-1}. In another study, an electrochemical aptasensor platform based on Mil101(Fe)-CQD-TiO_2 ternary composite achieved a detection limit of 0.001 ng L^{-1} for Crypto with a sensitivity of 0.529 mA μM^{-1}. The aptasensor demonstrated excellent performance in detecting Cd^{2+} and arsenic, achieving low detection limits of 0.073 ng L^{-1} for Cd^{2+} and 0.092 ng L^{-1} for arsenic, with sensitivities of 0.127 mA μM^{-1} and 0.0065 mA μM^{-1}. All developed aptasensor platforms demonstrated limits of detection within the limits reported in the literature. Thus, GCE-Mil101(Fe)-CQD-TiO_2-Apt-BSA platform showed a low limit of detection, demonstrating high sensitivities and selectivity compared to conventional techniques. The aptasensor platforms showed acceptable recovery rates when tested with real water samples and demonstrated

good stability, reproducibility, and selectivity. These aptasensors have significant potential for integration with microfluidic and on-chip technology, enabling the early detection of pathogens and trace metals.

Keywords

Aptasensor

Cryptosporidium

Cadmium

Arsenic

Electrochemical Detection

Water pollution

Water Quality

Nanomaterials

Carbon Quantum Dot

Titanium Dioxide

Metal–Organic Frameworks

Limit of detection

Selectivity

List of Figures

List of Tables

List of Schemes

List of Symbols and Abbreviations

AAS	Atomic absorption spectroscopy
AIDS	Immune Deficiency Syndrome
AFM	Atomic force microscopy
BRE	Biological recognition element
CQD	Carbon quantum dot
CV	Cyclic Voltammetry
Crypto	*Cryptosporidium*
DNA	Deoxyribonucleic Acid
E coli	*Escherichia coli*
EIS	Electrochemical impedance spectroscopy
EDS	Energy Dispersive X-ray Spectrometer
ELISA	Enzyme-Linked Immunosorbent Assay
EASA	Electrochemically active surface area
FTIR	Fourier transform infrared spectroscopy
GEMS	Global Enteric Multicenter Study
GCE	Glassy carbon electrode
HIV	Human Immunodeficiency Virus
HR-TEM	High-resolution transmission electron microscopy
ICP	Inductively Coupled Plasma Mass Spectroscopy
ICP-OES	Inductively Coupled Plasma Optical Emission spectroscopy
K_{et}	Rate transfer
LAMP	Loop-Mediated Isothermal Amplification
LOD	Limit of detection
LOQ	Limit of quantification
PCR	Polymerase Chain Reaction
R_{ct}	Charge transfer resistance
R_s	Solution resistance

XRD	X-ray diffraction
XPS	X-ray photoelectron spectroscopy
XRF	X-ray fluorescence
HR-SEM	High-resolution Scanning Electron Microscope
SWV	Square wave voltammetry
TGA	Thermogravimetric analyzer
TiO_2	Titanium dioxide
UV-VIS	Ultraviolet-visible spectroscopy
WHO	World Health Organization
PBS	Phosphate buffer solution
GCE	Glassy carbon electrode

Table of Contents

Table of Contents

CHAPTER ONE:

Introduction

1.1 Overview

This chapter summarises the adverse effects of contaminated water on human health, the marine environment, ecosystems, and animals. It also highlights the danger of consuming contaminated water with heavy metals and pathogens, which can lead to serious health issues such as kidney dysfunction, cardiovascular diseases, diarrheal diseases, gastrointestinal diseases, and nervous system damage. Furthermore, the chapter discusses the problems associated with heavy metals and Cryptosporidium (Crypto) in water, as well as traditional methods for quantifying and monitoring these pollutants, such as PCR, ICP-MS, and UV-Vis. Moreover, it examines the application of electrochemical biosensors, particularly aptasensors, as alternatives to traditional methods. The nanomaterials proposed as electrode modifiers, such as carbon quantum dot (CQD), titanium dioxide (TiO_2), and metal organic frameworks Mil101(Fe), are also discussed.

1.2. Introduction

Access to clean drinking water has become a global concern [1] due to environmental contamination [2]. According to reports by the World Water Council, approximately 1.2 billion people lack access to clean drinking water because of contaminated water sources [3]. Population growth [4], rapid urbanisation [5], industrialization [6], agricultural expansion, etc, have all contributed to this problem [7]. As a result, the availability of clean drinking water has been significantly limited, with a variety of contaminants, including pharmaceuticals [8], pesticides [9] viruses, pathogens [10] and potentially heavy metals [11]. Nowadays, research has emerged on monitoring parasites and potentially heavy metals due to their association with waterborne disease. Pathogen and heavy metal contamination pose serious health risks to humans, animals, and aquatic species [12]. Among the pathogens in water that negatively impact the environment is *Cryptosporidium (Crypto)*.

Crypto is a unicellular parasitic protozoan belonging to the phylum Apicomplexa. This zoonotic parasite was first discovered by Tyzzer in 1907 and was first detected in

humans in 1976 [13]. *Crypto* can infect various vertebrate animals with genotype names designated after the strain's host specificity. Infection in humans is most caused by *Cryptosporidium* (C) hominis or the cattle genotype C. parvum; however, other species, such as C. meleagridis, C. felis, and C. canis, rarely cause human infection [14]. The infection starts with the utilization of profoundly contagious material, and this parasite accomplishes its existence in just one host, where it replicates both asexually and sexually [15]. Oocysts of *Crypto* are shed in the tiny digestive tract, expelled in vast numbers, and replicate in the surrounding environment, repeating the cycle in a different host. The oocysts resist standard biological disinfection procedures, such as chlorination, because they are encased in a thick outer shell, which allows them to persist in the environment and facilitate transmission through contaminated food and water [16]. The infection can be transmitted in two ways: directly (from animal to animal or from animal to person) and indirectly (through contaminated water, for example, by drinking recreational waters and consuming contaminated food [17]. These routes are well-explained in Figure 1. The most recognised environmental routes of transmission are water and food [18].

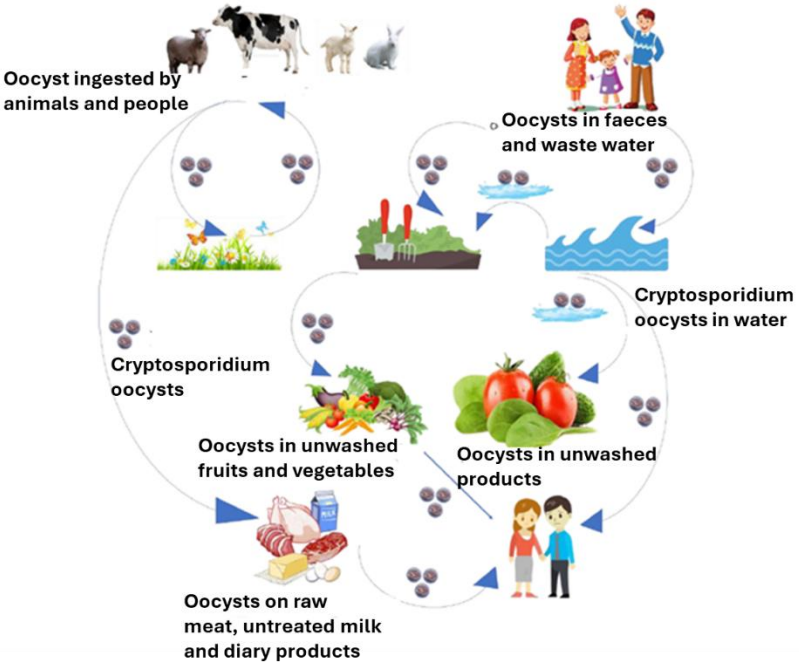

Figure 1: Shows the transmission pathways of *Crypto*.

On the other hand, heavy metals primarily enter the environment through several highly contaminated routes, including agricultural runoff, the food chain, contaminated fertilisers, water, industrial activities, and acid mine drainage [19] . Exposure to heavy metals has serious consequences for the ecosystem [20]. The most toxic and harmful elements often found in water supplies include lead, arsenic, cadmium and mercury [21]. In this study, we examine the quantification of cadmium and arsenic [22]. Research indicates that the toxicity of arsenic varies by form. Arsenic exists primarily in two forms: organic arsenic and inorganic arsenic, which includes arsenite (III) and arsenate (V) [23]. Consuming water contaminated with both cadmium ions and arsenic can lead to numerous health risks, including kidney dysfunction, cancer, impaired lung function, heart problems, and damage to the central nervous system [24]. Water quality standards have established acceptable limits for both arsenic and cadmium ions in water at 0.01 ng L^{-1} and 0.005 ng L^{-1} [25]. Figure 2 illustrates the water contaminated by various heavy metals.

Figure 2: Shows the contaminated water by heavy metals [26].

Therefore, the accurate detection and quantification of cadmium, arsenic, and *Crypto* in water bodies are essential. Therefore, various methods have been employed to detect pollutants in water bodies, but electrochemical methods have demonstrated high efficiency in terms of sensitivity, selectivity, low detection limits, and overall performance.

Electrochemical methods, such as biosensors, have demonstrated a high affinity for detecting pathogens and trace metals in water sources [27]. A biosensor is a transducer that detects changes in biological signals (biomarkers) and converts them into quantifiable signals [28]. There are numerous approaches to developing a biosensor. Depending on the type of transducer used, biosensors can be classified into five categories: electrochemical, piezoelectric, optical, mechanical, and thermal [29]. Amongst these, electrochemical sensors are the widely explored biosensors owing to their advantages associated with low detection limits, as low as picomoles, rapidness, and the low-cost equipment utilized for sensing [30]. They are essential for meeting social needs, such as hazard detection, environmental cleanup, pollution control, and biological therapy. These devices have become innovative platforms for analysing biological materials using a biological recognition element (BRE) linked with the transducer [31]. BRE molecules include enzymes, deoxyribonucleic acid (DNA) aptamers, cells, and antibodies, which exhibit the ability to recognise specific analytes [32]. Aptamers have demonstrated high efficiency compared to other biorecognition elements [33]. The properties include simplicity of modification, strong binding ability, stability, small size, and selectivity for pathogens and metal ions [34] .Aptamers can replace conventional antibodies in environmental conservation, food safety, and clinical diagnostics [35]. Additionally, this biomolecule can be quickly designed through inexpensive and simple laboratory processes [36].

Currently, improving the conductivity and sensitivity of biosensors by incorporating conductive nanostructured materials has become a cornerstone of research. Carbon-based materials such as carbon black, carbon nanotubes (CNTs), graphene oxide (GO), carbon quantum dot (CQD), organic metallic frameworks (MOFs), etc., have shown great potential due to their availability, physicochemical properties, processability, and low cost. These carbon materials offer unique characteristics due to different applications, e.g., sensors, energy storage, and biomedical imaging applications [37]. Among carbon-based materials, carbon quantum dot (CQD) have received much attention because of their remarkable features [38]. These properties include low cytotoxicity, resistance to photobleaching, ease of surface fabrication and modification, biocompatibility, and high-water solubility [39]. The unique characteristics of CQD make them ideal for homogeneous sensing experiments. CQD is ideal for use in sensors because of its excellent electron transport efficiency and large surface area

[40]. To enhance the electrochemical properties of CQD, they are doped with metal oxides such as titanium dioxide (TiO_2), manganese oxide (MnO_2), zinc oxide (ZnO_2), tin oxide (SnO_2), and nickel oxide (NiO_2), among others [41] . Therefore, TiO_2 have garnered considerable attention due to its outstanding features, such as high chemical resistance, a high catalytic efficiency, large specific surface area, high electrical conductivity, and physical strength [42]. Due to these properties, they are extensively used in sensing applications [43]. TiO_2 NPs can enhance the interaction between biomolecules and electrode surfaces, making them one of the most preferred metal oxides for sensing applications [44]. Nanocomposite-based biosensors offer enhanced properties, including improved electrical conductivity and a high surface area-to-volume ratio. These improvements facilitate more efficient interaction with the analyte, resulting in higher sensitivity and conductivity even at low concentrations. Additionally, the enhanced qualities of nanocomposites make them ideal for detecting various targets in biological samples [45]. Moreover, their compatibility with various development techniques enables the creation of portable and versatile sensor devices [46]. CQD-TiO_2-based biosensors have been shown to exhibit low limits of detection and high sensitivity for a wide range of biomolecules, making them useful for detecting small analytes in complex biological samples [40]. This study aims to develop a user-friendly nano-engineered electrochemical aptasensor to overcome the limitations of spectroscopic methods for detecting concentrations of *Crypto*, arsenic, and cadmium in water reservoirs.

1.3 Problem statement

The provision of safe drinking water has become increasingly difficult due to the contamination of water sources with *Crypto* and the potential presence of heavy metals such as arsenic and cadmium [47]. Recent estimates from the World Health Organization (WHO) [48], approximately 778 million people worldwide still rely on water reservoirs that are highly contaminated with heavy metals and pathogens. Over the past 25 years, *Crypto* has become a significant concern for humans and animals.

Crypto has recently been identified as a significant cause of diarrhoea in babies and children in impoverished nations by the Global Enteric Multicentre Study (GEMS) [49]. Consumption of contaminated water with *Cryptos* can lead to severe cryptosporidiosis, gastroenteritis in healthy adults, death in children, and immune-compromised people, particularly patients with acquired immunodeficiency syndrome, cancer and human immunodeficiency virus [50]. Every year, over 760,000 children die from diarrheal disease, and there are about 1.7 billion cases of diarrheal disease worldwide, according to reports [51]. Currently, no effective drugs for treating cryptosporidiosis infections [52]. As a result, detecting *Crypto* has become a top priority to prevent potential outbreaks [53]. Over the years, immunological techniques have been widely used for their ability to detect pathogens in environmental samples. These techniques include immunofluorescence assay, enzyme-linked immunosorbent assay (ELISA), and polymerase chain reaction (PCR) [54].

Heavy metal contamination negatively affects marine ecosystems due to its bioaccumulation tendency, toxicity, persistence, resistance to degradation and long-term consequences [55]. As a result, heavy metal contamination harms marine life, aquatic species, and threatens human health through the food chain and drinking contaminated water [56]. Heavy metals have been linked to major health consequences, including cancer, cardiovascular diseases, kidney dysfunction and neurological disorders [57]. Approximately 1 million people suffer from chronic heavy metal poisoning, and about 1.6 million children die each year from diseases associated with heavy metal ion contamination [58].

Various methods have been employed to detect arsenic and cadmium ions [59], including biochemical methods [60], atomic absorption spectrophotometry (AAS) [61],

inductively coupled plasma mass spectroscopy (ICP-MAS) [62], and atomic fluorescence spectrometry [63]. While these conventional methods for detecting pathogens and heavy metals are easy to perform, explicit, delicate, reproducible, and have a short completion time. However, they have some limitations, such as being time-consuming, having low sensitivity, and requiring modern facilities, large instruments for visual determination, and highly qualified staff, all of which are costly and not applicable for real-time detection [64]. It is essential to develop an efficient, environmentally friendly detection platform with improved detection limits and a broader linear range for continuous detection of Crypto and heavy metal ions in water reservoirs [65].

1.4 Motivation

Many countries, including South Africa, face significant challenges in accessing clean drinking water [66]. The insufficient availability of safe water resources forces people to use contaminated water for drinking, resulting in severe health risks, such as cholera and typhoid, caused by various pollutants in the water [67]. The World Health Organization has stated that 19 per cent of the rural population lacks access to a reliable water supply, and 33 per cent do not have essential sanitation services. Even urban and rural schools and clinics are affected, with over 26 per cent of all schools and 45 per cent of clinics having no access to water [68]. Over 40% of the water sources, including rivers, lakes, streams, and dams, are contaminated by heavy metal ions, which can dissolve in water [69]. When heavy metal ions are transported into water sources, they cause physical and chemical diseases, disrupt biodiversity, and reduce water quality [70]. *Crypto* is a leading cause of waterborne illness globally. South Africa has launched several initiatives to combat water contamination. These include the Blue Drop program, which aims to improve the quality of drinking water, and the National Water Act, which focuses on preventing pollution and monitoring water quality [71]. To effectively implement these strategies, a reliable monitoring device is needed to detect and quantify *Crypto* and heavy-metal ions in water [72]. Currently used methods for detecting this pathogen rely on expensive, complex techniques such as fluorescence microscopy, PCR, immunofluorescence assay (IFA), ICP-MAS, and AAS. These methods still suffer from drawbacks, including a lack of standardization,

limited field applicability, limited sensitivity and selectivity, high costs, and time-consuming processes [73]. As an alternative to traditional methods, electrochemical tools, specifically biosensors, have emerged as promising candidates for detecting pollutants in environmental water bodies [74]. Biosensors integrated into chips and portable analytical devices have transformed several research fields and show great potential for point-of-care (POC) applications. In this study, we propose using an aptasensor to detect heavy metal ions and *Crypto* in water samples. Aptasensor, which uses aptamers as biorecognition elements, are a more efficient alternative. An aptasensor can detect low concentrations of *Crypto* and potentially heavy metal ions in various environmental samples, making it an ideal tool for monitoring and managing these pollutants in water. These devices have reduced the need for power, sample preparation, and reagents, and their small size allows for integration into larger systems [75]. Minimal research has been conducted on portable analytical devices to detect waterborne microorganisms and heavy metal ions [76]. This project aligns with two Sustainable Development Goals: access to water and sanitation, and good health and well-being. This initiative is also aligned with South Africa's national agenda to enhance public health, ensure access to clean water, and promote sustainable development. The project aims to develop a portable and user-friendly aptasensor for detecting *Crypto a*nd heavy metals. This project supports South Africa's strategic goals of improving water quality monitoring and management, particularly in low-resource settings. Furthermore, the South African Constitution guarantees that everyone has the right to access water, food, and a safe environment that promotes their health and well-being. By addressing these critical issues, the project supports national efforts to improve health outcomes, reduce waterborne diseases, and promote economic and environmental sustainability.

To date, several studies have been conducted on detecting waterborne diseases and heavy metals in water. A study by Nugen and colleagues fabricated an electrochemical biosensor to detect *Crypto* oocysts in river samples [78]. Their research described the microfabrication and development of electrochemical biosensors using polymer substrates, thereby making the sensing platforms disposable and cost-effective. The utilization of quantum dot in the detection system enhances the detection signal due to the wide surface area, which allows for quantitative analysis and fluorescence imaging of the objective analyte [79]. These nanomaterials can be employed without

infrastructure, equipment, or trained staff [40]. Their results revealed that the sensor had limited selectivity, a significant drawback. Pie *et al*. [80] devised a biosensor based on carbon quantum dot to detect ferric iron in water. The results showed that the aqueous solution of CQD can rapidly, sensitively, and specifically distinguish Fe^{3+}, with a detection limit of 0.084 ng L^{-1} over the direct range of 0–330 ng L^{-1}. The disadvantage of their approach is that it requires labelling, which is incompatible with label-free and on-site detection. Additionally, Bhuvaneswari et al. [81] developed an MnO_2-CQD-based electrochemical sensor for detecting chromium and cadmium in water. This sensor demonstrated excellent detection capabilities, with limits of detection of 0.999 ng L^{-1} for Cr^{6+} and 0.32 ng L^{-1} for Cd^{2+}.

A few on-chip-based biosensors have been developed to detect *Crypto* oocysts and potentially heavy metals in water. However, these biosensors still have limitations in sensitivity and detection limits, a reliance on expensive labelling, and the need to shorten lengthy labelling steps. A simple, automated, cost-effective, label-free, and portable sensing platform for *detecting Crypto and heavy metal ions* remains unavailable. As a result, this work presents a nano-engineered electrochemical aptasensor to overcome and improve the limitations of existing electrochemical biosensors for *detecting Crypto and* heavy metals [82].

1.5 Aim and Objectives

1.5.1 Aim: This study aims to develop an efficient, user-friendly, and sensitive nanocomposite-based aptasensor for the detection of *Crypto* and potential heavy metals in various sources of water.

1.5.2 Objectives:

- ✓ To synthesize carbon quantum dot using the hydrothermal method
- ✓ To synthesize titanium dioxide using hydrothermal method
- ✓ To synthesize carbon quantum dot- titanium dioxide nanocomposite
- ✓ To synthesize metallic organic framework-iron-based using hydrothermal method
- ✓ To synthesize metallic organic framework-iron-based-carbon quantum dot-titanium dioxide ternary composite using hydrothermal method
- ✓ To characterize the synthesized materials to evaluate the chemical and physical properties using various techniques, such as ultraviolet-visible spectroscopy, Raman spectroscopy, X-ray diffraction, Fourier transform infrared spectroscopy, and Energy-dispersive X-ray spectroscopy
- ✓ To fabricate modified electrodes using synthesized materials
- ✓ To characterize the fabricated electrodes using electrochemical impedance spectroscopy and cyclic voltammetry
- ✓ To fabricate the electrochemical aptasensor using the synthesized materials and a synthetic aptamer with the sequences (R4-6): HS-CH_3CH_2-5′- CTC TGA CTG TAA CCA CGG TGG TCC CGC AAA ATG CAC GAC GAG TCT TGC TTC TGA TCT GCA TAG GTA GTC CAG AAG CC -3′, and (mini-crypto): HS-CH_3CH_2-5′- CTC TGA CTG TAA CCA CGG TGG TCC CGC AAA ATG CAC GAC GAG TCT -3’
- ✓ To characterize the developed electrochemical aptasensor using cyclic voltammetry, square wave voltammetry, and electrochemical impedance spectroscopy

- ✓ To optimize and test the performance of the developed aptasensor in a phosphate buffer using *Crypto* primers: CTC TGA CTG TAA CCA CGG TGG TCC CGC AAA ATG CAC GAC GAG, and real water samples
- ✓ To test Interference in different types of water from tap wastewater (E. coli: CAT GCC GCG TGT ATG AAGAA, and Giardia: GAC GGC TCA GGA CAA CGGTT)

1.6. Research questions

1. To what extent can the nano-enabled electrochemical aptasensor selectively and sensitively detect *Crypto* and heavy metals in different water sources?
2. How does the aptasensor perform in real-world ambient water samples compared to traditional detection methods like polymerase chain reaction for *Crypto* and inductively coupled plasma mass spectroscopy for heavy metals?
3. How does the integration of nanomaterials in the fabrication of electrochemical aptasensors influence their stability, repeatability, and shelf life of the sensor?

1.7 Thesis outline and framework

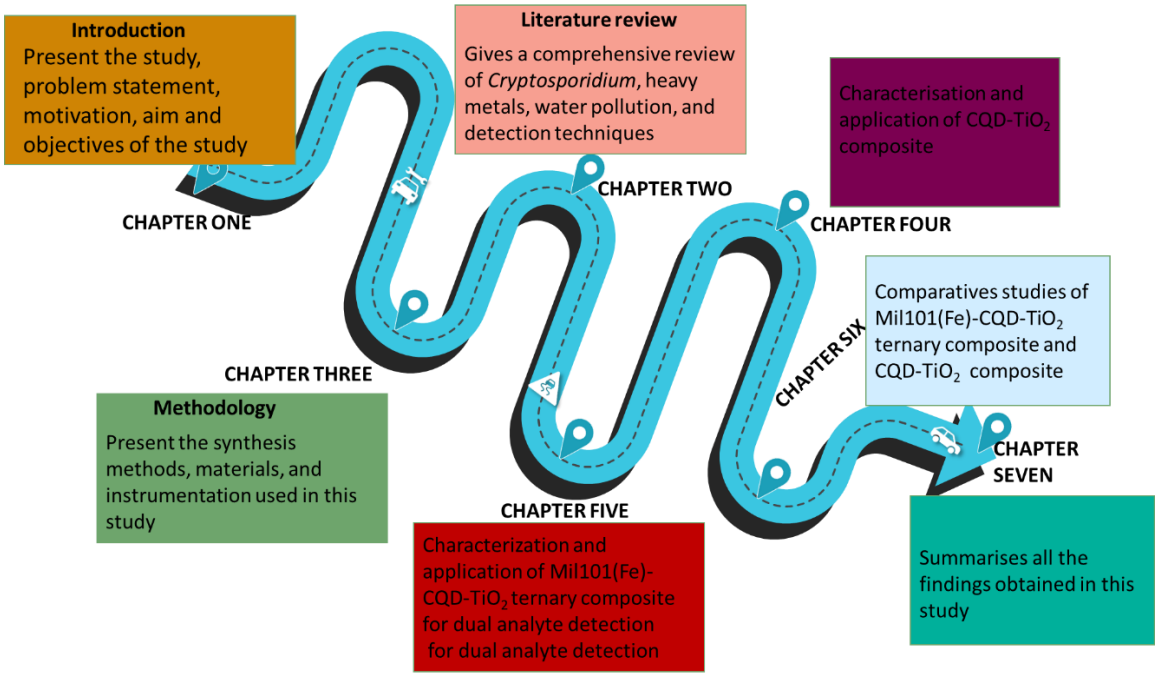

CHAPTER TWO:

Literature review

2.1 Overview

This chapter presents a comprehensive literature review of Crypto, encompassing its various species and traditional detection methods. It highlights the limitations of these methods in delivering sensitive, convenient, and accurate analysis of water samples for this parasite. The chapter also examines the effects of heavy-metal contamination of water. Additionally, it explains the spectroscopic techniques used to detect heavy metals in water sources. The discussion then shifts to the application of biosensors as alternatives for detecting both Crypto and heavy metal ions, examining the different biosensors developed for these purposes. A brief overview of nanotechnology is included, emphasising the potential applications of carbon quantum dot (CQD), titanium nanoparticles (TiO_2), Mil101(Fe), and aptamers in biosensor development.

2.2 Water pollution

All living organisms on Earth rely heavily on water. However, in recent decades, water contamination has become one of the most pressing global issues. Contaminants can enter water supplies through various channels, affecting the safety of drinking water. Millions of people worldwide suffer from waterborne diseases, including cholera, because of exposure to polluted water. Water pollution also affects aquatic ecosystems, introducing contaminants that have detrimental effects. Common water quality issues include decreased clarity, increased turbidity, altered chemical composition, and reduced suitability for human consumption. Certain pollutants are particularly harmful to aquatic life due to their high solubility, extreme toxicity, and long half-lives. The long-term and cumulative effects of water pollution can cause irreversible damage to these ecosystems.

Recently, researchers have focused on monitoring and quantifying pathogens and heavy metal ions in water due to their association with waterborne diseases and the persistence of non-biodegradable heavy metals. This study specifically examines the detection of *Crypto*, arsenic, and cadmium in river water.

2.3 *Cryptosporidium*: A waterborne pathogen

2.3.1 Transmission and Infection

Crypto has been identified as the primary cause of cryptosporidiosis infection [17]. Cryptosporidiosis is a dangerous infection with a high morbidity rate, particularly in low-resource settings [83]. Cryptosporidiosis can occur in any species exposed to sufficient numbers of infectious oocysts. Cryptosporidiosis is a parasitic infection that is more common in rural areas, primarily due to inadequate sanitation and increased exposure to animals. This infection can affect any species that comes into contact with contagious oocysts. Thus, exposure to farms or zoos with infected animals can facilitate the widespread transmission of the parasite. Common symptoms of cryptosporidiosis include vomiting, headaches, nausea, fever, abdominal pain, loss of appetite, and watery diarrhoea. Children under 12 months of age and adults over 70 years are particularly at risk of this infection. In children, the symptoms can persist for several years. Additionally, in individuals with chronic diseases such as HIV/AIDS or cancer, cryptosporidiosis can lead to severe complications or even death. Research by Morre et al. [84] has shown that malnutrition is both a consequence and a contributing factor to cryptosporidiosis in children under 12 months of age. Infected animals and humans release *Crypto* oocysts into the environment, which are then transmitted via the faecal route through ingestion of food containing oocysts or contaminated water. Oocysts can survive in the environment for over 16 months due to their thick protective wall. The small size of the oocysts (4-6 µm) and low infectious dose make them easy to spread in areas with poor hygiene and sanitation [85]. Cryptosporidiosis outbreaks have been documented since the 1980s. A significant outbreak occurred in 1993 in Milwaukee, Wisconsin, where over 403,000 people were affected out of a population of 1.6 million, leading to 56 potential deaths [86].

2.3.2 Environmental contamination

Crypto oocysts enter water bodies through agricultural runoff, increased rainfall, climate change and sewage discharge. Their presence in water bodies can harm marine ecosystems and pose health risks to people who drink river water. *Crypto* oocysts are highly resistant to one of the treatment methods, making their elimination very challenging [87]. As a result, even after treatment, there is a risk that oocysts may remain in water supplies and potentially spread, especially in residential areas [88]. The low levels of *Crypto* oocysts in water supplies make it challenging to detect this pathogen. Therefore, monitoring *Crypto* in water bodies is essential. Several techniques have been employed to detect *Crypto* in these environments, including both molecular and microscopic methods. Detecting *Crypto* oocysts is crucial for monitoring the widespread infections caused by this parasite and for preventing potential outbreaks. Over time, various spectroscopic and microscopic techniques have been developed and utilized to identify *Crypto* in water. These methods were adapted from those used initially to detect Giardia oocysts in environmental samples [89].

2.4 Standard Detection Methods for *Crypto*

2.4.1 Microscopic methods

Researchers have extensively used microscopic techniques to detect *Crypto* oocysts in food and water. However, the lack of distinct morphological traits makes the detection of oocysts using light microscopy unreliable [90]. As a result, several staining techniques have been used as alternatives to microscopic techniques to differentiate oocysts from other environmental residues. The most frequently used method is the acid-fast stain, also known as the Ziehl-Nelsen stain. Although these staining techniques are effective for detecting oocysts in clinical settings, they have limitations, including low specificity and sensitivity, as well as variability in stain uptake [91].

2.4.2 Immunology-based technique: enzyme-linked immunosorbent assay (ELISA)

Immunological methods are advantageous over microscopic methods, particularly in sensitivity, accuracy, and selectivity for detecting *Crypto* oocysts. Scientists have studied immunological-based techniques to overcome the limitations of microscopic techniques [51]. Immunological essays are essentially based on specific interactions between antigens and antibodies. The essays are exceptionally selective and accurate as they utilise immobilised antibody-antigen detection. The enzymes used in ELISA tests are crucial for their effectiveness in quantifying target analyte concentrations [92]. Horseradish and alkaline phosphatase are two common enzymes utilized in these tests [93]. The ELISA process was further explained by Sakamota et al. [94]. The enzymatic reaction then produces a coloured product, indicating the presence of the antigen in the test. ELISA can be categorized into three types, namely direct, indirect and sandwich ELISA, as illustrated in Figure 3 [95].

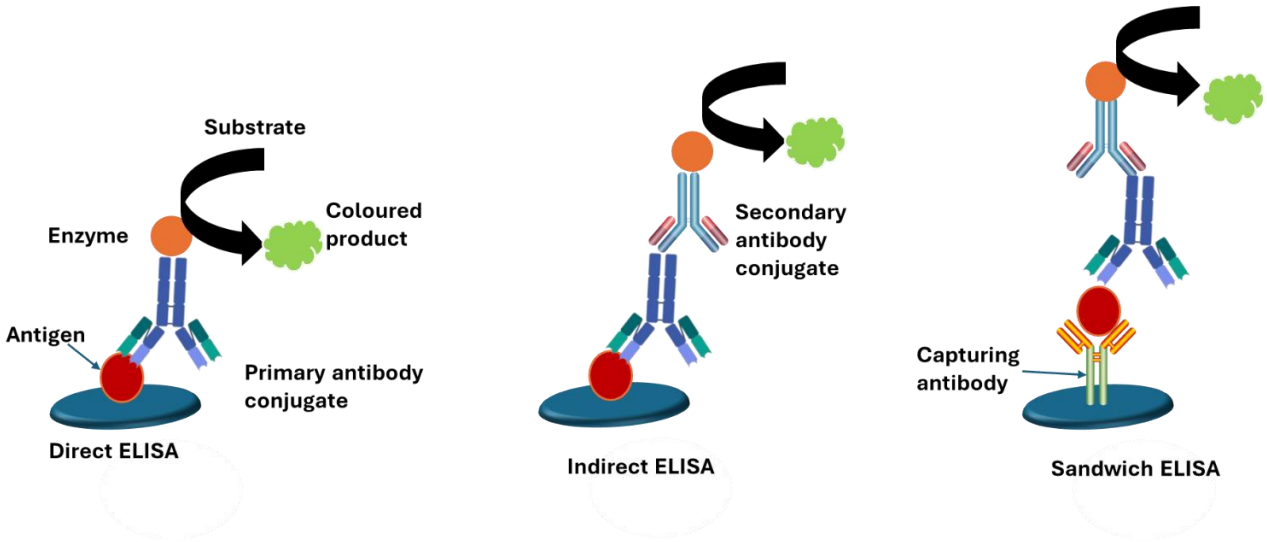

Figure 3: Different approaches to the ELISA technique

Several studies have employed ELISA to detect Crypto oocysts in various samples. For example, Nydam et al. [96] conducted a study focused on faecal analysis to diagnose exposure to *Crypto* oocysts using serum ELISA. This method demonstrated a relatively high sensitivity of 97% and a low specificity of 4%. Another study by Kapel et al. [97] focused on detecting *Crypto* oocysts in stool samples. The authors used ELISA, which requires minimal training. In their analysis, they tested 88 oocysts,

achieving a sensitivity of 98.6%, a specificity of 94.3%, and a positive predictive value of 89.89%.

Although ELISA is known for its sensitivity and high specificity, it has several drawbacks. Additionally, it can be expensive, leading to potentially false-positive results. Furthermore, the process is time-consuming, requires modern facilities and complex equipment, and needs skilled personnel to administer correctly. Moreover, the cross-reactivity with closely related antigens, improper storage protocols, inconsistency between tests and readers, and use of incorrect preservation temperatures [98]. All of these drawbacks prevent ELISA methods from being used for on-site detection [94].

2.4.3 Molecular methods: PCR

The drawbacks of immunological methods and microscopic techniques have led to the development of DNA methods, such as the PCR [99]. PCR has gained recognition for its high sensitivity, selectivity, and specificity in detecting *Crypto* oocysts compared with other methods [100]. This method was first applied in the detection of *C.* parvum in 1991 [101]. Since that time, PCR methods have been modified and employed in the detection of different species and subtypes of *Crypto* [102]*.* PCR is favoured by scientists over microscopic and immunological techniques because it can quantify even the smallest number of oocysts in a sample, utilising qualitative PCR (qPCR) [103]. Furthermore, qPCR is sensitive enough for simultaneous detection without the need for antibody binding, which saves both time and costs in identifying specific agents [104]. The PCR detection method consists of five processes. The first process involves breaking open the oocysts using methods such as boiling, freeze-thawing, and the use of beads. This is followed by preparing a PCR mixture containing primers specific to the desired analyte and the extracted DNA. The third process involves amplifying the DNA target product, followed by its purification. The final step involves visualising and separating the amplified product by gel electrophoresis. This approach is favourable due to the flexibility of primer design, which enables PCR to quantify target analytes without calibration.

The PCR technique has been effectively used for detecting *Crypto* oocysts in environmental samples. For instance, Stephan et al.[105] conducted the detection of oocysts in stool samples using the PCR assay. Their analysis demonstrated sensitivity as low as 200 oocysts g^{-1} of faeces. Additionally, Liu and his co-workers [106] also, a study was conducted to focus on the rapid detection of oocysts in diarrheic cattle faecal samples. Their PCR essay showed an excellent LOD of 14.2 oocysts with a sensitivity of 91%. Although the PCR methods have shown some promising results, they have certain limitations. There is a potential risk of contamination due to the multiple steps involved in DNA amplification and manipulation, making it unsuitable for on-site detection. Scheme 1 illustrates the PCR method.

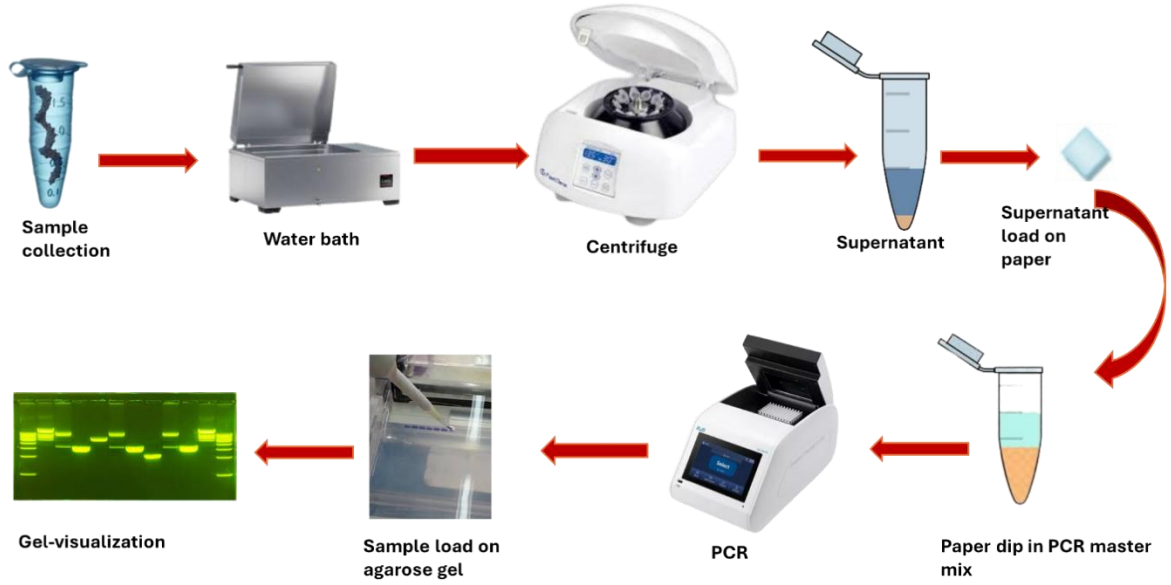

Scheme 1:Shows the schematic representation of the PCR method.

2.4.4 Loop-Mediated Isothermal Amplification (LAMP)

Loop-mediated isothermal amplification (LAMP) is a novel technology that has been identified as a promising diagnostic tool for detecting Crypto in water samples [107]. LAMP has substantial advantages over ELISA and PCR for detecting oocysts, particularly at low concentrations in environmental samples [108]. Comparative studies

using PCR, ELISA and LAMP for detecting oocysts have been investigated and reported [109]. For example, Iran et al. [110] found that LAMP achieved excellent limits of detection compared with PCR, ELISA, and IFA. Additionally, a study by Koloren and colleagues compared PCR with LAMP for detecting oocysts in water samples. The findings of this study indicated that LAMP technology can detect oocysts in low concentrations with a detection limit of 1.8 fg. In contrast, the PCR method had a detection limit of 100 fg [111]. Furthermore, Rabbee and his coworkers investigated the detection of oocysts using qPCR and LAMP technology. The result showed that both qPCR and LAMP exhibited higher sensitivity with low limits of detection of 0.17 μL^{-1} for LAMP and 0.3 copies μL^{-1} for qPCR [112]. While LAMP is a swift and efficient technology, it suffers from some drawbacks, including the limited availability of *Crypto* species sequences for primer design [113].

2.5 Heavy metals

2.5.1 Classification and Sources

Heavy metals (HMs) are elements in the periodic table with atomic numbers greater than 20 and densities above 5 g cm^{-3}, exhibiting metallic properties [114]. They are classified into two categories: essential and non-essential heavy metals. Essential heavy metals include cobalt (Co), iron (Fe), zinc (Zn), manganese (Mn), nickel (Ni), and copper (Cu) [115]. These metals are vital for living organisms and plants, playing crucial roles in essential processes such as organ development, growth, and metabolism [116]. In plants, these metals serve as cofactors that are both physically and functionally necessary for enzymes and other proteins. Although essential heavy metals are required for the health of plants and living organisms, they must be present in very low concentrations, typically around 10-15 parts per million (ppm) [117]. Non-essential heavy metals include cadmium (Cd), chromium (Cr), lead (Pb), arsenic (As), and mercury (Hg), which are considered toxic metals because they lack established biological functions [118]. These metals present significant health risks as they can cause damage even at very low concentrations [119]. Heavy metals can enter water bodies in significant amounts through various channels, including agricultural runoff, industrial discharges, wind-blown soil particles, fossil fuel combustion, improper waste disposal,

volcanic eruptions, rock weathering, biological processes and untreated wastewater. Additionally, mining poses substantial risks to the environment, as it can spread and displace heavy metals to surrounding areas through windstorms and flooding. Furthermore, sewage effluent often contains high levels of heavy metals, which can contaminate both water bodies and aquatic ecosystems [120]. The primary sources of potentially harmful heavy metals include the following paint production, earth's crust, pesticides, textile dyes, phosphate fertilizers, stainless steel production (which produces, Ni), Electroplating (which produces chromium, Cr), Forest fires (which release mercury, Hg), Agrochemical waste (which contains cadmium, Cd), Smelting and fertilizers (which can release arsenic, As).

2.5.2 Health impacts

Humans and animals are exposed to potential toxic heavy metals through food, air, and water worldwide. Currently, HM contamination has significantly impacted water quality, posing a considerable risk to both freshwater and marine environments [121]. Water pollution caused by heavy metal ions affects not only water sources but also biodiversity, community health, and economic activities [122]. Elevated levels of heavy metals in the bloodstream can lead to harmful cardiovascular effects, including arterial stiffness and increased heart rate. High levels of these metals can result in neurotoxic effects, such as cognitive impairments and neuropathy, as well as non-neurotoxic symptoms like vomiting and stomach inflammation [123]. These effects can increase the risk of poisoning and death. Research has indicated that continuous exposure to cadmium and lead can cause kidney diseases and is linked to a reduced glomerular filtration rate [124]. Additionally, Usuki et al. [125] reported that mercury exposure, even at trace levels of 1 ppm during pregnancy, can negatively affect brain development. To address this matter, the WHO has established maximum allowable concentrations of heavy metal ions in water, as summarised in Table 1. However, maintaining these standards is challenging due to the non-biodegradable nature of heavy metals, which leads to their accumulation in water bodies over time and increases the concentrations [126]. To address this issue, scientists have explored spectroscopic techniques to monitor and quantify even the lowest concentrations of these metals.

Table 1:Summarises the allowable concentrations of heavy metals in water and their health impacts on humans.

Heavy metal	Allowed limit (mg/L)	Health impact	Reference
Cadmium (Cd^{2+})	0.003	Respiratory system, kidney damage	127–129
Lead (Pb)	0.01	Nervous system, abdominal pain	134,135
Arsenic (As^{3+})	0.01	Cancer and cardiovascular disease	132,133
Mercury (Hg)	0.006	Lung damage, the immune nervous system	130,131
			136,137
Chromium (Cr)	0.05	Hypotension and liver damage	

2.5.3 Spectroscopic Detection Methods for Heavy Metals

Spectroscopic methods are widely employed for the detection of heavy metals in water due to the selectivity and sensitivity of these methods [138]. These methods include X-ray fluorescence (XRF), inductively coupled plasma optical emission spectroscopy (ICP-OES), ion chromatography with ultraviolet-visible detection (IC-UV Vis), AAS, inductively coupled plasma atomic emission spectroscopy (ICP-AES), ICP-MS, and others. Each of these techniques plays an important role in environmental monitoring and analysis [139] .

2.5.3.1 Inductively coupled plasma atomic emission spectroscopy

ICP-AES is a versatile analytical technique used for the identification of a wide range of elements in water and soil samples [121]. It is particularly effective for analysing metalloids and heavy metals because of its precision and ability to accurately detect multiple elements at extremely trace concentrations in the part per billion range [140] . Additionally, ICP-AES can achieve temperatures of up to 5500K – 6500K, which is sufficient to ionize many elements. This high excitation level yields a significant atomization rate and overall high sensitivity. The versatility and sensitivity of ICP-AES make it suitable for a wide range of applications, including large-scale environmental water analysis. Researchers have used ICP-AES to detect cadmium and arsenic in water samples. For example, Oshima and colleagues conducted a study to determine arsenic levels in water samples using ICP-AES. The results revealed a standard deviation of 3% and a detection limit of 0.004 ng L^{-1} [141]. However, ICP-AES has several drawbacks, including issues with reproducibility, suboptimal detection capabilities, poor detection limits, high costs, and potential for spectral interferences[142].

2.5.3.2 Atomic absorption spectrometry (AAS)

AAS is one of the earliest commercially established analytical methods for heavy metal analysis [143]. It is a quantitative analysis method that uses the sample's atomic vapour to absorb specific wavelengths of light. The method comprises five major components: an atomization system, a light source, a spectroscopy system, a detection system, and a display device [144]. AAS has several advantages, including high sensitivity, accuracy achieved through calibration curves, low detection limits, cost-effectiveness, minimal interference, and high selectivity [145].

Over the past few decades, several investigations have been conducted to identify heavy metals in both environmental and biological samples using AAS[146] . Although atomic absorption spectrometry offers some advantages in determining heavy metals, it still has limitations in terms of sensitivity for certain metals [147]

2.5.3.3 X-ray fluorescence spectrometry (XRF)

Byers et al. [148] define X-ray fluorescence spectrometry (XRF) as an analytical technique that utilizes the unique X-ray emission spectra of a sample. XRF is generally categorised into two types: wavelength-dispersive XRF (WDXRF) and energy-dispersive XRF (EDXRF). XRF works by exciting the sample with an X-ray, causing the elements in the sample to emit characteristic X-rays. A filter collimates these X-rays, which are then detected by a probe, such as a scintillation counter, and converted into electric signals. This technique comprises a spectroscopic detection system, an X-ray generator, and a counting and recording system. Additionally, XRF offers several advantages, including simplicity, accurate analysis, the ability to perform rapid analysis.

2.5.3.4 Inductively coupled plasma mass spectroscopy (ICP-MS)

ICP-MS is an effective technique for quantifying a variety of heavy metals [149]. This technique utilises plasma to neutralise ions from the sample, which are then directed into ion optics before being processed by the mass analyser according to their mass-to-charge ratios [150]. The signal is then amplified by the detector through secondary electron emission, resulting in high analytical sensitivity [151]. Additionally, this technique offers advantages over other spectroscopic methods [152]. Moreover, ICP-MS is recognised as a rapid analytical method with high sensitivity, exceptional spectral resolution, and the ability to analyse multiple elements simultaneously. Furthermore, ICP-MS present substantial advantages when it comes to detecting particles and analysing their interaction within a matrix [153]. This technique offers valuable insights into mass distribution, size, concentration and dissolution [154]. Notably, ICP-MS can detect extremely low concentrations of heavy metals at parts-per-trillion levels, with detection limits influenced by factors such as operating conditions and the sample matrix.

Various approaches have been used to quantify and detect *Crypto* oocysts in water, including spectroscopic and immunoassay methods. However, these methods still suffer from several limitations, including sensitivity, selectivity, portability, and simplicity. Heavy metals have been quantified, monitored, and detected using spectroscopic methods such as atomic absorption spectroscopy. Unfortunately, these methods also have drawbacks, including low sensitivity and selectivity, high costs, and limited applicability to on-site detection. As a result, this study proposes electrochemical methods as an alternative to spectroscopic and immunoassays.

2.6 Electrochemical Detection Methods

2.6.1 Biosensors

A sensor is a device that detects physical changes and converts them to measurable signals [155]. Sensors play a significant role in various systems, facilitating monitoring, automation, and control across different applications [156]. Additionally, they are categorised into different groups, each corresponding to a specific application. For example, gas sensors are designed to detect gases in the environment [157], while thermal fluctuations are monitored using temperature sensors [158], and pressure in liquids and gases [159]. Furthermore, biosensors are a specialised subset of sensors that integrate broad sensing capabilities with biological recognition elements such as aptamers [160], enzymes [161], and antibodies [162], combined with an electrical component to generate measurable signals [163]. The electronic components are designed to record, detect, and transmit information about physicochemical changes [164].

Biosensors come in a wide range of sizes, and they can detect and measure even trace amounts of pollutants at different pH levels [165]. These devices can be used in both biological and environmental samples [166]. Additionally, they offer numerous advantages compared to traditional lab-based detection methods for heavy metal ion

and pathogen detection, including reliability [167], accuracy, cost-effectiveness [168], portability, applicability in low-resource settings, and the ability to achieve low limits of detection [169], and selectivity. Furthermore, biosensors can be used for the dual analyte detection in complex environmental samples [170]. Scheme 2 illustrates the components of a typical biosensor, which include a transducer, a detector, and a recognition element [171]. The selectivity and specificity of the biosensor are determined by the recognition element used [172]. Various types of biosensors used for detecting *Crypto* and heavy metals are outlined in the following sections.

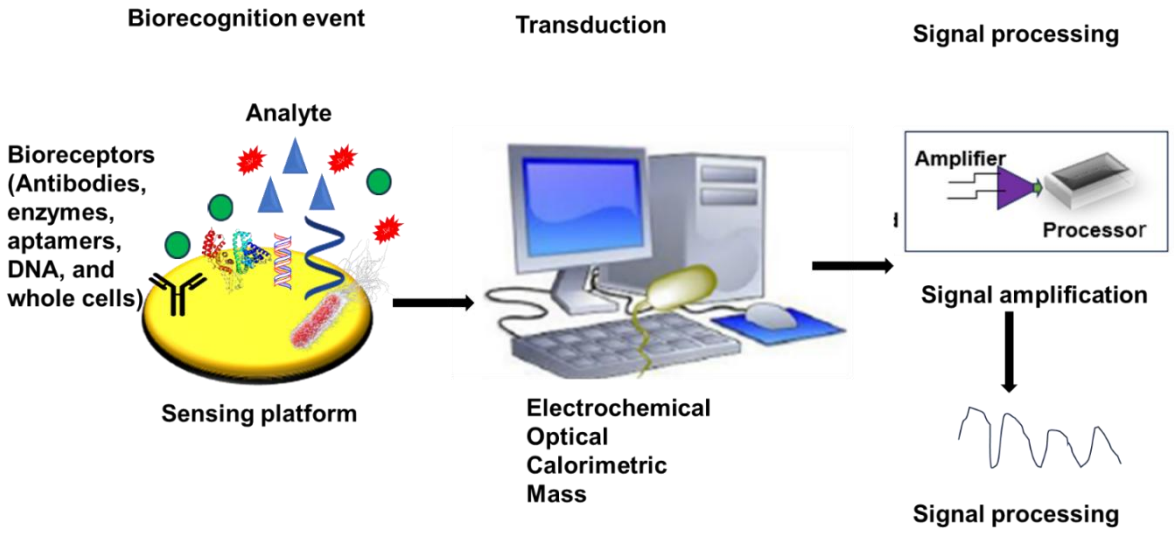

Scheme 2: Schematic representation of various components of biosensor (Reproduced from ref [155]. With permission from Elsevier).

2.6.1.1 Enzymatic biosensors

Enzymatic biosensors were the first type of biosensors developed. Clark and his team were the pioneers in incorporating enzymes onto electrodes for glucose detection [173]. Since their inception, enzymatic biosensors have been researched and utilized across various applications. The target analytes influence the enzymatic reactions within these biosensors, leading to changes in the levels of the resulting products [174]. Enzymatic biosensors offer several advantages, including user-friendliness [175], scalability, rapid processing, and ease of automation [176]. Additionally, enzyme-based

sensors are susceptible, enabling the detection and quantification of analytes at trace concentrations. This high sensitivity is attributed to the vigorous catalytic activity of enzymes and their wide availability for various functions and substrates [177].

A study by Thiruppathiraja and team fabricated an enzymatic sensor to detect *Crypto* [178] in water samples. The use of gold nanoparticles as the electrode modifier has enhanced the electrochemical response of the sensor, thereby achieving an LOD of 3 oocysts L^{-1} [235].

2.6.1.2 Immunosensors

Antibodies are a large family of glycoproteins produced by specific immune cells to recognise harmful antigens, such as chemicals and microorganisms [179]. They can bind to these antigens, resulting in long-lasting interactions between antibodies and antigens. Antibodies serve as biorecognition elements in the development of antibody-based biosensors, also known as immunosensors [180]. Immunosensors are devices that detect analytes through specific interactions between antibodies and antigens [181]. They can be classed according to the transduction process used, such as microgravimetric, optical, colorimetric, and electrochemical [182]. Additionally, immunosensors are categorised into two types: labelled and unlabelled immunosensors [183]. Unlabelled immunosensors are designed to accurately detect antibody-antigen interactions by evaluating the physical changes that occur upon formation. In contrast, in labelled immunosensors, the target analyte is attached to the marker that is sensitively detected.

Immunosensors offer several advantages, including high sensitivity and selectivity, as well as greater accuracy compared to traditional analytical methods. Several studies have been conducted for detecting various pollutants using immunosensors. As a result, Deng and colleagues [184] developed a sensitive immunosensor to detect *Crypto* oocysts in water samples. The reported sensor showed an LOD of 4 oocysts L^{-1} with a linear response range of 6-1600 oocysts L^{-1}. Additionally, Luka et al. [185] proposed an on-chip-based immunosensor for the label-free detection of *Crypto* oocysts in water samples. The fabricated sensor quantified oocysts in a linear range of 0-300 oocysts with an LOD of 20 oocysts L^{-5}. Furthermore, Saroja et al. [186] investigated the detection

of *Crypto* oocysts using an electrochemical-based sandwich immunosensor with an LOD of 3 oocysts L^{-1}. The immunosensor demonstrated good stability over time, with acceptable precision, making it suitable for detecting other pollutants. Another study by Houssin et al. [77] proposed a utilization of electrochemical impedance spectroscopy to detect *Crypto* in water samples. The device features four sensors mounted on a Pyrex substrate, with each sensor comprising interdigitated electrodes 4 mm wide, produced using traditional lithography. Additionally, the sensing platform includes four PDMS wells aligned with the sensor array. This designed sensor has a detection limit of less than 10 cells L^{-1}. The sensor was reported to have a low sensitivity, which is regarded as a limitation in biosensors

Jiang and the team developed an immunosensor for the label-free detection of Cd^{2+} in water and an LOD of 2 ng $L^{-1,}$ as well as a linear range (LR) of 5 ng L^{-1} - 50 ng L^{-1} [187]. Another study by Guo et al. [184] investigated the use of immunosensors for detecting arsenic concentration in seawater. The study showed an LR of 0.0071 to 1.125 µM.

2.6.1.3 Aptasensors

Aptasensors, employ aptamers as biorecognition components. Aptamers are short, single-stranded oligonucleotides of deoxyribonucleic acid or ribonucleic acid (either ssDNA or RNA), typically composed of 25 to 80 bases [188]. They specifically bind to target molecules and are considered a promising alternative to monoclonal antibodies, enzymes, and cells. Their tertiary structures, which include quadruplexes and internal loops, enable them to bind a wide range of targets, from small to large molecules. This results in the development of a diverse range of aptamer-based biosensors. Additionally, they are widely used in molecular biology, biotechnology, and healthcare due to their ease of synthesis, modification, target recognition capabilities, and stabilisation [189]. Aptasensors offer advantages over other biosensors, including cost-effectiveness, enhanced stability in diverse environmental applications, the ability to be customised for specific targets, high selectivity, and excellent sensitivity [190]. Recently, researchers have explored aptasensors for detecting pathogens and heavy metals in biological and environmental samples.

Moakhar and colleagues fabricated an electrochemical microfluidic aptasensor to detect *Crypto* oocysts in water. The electrochemical detection was performed at varying concentrations and demonstrated an acceptable limit of detection of 10 oocysts L^{-1} [191]. Another study by Angus et al. [192] focused on detecting *Crypto* oocysts in field water samples using an optical microfluidic biosensor. The study achieved a limit of detection of 1 oocyst L^{-1} with a linear range of 3 - 10 oocysts.

Zhan and colleagues fabricated an aptasensor for the sensitive determination of Cd^{2+} in water. The sensor showed an LR of 0.15-0.49 ng L^{-1} and an LOD of 0.20 ng L^{-1}, both below the WHO-set acceptable concentration limit. The sensor was considered suitable for in situ environmental monitoring of other pollutants based on the results obtained [193]. In a recent study by Zaras et al. [194] a label-free on-chip biosensor was introduced for detecting Cd^{2+} in water samples, achieving a detection limit of 9.5 ng L^{-1} and a linear range of 10–50 ng L^{-1}. Additionally, Wenjie et al. [195] proposed an electrochemical aptasensor for the determination of cadmium ions in tap water. The reported sensor exhibited a limit of detection of 0.00234 ng L^{-1} and a linear range of 0.001- 100 ng L^{-1}. Moreover, Mushiana et al. [196] detected arsenic concentrations in river water. The sensing platform showed a detection limit of 0.092 ng L^{-1} . Sara et al. [197] also reported an electrochemical aptasensor for arsenic detection in water. The sensor showed a detection limit of 0.12 ng L^{-1}, which is below the WHO concentration limit for arsenic in water. Furthermore, Hassan and colleagues demonstrated a dual detection of Cd^{2+} and Pb^{2+} in river water. The study achieved an LOD of 146.2 ng L^{-1} for Cd^{2+} and 58.8 ng L^{-1} for Pb^{2+} [198].

Biosensors present several advantages over conventional methods. However, they also face some challenges, including low limits of detection, selectivity, and sensitivity. To address these limitations, it is essential to integrate biorecognition elements with nanomaterials. The incorporation of nanotechnology has significantly enhanced the capabilities of biosensors, which are already impressive. By utilising nanomaterials, such as carbon-based materials and metal oxide nanoparticles, the performance of these sensors can be significantly enhanced, resulting in improved sensitivity, selectivity, and detection limits. The application of nanomaterials not only increases the surface area of the sensors but also enhances their electrocatalytic activities and improves the effective immobilisation of biorecognition elements on the electrode surface. The integration of nanomaterials and bio-recognised elements are used.

Furthermore, the development of new nanomaterials demonstrates significant potential for creating innovative aptasensors.

2.7 Nanotechnology in Biosensing

Nanoscience is a branch of science and engineering that explores the unique properties and phenomena of materials at scales ranging from 1 to 100 nanometres (nm) [199]. Nanotechnology is an expanding field that has garnered significant interest within the scientific community due to its potential applications in detecting, preventing, and addressing hazardous environmental chemicals [200]. The advancement of this emerging technology relies on the successful development and production of various nanomaterials and their applications across sensing, energy, food safety, and medicine [201]. Nanomaterials present significant opportunities for developing smart devices that aim to enhance environmental sensing and monitoring, thanks to their remarkable catalytic abilities, stability, electrical and thermal conductivity, optical characteristics, and flexibility [202]. The integration of nanotechnology into biosensing can achieve numerous advantages, including a large surface, enhanced expression of biological transduction and signalling systems, and improved electrochemical properties [203].

Recent research has highlighted the simplicity, sensitivity, and selectivity of various nanomaterials, including gold, iron, titanium dioxide, zinc oxide, silica, carbon, nanoparticles, polymers, silicon, silver nanowires, and quantum dot [204]. These nanomaterials have been widely utilised in environmental and sensing applications because they can be customised to create unique features for specific purposes. Due to their numerous reactive sites, nanoscale materials can exhibit high reactivity, facilitating increased interaction with contaminants and allowing for the rapid reduction of contaminant concentrations [205]. As a result, nanomaterials have largely replaced rigid, thick, and bulky materials in environmental sensing, monitoring, and detection due to their superior properties [206]. Researchers synthesize nanomaterials using various approaches, including biological, physical, and chemical methods. These synthesis methods are essential for modifying the properties and performance of

nanomaterials, particularly for biosensor development and other applications [207]. Increasingly, chemical, physical, and green synthesis methods are being utilised to produce nanoscale materials [208]. However, green synthesis methodologies are gradually replacing traditional physical and chemical processes due to high energy consumption and the emissions of hazardous compounds [209]. Figure 4 shows the different types of nanomaterials. To enhance the properties of nanomaterials, research has concentrated on the synthesis of nanocomposites and ternary composites.

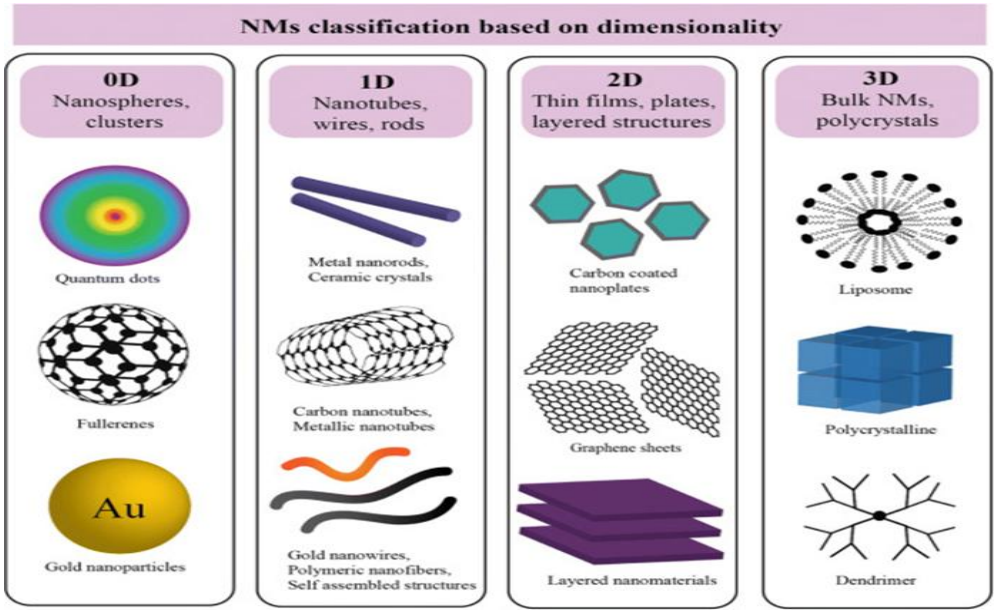

Figure 4: Shows different types of nanomaterials. Reproduced with permission from Ref. [210] Copyright© 2018 Springer Nature.

2.7.1 Carbon quantum dot

Carbon dot are zero-dimensional nanostructures less than 10 nm in all dimensions, were discovered accidentally by Xu et al. [211] in 2004 while they were purifying single-walled carbon nanotubes (SWCNTs) [212]. These nanostructured materials are classified into three categories: (1) polymer dots (PD), (2) carbon nanodot (CD), and (3) graphene quantum dot (GQD). Although carbon is generally not very soluble in water, carbon quantum dot (CQD) have numerous carboxyl groups around their edges, which makes them highly soluble in water.

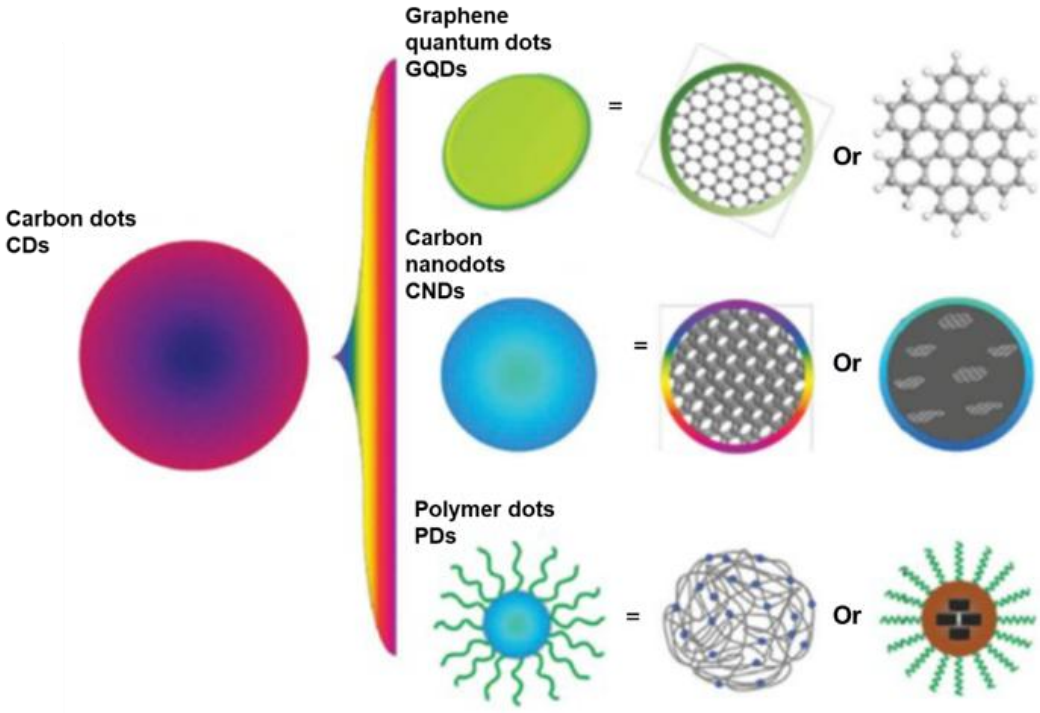

Figure 5: Classification of carbon dot. Reproduced with permission from Ref. [213] Copyright© 2015 Tsinghua University Press.

Researchers have recently discovered carbon quantum dot (CQD), a class of carbon nanomaterials that have generated considerable interest as potential alternatives to carbon nanotubes, graphene, and fullerenes [214]. These nanomaterials demonstrate promising applications in various fields, including biosensing [215], bioimaging [216], drug delivery [217], biomarker detection, food analysis [218], disease treatment, and drug

formulation. CQD are favoured over conventional semiconductors due to their high tunable fluorescence, low toxicity, high stability, resistance to photobleaching, and excellent cellular compatibility [219]. Structurally, CQD exhibits unique particulate formations at the nanometre scale (less than 10 nm), with carbon atoms typically arranged in hexagonal configurations, similar to those found in graphene [220]. Researchers synthesise carbon quantum dot using various methods, including hydrothermal treatment, chemical oxidation, pyrolysis of carbon precursors [220], microwave-aided synthesis, and green synthesis [221]. For example, Ghosh et al. [222] Produced CQD from potato peels using a green synthesis method. In this study, CQD were created through an eco-friendly and economical hydrothermal process. Green synthesis often employs renewable, affordable, and abundant natural resources, such as plant extracts, fruit peels, and other organic waste [223]. These materials are not only environmentally friendly but also contribute to waste reduction. The synthesis of CQD via green chemistry is advantageous because it provides cost-effective and safer alternatives to traditional methods [224]. Additionally, this approach yields high-quality, non-toxic, and biocompatible materials suitable for a variety of applications. Huang et al. [225] developed carbon quantum dot through a one-pot hydrothermal method, using a by-product from the biorefining process as the carbon source. They analysed the morphology, structure, and optical properties of the CQD using various characterisation techniques. Their findings revealed that the CQD had a size distribution ranging from 2.0 - 6.0 nm, a high proportion of sp^2 and sp^3 carbon bonds, and exhibited blue-green fluorescence emission.

Further modifications through repeated carbonisation and polymerisation enable precise control over the chemical properties, surface functionalization, passivation, fluorescence tuning, and other physical and biological characteristics of these materials [226]. Researchers attribute the enhanced performance of these nanomaterials to factors such as stability, biocompatibility, reactivity, conductivity, high surface area and structural tunability. Additionally, easily adjustable functional groups are tailored to improve interactions with target analytes or contaminants [227]. For example, Wang et al. [228] utilised CQD in clinical practice, demonstrating exceptional effectiveness in guiding precision surgery for papillary thyroid carcinoma. In contrast, Chen et al. [229] developed a CQD-based biosensor to detect pesticides in water. Additionally, Zhang et al. [230] developed GQD-based biosensors for detecting Cu^{2+} in water bodies. This

biosensor demonstrated high sensitivity, with a linear concentration range of 0 to 8 ng L^{-1} and a detection limit of 0.29 ng L^{-1}. Another study by Shayeh and the team reported a CQD-based electrochemical aptasensor for detecting prostate cancer. The sensor showed a detection limit of 2 ng L^{-1} [229].

2.7.2 Organic metal frameworks (Mil101(Fe)

Metal-organic frameworks (MOFs) are crystalline, highly porous materials made up of organic linkers and inorganic metal ions or clusters [231]. Due to their numerous advantages, such as a large surface area, ease of functionalization, adjustable frameworks, controlled active sites, and high stability, MOFs hold great promise for various applications [232]. Researchers have explored metal-organic frameworks (MOFs) and metal-organic frameworks (MILS), a specific type of metal-organic framework, for use in catalysis, energy storage [233] sensing [234]. Mils are commonly synthesised using carboxylates and trivalent cations, and their naming typically reflects the type of ligand, metal ion, and their unique characteristics [235]. For example, Mil53, Mil100, Mil101, and Mil125 are well-known types of metal-organic frameworks (MOFs). Mil101, which contains iron (Fe), is made up of a 1,4-benzenedicarboxylate (1,4-BDC) ligand and an iron (III) cation, and it is recognised for its excellent water stability. Due to their desirable properties, MOFs have been widely utilised for removing organic substances from water [236]. They have successfully extracted dyes, metals [237], pharmaceuticals [238], and pesticides from wastewater [237].

Many MOF materials are currently being studied as potential catalysts for degrading pollutants, owing to their extremely high specific surface area, stability, and low toxicity. [239]. The use of Mil101(Fe) in this study is generally considered safe and environmentally friendly when appropriate conditions are met, such as avoiding high temperatures and using compatible solvents [240,241]. The material exhibits good stability and, when used as a catalyst, minimises the potential for hazardous byproducts. Among various preparation methods, such as diffusion and microwave techniques, the hydrothermal method stands out as a highly competitive option due to its cost-effectiveness and suitability for commercial use [242]. Moreover, the hydrothermal

method operates under low-temperature, isostatic-pressure conditions and liquid-phase reactions, allowing for easy control over the particle size and morphology of the resulting products. Iron (Fe) is not known to pose significant toxicity issues, making it an appropriate choice for applications where environmental safety is a priority. For instance, Wang et al. [243] investigated the use of MIl53(Fe) as a catalyst for degrading tetracycline using hydrogen peroxide (H_2O_2). Additionally, Teng et al. [244] tested the adsorption capabilities of a polyacrylonitrile@carbon composite for the removal of tetracycline.

2.7.3 Titanium dioxide

Titanium dioxide (TiO_2) is a high-resistance n-type semiconductor material with a band gap of approximately 3 eV [245]. Researchers frequently utilise TiO_2 due to its whiteness, corrosion resistance, and photocatalytic properties. Its environmental friendliness, chemical stability, and catalytic characteristics, along with its ability to modulate structural, optical, and transport properties, have established it as a popular choice for applications in photocatalysis, solar cells, and gas sensors [246,247]. Additionally, TiO_2 nanoparticles (NPs) have unique attributes, including easy control, low cost, non-toxicity, and high resistance to chemical erosion [248]. TiO_2 exists in three crystal structures: anatase, brookite, and rutile. Rutile is the most stable phase of titanium dioxide, while anatase and brookite are metastable forms that can be converted into rutile [249]. Heating titanium dioxide at temperatures between 600 and 800 °C irreversibly transforms it into the rutile phase. As an essential photocatalyst, titanium dioxide is particularly active in the ultraviolet range [250].

Titanium dioxide is less expensive than other semiconductors used in water applications and can be easily synthesised in a laboratory. Additionally, TiO_2 has a significant advantage over other semiconductors, such as cadmium (Cd^{2+}) and zinc oxide (ZnO), because it does not release hazardous chemicals during decomposition [251]. In this aspect, it also outperforms traditional chlorination methods. The surface of titanium dioxide is highly adjustable, and the morphology of TiO_2 can be modified to include nanotubes. These nanotubes offer higher mass transfer rates and can adsorb non-biodegradable organic molecules. Additionally, the use of mesoporous surfaces

can enhance ion transport between particles [252]. Titanium dioxide can be synthesised through various methods, including hydrothermal, microwave, chemical precipitation, and the sol-gel process. Among these, sol-gel synthesis is particularly notable for its versatility. It allows precise control over the material's composition, properties, and structure, ensuring uniform porosity and particle size, as well as high purity. Furthermore, this method operates at lower temperatures, making it a user-friendly process that consumes minimal energy. Titanium nanoparticles have also been investigated for a wide range of applications. For instance, Rupesh et al. [253] fabricated a TiO_2-based electrochemical sensor for detecting phenolic compounds in water samples. The sensor exhibited a detection limit of 348 ng L^{-1}. Samuel et al. [254] conducted a study proposing a TiO_2-based electrochemical sensor for detecting nitrite in water, achieving a detection limit of 0.076 ng L^{-1}.

2.7.5 Nanocomposite

A nanocomposite is a solid material made up of two or more materials, at least one of which has dimensions at the nanometre scale [255]. According to Saleh, a nanocomposite combines different materials with nanoscale diameters [256]. The aim of creating nanocomposites is to merge the properties of multiple materials to produce a new nanomaterial with enhanced physical and chemical properties [257]. Additionally, nanocomposites are particularly intriguing because their characteristics often surpass those of the individual materials [258]. The unique mechanical, electrical, thermal, optical, electrochemical, and catalytic properties of composite materials arise from the distinct attributes of each embedded phase [259]. The nanocomposite consists of a solid matrix phase that shapes the platform and a reinforcing phase that enhances functionality [260]. The reinforcing material, which is incorporated at the nanoscale, can be in the form of nanoparticles (such as metals or metal oxides), nanosheets (like graphene oxide) and carbon quantum dot [261].

For instance, in a study by Rahman and colleagues, the team developed an electrochemical sensor for detecting Hg^{2+} in tap water using graphene oxide (GO) and silver (Ag) nanowire nanocomposites. Due to the superior conductivity of the

nanocomposite, the fabricated sensor demonstrated high selectivity for Hg^{2+} [262]. In another study, Thakur et al. [263] demonstrated the effectiveness of GO-based nanocomposites by degrading organic pollutants from water sources. A thorough analysis was conducted by incorporating nanomaterials into the appropriate matrix. The synergistic effects of the new nano-matrix were leveraged to significantly enhance the sensitivity of aptamer sensors. Another study, conducted by Meena et al. [264] of aptamer sensors involved the fabrication of a TiO_2-adenine-based composite for detecting the swine flu virus [264]. This developed sensor demonstrated a high sensitivity of 10.6 μA ng L^{-1}, with an LOD of 6.7 × 10^{-8} ng L^{-1}. Additionally, Liu et al. [265] utilised a graphene-polyaniline nanocomposite film to develop a label-free aptamer-based sensor for detecting dopamine. The study exhibited a LOD of 0.00198 ng L^{-1}. Additionally, Zhang et al. [266] employed a sensitive electrochemical immunosensor based on a gold nanoparticle (AuNP) nanocomposite to detect *Escherichia coli* (E. coli) in water, achieving a LOD of 50 CFU·mL^{-1}. The schematic representation of the biosensor is shown in Scheme 3.

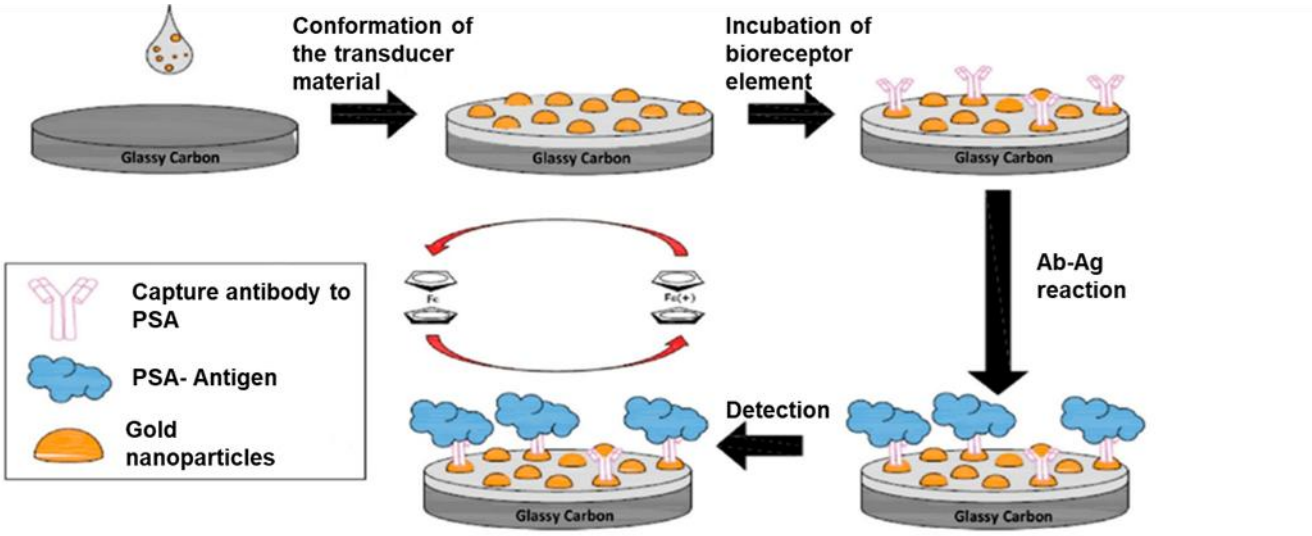

Scheme 3: Schematic representation of gold nanocomposite-based sensor for detecting E.coli in water. Reproduced with permission from Ref. [267] Copyright© 2020 Frontiers.

Wang et al. [241] also examined the effectiveness of MIl88A(Fe) combined with cotton fibres as a catalyst for tetracycline removal. Meanwhile, Hu et al. [268] employed an Fe/Co_3O_4 composite to degrade tetracycline in the presence of sodium persulfate ($Na_2S_2O_8$) under visible light. Suman et al.[269] investigated the use of a TiO_2-silica nanocomposite for the electrochemical detection of ascorbic acid in water. Their method demonstrated an LOD of 383.3 ng L^{-1} and a sensitivity of 269 µA ng L^{-1}. Additionally, Chen et al. [60] in water. This sensor exhibited an LOD of 0.088 ng L^{-1}, which is within the permissible limit for Cd^{2+} levels in water bodies, with a linear range of 0.1 to 100 ng L^{-1}. Huali and the team developed an aptasensor based on a disulfide-Au nanocomposite for detecting Cd^{2+} in river water. The authors noted that the synthesised nanocomposite improved aptamer immobilisation and enhanced conductivity, thereby facilitating electron mobility. The study demonstrated an LOD of 0.0234 ng L^{-1}, with a linear response range of 0.01 - 0.3 ng L^{-1} [270]. Gopinath and colleagues developed a graphene-based nanocomposite for arsenic detection in tap water. The sensor exhibited an LOD of 0.001 ng L^{-1} [271]. Furthermore, Xing and the team utilised a CQD-Mof-based electrochemical sensor for Pb detection in water samples. The sensor showed an LOD of 1.55 ng L^{-1} and good selectivity towards Pb [272]. Lastly, Nguyen et al. [273] conducted research on the development of a sensitive electrochemical immunosensor for detecting Bacillus in water. The team utilised a carbon nanotube (CNT) composite to create this immunosensor. The synthesised composite exhibited excellent selectivity for Bacillus detection, with a linear concentration range of 10 ng L^{-1} - 1000 ng L^{-1} and a LOD of 5 ng L^{-1} . The schematic representation of the sensor is shown in Scheme 4.

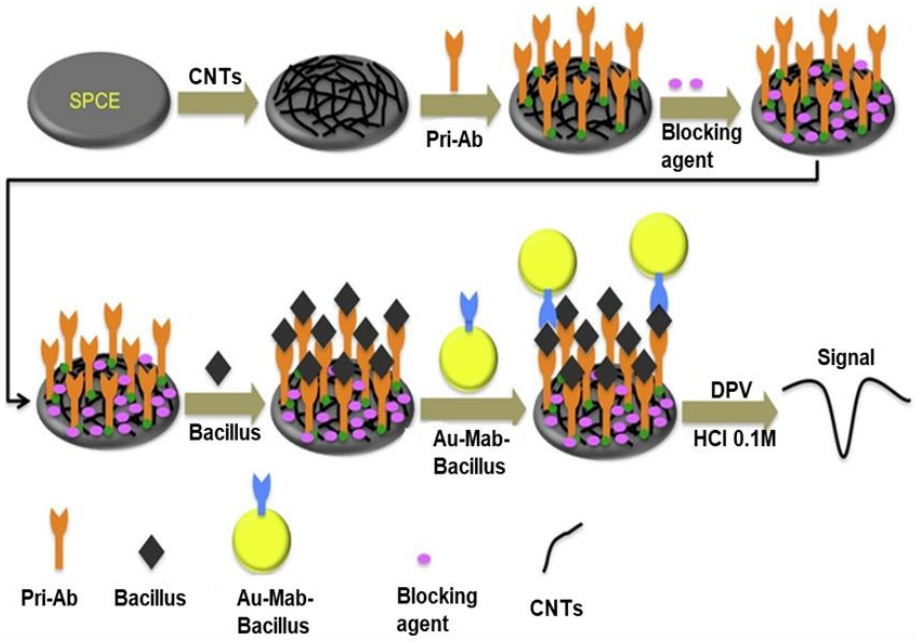

Scheme 4: Display the schematic representation of a CNT-based immunosensor for detecting Bacillus in water samples. It is reproduced with permission from Ref. [273] Copyright© 2019 Elsevier B.V.

Nanotechnology has been shown to improve the sensitivity of biosensors, particularly aptasensors, for detecting various pollutants. Although advances in CQD-based biosensors have been made, no study has explored integrating CQD with Mil101(Fe) into a cohesive platform for the simultaneous detection of protozoa and heavy metals.

2.8 Summary and Sub-conclusion

Conventional detection methods for *Crypto* and heavy metals, such as PCR and ICP-MS, have been used to quantify and monitor *Crypto* parvum and heavy metals in water bodies. However, these methods have several drawbacks, including a lack of selectivity and sensitivity, inapplicability for onsite detection, complexity, high costs, and limitations in achieving low detection limits. These limitations have prompted the development of electrochemical techniques, specifically aptasensors. The incorporation of nanomaterials into aptasensor fabrication enhances both selectivity and sensitivity. Additionally, aptasensors are portable, user-friendly, suitable for on-site detection, and capable of achieving low limits of detection. These characteristics make them excellent candidates for detecting heavy metals and *Crypto* at low concentrations. The integration of aptasensors with on-chip technology further enhances their potential as powerful sensing platforms for water monitoring.

CHAPTER THREE:

Methodology

3.1 Overview

This chapter describes the synthesis methods, materials, and instrumentation used for synthesizing and characterizing the CQD, Mil101(Fe), TiO_2, CQD-TO_2, CQD-TiO_2-MIl101(Fe), nanomaterials and the fabrication of the aptasensor. It also explains the principles of the characterization techniques.

3.2 Chemicals and Materials

3.2.1 Materials

The chemicals utilized in the proposed work are analytical grade. All organic salts, solvents, and buffer solutions were purchased from Sigma-Aldrich. These includes: , bovine serum albumin (BSA), N'N-Dimethylformamide (DMF), terephthalic acid (H_2BDC), absolute ethanol, hydrochloric acid (H_2SO_4, 98%), sodium tetrachloride, alumina polishing powder (99.99%) (1, 0.3, 0.05 µM), polishing pads, 1- ethyl-3.3-dimethylamino propyl carbodiimide hydrochloride (EDC, 98%), titanium isopropyl-oxide (TIP, 97%),N-Hydroxy succinimide (NHS, 98%), dichloromethane (98.8%), sodium hypochlorite, Na_2HPO_4 (≥ 99%) and NaH_2PO_4 (≥ 99%), $FeCl_3 \cdot 6H_2O$, 50 mM Tris-HCl-pH 7.5, cadmium nitrite (98%), and arsenic oxide (96%). Lemons were purchased from the market at Florida. A synthetic aptamer with the sequences (R4-6) ,mini-crypto and crypto primer. *E. coli* sequence: CAT GCC GCG TGT ATG AAGAA, and Giardia sequence; GAC GGC TCA GGA CAA CGGTT were manufactured by Inqaba Biotechnical Industries (PTY) Ltd, Pretoria, South Africa. 100 µM of the oligonucleotides were prepared using 0.1 M PBS, pH 7.2, and kept at –20 °C.

3.3 Instrumentation

Different characterization techniques were used to confirm the synthesis of nanomaterials. Functional groups of prepared materials (CQD and TiO_2, CQD-TiO_2, Mil101(Fe), CQD-TiO_2-Mil101(Fe), were studied using a PerkinElmer FT-IR

spectrometer Frontier, Spotlight (400,) using the pellet KBr. Raman microscope and 532 nm laser was carried out using the WITec alpha300 confocal at (a power of 50×/0.75 *Naa* and 3 mW,*)* objective to examine the chemical bonds and atomic oscillations of the materials. Cu Ka radiation was used to record XRD patterns and confirm the crystallinity of the nanomaterials using a Rigaku Smart Lab X-ray diffractometer, as well as to analyze the surface morphology. The particle size and morphology of the synthesized materials were evaluated using a JEOL JEM 2100 at 200 Kv (HR-TEM) and an EDS detector from Thermo Fischer to detect the energy for the evidence of the elemental composition, while scanning electron microscopy (HR-SEM) (JOEL IT 300) was used to utilize the morphology of the synthesized materials. Thermogravimetric analyser (TGA) (5500) was examined to investigate the thermal stability and composition of the materials over time and the optical properties of the nanomaterials were assessed using Ultraviolet-visible spectroscopy. The elemental composition and oxidation states of the materials were evaluated using X-ray photoelectron spectroscopy. The electrochemical redox properties of the materials were examined using electrochemical techniques, such as SWV, CV, CP, EIS, and CA. The developed electrochemical aptasensor was optimized using to evaluate the electrochemical features of the modified electrodes in a window of -1 - 0.5 V vs Ag/AgCl using EC-lab V11.50 Biologic (Biologic Science Instruments GmbH, Gottingen, Germany, Rodeweg 20, D-37081. Multiparameter, inductively coupled plasma mass spectroscopy.

3.4. Synthesis of nanomaterials: CQD, TiO_2, Mil101(Fe)

3.4.1 Synthesis of carbon quantum dot using the Hydrothermal method

CQD were synthesized using lemon peels as the carbon source [274]. The peels were cleaned several times using DI H_2O and dried at 60 °C for 10 h. 10 g of powdered lemon peel was digested in 100 mL of 0.1 M H_2SO_4 stock solution. The collected product was rinsed with DI H_2O and filtered, then dried at 100 °C for 24 h in an oven. 200 mL of sodium hypochlorite solution was combined with the material and stored for 4 h at room temperature, followed by adjusting the pH to 7. The solution was

transferred into a Teflon reactor and heated at 180 °C for 12 h. Unreacted organic molecules were eliminated by rinsing the samples with DI H_2O several times. The collected product centrifuged for 1,3 h at 500 rpm. The obtained material was dried at 100 °C for 24 h. CQD synthesis is illustrated in Scheme 5.

Scheme 5: Schematic diagram showing the Synthesis of CQD.

3.4.2 Synthesis of Mil101(Fe) using Hydrothermal method

The targeted MIl101(Fe) MOFs were synthesized from AMD-derived Fe $(OH)_3$, wherein 5.2 mmol of AMD-derived Fe $(OH)_3$ was first dissolved in a stoichiometric amount of HCl by heating at minimal temperatures [275]. The solution was then mixed with a solution of dissolved PET-derived terephthalic acid (H_2BDC) in dimethylformamide (DMF). The resultant solution was subjected to hydrothermal treatment at 110 °C for 20 h under autogenic pressure. Once the reaction time had elapsed, the product was filtered, washed using centrifugation, and dried at 90 °C overnight to remove any remaining solvents that may have been trapped in the MOF pores. Scheme 6 shows the schematic synthesis of Mil101(Fe).

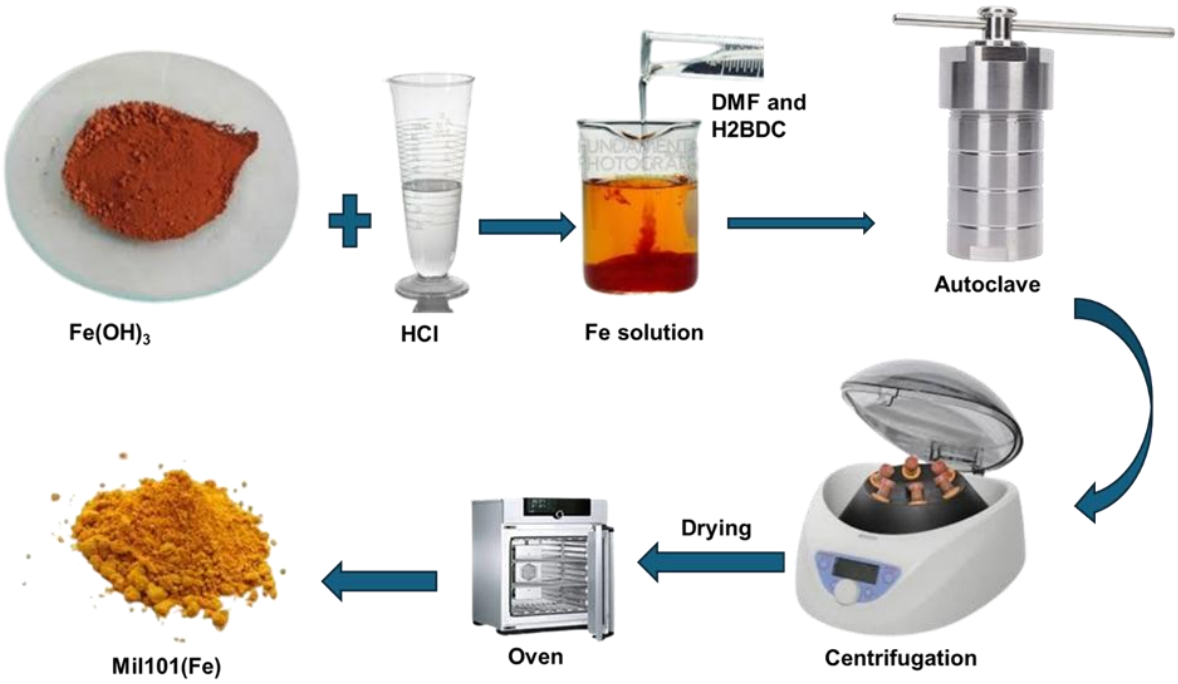

Scheme 6: Shows the schematic representation of Mil101(Fe) synthesis.

3.4.3 Synthesis of TiO_2 nanoparticles using the Hydrothermal method

The synthesized TiO_2 NPs were synthesized as follows. 100 mL of absolute ethanol was added with 6mL of titanium isopropoxide and continuously stirred at ambient temperature for 30 min [276]. Afterwards, 4 mL of DI H_2O was poured to the solution under continuous stirring for 7 min until a white solution was formed. The solution underwent hydrothermal treatment. The autoclave was maintained at 200 °C for 14 h. The resultant material was centrifuged and rinsed three times using DI H_2O. The collected material was dried at 100 °C for 24 h. The collected white powder was calcined at 450 °C for 4 h. Scheme 7 illustrates the TiO_2 synthesis.

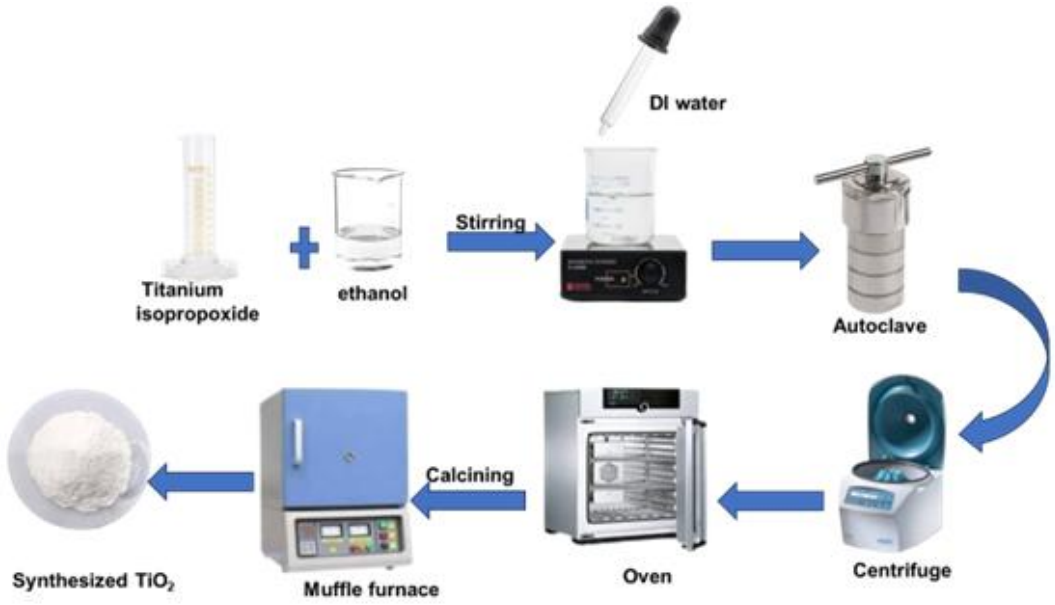

Scheme 7: Schematic representation of TiO_2 synthesis.

3.5 Synthesis of nanocomposites

3.5.1 Synthesis of CQD-TiO_2 nanocomposite using the precipitation method

CQD-TiO_2 nanocomposite was synthesized following the procedure by Adan-mas [277]. 1 g of the synthesized CQD was dispersed in 200 mL of ethanol, and 2 g of TiO_2 nanoparticles were added to the mixture under vortex agitation for 10 min. To this solution, was added. This mixture was stirred at 500 rpm for 30 min at room temperature. The obtained solution was collected by centrifugation, rinsed three times with ethanol, and dried at 60 °C in the oven for 24 h. The schematic representation is shown in Scheme 8.

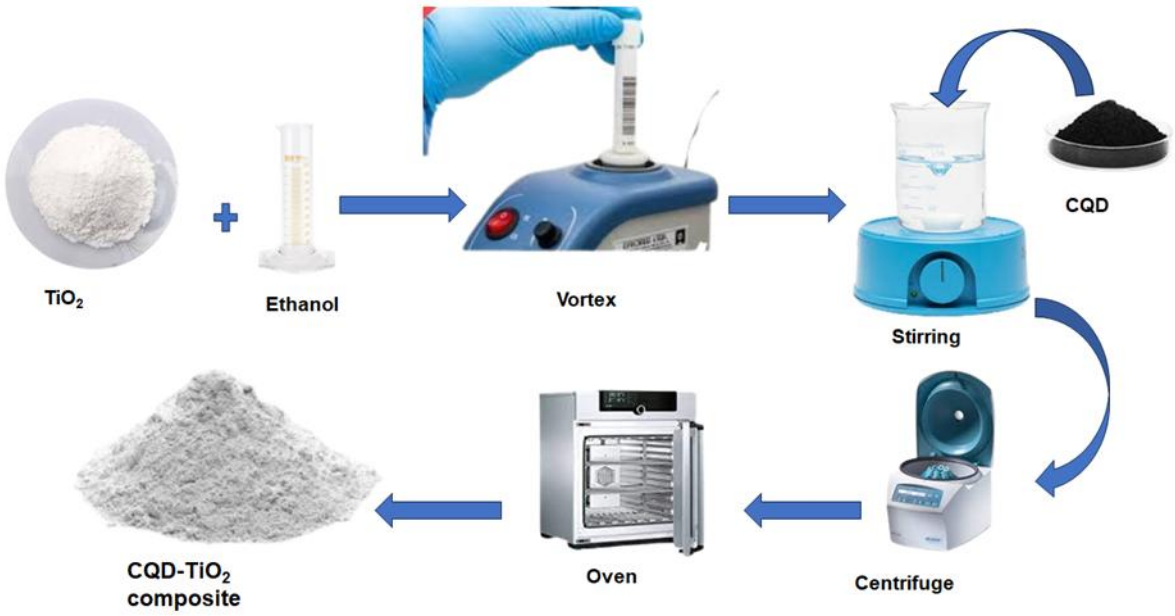

Scheme 8: Schematic representation of CQD-TiO_2 composite synthesis.

3.5.2 Synthesis of Mil101(Fe)-TiO_2 composite using Hydrothermal method

158 mg of prepared Mil101(Fe) was dissolved in 20 mL of DI H_2O. Subsequently, 0.164 mL of titanium isopropyl oxide was added dropwise under stirring [278]. After 20 min, the solution underwent hydrothermal treatment at 200 °C for 24 h. The resulting solution was centrifuged and rinsed with DI H_2O, followed by three rinses with absolute ethanol. The resulting material was dried in an oven set to 70 °C 24 h. The synthesis representation is shown in Scheme 9.

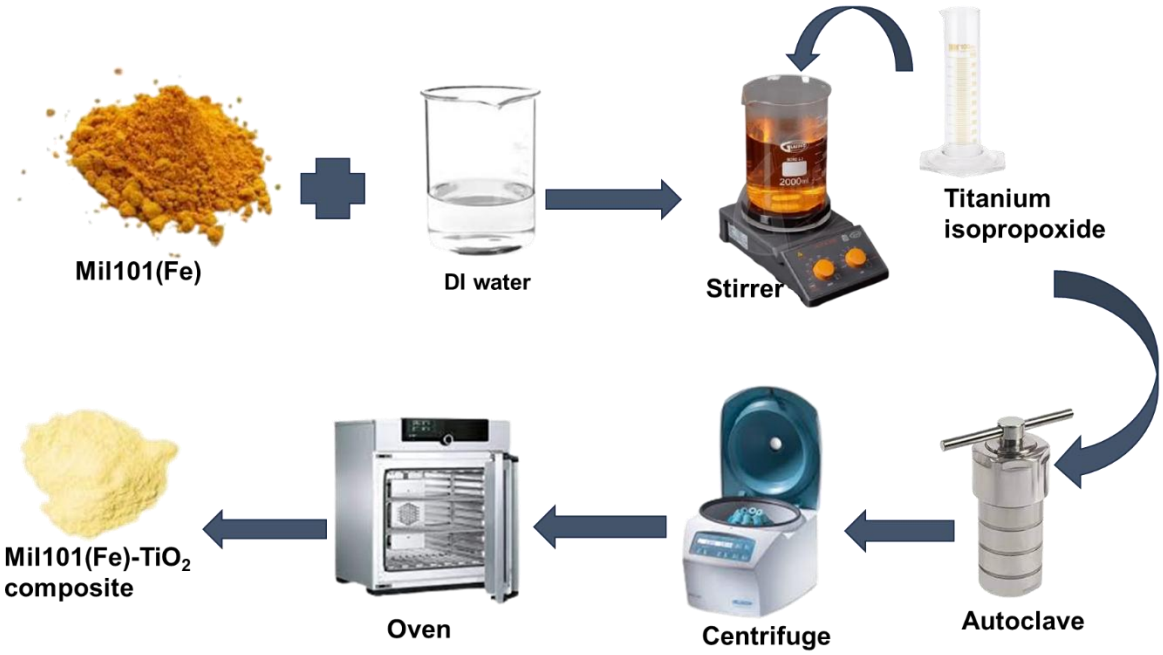

Scheme 9: Schematic representation of Mil101(Fe)-TiO_2 composite.

3.6 Synthesis of a ternary composite

3.6.1 Synthesis of MIl101(Fe) -CQD-TiO_2 composite using Hydrothermal method

0.5 g of the prepared MIl101(Fe) and 2 g of the synthesized CQD-TiO_2 composite were dissolved in 150 mL of DI H_2O. The mixture was sonicated for 2.5 h [279]. The solution underwent a hydrothermal treatment for 12 h at 180 °C. The collected solution was centrifuged and rinsed with absolute 3 times. The resulting product was dried at 60 °C in an oven for 24 h. Scheme 10 shows the Schematic diagram of Mil101(Fe)-CQD-TiO_2 synthesis.

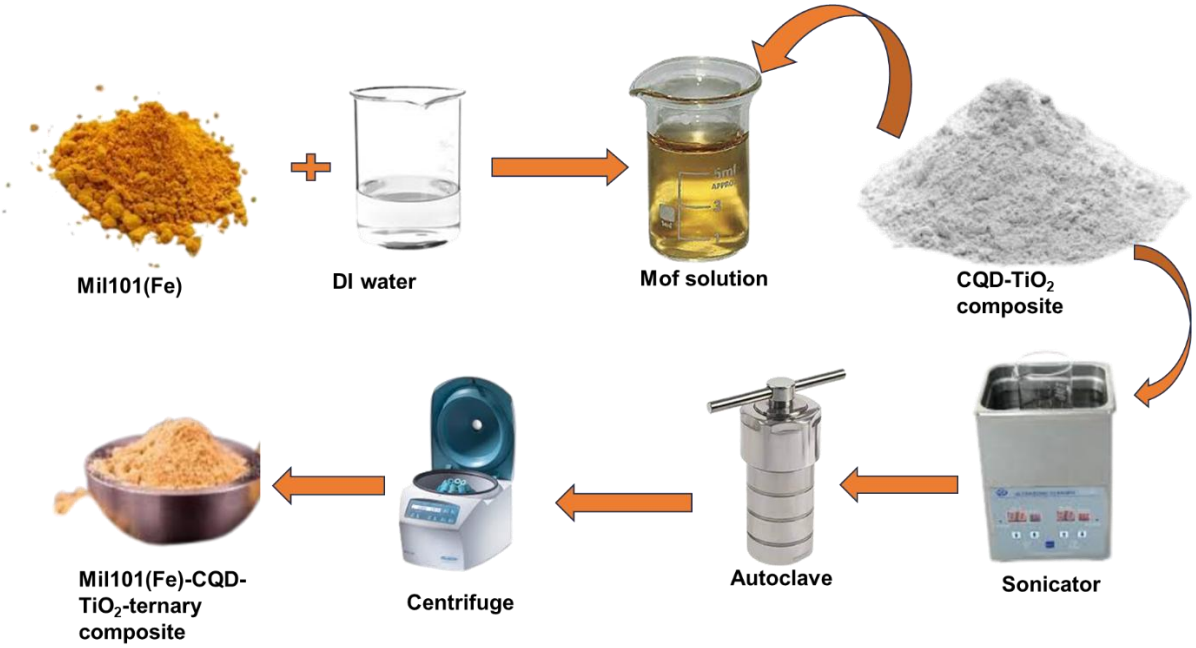

Scheme 10: Schematic representation of Mil101(Fe)-CQD-TiO_2 ternary composite synthesis.

3.7 Fabrication of the aptasensor

The aptasensor was fabricated by incubating the working electrode in a solution composed of 5 mg of CQD-TiO_2 nanocomposite and DI H_2O, along with a 10 µg mL^{-1} aptamer solution. Additionally, 1 mL of a solution containing 8.00 mM 1-ethyl-3,3-dimethylaminopropyl carbodiimide (EDC) and 8.00 mM N-hydroxysuccinimide (NHS) was included. A tris buffer was also added to this solution. The cleaned working electrode was then incubated in the solution at 4 °C for 3 hours. After incubation, the electrode terminal was immersed in a BSA solution for 10 min to block the active sites on the electrode surface. Before fabrication, the working electrode was cleaned by using alumina slurries of different microns. After polishing, the electrode was rinsed with DI H_2O. Any absorbed species were removed by ultrasonication of the electrode in absolute ethanol and DI H_2O for 15 min. Scheme 11 illustrates the schematic diagram of the aptasensor fabrication. All developed aptasensors in this study followed the same schematic.

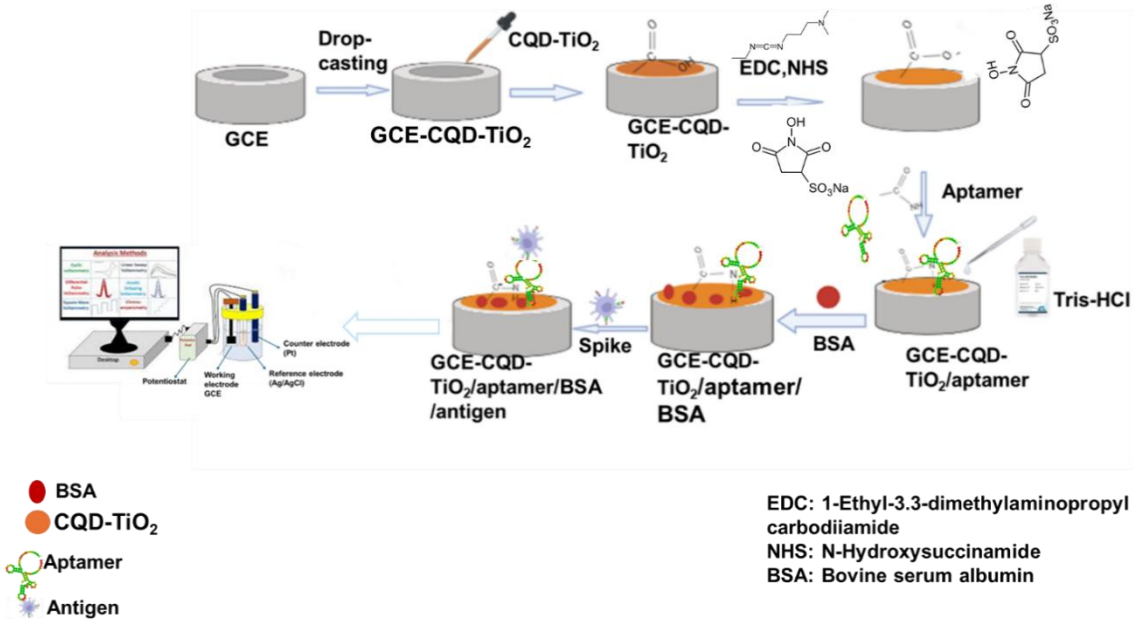

Scheme 11: Schematic diagram showing the fabrication of the aptasensor.

3.8. Preparation of Analytes

3.8.1 Preparation of cadmium (Cd^{2+}) working concentrations

A mass of 30.85 mg of cadmium nitrate was measured and dissolved in 10 mL of DI H_2O. The solution was agitated to ensure homogeneity, yielding a 0.1 M stock solution. 100 µL of the solution was diluted in 10 mL of DI H_2O (0.1 mM stock solution). The resulting solution was then used to prepare various working concentrations of Cd^{2+}, ranging from 1 to 22 µM, using equation.

$C_1V_1 = C_2 V_2$ equation 1

3.8.2 Preparation of arsenic oxide working concentrations

A total mass of 0.039 g of arsenic was measured and dissolved in 10 mL of DI H_2O. The solution was stirred for 15 min to ensure homogeneity, resulting in a 0.1 mM stock

solution. The working concentrations of arsenic were prepared from this stock solution, ranging from 1 to 22 µM, using equation 1.

3.8.3 Preparation of *Crypto*, *Giardia and E. coli* working concentrations

The preservation of *Crypto*, E. coli and Giardia was carried out using the same method. The oligonucleotides were diluted in 50 mL of PBS (pH 7.2) to make a 1 M stock solution. 5 µL of each oligonucleotide was further diluted in 4 mL of PBS in vials to produce 1 mM stock solutions. Working concentrations of E. coli, Crypto, and Giardia were then prepared from this solution, yielding concentrations of 2-10 µM. The stock solutions and working concentrations were kept in the fridge (4°C) when not in use. equation1 was used when doing the calculations.

All the synthesized catalysts were characterized using various characterization techniques. These characterisation techniques provide insights into the material's morphology, chemical composition, and physical and chemical properties. For instance, transmission electron microscope and x-ray diffraction are used to examine the crystalline structure, surface morphology and composition of the synthesized materials. Additionally, these techniques help to determine particle size, which is essential for tailoring the synthesis processes to meet specific applications. Furthermore, electrochemical techniques were employed to investigate the catalyst's electrochemical features.

3.8.4 Preparation of real water samples

Before sampling, the bottles used for collecting samples were thoroughly cleaned. This process involved washing the bottles with detergent, rinsing them 3 times with DI H_2O to remove any detergent residue, and allowing them to air-dry. The dried bottles were soaked in a 10% nitric acid solution overnight to remove any possible contaminants.

Following this, they were rinsed three times with DI H_2O to remove all traces of acid and then dried in an oven.

For wastewater sample collection, a direct sampling method was used. A multimeter was employed to measure various parameters in the water samples, including pH, conductivity, total dissolved solids (TDS), turbidity, dissolved oxygen, and total suspended solids. The samples underwent multiple filtration steps to remove all suspended solids. Lastly, the samples were stored at 4 °C until ready for use. A 15 mL aliquot of the prepared water samples was used for electrochemical experiments, and various analyte concentrations were spiked into the samples to assess recovery rates.

3.9 Electrochemical experiments

Electrochemical tests were carried out using the EC-Lab. A three-electrode system was used, consisting of a silver-silver chloride (Ag-AgCl) reference electrode, a platinum (Pt) wire as the counter electrode, and a working electrode (GCE, with an area of 0.071 cm^2, made of PEEK and having a diameter of 3 mm. EIS and CV experiments were conducted at room temperature, using 0.1 M PBS (pH 6.8 and 7.2) purged with N_2 as an electrolyte. Cyclic voltammetry measurements were utilized to determine electrochemical properties at various scan rates (15-100 mV s^{-1}) with a window of -1 V. - 0.5 V.

3.9. Characterization Techniques

3.9.1 Electrochemical techniques

Electrochemical techniques utilise electrodes to investigate chemical changes occurring on the working electrode. All electrochemically driven characteristics are commonly characterized by changes in current, charge accumulation with time and the potentiostat. Electrochemical techniques, including CP, SWV, CA, EIS, CV

3.9.1.1The three electrochemical systems

The existing system for voltametric measurements comprises an electrochemical cell, a computer and a potentiostat. The cell generates current and voltage via chemical processes using electrochemical signals. A potentiostat is designed to monitor the current generation and apply a precisely controlled potential. The existing system for voltametric measurements consists of an electrochemical cell, a computer and a potentiostat. The electrochemical cell generates current and voltage through chemical processes that utilize electrochemical signals. The potentiostat is designed to apply a precisely controlled potential while monitoring current generation. A typical three-electrode electrochemical cell system includes an Ag/AgCl reference electrode, a GCE, a Pt wire, and a supporting electrolyte. The chemical reaction occurs at the working electrode. The voltage is constantly monitored between the reference electrode and working electrode, whilst the current flows between the working electrode and the counter electrode. Scheme 12 illustrates the three-electrode electrochemical systems.

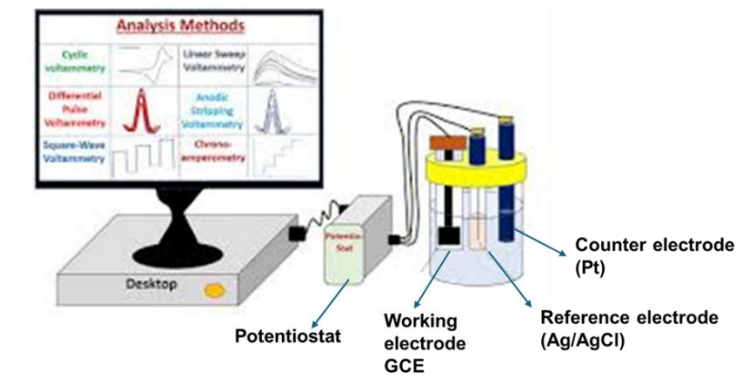

Scheme 12: Illustration of three electrochemical systems.

3.9.1.2 Cyclic voltammetry (CV)

CV is a commonly employed voltametric technique in electrochemistry for studying the kinetics at the electrode surface. This approach measures current density over time, while also applying a time-varying potential. The voltage can be utilized between two limitations by sweeping from an initial point to a final point and then returning to the starting point at a constant speed $V = \frac{dE}{dt}$ during the experiment [280]. CV data is important because it can instantly offer essential information regarding the kinetics occurring between the electrode and the electrolyte, related chemical reactions, and the adsorption processes [281]. Figure 6 shows the cyclic voltammogram.

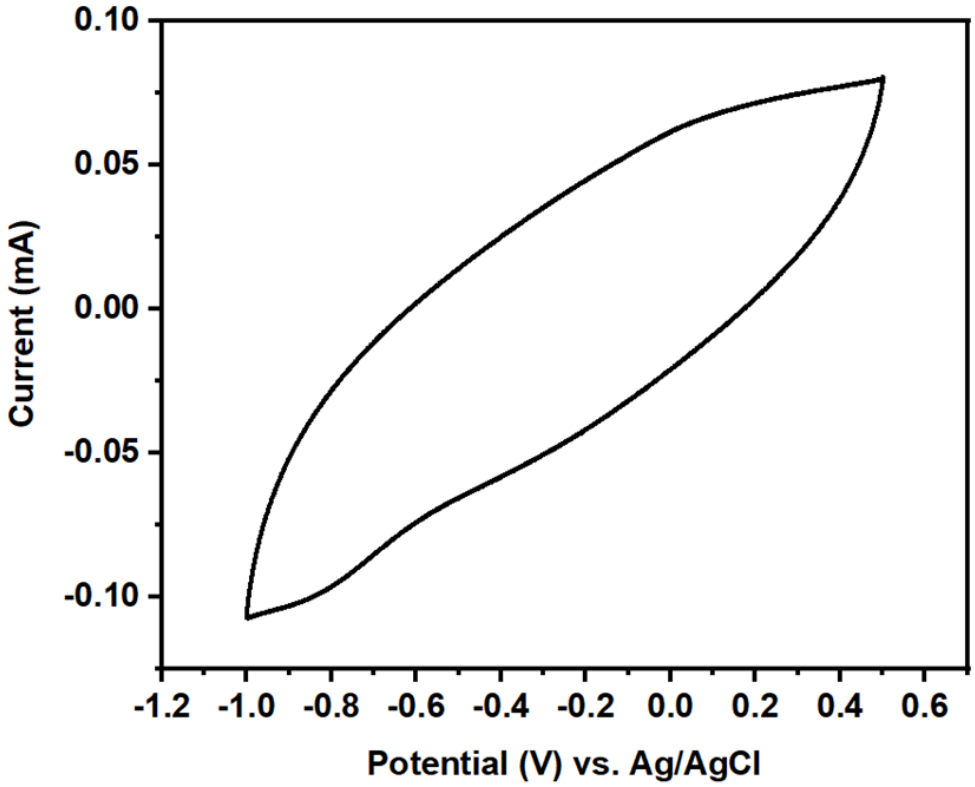

Figure 6: Shows an example of the cyclic voltammogram

3.9.1.3 Electrochemical Impedance spectroscopy (EIS)

Electrochemical Impedance spectroscopy is an electrochemical technique used to study the electron mobility of the modified electrode. Researchers commonly use EIS in biosensors to study parameters such as charge transfer resistance and rate transfer in the presence of analytes [282]. EIS is also used to examine the changed surface's electron transport characteristics and better understand chemical transformation [283]. Theoretically, impedance measurements can be used to investigate any intrinsic properties of nanomaterials, such as the solution interface of nanoparticles. The measure of current is linearly proportional to the applied potential, as shown in equation 2.

$$V\ (f) = I(f)x\ Z\ (f) \qquad \textit{equation 2}$$

The parameters of electrochemical impedance spectroscopy are analyzed by fitting the data to a Randles equivalent circuit. The processes occurring in the electrochemical cell, such as electron transfer, polarization resistance, and electrolyte resistance, exhibit distinct impedance characteristics and can be represented as electrical components [284].Figure 7 shows an example of a Nyquist plot.

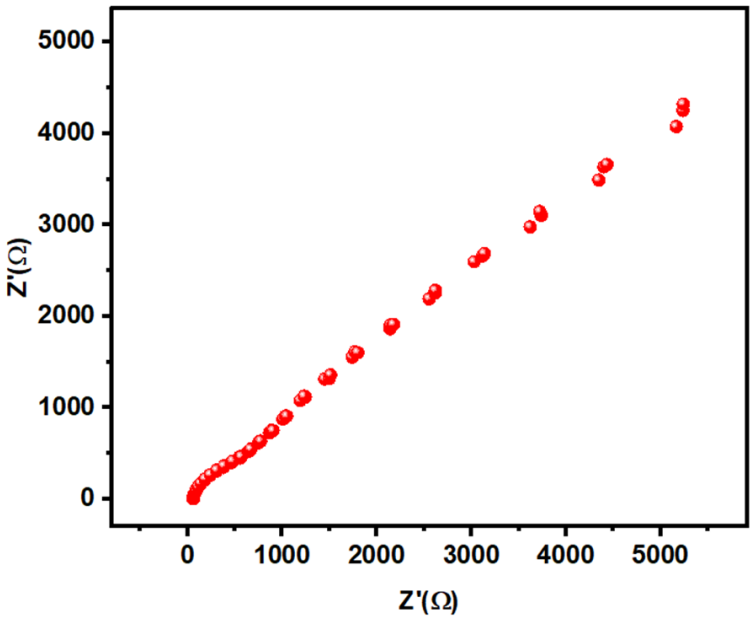

Figure 7: Shows an example of a Nyquist plot.

3.9.1.4 Chronoamperometry (CA)

Chronoamperometry is a technique that employs a step potential to measure the current over time [285]. This method can be used to analyze the time-dependent current related to diffusion-controlled processes at the electrode surface. The current-time response consists of two components: the current required to charge the double layer and the current associated with the electron transfer reaction between the electrode and the electroactive species [286]. These electroanalytical techniques offer advantages over CV, including the ability to determine diffusion coefficients, reaction kinetics, and mechanisms in a single experiment [282]. Figure 8 illustrates an example of a chronoamperometric response.

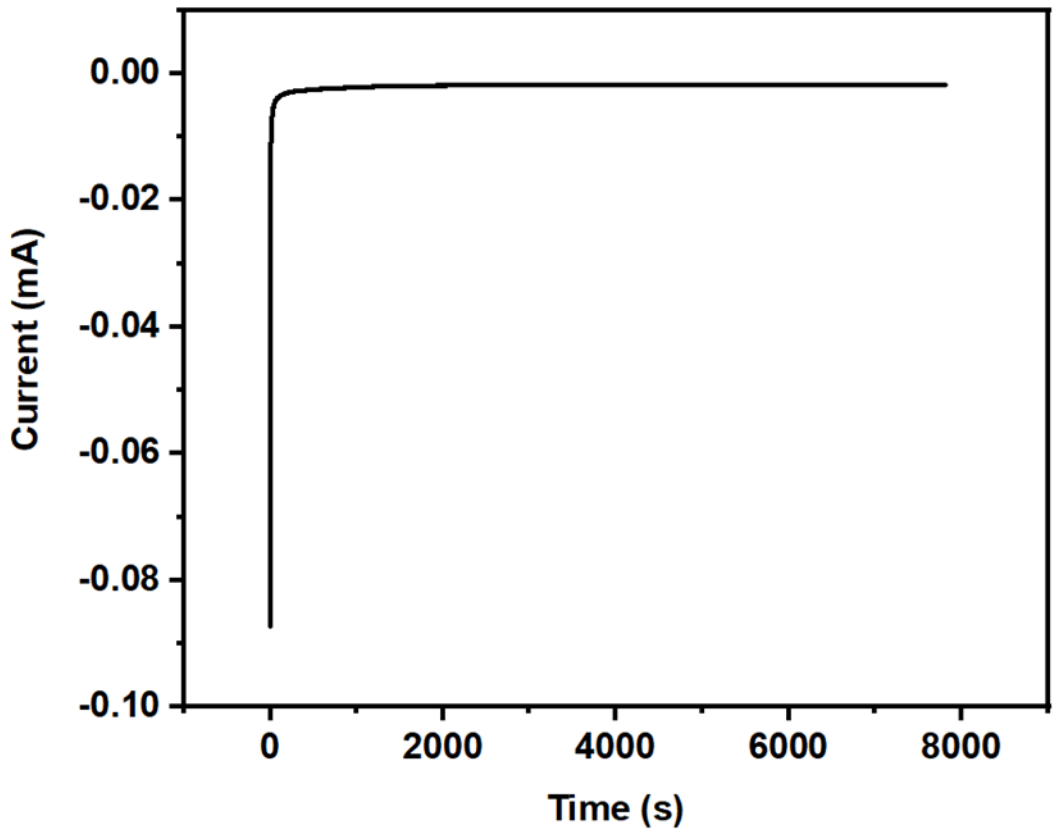

Figure 8: An example of chronoamperometric response.

3.9.1.5 Square wave voltammetry (SWV)

Square wave voltammetry is a versatile technique that is effective for both electrokinetic and analytical studies [287]. This technique is based on the Kalousek commutator [288] and Barker's square-wave polarography [289]. Kalousek developed an apparatus featuring a revolving commutator, which alternated the voltage of a mercury electrode between two levels at a frequency of five cycles per second [290]. SWV is categorized as a subtype of Differential Pulse Voltammetry (DPV) [291]. It is a high-amplitude differential method that employs a staircase potential and a square wave to a working electrode [292]. SWV is a popular choice for analyte determination and offers high-sensitivity screening because non-faradaic currents contribute minimally to the results [293]. This technique is more sensitive than other electroanalytical methods since SWV employs a differential current plot rather than a reverse current plot [294] . Figure 9 shows a typical plot of SWV response.

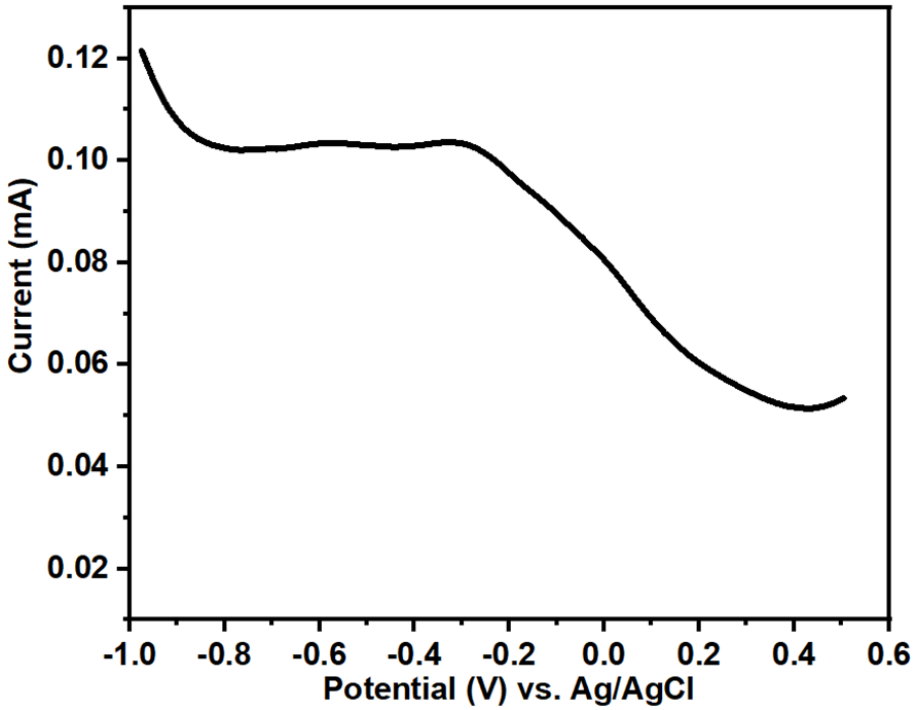

Figure 9: Depicts an example SWV response.

3.10. Spectroscopic techniques

Spectroscopic techniques are used to investigate the structures of the synthesized nanomaterials [295]. These techniques use light to interact with matter, probing certain aspects of a sample to determine its structure. The huge number of wavelengths emitted by these techniques allows for a detailed investigation of the electron configurations of ground and excited states [296].

3.10.1 Fourier transform infrared spectrometer (FTIR)

Fourier transform infrared spectrometer is employed to analyze the functional groups on the synthesized nanomaterials in a wavelength range of 4000 cm^{-1} – 400 cm^{-1} [297]. In FTIR (Fourier Transform Infrared Spectroscopy), samples are analyzed in powder form, and all experiments are conducted at ambient temperature. Before the analysis, a background scan is performed. Next, the synthesized nanomaterial is mixed with potassium bromide (KBr) for scanning [298]. The layout used for these experiments is shown in Scheme 13.

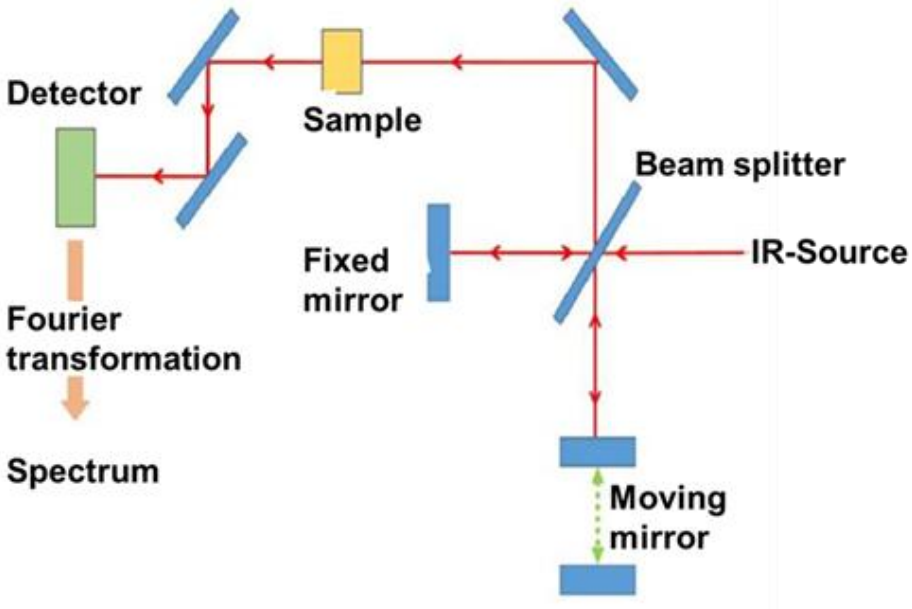

Scheme 13: Depicts the FTIR schematic diagram.

3.10.2 Ultraviolet-vis (UV-Vis) Spectroscopy

UV-vis spectroscopy determines the absorbance spectra of a substance in solution or as a solid. Spectroscopy observes the absorbance of light energy or electromagnetic radiation, which excites electrons from the ground state to the compound's or material's first singlet excited state [299]. The UV-vis region of the electromagnetic spectrum spans an energy range of 1.5 - 6.2 eV, corresponding to a wavelength range of 800 to 200 nm. Absorbance spectroscopy is based on the Beer-Lambert Law equation 3

$$A = \varepsilon bc \qquad \textit{equation 3}$$

For a single wavelength, A is absorbance (typically regarded as arbitrary units), ε is the molar absorptivity of the substance or molecule in solution ($M^{-1}cm^{-1}$), and b is the path length of the cuvette or sample holder (1 cm). C is the concentration of the solution (M) [300]. The UV-Vis principle is shown in Scheme 14.

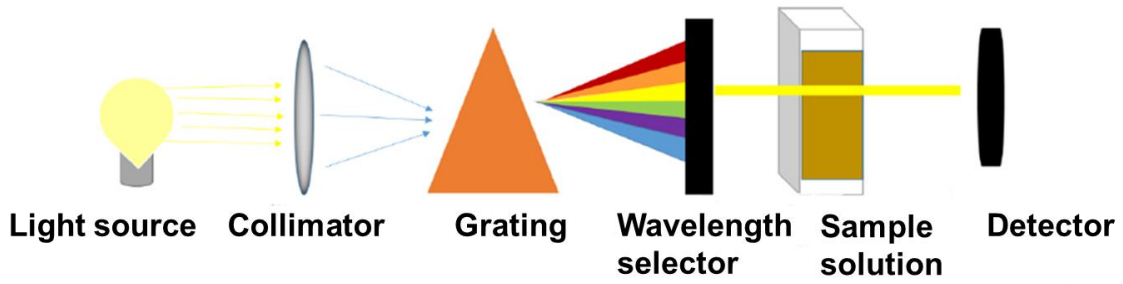

Scheme 14: Shows the schematic diagram of UV-Vis measurement.

3.10.3 X-ray photoelectron spectroscopy (XPS)

X-ray photoelectron spectroscopy is a method for determining the surface chemistry, oxidation states and chemical composition of synthesized nanomaterials [301]. XPS equipment is housed in ultra-high-vacuum (UHV) chambers. This system typically has lower base pressures, around 10^{-9}-10^{-10} mbar, [302]. This method is sensitive to the surface, making it highly affected by any contamination present on the material [303]. At a pressure of 1×10^{-6} mbar and a sticking coefficient of 1 (every molecule that impacts the surface clings to it), there would be one monolayer of contamination every 2 seconds. As a result, XPS devices use the UHV environment to limit surface contamination inside the chamber [304].

XPS analyses the kinetic energy of released electrons by irradiating the materials with soft X-rays [305]. The generated photoelectron results from the transfer of x-ray energy to a core-level electron. This is expressed formally in equation 3**.** The energy of an x-ray (hvv) is equal to the electron's binding energy (BE), kinetic energy (KE), and spectrometer work function (Φspec), which is a constant [306]. Scheme 15 shows the schematic representation of XPS instruments.

$$hv = BE + KE + \phi spec \quad \textit{equation 4}$$

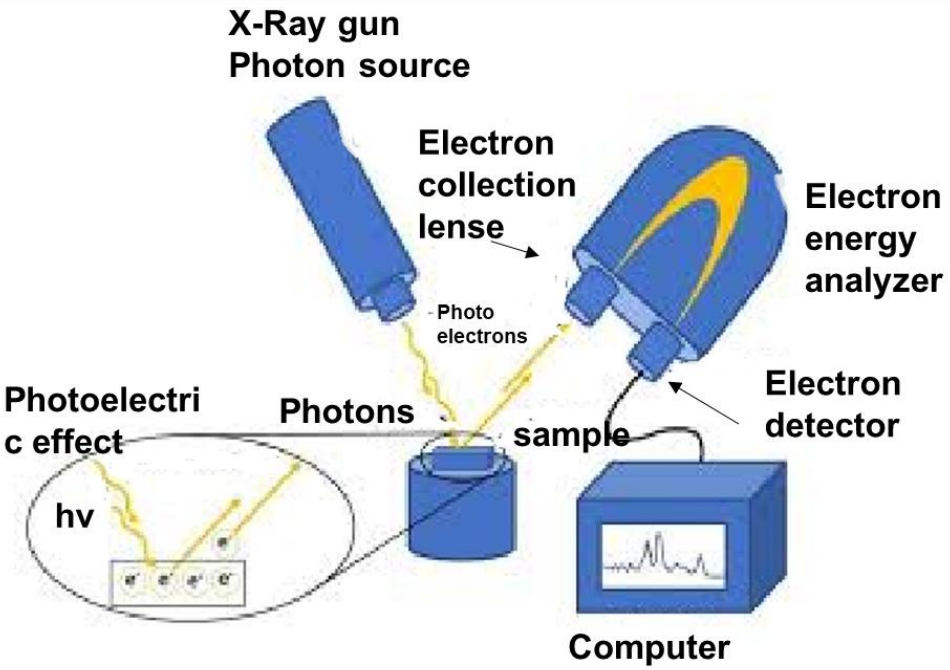

Scheme 15: Shows the components of the XPS instrument.

3.10.4 Raman spectroscopy

Raman spectroscopy is an analytical technique that measures a sample's vibrational energy modes by using scattered light. It is named after C. V. Raman, an Indian physicist who discovered Raman scattering in 1928 with his research partner K. S. Krishnan [307]. This technique provides valuable chemical and structural information, allowing for the identification of substances based on their unique Raman "fingerprint" [308].The information is obtained by detecting Raman scattering from the sample. The Raman effect is a phenomenon involving the scattering of light in two forms: elastic scattering (Rayleigh scattering), where the light retains the same wavelength as the incident light, and inelastic Raman scattering, which occurs when light interacts with molecular vibrations, resulting in different wavelengths. Raman scattering is approximately a million times less intense than Rayleigh scattering. To obtain Raman spectra, it is essential to minimise the interference from Rayleigh scattering, so it does not overshadow the weaker Raman scattering signals [309]. Scheme 16 shows the principles of Raman spectroscopy.

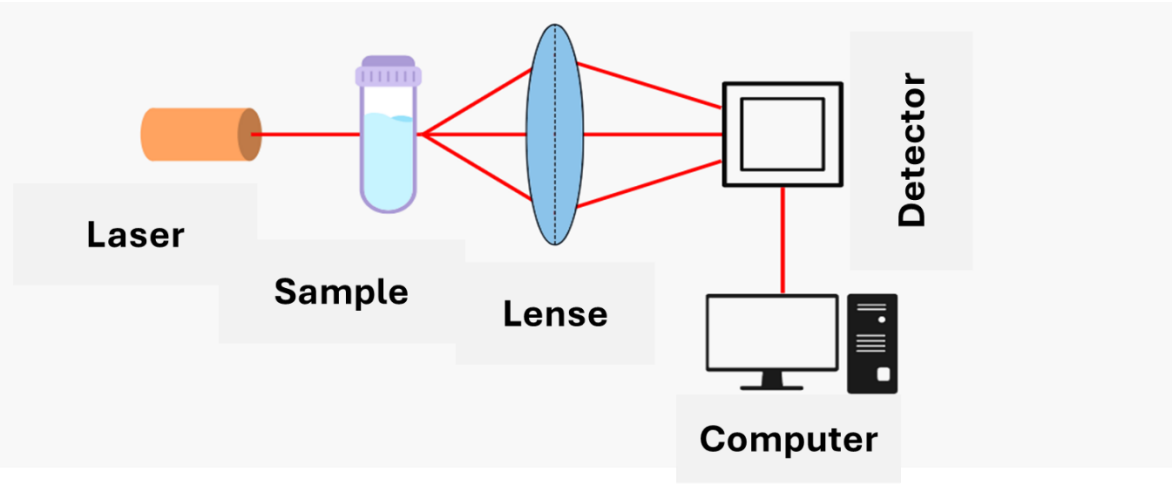

Scheme 16: Display the basic principle of Raman spectroscopy.

3.10.2 Microscopic techniques

Generally, microscopy techniques are used to observe the different structural characteristics of the synthesized nanomaterial that are not visible to the naked eye [310]. Microscopy techniques aim to capture images that accurately represent the structural features of nanomaterials. Microscopy lets scientists directly observe nanostructures within the bulk solution and the nano surface [311]. Examples of microscopic techniques are HRTEM, HR-SEM, XRD, and AFM.

3.10.2.1 High-resolution transmission electron microscopy (HR-TEM.)

HR-TEM is a spectroscopic technique utilized to image NPs at an atomic level. HR-TEM is employed to examine the size distribution, size of the materials and the morphology [312]. When analyzing the samples, the electrons are emitted using electron gun through the vacuum tube of the microscope [313]. The setup used for these experiments is shown in Scheme 17.

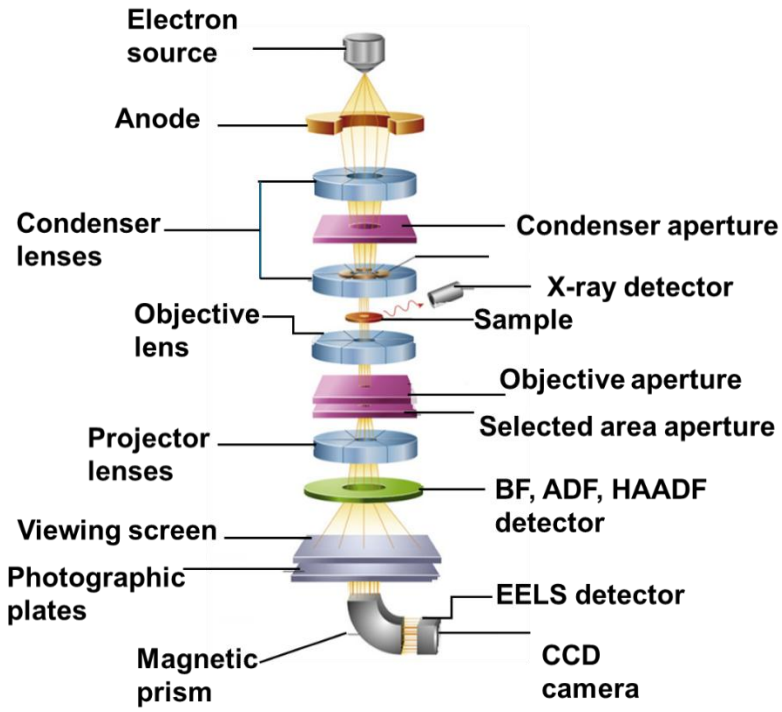

Scheme 17: Display the schematic diagram of the HR-TEM instrument.

3.10.2.2 High-resolution scanning electron microscope (HR-SEM)

HR-SEM is the most common and traditional method for acquiring detailed information on a sample's physical nature and surface. This approach employs high-energy electron-beam contacts that react with the analysed sample [314]. The HR-SEM operates under vacuum (10^{-6} torr), a variable electromagnetic field, and requires cooling equipment and a steady source of power. A gun generates a high-energy electron beam, which is directed at the sample, positioned on a mobile stage. This shower of electrons is created by the gun's field-emission or thermionic-emission process. When these electrons (primary) collide inelastically with the sample, they decelerate. The secondary electron detector collects these electrons and uses them to generate images [315]. The setup used for these experiments is shown in Scheme 18.

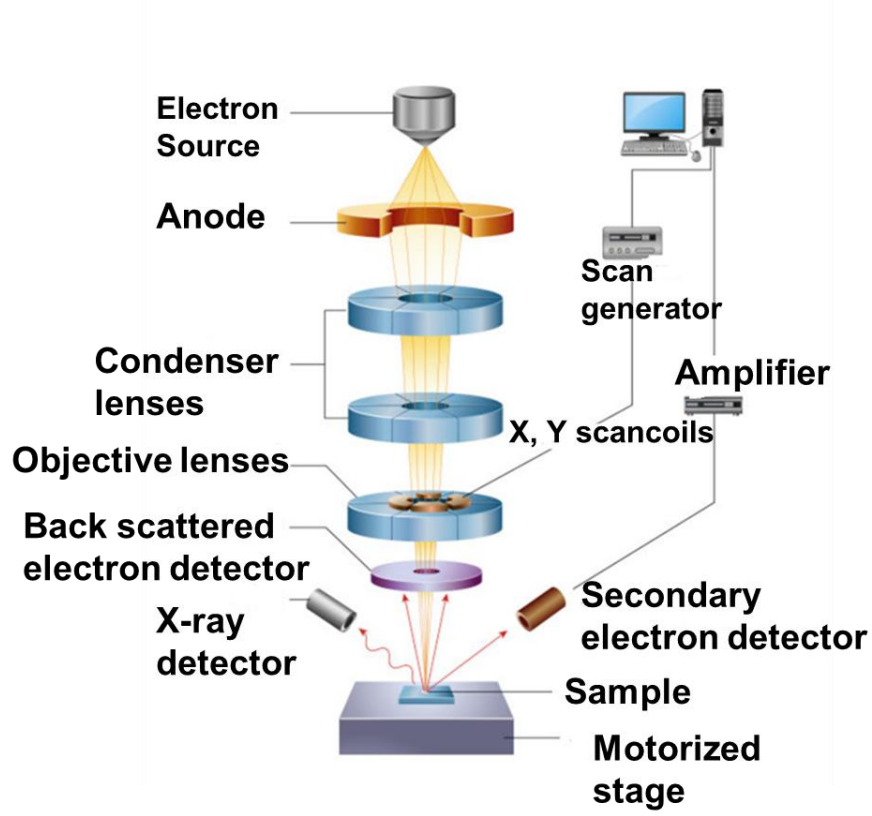

Scheme 18: Shows the components of a scanning electron microscopy instrument.

3.10.2.3 Atomic Force Microscope (AFM)

Gerber et al.[316] introduced AFM in 1985 as a high-resolution, non-optical imaging technology. Since then, AFM has evolved as a powerful tool for surface analysis. An Atomic Force Microscope is used to map the atomic-scale topography of a surface by utilizing the repulsive electrical interactions between the surface and the tip of a probe as it moves above [317]. It provides precise and non-destructive measurements of electrical, magnetic, chemical, optical, and mechanical properties in various environments, including air, liquids, and ultrahigh vacuum. The unique capabilities of AFM make it a versatile, invaluable asset in the world's leading research and technology laboratories [318]. AFMs differ from traditional microscopes, which produce images by focusing light or electrons on the sample surface. Instead, AFMs use a pointed probe to physically feel the sample surface, generating precise three-dimensional topographical representations with nanoscale resolution [319]. This high

resolution allows AFM to examine the arrangement of atoms in a material or study the structure of individual molecules [320]. Scheme 19 depicts the components of AFM.

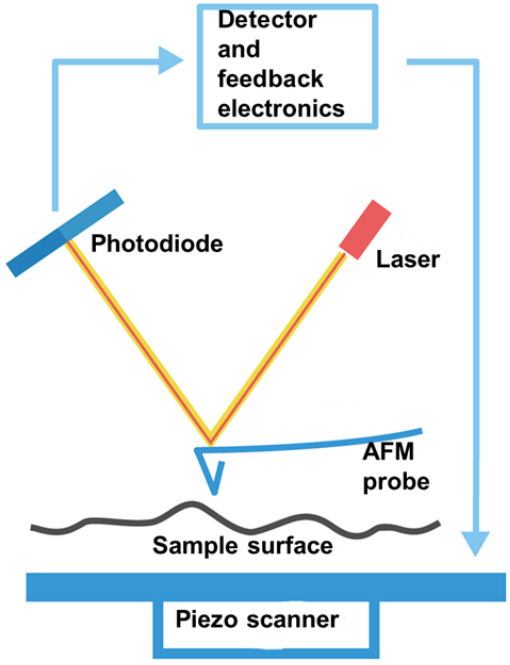

Scheme 19: Shows the schematic representation of AFM instrument.

3.10.2.4 X-ray diffraction (XRD)

XRD is a radiation technique that uses photons with energies ranging from 100 eV to 1000 keV and wavelengths from 10^{-2} nm to 10 nm. Bragg developed the theory to explain why crystal cleavage faces reflect X-ray photons at a specified angle (theta, 2θ) [321]. XRD is a powerful instrument that provides precise details about the crystalline structure of both natural and manufactured materials. A crystalline lattice is a uniform 3-D arrangement of atoms in space, which can take forms such as cubic or rhombic. [322]. The atoms are organised to form a series of straight planes separated by a variable distance (d) determined by the material's characteristics [323]. This phenomenon can be described by the following equations 5 and 6.

$n\lambda = 2dSin\theta$ equation 5

The Scherer equation can be used to calculate the average particle size. The setup used for these experiments is depicted in Scheme 20.

$D = \frac{0.9\lambda}{\beta Cos\ \theta}$ equation 6

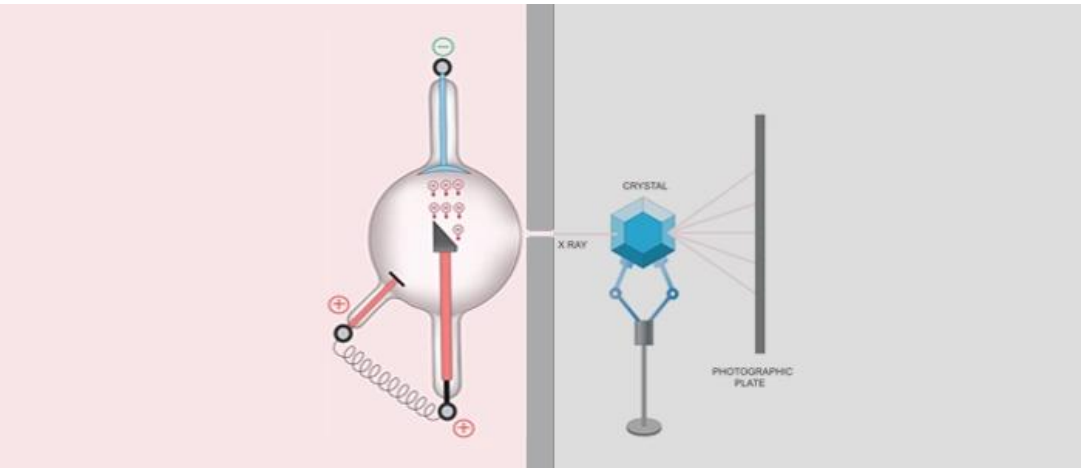

Scheme 20: Illustrate the schematic diagram of the XRD instrument.

CHAPTER FOUR:

Characterization and application of CQD-TiO_2 composite

4.1 Overview

This chapter details the characterization of CQD, TiO_2 NPs, and CQD-TiO_2 composites. The materials were characterized using various techniques, including XRD, FTIR, Raman spectroscopy, and HR-TEM. These methods confirmed the successful synthesis of the materials and the incorporation of both CQD and TiO_2. The electrochemical properties of the materials were studied using CV and EIS. The results revealed that the CQD-TiO_2 composite exhibited a faster charge-transfer rate and greater electrochemical stability than pure TiO_2 and CQD. An electrochemical aptasensor was developed by modifying the electrode with a CQD-TiO_2 composite. This aptasensor demonstrated impressive performance, with a limit of detection of 0.0024 ng L^{-1} and a linear concentration range of 0.0025-0.0045 ng L^{-1}, making it suitable for various applications. The aptasensor was used to detect cadmium ions in wastewater and Crypto in both wastewater and tap water samples. Its selectivity was evaluated by detecting Crypto in the presence of interferences, demonstrating remarkable selectivity. Notably, the aptasensor demonstrated a high sensitivity of 0.2706 mA nM^{-1}, which is particularly significant for detecting traces of Crypto.

4.2. Introduction

Crypto is a waterborne protozoan parasite that poses serious health risks due to its high infectivity and resistance to conventional disinfectants. Detecting trace levels of *Crypto* oocysts in contaminated water remains a significant challenge. Owing to their high specificity and sensitivity, aptasensors have emerged as promising devices for pathogen monitoring. A novel electrochemical aptasensor was fabricated via CQD-TiO_2 composites as electrode modifiers. The properties of the material [324], such as a large surface area [325], and high conductivity [326], have enhanced electrochemical performance [327]. This chapter focuses on the physicochemical characterization of the materials, the electrochemical evaluation of modified electrodes, and the application of the developed aptasensor in detecting *Crypto.*

4.3. Results and Discussions

4.3.1. Morphological and structural characterization of CQD, TiO_2 and CQD-TiO_2

4.3.1.1. Raman analysis of CQD, TiO_2 and CQD-TiO_2

Raman analysis is a powerful instrument used in a wide range of scientific disciplines to investigate atomic oscillation patterns. Raman spectroscopy provides information on oscillation patterns and chemical bonds within the synthesized materials. In this study, Raman spectroscopy was used to investigate the chemical bonds present in CQD, TiO_2 and CQD-TiO_2 composite. Figure 10 shows the Raman spectra of CQD, TiO_2 and CQD-TiO_2. Four Raman bands were identified in the TiO_2 spectrum at 641, 521, 402, and 149 cm^{-1}, corresponding to anatase vibrational modes (Eg, A1g, B1g, and Eg). These distinct intensities and vibrational frequencies confirmed the presence of the anatase phase of titanium dioxide [328]. The CQD spectrum revealed three Raman bands at 1363 cm^{-1}, 1588 cm^{-1} and 2793 cm^{-1}. These bands correspond to the D and G bands of sp^3 and sp^2 hybridization [329]. The presence of the peak at 2793 cm^{-1} confirms that CQD are amorphous. These results are compatible with the HR-TEM and XRD investigations. The D band is associated with vibrations of carbon molecules with the loose bonds at the edge of the disorganised carbon. The G band represents the graphite's E_{2g} and is produced by sp^2-bonded carbon molecules vibrating in a 2D hexagonal configuration [80]. The integration of TiO_2 on the surface of CQD caused a shift in the D and G bands on the CQD-TiO_2 spectra, confirming the successful synthesis of the composite, as shown in Figure 10.

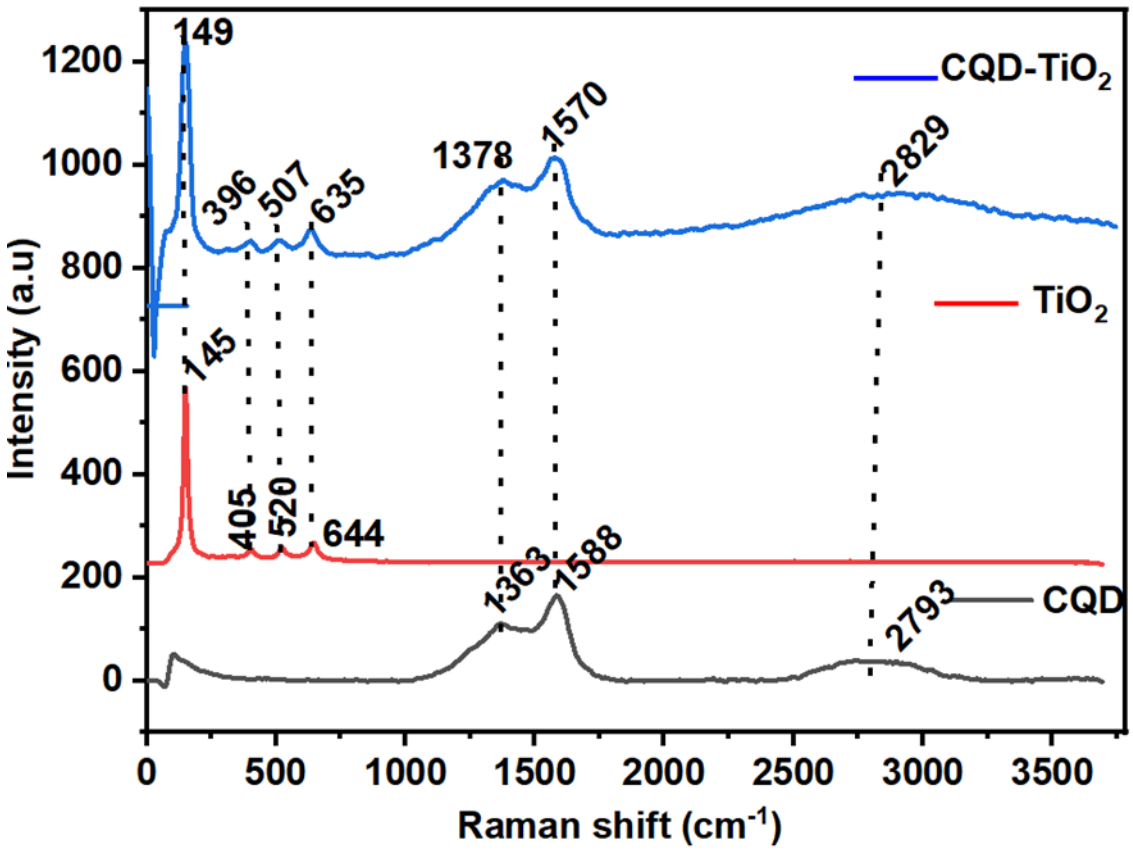

Figure 10: Illustrate the Raman spectra of CQD, TiO_2 and CQD-TiO_2

The synthesized materials (TiO_2, CQD, and CQD-TiO_2) were further analyzed using the HR-TEM technique to understand the morphology and lattice fringes within the materials. HR-TEM was employed to examine the morphological and structural characteristics of the synthesized materials.

4.3.1.2. HR-TEM analysis of TiO_2, CQD and CQD-TiO_2

Figure 11 (A-F) presents HR-TEM images of TiO_2, an enhanced image of TiO_2, CQD, CQD-TiO_2, particle size distribution in CQD and TiO_2. highlighting their particle size distributions, morphologies, and overall particle sizes. J-image software was used to measure and calculate the particle size distribution of the nanomaterials. In Figure 11A and Figure 11B, the HR-TEM image of TiO_2 reveals an uneven morphology resulting from the aggregation of nanoparticles [330]. The circular morphology and uniform,

rounded structure of TiO_2 NPs indicate a large surface area, with an average particle size of 15 ± 8.6 nm. This observation suggests that TiO_2 NPs can be well-dispersed in various solutions, demonstrating structural stability [331]. Additionally, the TiO_2 structure can accommodate a wide range of optical properties. The nearly spherical shape of the nanoparticles is beneficial, as it enhances stability [332], facilitates interactions with other materials, and promotes dispersibility in various environmental applications [333]. The TiO_2 NPs also exhibit well-defined lattice fringes with a consistent interspacing of 0.36 nm.

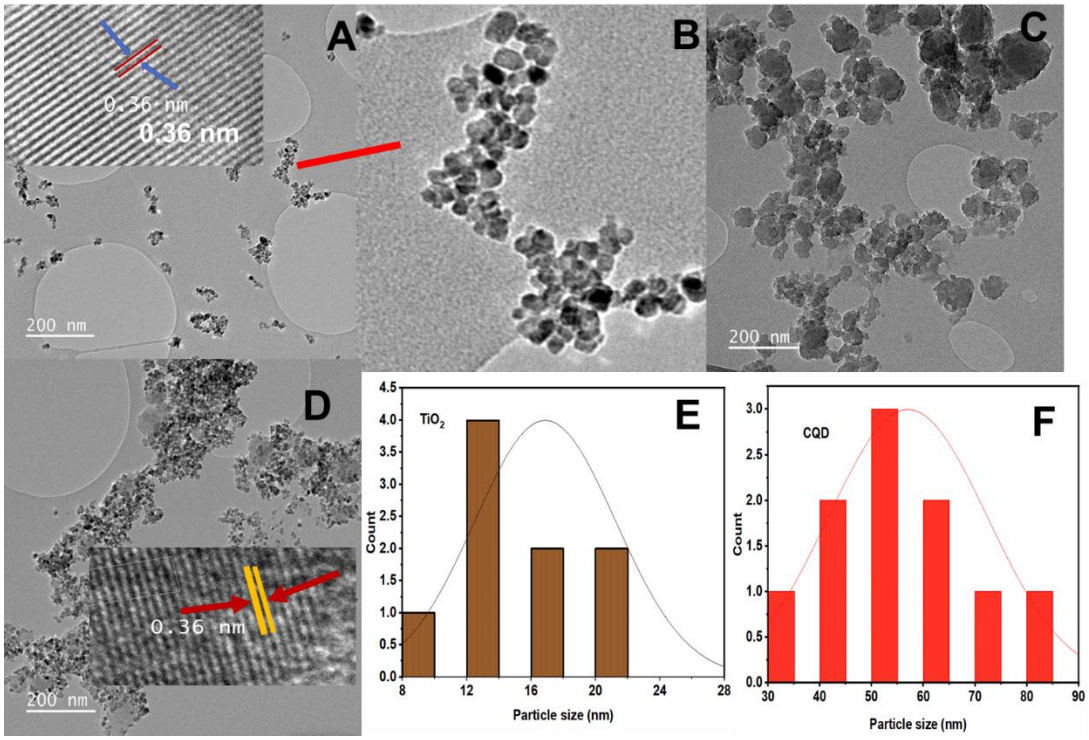

Figure 11: Display the HR-TEM images of (A) TiO_2, (B) enhanced image of A, (C) CQD, (D) CQD-TiO_2, panels (E) and (F) show particle size distribution of TiO_2 and CQD.

Figure 11C illustrates the structure and morphology of a CQD sample obtained from HR-TEM investigations. The synthesized CQD exhibits a highly monodisperse and homogeneous spherical shape with an average particle size of 20 ±14.5 nm. Cheng et al. [334] identified CQDs in a quasi-zero-dimensional state. Figure 11D shows an HR-TEM image of the CQD-TiO_2 nanocomposite, revealing a well-defined lattice structure and uniform spacing. The HR-TEM image of CQD-TiO_2 revealed TiO_2 nanoparticles with a spherical, rounded shape on the CQD surface. This underlines the applicability of heterostructures for charge separation. As a result, the composite's electrocatalytic activity was enhanced compared to that of TiO_2 nanoparticles [335]. CQD-TiO_2 had a

lattice fringe with a constant spacing of 0.36 nm [336]. The crystal structure with an interspacing of 0.36 nm is attributed to the anatase (101) plane, demonstrating that TiO_2 nanoparticles exhibit strong crystallinity and a consistent structure. These findings are consistent with XRD studies, indicating that TiO_2 is naturally crystalline. Figures 11C and 11 show histograms of particle size distribution for TiO_2 NPS and CQD.

The surface shape, crystal orientation, and size distribution of the CQD, TiO_2, and CQD-TiO_2 were evaluated using HR-SEM technique. HR-SEM is a powerful instrument used to study the properties of synthesized materials at the nanoscale. The average size distribution and the morphology of the synthesized nanomaterials were evaluated using HR-SEM.

4.3.1.3 HR-SEM-analysis of CQD, TiO_2 and CQD-TiO_2

Figure 12(A-C) displays the HR-SEM images of CQD, TiO_2 and CQD-TiO_2. J-image software was used to measure and calculate the particle size distribution of the nanomaterials. The synthesized CQD revealed monodispersed nanoparticles with a round sphere-like morphology with an average particle size of 3.56 ± 0.77 nm. This finding aligns with the HR-TEM analysis of CQD. The HR-SEM image of the synthesised TiO_2 indicated that agglomerated nanoparticles increased particle size, as shown in Figure 12B. The image also revealed that the TiO_2 particles exhibited a sphere-like morphology with an average particle size of 68.86 ± 38. 12 nm. Figure 12C revealed that the TiO_2 nanoparticles were dispersed on the surface of CQD, confirming the successful synthesis of the CQD-TiO_2 composite. The observation is consistent with the HR-TEM analysis. The HR-TEM images revealed a clearer distribution of particle sizes in the nanomaterials than the HR-SEM images.

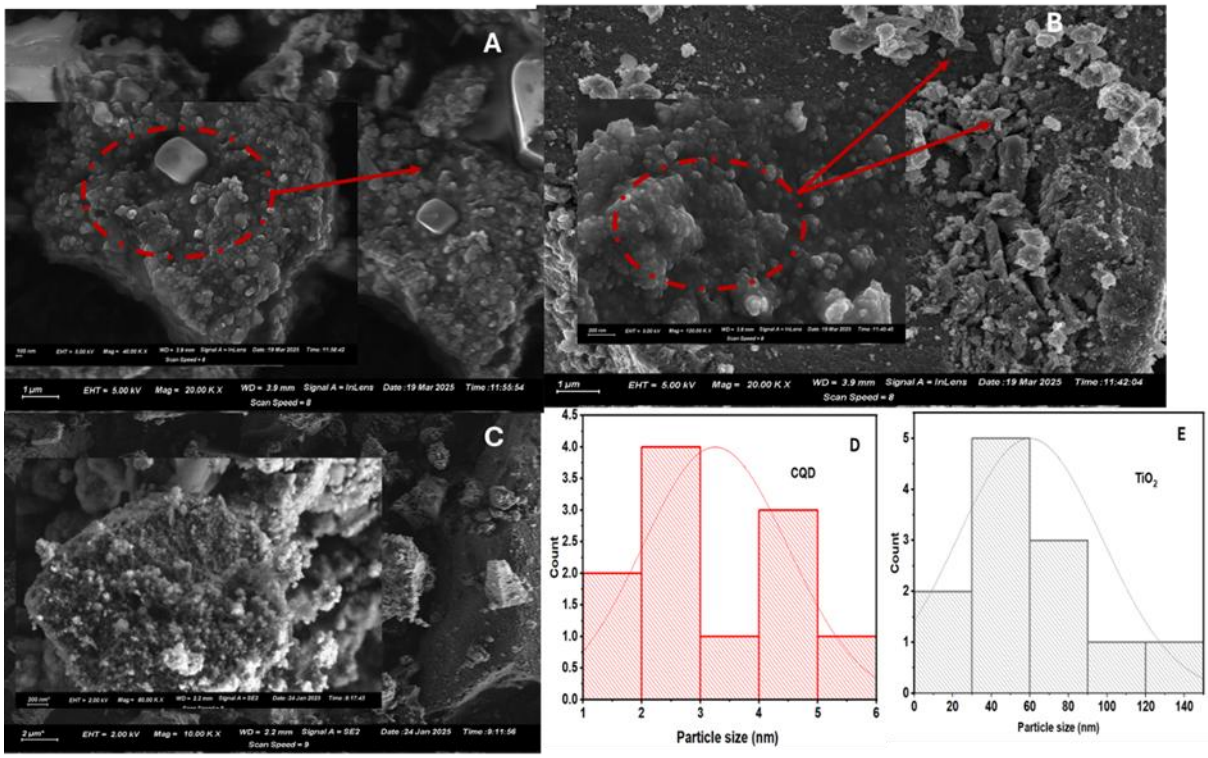

Figure 12: Shows the HR-SEM images of (A) CQD, (B) TiO_2, (C) CQD-TiO_2, displays the histogram showing the size distribution of CQD and TiO_2.

The crystalline structure, size, and thermal stability of the synthesized CQD, TiO_2, and CQD-TiO_2 materials were examined using XRD and TGA. X-ray diffraction (XRD) analysis using Cu Kα radiation was conducted to assess the phase purity and crystallinity of the synthesized materials. A thermogravimetric instrument was also used to evaluate the thermal stability, composition and purity of nanomaterials over a temperature range [337].

4.3.1.4. XRD and TGA analysis of CQD, TiO_2 and CQD-TiO_2

Figure 13(A-B) displays the XRD patterns for CQD, TiO_2, and the CQD-TiO_2 composite, and Figure 13B shows the TGA curves of CQD, TiO_2 and CQD-TiO_2 composite. The spectra for both TiO_2 and the CQD-TiO_2 composite exhibited narrow, intense, and high XRD peaks, indicating that these nanomaterials possess a high level

of crystallinity [338]. Carbon quantum dot do not have a periodic crystal structure [339], have an amorphous ring with a peak around 20.4°-24.6° in X-ray diffraction [340], and they cannot scatter electrons [341]. In this work, the synthesized CQD exhibited a strong peak at a 2θ angle of 9.6°. The broad peak is typically detected at around 2θ = 22°-25°, depending on the temperature, duration, and carbon source used during synthesis [342]. This peak is associated with the graphite (002) reflection plane and confirms the amorphous nature of the CQD. These results are compatible with the Raman analysis. The XRD pattern of titanium dioxide displayed significant peaks at 2θ values of 73.3°, 62.9°, 54.6°, 55.1°, 37.8°, and 25.3°. These peaks are associated with the crystal planes (107), (204), (211), (105), (200), (004), and (101), which confirms that the synthesized TiO_2 is in the anatase phase [343]. This finding is consistent with the results from the Raman analysis, XRD and UV-Vis analysis. The CQD-TiO_2 composite displayed peaks at 71.1°, 62.6°, 54.4°, 47.9°, 37.6°, and 25.5°, which correspond to the crystal planes (107), (204), (211), (105), (200), (004), and (101) [344]. The XRD patterns observed for the CQD-TiO_2 were identical to those of pure TiO_2, indicating that the crystallinity of TiO_2 was maintained within the composite. These observations are consistent with previous reports in the literature [343].

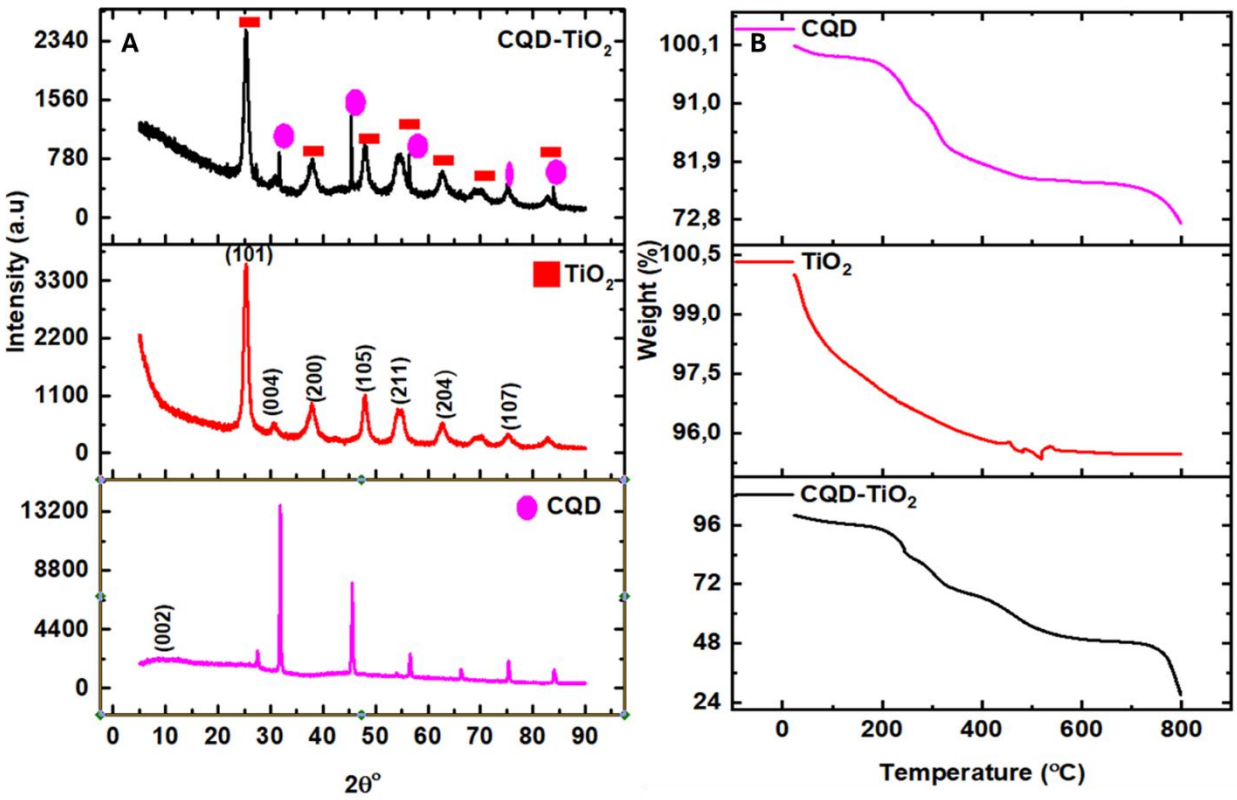

Figure 13: Illustrates (A) the XRD patterns of CQD, TiO_2 and CQD-TiO_2 composite and (B) shows the TGA curves of CQD, TiO_2, and CQD-TiO_2.

.

To calculate the average crystallite size, the Scherrer equation was applied to the apparent full width at half-maximum intensity (FWHM) of the prominent peak, as shown in equation 6.

$$d = \frac{k\lambda}{\beta\cos\theta} \quad \text{equation 6}$$

In the equation, λ represents the wavelength, equal to 0.15405 nm, d denotes the average crystallite length, β signifies the full width at half maximum (FWHM), k is set to 0.9, and θ represents the peak's Bragg angle. Table 2 presents the d-spacing and the calculated crystallite size.

Thermogravimetric analysis involves monitoring the weight loss of the sample as a function of temperature and time [345]. TGA was performed to evaluate the thermal stability of CQD, TiO_2, and the CQD-TiO_2 composite. Figure 13B depicts the TGA curves for each of these materials. The chemical behaviour, moisture content and

stability of the synthesized materials were evaluated by using 15 mg of the samples. The samples were heated at a rate of 5-10 °C/min over a temperature range of 30-800 °C. The initial weight loss (2.15%) on the CQD curve at temperatures up to 180 °C is due to the removal of water molecules from the CQD surface [346]. A weight loss of 6.06% between the temperatures of 189 ˚C and 259 ˚C is attributed to the transformation of hydroxyl, carboxylic and carbonyl groups on the surface of CQD to gaseous products [347]. Additionally, a weight loss of (10.71 %) observed at temperatures ranging from 270 – 490 ˚C is due to the reaction of carbon with the formed gaseous products [348]. The weight loss of 0.72% at 490 and 680 ˚C temperatures correspond to the degradation of unreacted functional groups on the surface of CQD [349]. At temperatures above 690 °C, CQD are completely degraded. The TGA curve for TiO_2 showed a weight loss of 4.26% over the temperature range of 40 °C to 450 °C, corresponding to the loss of surface hydroxyl groups on titanium dioxide. It can be observed that from 550 °C to 780 °C, TiO_2 becomes stable. CQD-TiO_2 exhibited a higher weight loss of 6.06 % compared to CQD between the temperature range of 40 ˚C -209 ˚C, which is due to an increased presence of surface absorbed moisture [350]. The weight loss of 13.29% between 250–342 °C is due to the removal of hydroxylated groups from the surface of the CQD-TiO_2 composite [351].

Table 2: Shows the d-spacing and calculated crystallite size of CQD, TiO_2 and CQD-TiO_2.

Material	**d-spacing (nm)**	**Crystallite size (nm)**	**2θ**
CQD	0.28	30.8	31.8˚
TiO_2	0.35	8.10	25.3˚
CQD-TiO_2	0.35	8.36	25.5˚

The elemental analysis and mapping showing elemental distribution within the synthesized CQD, TiO_2 and CQD-TiO_2 were examined using EDS.

4.3.1.5. EDS analysis of CQD, TiO_2 and CQD-TiO_2

Figure 14 (A-C) displays the elemental analysis results for CQD, TiO_2, and CQD-TiO_2. The EDS spectra of CQD indicated the presence of carbon, oxygen, copper, chlorine, and calcium. The detection of copper (Cu), chlorine (Cl), and calcium (Ca) can be attributed to unreacted species. The identification of carbon (C) and oxygen (O) in the EDS spectra confirms the presence of carbon and oxygen-related functional groups on the surface of the CQD. These findings align with the results of the FTIR analysis. The elemental analysis of TiO_2 showed that titanium is primarily associated with oxygen, forming titania. The presence of a copper peak is due to the impurities in the sample. The CQD-TiO_2 spectra showed peaks for Ti, oxygen, and carbon, confirming the synthesis of the composite. The results are summarized in Table 3.

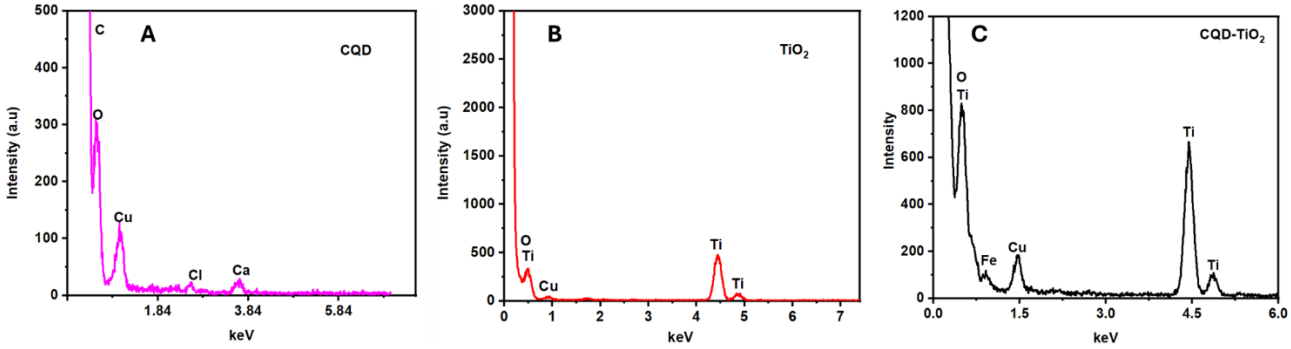

Figure 14: Shows the EDS spectra (A) CQD, (B) TiO_2, and (C) CQD-TiO_2 composite.

Figure 15 (A-C) shows the elemental mapping images of the synthesized samples and distribution of constituents within the samples. Figures 15A, 15B, and 15C show the effective synthesis of TiO_2 and CQD. These mappings validate the elemental existence and distribution inside the materials and are consistent with the spectra shown in Figure 15.

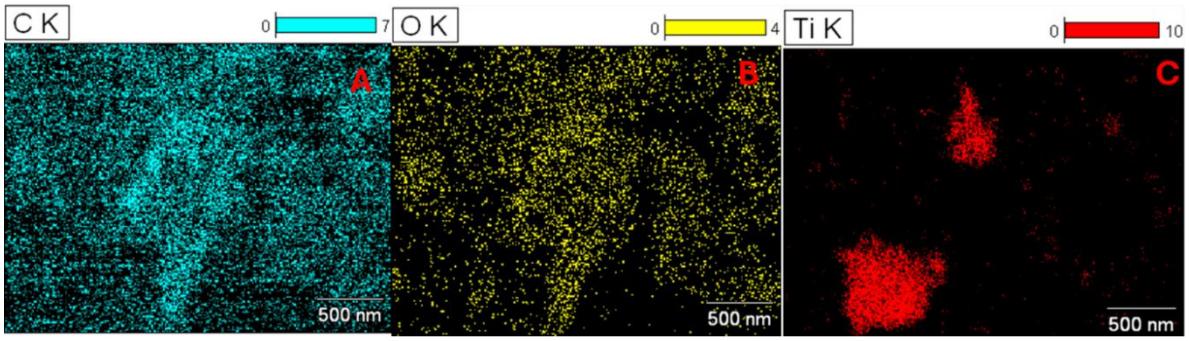

Figure 15: Shows the elemental mapping of (A) carbon, (B) oxygen and (C) titanium.

Table 3: Summarises the atomic weight% of CQD, TiO_2 and CQD-TiO_2 composite.

Material	Element	Atomic %	Error	weight %	Error %	Formula
Carbon quantum dot (CQD)						
	O K	99.27	± 2.57	98.10	2.61	O
	Cl K	0.41	± 0.16	0.89	0.07	Cl
	Ca K	0.00	± 0.06	0.17	0.03	Cu`
	C	0.00	± 0.00	0.00	0.00	C
	Cu K	0.06	± 0.00	0.00	0.00	Cu
	Total	100		100		
Titanium dioxide NPs (TiO_2)						
	O K	98.76	± 1.11	96.28	1.14	O
	Cu K	0.45	± 0.01	0.12	0.00	Cu
	Ti K	3.27	± 0.03	1.12	0.01	Ti
	Total	100		100		
CQD-TiO_2 nanocomposite						
	O K	95.12	± 1.20	96.76	1.14	O
	Ti K	3.27	± 0.03	1.12	0.01	Ti
	Fe K	0.03	± 0.00	0.00	0.00	Fe
	Cl K	1.33	± 0.01	0.12	0.00	Cl
	Cu K	0.41	± 0.01	0.11	0.00	Cu
	Total	100		100		

The functional groups and structure of the synthesised CQD, TiO_2, and CQD-TiO_2 were analyzed using the FTIR technique. FTIR is a technique used to study and identify the functional groups present in samples. In this study, FTIR was employed to examine the absorption bands associated with functional groups in broth, CQD, TiO_2, and the CQD-TiO_2 composite.

4.3.1.6. FTIR analysis of CQD, TiO_2 and CQD-TiO_2

Figure 16(A-D) displays the FTIR spectra for the broth, CQD, TiO_2, and CQD-TiO_2 in the range of 4000 cm^{-1} to 400 cm^{-1}. The broad spectrum revealed absorption peaks between 3000 cm^{-1} and 3400 cm^{-1}, confirming the presence of hydroxyl groups (-OH) [352]. The same peaks were observed in the CQD with low intensities, indicating the conversion of hydroxyl groups during the hydrothermal synthesis. Additionally, C-H stretching produced a prominent set of peaks at 2850 cm^{-1} to 2928 cm^{-1}, which were identified in the broth spectrum [353]. This set of peaks was also observed on the CQD spectrum. Another narrow and intense peak was observed at 1642 cm^{-1}, corresponding to the C=O stretching vibration of the carbonyl group [354]. The same peak was also observed in the CQD spectrum at 1614 cm^{-1}, but its intensity decreased, and its wavelength shifted. Another band observed at 1392 cm^{-1} corresponds to the development of an O-H group, as reported in the literature [355]. The observations from the broth and CQD spectra confirmed the presence of functional groups, indicating the successful synthesis of CQD from lemon peels. The TiO_2 spectrum exhibits a broad absorption band at 3290 cm^{-1}, corresponding to the hydroxyl stretching mode. O-H vibrations account for the conspicuous peak at 1620 cm^{-1} [356]. The peak at 1250 cm^{-1} could be attributed to a C=O surface, as described in the literature [357]. The incorporation of TiO_2 on the CQD surface resulted in deformation and changes to the peaks observed in the CQD spectrum. The peak at 2752 cm^{-1} in the CQD-TiO_2 spectrum was found at 3017 cm^{-1} in the CQD spectrum. The O-H stretching peak has shifted to 1691 cm^{-1} in the TiO_2 spectrum, indicating successful synthesis of the composites.

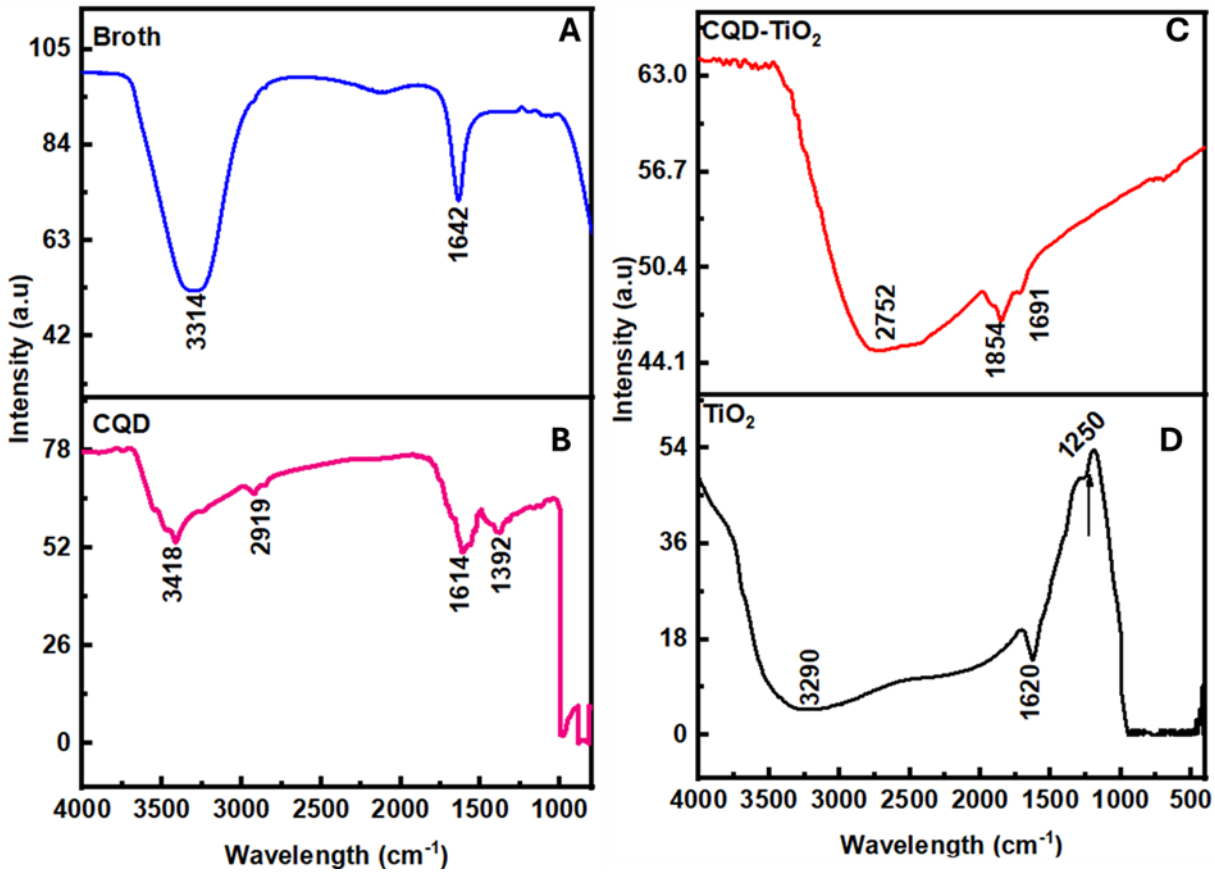

Figure 16: Shows the FTIR spectra (A) broth, CQD, (B)TiO_2 and CQD-TiO_2.

The elemental analysis of the CQD, TiO_2, and CQD-TiO_2 nanomaterials was further investigated using XPS. X-ray photoelectron spectroscopy is a user-friendly core electron technique that uses the photoelectric effect [358]. XPS is used to analyse the surface of nanomaterials, providing information on their elemental composition and oxidation states [359].

4.3.1.7 XPS analysis of CQD, TiO_2 and CQD-TiO_2 composite

XPS was employed to study the elements present on synthesized CQD, TiO_2 and CQD-TiO_2 and their chemical states. Figure 17(A-D) shows the XPS spectra for CQD, TiO_2 and CQD-TiO_2 composite. The CQD XPS spectra demonstrated 5 carbon valence states. The high resolution of C1s, exhibited 5 distinct peaks at 283.8 eV,

284.3 eV, 286.3 eV, 287.5 eV, and 288.7 eV. The exhibited peaks correspond to C-C sp^2, C-C sp^3, C-O, C=O and O-C=O. The results suggest that the carbon quantum dot are made up of graphitic carbon and oxygen-containing functional groups, such as hydroxyl, carbonyl and carboxyl groups. This analysis is consistent with the reported literature and aligns with the findings from Raman, FTIR, and UV-Vis spectroscopy analysis. The TiO_2 XPS spectrum exhibited 2 well-defined peaks with a shoulder, as illustrated in Figure 17B. The exhibited peaks appeared at 457 eV, 463 eV, and a shoulder at 471 eV. The detected peaks correspond to the binding energies of $Ti2p_{2/3}$ and $Ti2p_{1/2}$, indicating the Ti^{4+} oxidation state in TiO_2 [360]. The XPS spectrum of the CQD-TiO_2 composite exhibited the C1 spectrum with 5 peaks at 282 eV, 284 eV, 286 eV, 288 eV and 288.9 eV as shown in Figure 17C. The observed peaks are attributed to 5 different chemical valency states of carbon [361]. Compared to the TiO_2 XPS spectrum, the $Ti2p_{2/3}$ and $Ti2p_{1/2}$ of CQD-TiO_2 shifted to lower binding energies. The shift suggests that the chemical environment of TiO_2 in the composite changes due to the strong interaction between CQD and TiO_2, mediated by Ti-O-C bonds [362]. Figure 17D shows the presence of O1S, Ti 2p, and C 1s peaks, confirming the successful incorporation of CQD and TiO_2 and indicating that the composite contains surface oxygen groups.

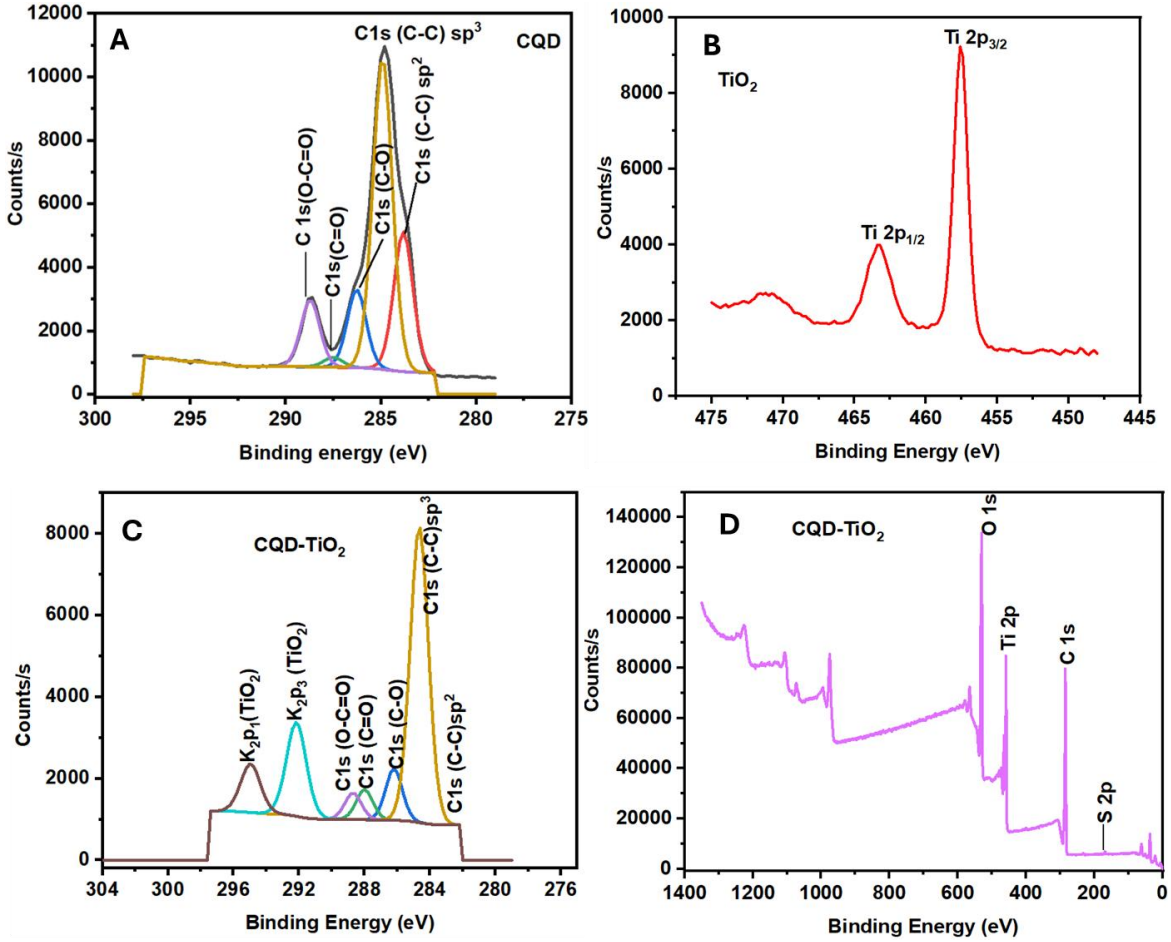

Figure 17: Shows the XPS spectrum of (A) CQD, (B) TiO_2, (C) CQD-TiO_2, and (D) CQD-TiO_2

Various techniques confirmed the structural and morphological analysis of CQD, TiO_2, CQD-TiO_2 and integration of CQD-TiO_2 composite. The electrochemical properties of the modified electrodes (GCE-CQD, GCE-TiO_2, and GCE-CQD-TiO_2) were examined by CV and EIS to investigate reaction kinetics at the electrode interface.

4.4 Electrochemical analysis

4.4.1 CV Analysis of GCE, GCE-CQD, GCE-TiO_2, GCE-CQD-TiO_2

Cyclic voltammetry experiments were conducted to investigate the redox properties of the modified electrodes and the kinetics occurring on the electrode surface. Figure 18 shows the cyclic voltammograms of GCE, GCE-CQD and GCE-TiO_2. The bare electrode was used for comparison purposes. The GCE-CQD electrode did not exhibit

any redox property. According to Montemor et al. CQD-modified electrodes exhibit redox properties when functionalized with redox groups [363]. The GCE-TiO_2 electrode showed a distinct anodic peak of 0.2 mA, which was ten times greater than the 0.04 mA current exhibited by the GCE-CQD and the 0.02 mA for the GCE electrodes. This observation suggests that TiO_2 nanoparticles successfully modified the GCE surface. The oxidation peak was observed at a peak potential of -0.67 V and is attributed to the oxidation of O_2 and the formation of Ti^{3+}, Ti^{4+} [364]. This redox mechanism is common in titanium and involves a shift in the oxidation state of TiO_2. A hydrogen absorption-desorption peak was observed on the GCE-TiO_2 electrode, overlapping with the reduction of Ti^{4+} to Ti^{3+} at the GCE-TiO_2 surface. These results are aligned with the XPS analysis of TiO_2. When hydrogen is desorbed or adsorbed at the electrode surface, a sharp peak appears on the tail of the voltammogram. This peak is frequently robust and identifiable because hydrogen adsorption and desorption are rapid surface responses [365].

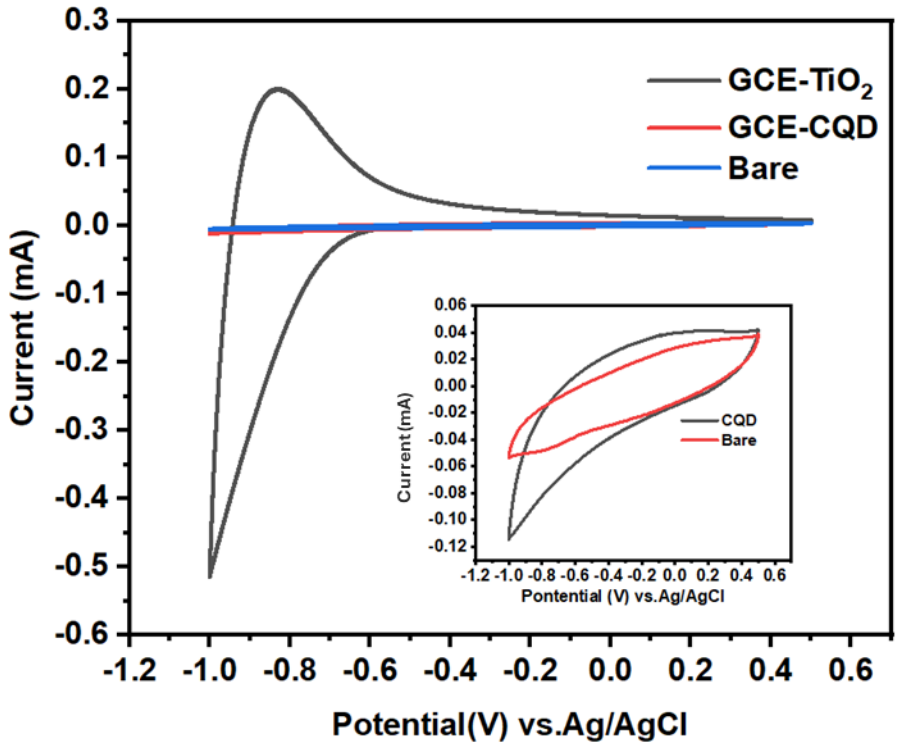

Figure 18: Depicts the cyclic voltammograms for GCE, GCE-CQD and GCE-TiO_2 in 0.1 M PBS (pH, 6.8) at a sweep rate of 50 m Vs^{-1}..

4.4.2 Scan rate dependence studies

The scan rate studies were conducted using cyclic voltammetry experiments within a potential window of -1 V - 0.5 V. The goal was to investigate the reaction kinetics at the electrode interface to determine parameters such as surface coverage, diffusion coefficient, and absorption-desorption and diffusion-controlled processes. Figure 19(A-C) presents cyclic voltammograms at different scan rates, a linear plot of $(mV\ s^{-1})^{1/2}$ versus peak current, and the correlation between potential shift and peak current. The GCE-CQD-TiO_2 exhibited distinct redox characteristics, with an oxidation peak at a potential of -0.061 V and a reduction peak at a potential of -0.62 V. The observed reduction peak is attributed to the reduction of Ti^{4+}, Ti^{3+} and O_2 in TiO_2 [366]. This observation is frequently observed in TiO_2 and is consistent with the reported work [367]. The modification of the composite has resulted in a cathodic peak at -0.62 V, compared with GCE-TiO_2. This observation indicates that CQD and TiO_2 were successfully incorporated. Figure 17B shows that the reduction and oxidation peak currents increase proportionally with the scan rate, with the correlation coefficient of (r^2 = 0.99 and 0.95), denoting that there is a diffusion-controlled process occurring at the interface of the electrode. Diffusion-controlled and adsorption-controlled processes are both scan-rate-dependent processes. In a diffusion-controlled system, the peak current is directly proportional to $(mV\ s^{-1})^{1/2}$, with a correlation coefficient approaching. During an adsorption-controlled process, the peak current increases linearly with scan rate. A consistent shift in peak potential with a rise in scan rate was observed, as shown in Figure 19C, indicating electrochemical reversibility of the electron transfer [368]. However, the slight shift in peak potential was calculated to be $\Delta E > 59$ mV, suggesting a quasi-reversible electrochemical reaction at the electrode interface.

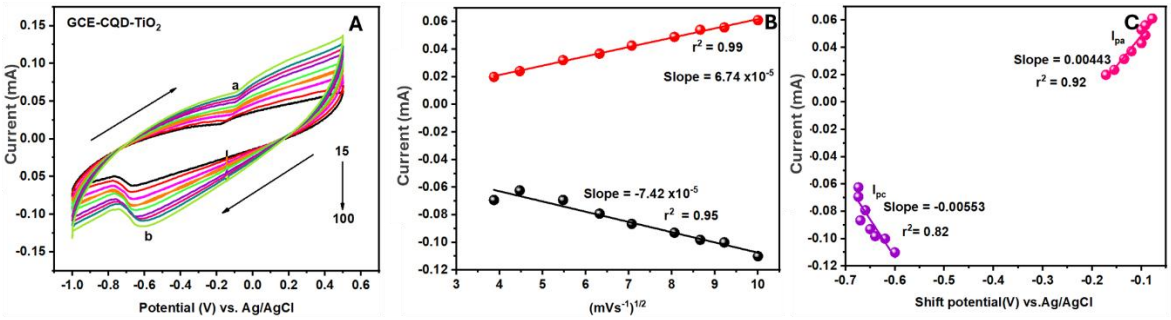

Figure 19: Shows (A) cyclic voltammogram plots at various scan rates in 0.1 M PBS (pH, 6.8), (B) linear plot of $(mV\ s^{-1})^{1/2}$ vs. peak current, and (C) shift in peak potential vs. peak current.

The surface coverage of the modified electrode was determined using the Laviron equation, and the Randles-Sevick equation was used to calculate the diffusion coefficient. For quasi-reversible systems, equations 7 and 8 were used.

$$I_p = 2.99x10^5 na(\alpha na)^{\frac{3}{2}} AD^{\frac{1}{2}} V^{\frac{1}{2}} C \quad \text{equation 7}$$

$$I_p = \frac{n^2 F^2 AV\Gamma}{4RT} \quad \text{equation 8}$$

Where R represents the universal gas constant (8.3145 J mol^{-1}), Ip is the peak current in amperes, C is the concentration of the electrolyte in mol cm^{-3}, and V refers to the potential sweep used in mV s^{-1}. Additionally, A represent the area of the electrode (cm^2), D refers to the diffusion coefficient, α represents the transfer coefficient, Γ is the surface coverage in mol cm^{-2}, T is the temperature in K, na is the number of transferred electrons, and F is the Faraday's constant (96485 C mol^{-1}).

To investigate the absorbed species on the electrode surface, surface coverage was determined. The calculated Γ is equal to 2.400×10^{-10} mol cm^{-2}, suggesting a double-layer formation at the electrode surface [369]. To determine the electron mobility, the diffusion coefficient was calculated. The determined D is equal to 4.541×10^{-14} $cm^2\ s^{-1}$. The calculated D value is comparable to the reported values in other studies [370]. The electroactive surface area (EASA) is a parameter used to determine the activity of a

catalyst. It refers to the region of the electrode's active area where the electron transfer reaction occurs during an electrochemical process [371]. EASA provides information on the electrode's ability to facilitate electron transfer [372]. The slope value of the peak current vs. the $(mV\ s^{-1})^{1/2}$ plot (Figure 19B) was used to calculate the EASA of the GCE-CQD-TiO_2 using the Randles-Sevcik equation (7). Where m is the slope of the linear curve in Figure 19B. The calculated EASA was 0.548 cm^2, which is superior to that reported by Arham et al. [373].

$$I_p = 2.99\text{x}10^5\text{n(na)}^{\frac{3}{2}}\text{AD}^{\frac{1}{2}}\text{V}^{\frac{1}{2}}\ \text{C}$$

$$EASA = \frac{m}{(2.99\times10^5)\times n_2^3\times A\times D_2^1\times C} \quad \text{equation 9}$$

4.4.3. Electrochemical impedance analysis of GCE-CQD, GCE-TiO_2, and GCE-CQD-TiO_2

Electrochemical impedance spectroscopy operates by perturbing a system in equilibrium to examine electrode interactions, including electron transfer between the electrolyte and the electrode surface [374]. Experiments were conducted to investigate the EIS parameters of the modified electrodes. The experiments were conducted over a frequency range of 100 kHz to 100 MHz for all modified electrodes to evaluate charge-transfer kinetics. Figure 20 shows the Nyquist plots for the modified electrodes. The arch of the Nyquist plot determines the electron transfer resistance (R_{ct}), which is used to analyze the electrochemical system's performance. All the EIS parameters, including phase angle, R_{ct}, and electron transfer rate constant (K_{et}), resistance solution (R_s), and Warburg (W), were determined by fitting the Randles' equivalent circuit. These parameters are summarized in Table 5.

A low R_{ct} value indicates a good electron-transport ability [375]. The GCE-CQD-TiO_2 electrode exhibited a smaller charge transfer resistance relative to the GCE-TiO_2 and GCE-CQD electrodes. CQD-TiO_2 exhibits a small diameter in the impedance arc, with an R_{ct} of 45.91 Ω. The GCE-TiO_2 exhibited an R_{ct} of 54.05 Ω, while the GCE-CQD

exhibited an R_{ct} of 82.83 Ω. It is worth noting that the rate constant is inversely proportional to R_{ct} [376]. The low charge-transfer resistance and the higher electron-transfer rate constant for the GCE-CQD-TiO_2 electrode indicate that it facilitates faster electron transfer. This makes it a more effective electrode modifier compared to the other materials, CQD and TiO_2. This finding is consistent with the literature [377]. As shown in Table 4, the GCE-CQD-TiO_2 exhibits a higher phase angle and shifts to lower frequencies compared to GCE-CQD and GCE-TiO_2. This suggests that the CQD-TiO_2 composite behaves as a semiconductor [378] and demonstrates a more conductive system [379].

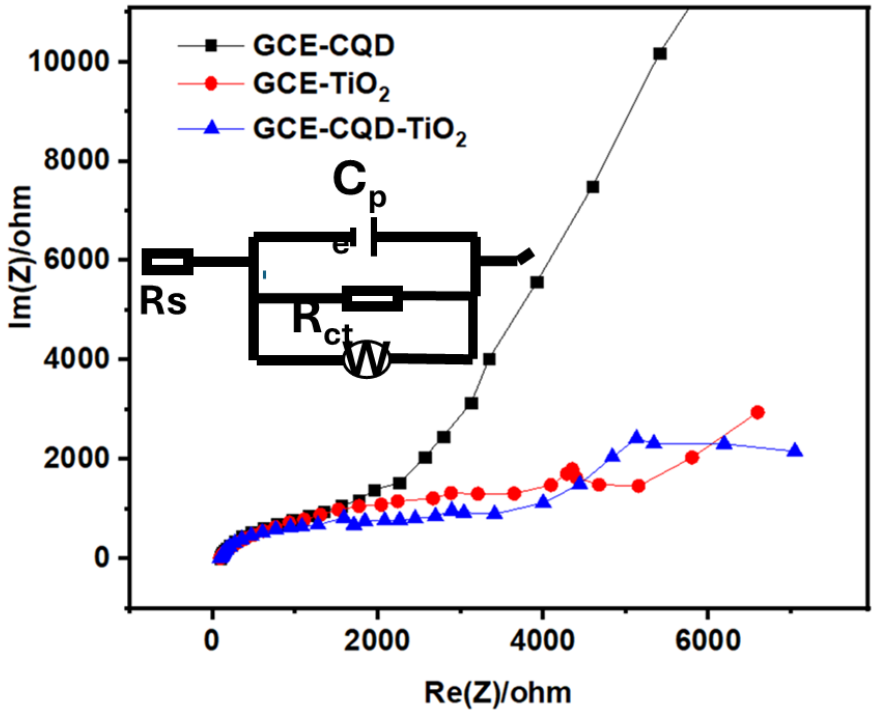

Figure 20: Depicts the Nyquist plots of the GCE-TiO_2, GCE-CQD and GCE-CQD-TiO_2 in 0.1 M PBS (pH, 6.8).

Table 4: Electrochemical parameters obtained from EIS analysis for modified electrodes (GCE-CQD, GCE-TiO_2 and GCE-CQD-TiO_2).

Material	**R_{ct}(Ω)**	**R_s (Ω)**	**Phase angle (degree)**	**K_{et} (S^{-1})**	**Frequency (Hz)**	**Warburg (Ω $s^{-1/2}$)**
TiO_2	54.45	69.45	48	4.750 x10^{-4}	207	753
CQD	80.83	81.88	45	3.176 x10^{-4}	463	1300
CQD-TiO_2	45.91	94.57	57	5.593 x10^{-4}	120	753

4.5. Biosensor Response

4.5.1. Biosensor optimization

Key parameters were optimized during the fabrication of the electrochemical aptasensor, with a particular focus on the incubation time of the aptamer on the working electrode. To improve the responsiveness of the aptasensor, this study examined various incubation times for the aptamer layer on the surface of the working electrode. Figure 21 (A-B) presents the electrode incubation results over various periods, along with the linear curve of peak current versus time. Figure 21A illustrates the cyclic voltammetry plots obtained at various incubation times: 1 h, 2 h, 3 h, 4 h, 5 h, and overnight. Figure 21B shows the binding inhibition of the aptamer on the electrode for the same incubation times, compared to the current readings obtained from the CV plots. The GCE-CQD-TiO_2-Apt-BSA showed an increasing current response from 1 h to 3 h, as illustrated in Figure 21A. However, extending the incubation time to overnight reduced the modified electrode's peak current. The results demonstrated that 3 h of incubation was sufficient to saturate all active sites on the working electrode.

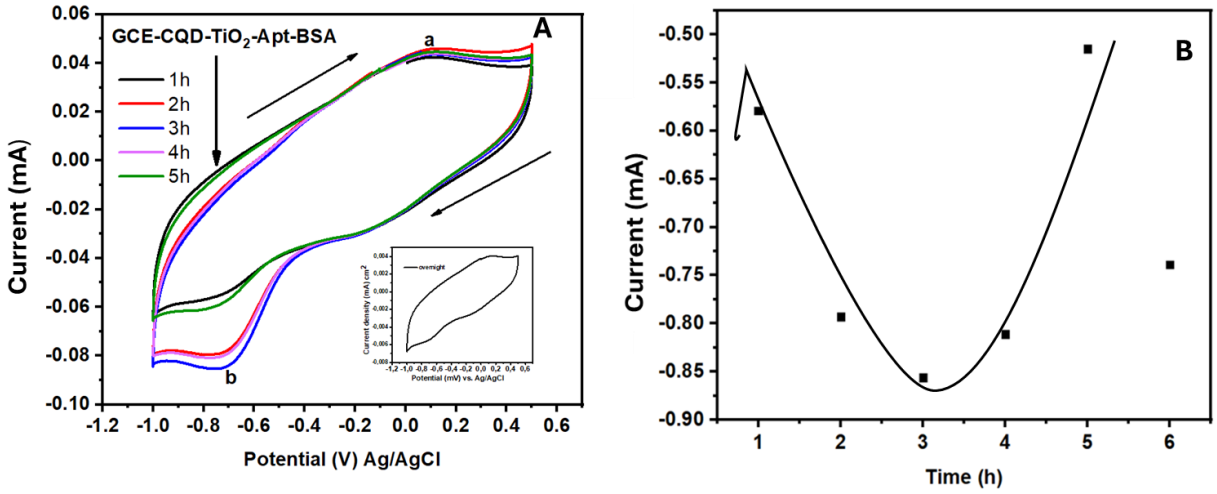

Figure 21: Depicts (A) cyclic voltammograms obtained at various incubation periods in 0.1 M BPS (pH, 7.2) and (B) shows the inhibition curve.

4.5.2 Electrochemical characterization of the aptasensor

4.5.2.1 Comparative cyclic voltammograms and stability of GCE-CQD-TiO₂-Apt-BSA

The comparative study of modified electrodes was conducted using cyclic voltammetry. Figure 22(A-B), which shows cyclic voltammograms for the modified electrodes GCE-CQD-TiO_2, GCE-CQD-TiO_2-Apt, and GCE-CQD-TiO_2-Apt-BSA. The GCE-CQD-TiO_2 exhibited redox characteristics but showed a lower peak current than the other modified electrodes. However, the CQD-TiO_2-Apt showed an increased redox current peak compared to that of the GCE-CQD-TiO_2. This increase in the redox oxidation current indicates that the aptamer was successfully immobilised on the GCE-CQD-TiO_2-Apt surface. This process formed a stable amide bond between the carboxylate group (COO-) of the composite and the amine functional group on the tail of aptamer [380]. Additionally, a further increase in current was observed when the GCE-CQD-TiO_2-Apt was immersed in a bovine serum albumin solution to block all the active sites on the developed aptasensor [381]. This suggests that the active sites on GCE-CQD-TiO_2-Apt may be inhibited by other species, leading to a low peak current [382]. The stability of the developed aptasensor. GCE-CQD-TiO_2-Apt-BSA was assessed

through CV experiments, which involved conducting 100 cycles to evaluate its performance over time. The test was performed in 0.1 M PBS at a sweep rate of 100 mV s^{-1}, as illustrated in Figure 22B. This evaluation is crucial for determining the reliability and long-term stability of the electrochemical system.

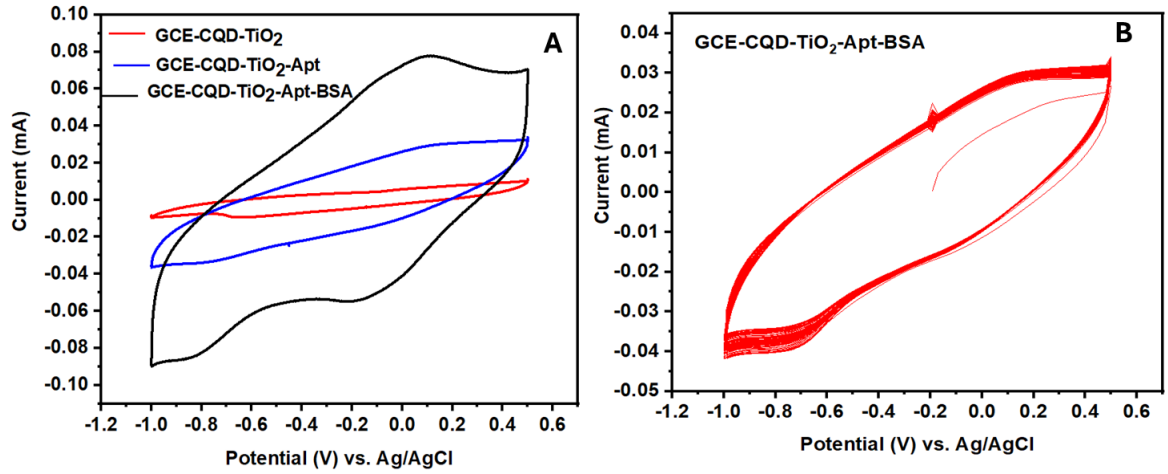

Figure 22: Shows (A) the cyclic voltammograms for GCE-CQD-TiO_2, GCE-CQD-Apt, GCE-CQD-TiO_2-Apt-BSA and (B) depicts the 100 cyclic voltammograms for GCE-CQD-TiO_2-Apt-BSA, all measurements conducted in 0.1 M PBS (pH, 7.2).

4.5.2.2 Scan rate dependence studies

Cyclic voltammetry was used to conduct the scan rate dependence studies to investigate the relationship between cathodic and anodic peak currents and the scan rate. This approach was used to examine the electrochemical properties, as well as the adsorption, desorption, and diffusion processes, to determine the surface coverage of the developed sensor. Figure 23(A-C) illustrates 23A the CV plots of the aptasensor, 23B the relationship between current and the $(mV\ s^{-1})^{1/2}$, and 23C the potential shift against current. The scan rate study was conducted using CV experiments over the potential range of -1 V to -0.5 V. The platform exhibited an oxidation-reduction (redox) couple with a potential difference of 1.7 V, indicating that the aptasensor operates in a quasi-irreversible manner [383]. The aptasensor showed an oxidation peak current at a potential of -0.17 V, and reduction peak currents at

potentials of -0.84 V and -0.19 V. This behaviour suggests the possibility of electrostatic interaction between the active sites in the composite (carboxyl (-COOH) groups) and the amine bonds from the aptamer sequence, resulting in the formation of stable amide bonds [384] as shown in Figure 23A.

Both the oxidation peak current and the reduction peak current increased with the scan rate, as shown by the two linear curves in Figure 23B, with correlation coefficients of $r^2 = 0.99$ and $r^2 = 0.98$. This increment in current response with the $(mV\ s^{-1})^{1/2}$ indicates the stability of the developed aptasensor and suggests a diffusion-controlled electrocatalytic process [385]. Additionally, a slight shift in peak potential was observed with increasing scan rate, as illustrated by the linear curve in Figure 23C**.** The diffusion coefficient and surface coverage were calculated using the Randles-Sevcik and Laviron equations to confirm the electron kinetics. The calculated D was found to be $8.134 \times 10^{-13}\ cm^2\ s^{-1}$ and $\Gamma = 1{,}015 \times 10^{-9}\ mol\ cm^{-2}$. These results indicate significant electron transfer from the electrode-electrolyte interface. The determined EASA was 0.548 cm^2, which is higher than the value provided by [386]. This suggests that GCE-CQD-TiO_2-Apt-BSA has more active sites for analyte detection.

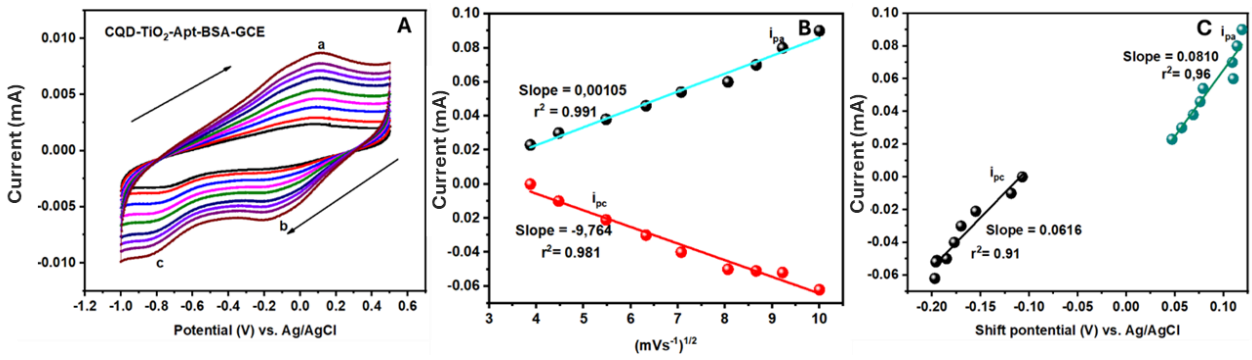

Figure 23: Displays the cyclic voltammograms at various scan rates in 0.1M PBS (pH 7.2), (B) linear plot of $(mV\ s^{-1})^{1/2}$ against peak current, and (C) shows the peak current vs shift potential.

4.5.2.3 Electrochemical impedance spectroscopy analysis of GCE-CQD-TiO_2, GCE-CQD-TiO_2-Apt and GCE-CQD-TiO_2-Apt-BSA

The EIS technique was employed to determine different electrical parameters and analysed them by fitting the data to Randles' equation. These parameters include charge transfer resistance (R_{ct}), the phase difference between the applied voltage and the resulting current (phase angle), the rate constant for electron transfer at the electrode-electrolyte interface (K_{et}), and frequency shifts. Figure 24 displays the Nyquist plots for the modified electrodes, GCE-CQD-TiO_2, GCE-CQD-TiO_2-Apt, and GCE-CQD-TiO_2-Apt-BSA. The R_{ct} value can be determined from the diameter of the semi-circular portion observed at higher frequencies on the Nyquist plot. The semicircle of the Nyquist plot indicates charge transfer and reflects the electrochemical behavior of the system. R_s denotes the electrolyte resistance, while K_{et} denotes the electron-flow rate. The Warburg element denotes the electron diffusion and electron flow. The impedance arc shows a larger semicircle for the GCE-CQD-TiO_2 electrode, with an R_{ct} value of 45.91 Ω. After incubating the aptamer on the surface of GCE-CQD-TiO_2, the R_{ct} value decreased to 40.11 Ω for the GCE-CQD-TiO_2-Apt electrode, indicating enhanced electron transfer. This reduction suggests an interaction between the active sites of the composite and the tail of the aptamer, resulting in stable bonds [387]. Furthermore, when the modified electrode was exposed to a blocking agent, the R_{ct} value decreased further to 35.07 Ω for the GCE-CQD-TiO_2-Apt-BSA. The EIS data obtained aligns with the findings from CV experiments, confirming the successful development of the aptasensor [388]. Phase angle is a key parameter used to assess process kinetics. GCE-CQD-TiO_2-Apt-BSA demonstrated a higher K_{et} value, a lower R_{ct} value, and a higher W value compared to other modified electrodes, thereby facilitating higher electron efficiency at the electrode interface due to the synergy between Ti-O bonds and CQD. This finding is consistent with the reported literature [389] . Additionally, the GCE-CQD-TiO_2-Apt-BSA exhibited a high phase angle value, achieved in the low-frequency region, indicating that the system is more conductive [390]. The obtained results are summarised in Table 5.

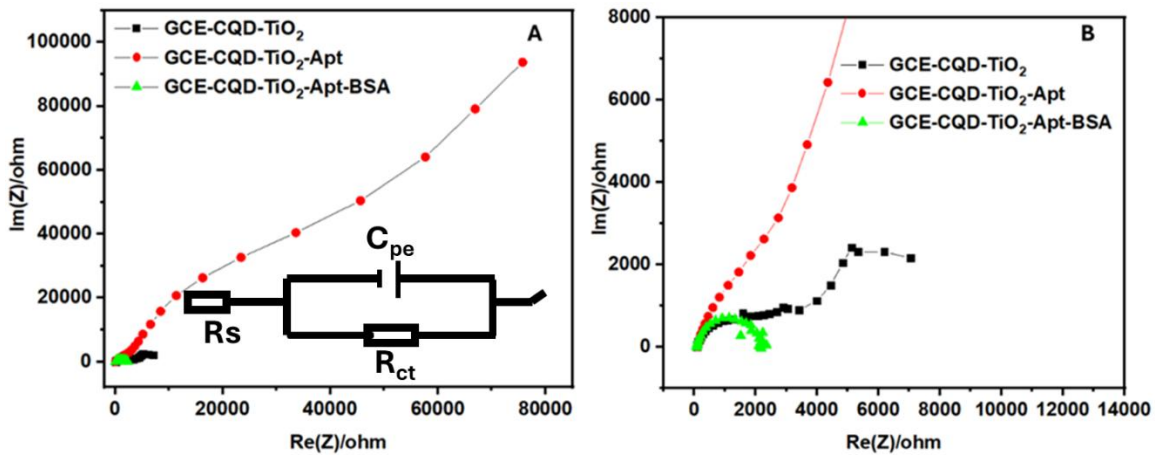

Figure 24: Depicts the Nyquist plots of GCE-CQD-TiO_2-Apt, GCE-CQD-TiO_2 and GCE-CQD-TiO_2-Apt-BSA in 0.1 M PBS (pH,7.2).

Table 5: Summarises the electrochemical impedance spectroscopy results obtained from different modified electrodes.

Material	**R_{ct} (Ω)**	**R_s (Ω)**	**K_{et} (S^{-1})**	**Phase angle (degree)**	**Frequency (Hz)**	**Warburg (Ω $s^{-1/2}$)**
CQD-TiO_2-Apt-BSA	35.07	120	7.322 x10^{-4}	65	96	603.19
CQD-TiO_2-Apt	40.11	100	6.04 x10^{-4}	60	112	703
CQD-TiO_2	45.91	94.57	5.593 x10^{-4}	57	120	753.98

The developed GCE-CQD-TiO_2-Apt-BSA was assessed for electrochemical detection *Crypto* in phosphate buffer solution using SWV, CV and EIS techniques. The current responsiveness and charge transfer were examined throughout the experiments.

4.6. Application of GCE-CQD-TiO_2-Apt-BSA

4.6.1. Electrochemical detection of *Crypto*

The efficacy of the proposed aptasensor was assessed in buffer solutions containing Crypto at various concentrations using SWV, EIS, and CV. All experiments were conducted in 0.1 M phosphate buffer (pH 7.2) at a potential scan rate of 50 mV s^{-1},

using *Crypto* concentrations ranging from 1 to 30 nM. Figure 25(A-D) shows the SWV measurements of different spiked *Crypto* concentrations, 25B linear curve of spiked *Crypto* concentration vs current density, 25C linear curve of spiked *Crypto* concentration vs current density and 25D concentration of *Crypto* spikes vs shift in potential. Figure 25A shows the SWV measurements for different spiked concentrations of Crypto. The peak current increased as the concentration of *Crypto* rose. This increase is attributed to the aptamer adopting a conformation that enhances electron flow on the GCE-CQD-TiO_2-Apt surface.

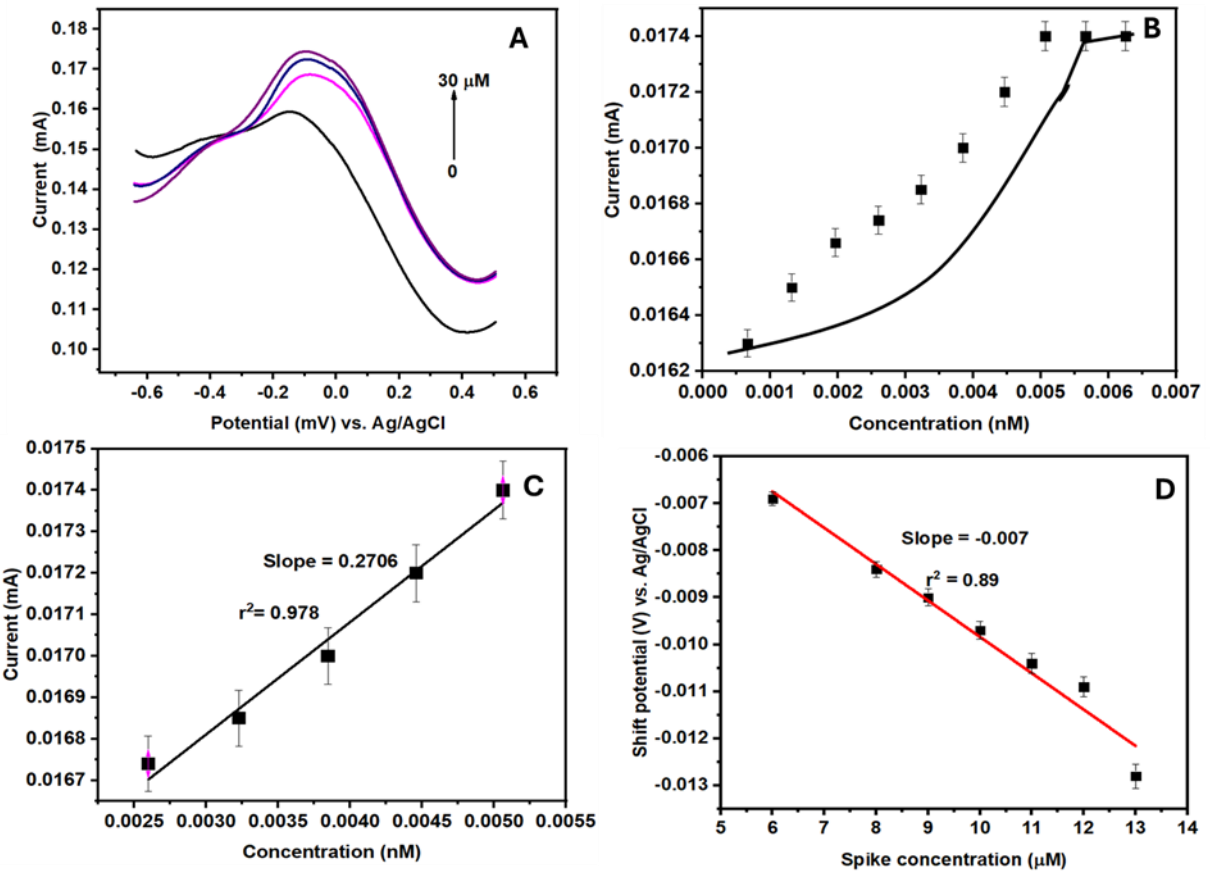

Figure 25: Shows (A) SWV measurements to different spiked *Crypto* concentrations in 0.1 M BPS (pH,7.2), (B) linear plot of spiked *Crypto* concentration vs. current density, (C) linear curve of spiked *Crypto* concentration vs current and (D) spiked *Crypto* concentration against shift potential.

The proposed aptasensor reached saturation upon the spike in the 11 nM *Crypto* concentration, as shown in the linear plot of the binding inhibition curve versus peak current in Figure 25B. A correlation between peak current and spiked concentrations was investigated by plotting a linear relationship between spiked concentration and current response, yielding a correlation coefficient of $r^2 = 0.92$, as depicted in Figure 25C. A slight shift in potential was observed as spiked concentrations increased, with an r^2 of 0.96, as shown in Figure 25D.The detection limit was determined using equation 10:

$$LOD = \frac{3\partial}{m}$$ equation 10

Where m represents the slope of the linear plot of spiked concentration vs. peak current, ð is the standard deviation of the 10 blanks. The calculated LOD is 0.0024 ng L^{-1}, with a sensitivity of 0.02705 mA nM^{-1} and a linear range of 0.0025-0.0045 ng L^{-1}.

Cyclic voltammetry experiments were also conducted in the presence of varying concentrations of *Crypto*, using a scan rate of 50 mV s^{-1}. Figure 26(A-D) shows the CV plots obtained at varying spiked concentrations, 26B the inhibition curve, 26C linear plot of peak current against spiked concentration and 26D shift in potential vs. peak current plot. Figure 26A shows that both oxidation and reduction peaks increase linearly with spiked concentration. These results indicate that the proposed aptasensor exhibits enhanced electrocatalytic activity toward the electro-oxidation of *Crypto*. Meanwhile, Figure 26B presents the inhibitory binding curve, illustrating the relationship between spiking concentration and the peak current. The saturation point for the proposed aptasensor was reached at 15 nM. Figure 26C shows that the aptasensor responded linearly to spiked *Crypto* concentrations, with a correlation coefficient (r^2) of 0.99. The interaction between the aptasensor and the spiking *Crypto* concentrations resulted in a modest shift in potential, indicating rapid electron-transfer kinetics, as evidenced by the linear curve in Figure 26D ($r^2 = 0.96$).

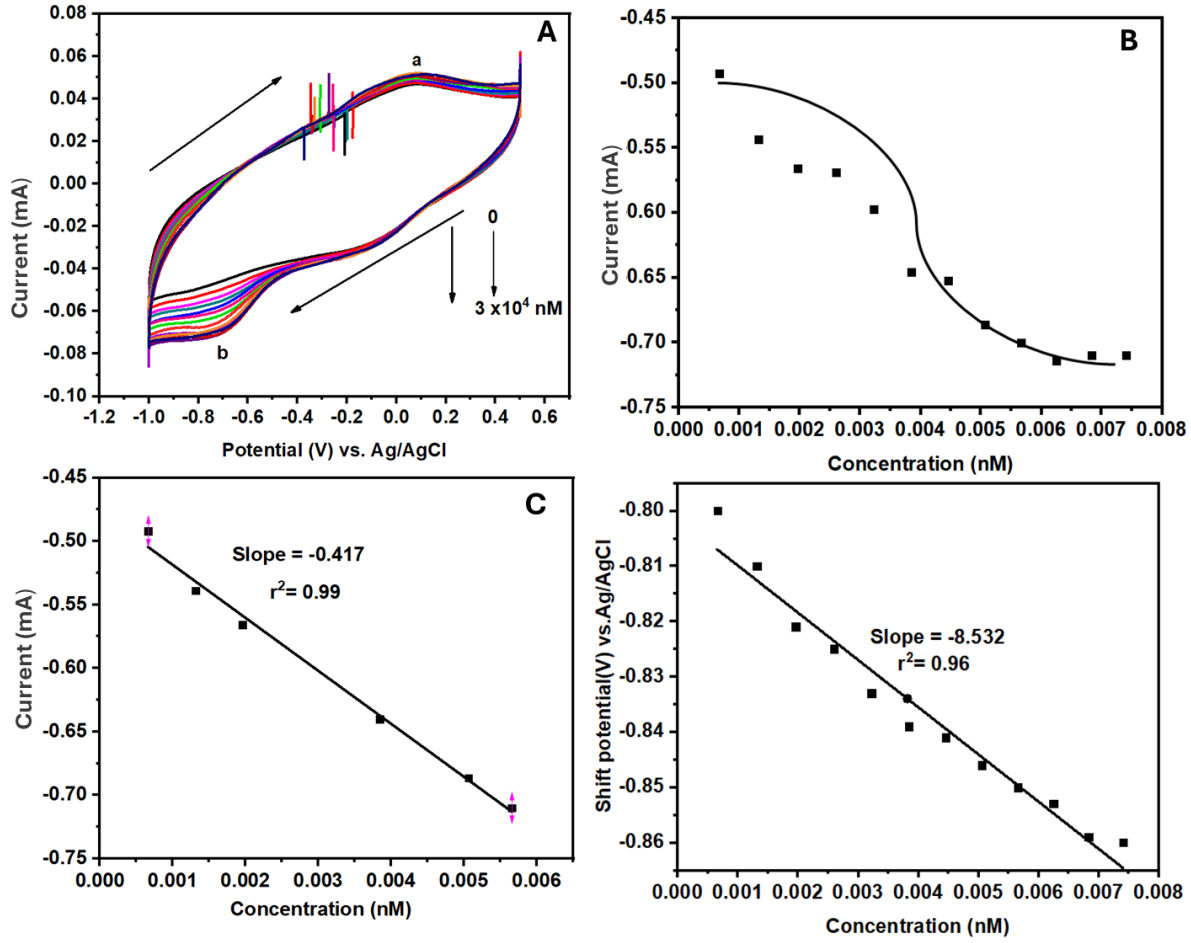

Figure 26: Displays (A) the CV measurements of different spiked *Crypto in 0.1 M PBS (pH,7.2)* (B) the binding curve of spiked *Crypto* concentration vs. current, (C) spiked *Crypto* concentration vs. current, and (D) linear curve of shift in potential vs spiked *Crypto* concentration.

The electrochemical performance of the proposed aptasensor was evaluated using electrochemical impedance spectroscopy to assess charge-transfer resistance in the presence of spiked *Cryptosporidium* concentrations. The EIS experiments were conducted using three spiked concentrations, ranging from 2 µM to 20 µM. The experiment was conducted over a frequency range of 200 kHz to 100 Hz to investigate charge-transfer kinetics in the presence of various *Crypto* concentrations. Figure 27(A-D) shows the Nyquist plots of GCE-CQD-TiO_2-Apt-BSA at various concentrations. Figure 27B shows the Nyquist plot of GCE-CQD-TiO_2 for 3 spiked concentrations, and Figure 27C depicts the inhibition curve of charge transfer resistance against spiked *Crypto* concentrations, and Figure 27D represents the spiked concentrations vs. charge transfer resistance. The observed EIS data were fitted using a Randles-Sevick

electrical circuit to determine parameters such as charge transfer resistance (R_{ct}), solution resistance (R_s), electron transfer rate (K_{et}), and Warburg coefficient (W) [375]. Charge transfer resistance is related to the reaction kinetics occurring at the interface between the electrode and the electrolyte. A low R_{ct} is a good indication of rapid electron transfer at the electrode surface [375]. The results, illustrated in Figure 34A, show a decrease in R_{ct} with increasing concentrations of spiked Crypto, suggesting that *Crypto* binds to the immobilised aptamer surface. The blank sample without the spiked concentration was included for comparison.

The blank exhibited a high R_{ct} value of 56.78 Ω. Upon the spiking of the *Crypto* concentration, the R_{ct} value decreased. For example, upon addition of 2 µM, the R_{ct} value decreased to 51.01 Ω, while at 6 µM it was 50.91 Ω. A decrease in charge-transfer resistance was observed with increasing electron-transfer rate, as shown in Table 7. This observation suggests that electrons are moving rapidly at high concentrations [391]. A high electron transfer rate (K_{et}) with a low charge transfer resistance (R_{ct}) facilitates high electron transfer at the electrolyte interface, as observed upon spiking with a 20 µM concentration [392]. The findings indicate that the developed system enables rapid electron flow even at high concentrations. These findings align with those reported by Luka et al. [185]. Figure 27B shows the Nyquist plot of different concentrations, while Figure 34C shows the binding inhibition curve of spiked concentrations against R_{ct}. The peak current and R_{ct} showed a linear relationship ($r^2 = 0.99$). The parameters obtained from the EIS data are summarised in Table 6. The slope of the linear curves shown in Figure 27D was used to calculate the LOD of the sensor using equation 10.

Where ð is the standard deviation of the blanks (n = 7), m is the slope of the linear curve of spiked concentration vs R_{ct}. The calculated ð is 0.002, and the obtained LOD is 0.09 ng L^{-1}.

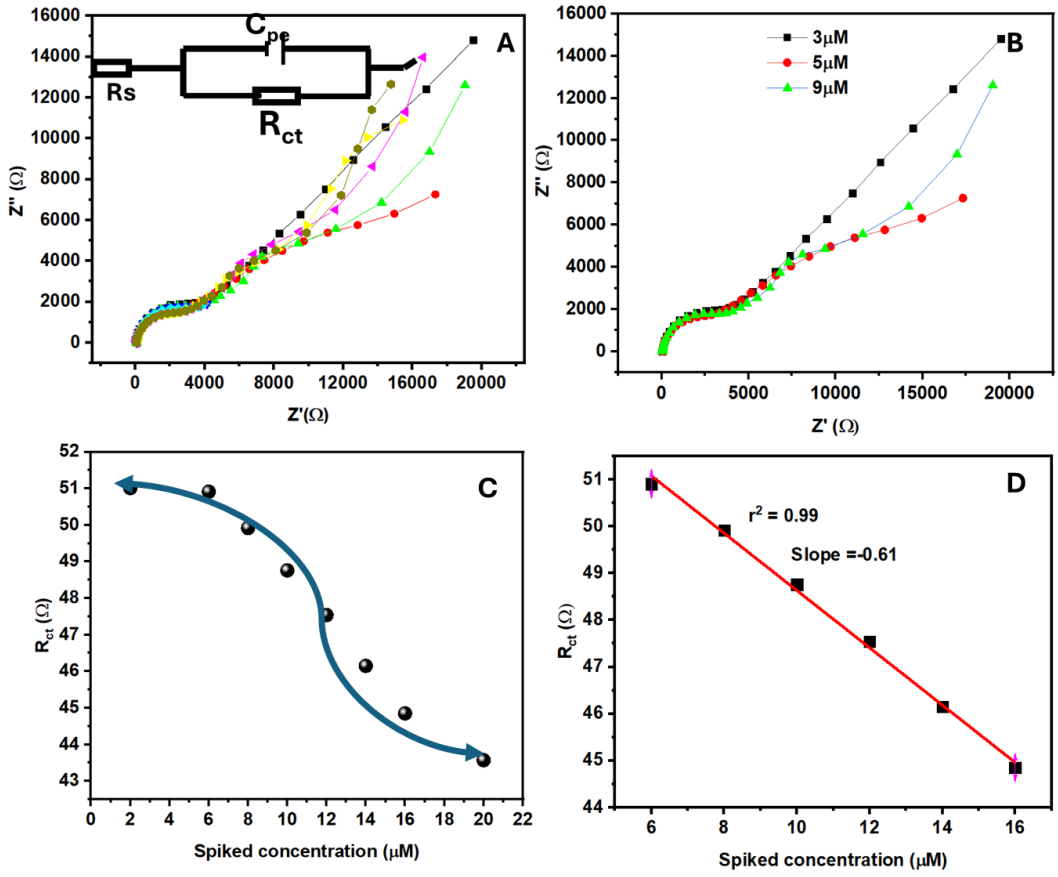

Figure 27: Depicts (A) the Nyquist plots at different spiked *Crypto* concentrations in 0.1 M PBS (pH, 7.2), (B) spiked *Crypto* concentration vs R_{ct}, (C) the binding curve of spiked *Crypto* concentration vs R_{ct} and (D) shows the linear curve of spiked concentration vs R_{ct}.

Table 6: Shows the EIS parameters obtained at different spiked *Crypto* concentrations.

Concentration (µM)	R_{ct} (Ω)	R_s (Ω)	K_{et} (S^{-1})	Warburg
3	51.01	52,51	0.070	600.11
5	50.91	52.49	0.071	282.42
8	49.92	53.85	0.072	382.01
9	48.76	54.5	0.074	413.8
12	47.54	55.43	0.075	566.42
14	46.15	57.77	0.078	581.32
16	45.85	59.90	0.079	589.67

20	43.57	62.78	0.084	590.62

An electrochemical aptasensor plays a crucial role in detecting pathogens by electro-oxidising *Crypto*. This represents a significant advancement in disinfection and water treatment. Metal-oxide electrodes play an essential role as vehicles for aptamer immobilisation on the working electrode surface. The interaction between the active sites of the metal oxides and stable bonds of the aptamers is crucial for these biosensors. These metal oxide surfaces enhance the sensor's overall performance by facilitating stable attachment and electron transfer. Surface modification techniques, most notably covalent bonding via EDC/NHS chemistry, are employed to provide robust, precise immobilisation. This approach activates the carboxyl groups on aptamers or linker molecules, enabling them to form strong amide bonds with amine-functionalized metal oxide surfaces. These chemical bonds ensure the necessary sensitivity and durability for effective pathogen detection. As a result, this interface becomes a crucial component of biosensor technology for both environmental and biomedical applications.

Reaction:

The terminal -$\mathbf{NH_2}$ group interacts with a **carboxyl-modified aptamer** via **EDC/NHS**:

$$\boldsymbol{Aptamer - COOH + NH_2 - (Surface) \rightarrow \frac{EDC}{NHS} \rightarrow Aptamer - CO - NH - Surface}$$

When aptamers are immobilised on the surface of a metal oxide electrode, they serve as a highly selective biorecognition element for the target analyte, such as a *Cryptosporidium* antigen. When the target binds to the aptamer, the electrochemical environment at the electrode interface changes significantly, leading to a conformational change in the aptamer. The primary technique used to detect this shift is electrochemical impedance spectroscopy, a powerful technique that measures the electrode's surface resistance to charge transfer. As the binding event progresses, the formation of the aptamer-target complex makes the electrode surface more insulating, hindering the free flow of electrons. As a result, the impedance increases, thereby increasing the charge-transfer resistance. Figure 28 shows the mechanism of electro-oxidation of *Crypto.*

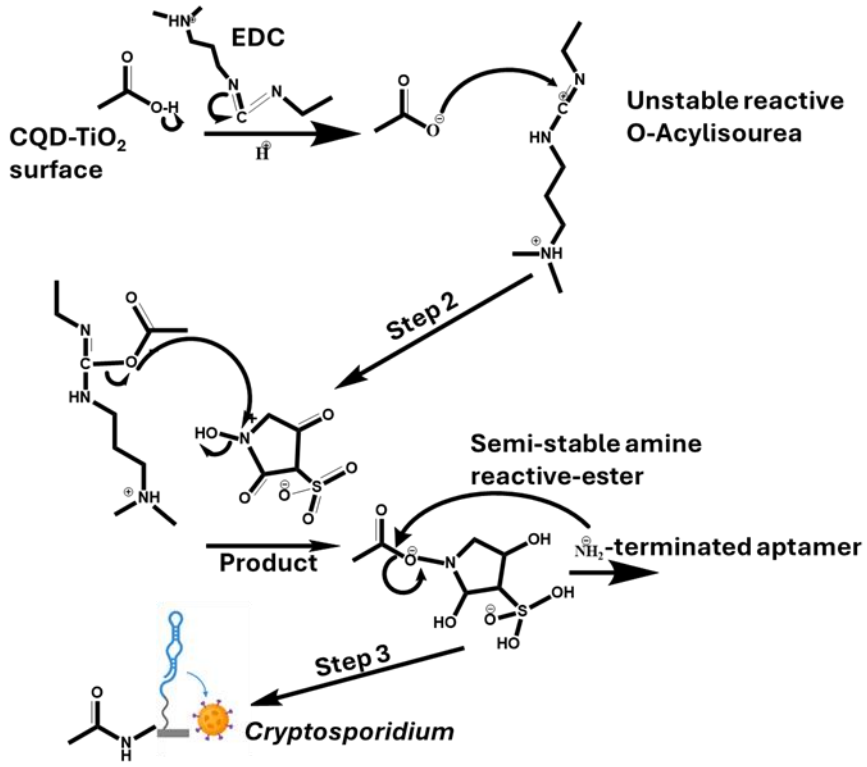

Figure 28: Shows the mechanism of electro-oxidation of *Crypto*.

The interaction of aptamers with metal oxide surfaces is a crucial component of modern electrochemical biosensing platforms. Aptamers can be effectively immobilised on TiO_2 surfaces by electrostatic and covalent interactions. In addition to serving as physical scaffolds, these metal oxides actively participate in electron transport, enabling highly sensitive and specific identification of illnesses such as *Cryptosporidium*. Understanding these mechanisms allows researchers and engineers to optimise sensor design for a wide range of diagnostic and environmental monitoring applications.

The optical properties of the CQD, TiO_2, and the CQD-TiO_2 composite were further investigated using ultraviolet-visible (UV-Vis) spectroscopy. This technique was also employed for detecting *Crypto*. UV-Vis spectroscopy is an analytical method that measures the amount of light absorbed by a sample at various wavelengths.

4.6.2 UV-vis analysis of CQD, TiO_2 and CQD-TiO_2 composite

Figure 29(A-B) depicts the absorption spectra of CQD, TiO_2, and the CQD-TiO_2 composite and Figure 29B shows Tauc plot of TiO_2 and CQD-TiO_2. The spectra were observed between 200 and 800 nm. The absorption peak observed at 321 nm on the spectrum of TiO_2 had an absorbance of 0.89 (<1), indicating good absorption under the UV region [393]. UV-vis absorption spectra of CQD display a band at 280 and a shoulder at 320 nm, corresponding to π-π* transitions of sp^2 C═C bonds and n-π* transitions of C═O (related to sp^3 system) and the related electron transitions in oxygen-containing CQD, as previously reported for amorphous carbon quantum dot [394,395]. The π-π* transitions of sp^2 C═C bonds and n-π* transitions of C═O observed indicate that CQD possess both conjugated structures and oxygen-containing functional groups, as observed in the FTIR spectra [396]. The spectrum of CQD-TiO_2 shows a shift in the absorption peaks. As reported in the literature, the absorption peak of TiO_2 is now observed at 212 cm^{-1}, indicating the chemical bonding between TiO_2 and specific sites of CQD [397]. The direct optical band gap of the samples was determined by extrapolating the Tauc plot of $E(\alpha h\nu)^2$ versus hv in Figure 29B. The determined band gaps for TiO_2 and CQD-TiO_2 were 3.2 eV and 2.68 eV. The band gap of 3.2 eV for TiO_2 confirms the anatase phase of TiO_2. This finding agrees with the XRD and HR-TEM analysis [398] . The decrease in bandgap for CQD-TiO_2 (2.68 eV) suggests that the composite will absorb more photons in the visible region [399].

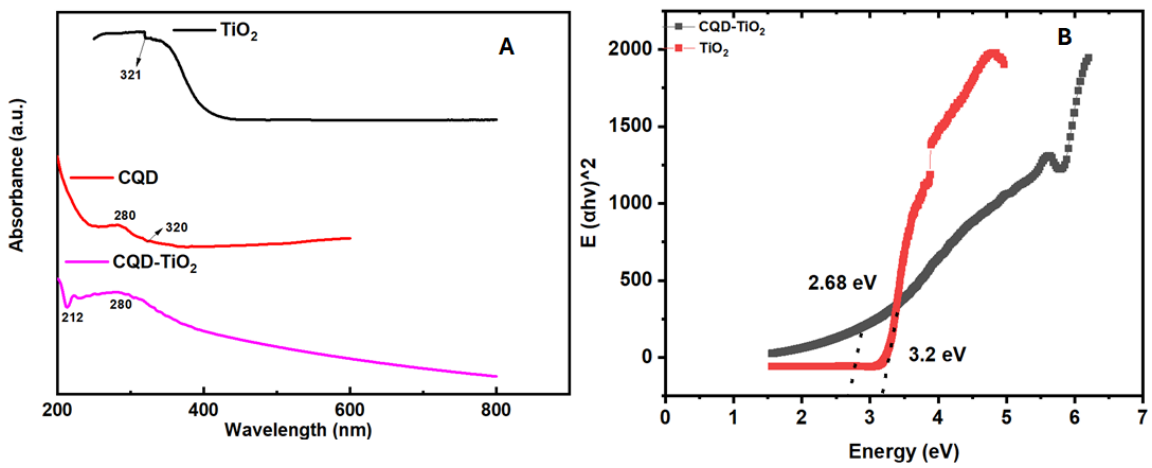

Figure 29: Shows the UV-Vis plot of CQD, TiO_2 and CQD-TiO_2, (B) shows the Tauc plot of TiO_2 and CQD-TiO_2.

To confirm the conjugation of the CQD-TiO_2 composite with the aptamer, a UV-Vis experiment was conducted at wavelengths ranging from 250 nm to 400 nm. The UV-vis spectra were recorded before and after the conjugation. The CQD-TiO_2 composite exhibited an absorption peak at 300 nm. After conjugation with the aptamer solution, a decrease in absorbance was noted. This reduction suggests that the aptamer had bound to the surface of the composite. To prevent the formation of unbound residues or active sites after aptamer binding, bovine serum albumin (BSA) was used as a blocking agent. The addition of BSA also decreased absorbance, as shown in Figure 30.

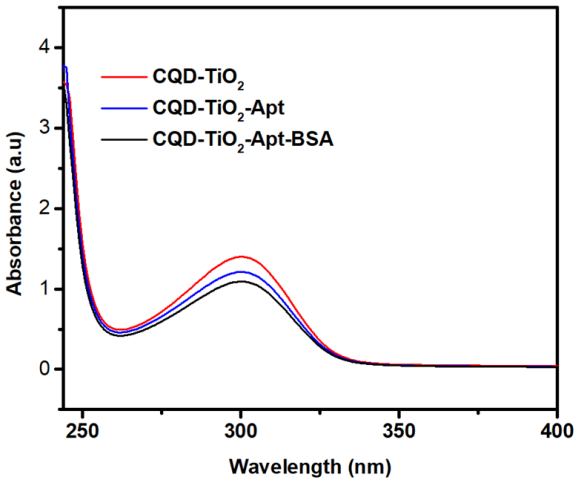

Figure 30: Shows the UV-Vis spectra of CQD-TiO_2 composite, CQD-TiO_2-Apt and CQD-TiO_2-Apt-BSA.

UV-Vis spectroscopy was also used to detect *Crypto* in phosphate buffer. Optical detection was performed over the range 200-400 nm. The UV-Vis experiments were conducted by using different *Crypto* concentrations ranging from 4 to 22 µM. For each concentration,100 µL was added to a cuvette containing 380 µL of 0.1 M phosphate buffer solution, 10 µL of aptamer solution, 2 µL of the tris binding buffer, 2 µL of EDC and NHS, 4 µL of bovine serum albumin (BSA) and 500 µL of composite solution (CQD-TiO_2). Figure 31(A-C) shows the UV-Vis experiments in response to spiked *Crypto* concentrations, 31B depicts the binding curve of spiked *Crypto* concentrations against absorbance, and 31C shows a linear relationship between spiked concentrations and absorbance. Figure 31A shows the absorption spectra of different spiked *Crypto* concentrations. Increasing the concentration of *Crypto* from 4 µM to 22 µM resulted in a gradual decrease in absorbance. This observation suggests that the *Crypto* was binding with the aptamer. Figure 31B shows the calibration curve of spiked concentration vs absorbance. The calibration curve indicates a saturation point was observed at 16 µM. Figure 31C shows the relationship between the spiked concentrations and absorbance, with a slope of -0.036 and a correlation coefficient of $r^2 = 0.99$. To calculate the limit of detection, 10 absorbance measurements were taken of the blank solution to determine the standard deviation. The LOD was calculated using equation 10. Where ð is the standard deviation of the blanks (n = 10), m is the slope of the linear calibration curve of absorbance vs concentration. The calculated ð is 0.0003, and the LOD was determined to be 0.025 ng L^{-1}.

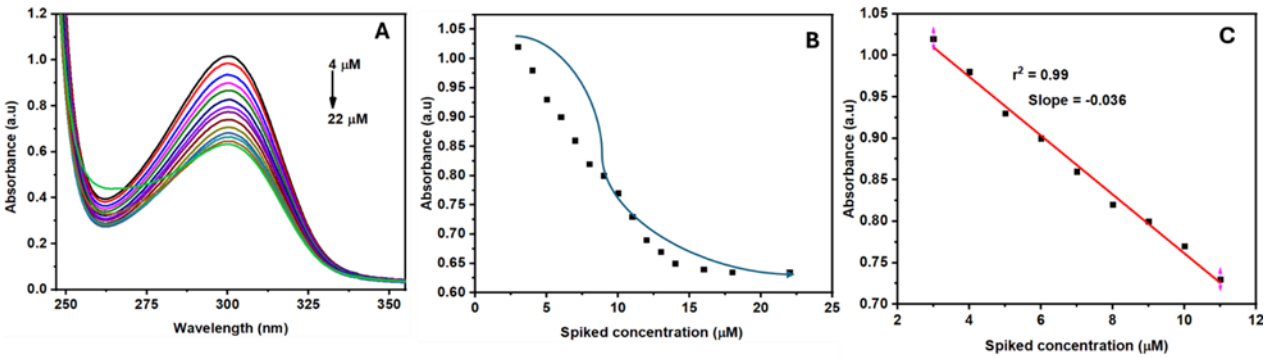

Figure 31: Depicts (A) the detection of *Crypto* using UV-Vis, (B) shows the binding i curve of absorbance against spiked *Crypto* concentration and (C) shows the linear curve of absorbance against spiked *Crypto* concentration.

Table 7 presents the electrochemical characteristics and analysis efficiency of a newly constructed sensor with a CQD-TiO_2-Apt-BSA-modified electrode. The sensor's effectiveness was evaluated using square-wave voltammetry, electrochemical impedance spectroscopy, and cyclic voltammetry at different analyte concentrations. The sensor's excellent performance is attributed to the synergistic interaction between CQD and the TiO_2 nanocomposite, which enhances electron transfer and promotes efficient immobilisation of the aptamer within the BSA blocking layer. The GCE-CQD-TiO_2-Apt-BSA-modified electrode exhibits excellent electrochemical properties and analytical sensitivity, making it a viable platform for ultrasensitive detection of target analytes in both biomedical and environmental applications. The aptasensor developed in this work demonstrated the lowest detection limit for *Crypto*, with an LOD of 0.0024 ng L^{-1}.

Table 7: Presents the electrochemical characteristics and analysis efficiency of a newly constructed GCE-CQD-TiO_2-Apt-BSA-modified electrode.

Modified electrode	**Method**	**Linear range (ng L^{-1})**	**Limit of detection (LOD) (ng L^{-1})**	**Reference**
Au-SPCE	EIS	5 – 200	10	[400]
ITO-AUNPs	DPV	0.003 - 0.005	0.003	[401]
GNPs-SPCE	SWV	0.15 – 0.8	0.1	[185]
Au-SPCE-Apt	SWV	0.25	0.04	[402]
GCE-CQD-TiO_2-Apt-BSA	**EIS**	**0.0045 -0.007**	**0.009**	**This work**
	SVW	**0.0025-0.0045**	**0.0024**	**This work**

GCE-CQD-

TiO_2-Apt-

BSA

The GCE-CQD-TiO_2-Apt-BSA platform was further applied to real water (wastewater and tap water) to assess its selectivity towards *Crypto* using the SWV technique. The sensor platform was also tested in detecting Cd^{2+} recoveries obtained from the experiments, which are also presented.

4.6.3 Real water application

4.6.3.1 Detection of Crypto

The developed aptasensor was evaluated in both tap water and wastewater to assess its performance and accuracy in detecting *Crypto* using the SWV technique. SWV is known as the most sensitive electrochemical technique for detecting analytes at low concentrations. The experiment was conducted using the SWV technique at a scan rate of 25 mV s^{-1}, within a potential window of -0.8 to V to 0.5 V. Working concentrations of *Crypto* were prepared, ranging from 2 µM to 10 µM. The wastewater samples were filtered, and the pH was adjusted to 7. A control experiment using a blank solution was conducted in both tap water and wastewater for comparison purposes. Figure 32(A-D) illustrates the SWV measurement of spiked water samples. Figure 32A shows the SWV measurements of different spiked concentrations of *Crypto* in the wastewater sample. The peak current was monitored after introducing various concentrations of *Crypto*. The blank solution exhibited a current response of 0.084 mA, demonstrating the presence of *Crypto* in the wastewater sample. The peak current increased with rising spiked *Crypto* concentrations, indicating a binding affinity between *Crypto* and the aptamer surface. Figure 32B illustrate the relationship between spiked

concentrations and peak current, with $r^2 = 0.97$. Although several peaks were observed in the wastewater, they did not interfere with the *Crypto* peak, demonstrating that the aptasensor is selective towards *Crypto*. Figure 32C shows the SWV response at different spiked concentrations in tap water. 2 peaks were identified on the blank solution and upon the spiking of 2 µM concentration. The peak observed at a peak potential of -0.24 V is attributed to the *Crypto* peak, while the peak at -0.011 V is attributed to ions present in tap water. Additionally, the peak current increased with higher spiked concentrations of *Crypto*. Figure 32D illustrates the linear relationship between spiked concentration and peak current, with a correlation coefficient of $r^2 = 0.98$. Table 8 summarizes the findings observed from the analysis of real water samples. The recoveries detected by the developed aptasensor ranged from 91% to 109% for wastewater samples and from 78% to 98% for tap water. Overall, the aptasensor demonstrates higher performance in detecting *Crypto* in wastewater samples compared to tap water.

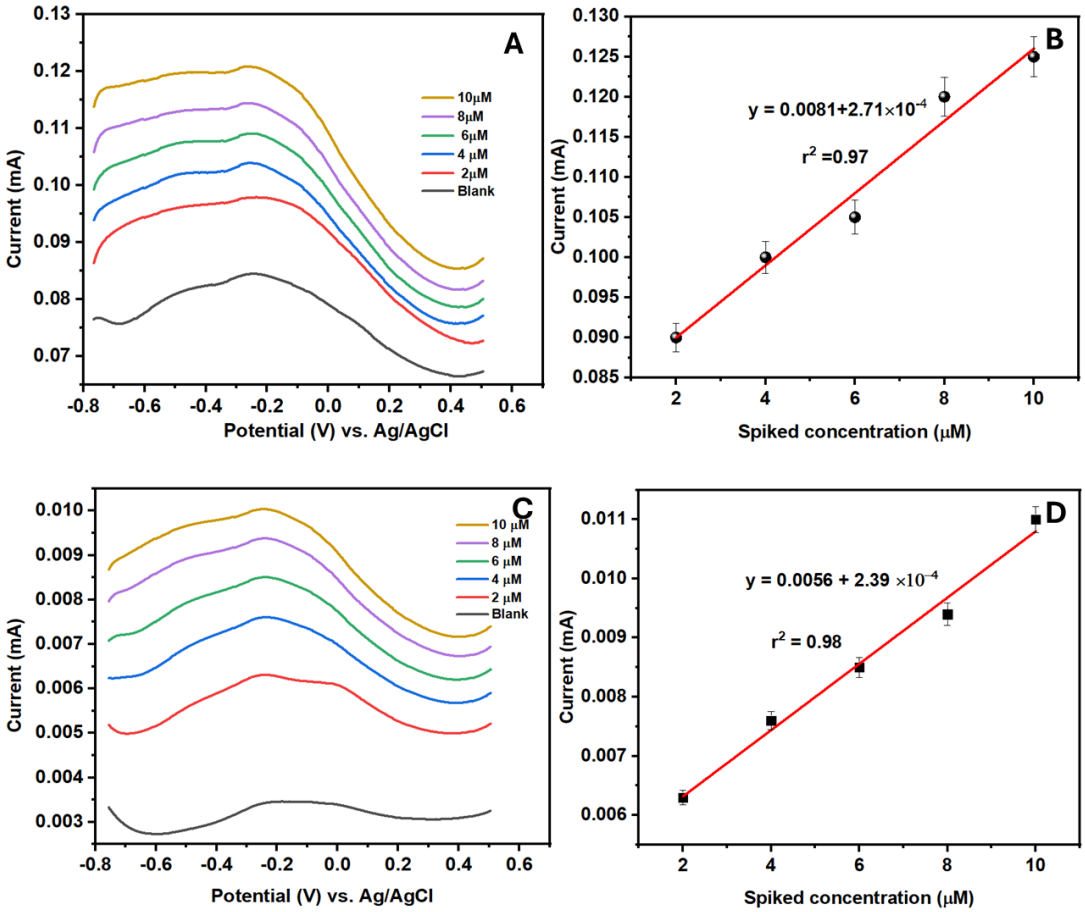

Figure 32: Illustrates (A) the SWV measurements of various spiked *Crypto* concentrations on wastewater, (B) a linear curve of spiked concentration vs peak potential, (C) the SWV measurements of spiked *Crypto* concentrations on tap water and (D) the linear curve of peak current vs spiked concentration.

The F-test was employed to evaluate the precision recovery values. The standard deviation (σ) and mean of the recoveries were determined to fit Equation 11. The results indicated that practical observations were 90% and 94% accurate for tap water and wastewater. Accuracy reflects satisfactory reproducibility.

$$F = \frac{\partial n f^2}{\partial f^2}$$ equation 11

Table 8: Summarises the results obtained on real water samples.

Sample	Added (μM)	Found (μM)	Recovery %
Wastewater	2	0.91	91
	4	1.62	94
	6	1.96	96
	8	2.1	101
	10	3.02	109
Tap water	2	0.775	78
	4	1.59	80
	6	1.90	83
	8	1.97	85
	10	2.1	90

4.6.3.2 cadmium detection

The application of GCE-CQD-TiO_2-Apt-BSA was investigated using wastewater samples for detecting Cd^{2+}. The parameters used for the *Crypto* experiment were also applied in this study. Cd^{2+} working concentrations were prepared, ranging from 2 µM to 10 µM. Figure 33(A-B) shows the SWV measurements of varying spiked concentrations and the linear curve obtained from the SWV experiment. A blank experiment (insert) was conducted before spiking with the working concentrations, which exhibited a peak current of 0.0053 mA at a peak potential of -0.25 V. This peak corresponds to the oxidation states of Ti^{3+}, $Ti^{4+,}$ and O_2 in the CQD-TiO_2 composite [183]. This observation is aligned with the XPS analysis of TiO_2. Upon the addition of Cd^{2+} working concentrations, a second peak was observed at a peak potential of -0.68 V. Generally, the cadmium peak is detected between -0.6 V and -1.0 V, depending on the pH and type of electrolyte used [403]. In this study, Cd^{2+} was detected at -0.68 V. This observation is in agreement with the reported literature [404]. It was noted that the Cd^{2+} peak current decreased as the spiked concentration increased. This observation can be attributed to competition among pollutants in the water matrix, which affected the signal of the Cd^{2+} detection peak and hindered diffusion at the electrode interface. The correlation between spiked concentrations and peak current is shown in Figure 33B.

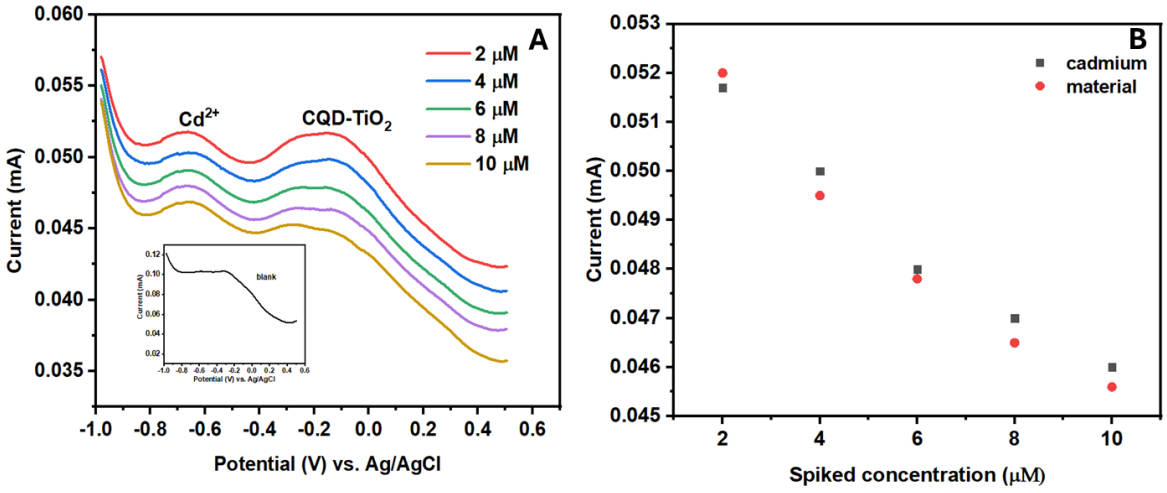

Figure 33: Displays the SWV measurements of various spiked Cd^{2+} concentrations in wastewater are shown. (B) shows the linear curve obtained from SWV scans.

The selectivity of GCE-CQD-TiO_2-Apt-BSA towards *Crypto* was evaluated in phosphate buffer solutions by detecting *Crypto* in the presence of E. coli and Giardia. The detection of mismatched analytes was also carried out in phosphate buffer solutions.

4.6.4. Selectivity studies

Selectivity in biosensors is a crucial aspect of their performance, ensuring that the developed sensor accurately identifies the target analyte within complex biological samples [405,406]. This study examined the electrochemical response of the developed aptasensor (GCE-CQD-TiO_2-Apt-BSA) in detecting a mismatched analyte and *Crypto* in the presence of interferences. *Giardia and E. coli* were chosen as interference species for this experiment. The testing was conducted over a potential of -1 V - 0.5 V with a scan rate of 25 mV s^{-1} in phosphate buffer at pH 7.2, using square wave voltammetry to assess selectivity. Various concentrations of the mismatched analyte were tested, ranging from 0 to $3x10^8$ nM, and 4 µM concentrations of *Crypto*, Giardia, and *E. coli.* Figure 34(A-D) illustrates 34A the comparison of *Crypto* and mismatched analyte detection, 34B SWV response to *Crypto* concentrations, 34C displays SWV response to mismatched analyte concentrations, and 34D shows the linear curves obtained from *Crypto* and mismatched analyte detection.

Figure 34A illustrates the current responses obtained after adding *Crypto* and the mismatched analyte. The aptasensor exhibited a higher peak current response to Crypto than to the mismatched analyte, indicating robust, precise binding of the aptamer to *Crypto*. This reveals the aptamer's high specificity and affinity, which are necessary for selective detection. Figure 34B depicts the SWV response to different spiked concentrations *of Crypto*. The peak current rose with an increase in spiked concentrations. This is due to the aptamer's conformational alteration during target recognition, which enhances electron transport at the electrode-electrolyte interface. Figure 34C shows the SWV response as the concentration of the mismatched analyte increases. No specific interaction between the mismatched analyte and the aptasensor was observed, as no obvious change in current was noted over the spiked

concentrations. The binding inhibition curves presented in Figure 34D provide additional support for these observations. Although the signal increased dramatically and continuously with *Crypto*, the mismatched analyte caused minor signal changes, implying little to no chemical interaction.

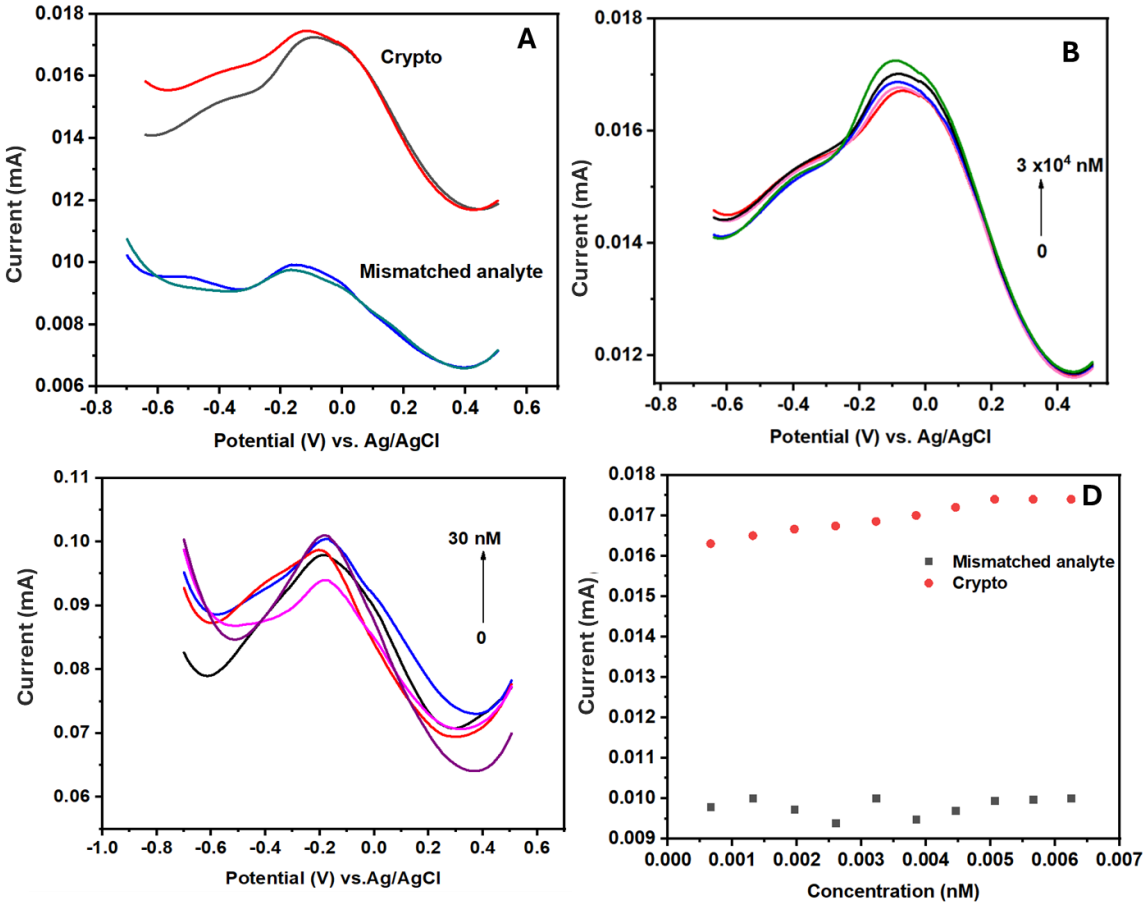

Figure 34: Depicts (A) the SWV response on *Crypto* and mismatched analyte at spiked concentrations in 0.1M PBS (pH,7.2), (B) SWV response at varying *Crypto* concentrations, (C) SWV response at various mismatched concentrations and (D) the linear plot of peak current vs. concentration obtained from *Crypto* and mismatched detection.

The current response of *Crypto* was assessed in the presence of interferences. Figure 35(A-B) shows the SWV response for detecting *Crypto* in the presence of potential interferences, and Figure 35B displays the detection of *E. coli and Giardia*. The aptasensor exhibited a current response of 0.0145 mA in the absence of interference, as shown in Figure 35A. Upon the addition of Giardia concentration, a decline in the

current response was observed. The current response decreased further upon the addition of *E. coli*, accompanied by a slight shift in the peak potential. These findings indicate that the developed aptasensor is selective towards *Crypto*, as the peak did not shift significantly and no new peaks were observed.

Figure 35B displays the detection results for *Giardia and E. coli* under the same conditions as for *Crypto.* Notably, the aptasensor exhibited a higher current response for *Giardia* than for *E. coli.* This observation suggests that Giardia binds to the electrode surface. This finding is also due to the similarity between Giardia and *Crypto*, as both species belong to the same family within the phylum Apicomplexa.

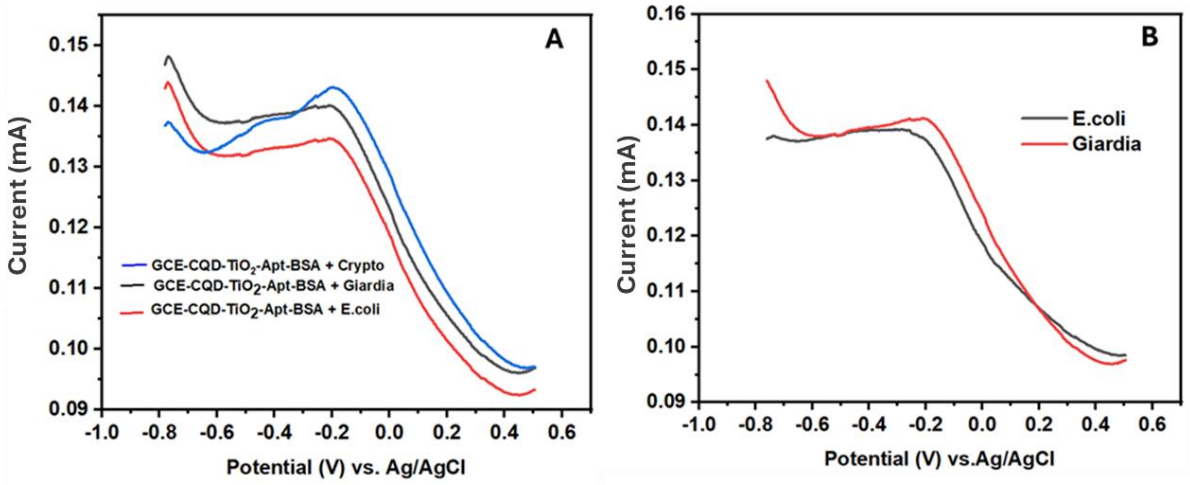

Figure 35: Shows (A) the *Crypto* detection in the presence of interferences in 0.1 M PBS (pH, 7.2), (B) shows the detection of *E. coli and Giardia*.

4.6.5. Summary and Sub-conclusion

CQD-TiO_2 composite was prepared through precipitation and characterized using physicochemical techniques to confirm the formation of the composite. The synthesized composite was then utilized as an electrode modifier in the development of an aptasensor for detecting *Crypto* in buffer solutions. The doping of CQD with TiO_2 improved the electrochemical behaviour of GCE-CQD-TiO_2. The results indicated that a 3 h incubation period was sufficient to cover all available active sites on the electrode

surface, effectively preventing fouling, a common issue in electrochemical sensors. All experiments were conducted with a 3 h incubation time. The electrochemical aptasensor showed a larger electroactive surface area than previously reported, providing more active sites for analyte detection. Selectivity was confirmed by detecting a mismatched analyte and *Crypto*, which caused a notable change in electron flow. The aptasensor specifically targeted Crypto, with slight decreases in peak current observed in the presence of interferences. The developed aptasensor was employed to detect *Crypto* in spiked buffer solutions using three techniques, yielding varying LOD: EIS at 0.009 ng L^{-1} , UV-Vis at 0.025 µM, and SWV at 0.0024 ng L^{-1}, with SWV demonstrating a broad linear range of 0.0025 to 0.0045 nM and high sensitivity at 0.2706 mA nM^{-1}. In real-world water applications, the aptasensor achieved recovery rates of 91%- 109% for wastewater and 90% for tap water. The GCE-CQD-TiO_2-Apt-BSA was also evaluated for cadmium detection, revealing diffusion blockages at the electrode interface. Overall, the CQD-TiO_2 combination excelled at detecting *Crypto* but was unsuitable for heavy-metal detection.

CHAPTER FIVE:

Characterization of M101(Fe)-CQD-TiO_2 ternary composite for dual analyte detection

5.1 Overview

This chapter provides a summary of the characterization of MII101(Fe), carbon quantum dots, titanium dioxide, and the MII101(Fe)-CQD-TiO_2 ternary composite. The structural, morphological, and chemical features were examined using XRD, FTIR, HR-TEM, EDS, and Raman, confirming the successful integration of the above components. It also discusses the ternary composite used as an electrode modifier in the development of an electrochemical aptasensor for detecting cadmium ions, arsenic, and Crypto in wastewater and tap water samples. The aptasensor platform was optimized and tested in phosphate buffer solution, tested for interferences in both in real water samples and buffer solutions, using square wave voltammetry. Furthermore, the sensor achieved a limit of detection of 0.001 ng L^{-1} for Crypto and 0.05 ng L^{-1} for cadmium, demonstrating high sensitivities of 9 x 10^{-4} mA μM^{-1} and 0.127 mA μM^{-1} in buffer solutions.

5.2 Introduction

Crypto is a protozoan parasite that causes diarrheal disease, primarily affecting young children, immunocompromised individuals, and healthy adults through the consumption of contaminated water [407]. On the other hand, cadmium ions (Cd^{2+}) are toxic metals that can accumulate in organisms and cause health issues like cancer and organ damage [408]. To mitigate these risks, water quality regulations have established an allowed limit for Cd^{2+} concentrations of 0.003 ng L^{-1} [409] . Both *Crypto* and cadmium pose threats to humans, animals, and aquatic species, highlighting the need for an aptasensor platform to monitor their concentrations in water bodies [410]. Detecting both chemical and biological pollutants simultaneously in water matrices is still a challenge. To overcome this challenge, MI101(Fe)-CQD-TiO_2 ternary composite was prepared and utilised as an electrode material for the fabrication of an aptasensor platform [411]. The large surface area of the ternary composite facilitates effective interaction with the analyte, enabling the aptasensor to detect *Crypto* and cadmium ions at trace levels [412]. This effectiveness is further enhanced by the unique d-electron configuration of iron and its various valence states (Fe^{3+}, Fe^{2+}), which promote electron movement [413,414]. Additionally, the conductivity of the ternary composite enhances the

sensitivity and selectivity of the aptasensor, resulting in higher accuracy and achieving lower limits of detection [415].

5.3 Results and discussions

5.3.1 Structural and morphological characterization of Mil101(Fe), CQD, TiO_2 and Mil101(Fe)-CQD-TiO_2

5.3.1.1 XRD analysis of Mil101(Fe), CQD, TiO_2, CQD-TiO_2 and Mil101(Fe)-CQD-TiO_2

X-ray diffraction (XRD) is an effective analytical technique for determining the crystalline structure and phase composition of materials [416]. The technique involves shining X-rays on a material and analysing how they diffract, revealing the material's atomic arrangement. This provides information on the material's crystal structure, phase composition, crystal orientation, size, and phase identification [417]. XRD was utilized to assess the crystalline structure, d-spacing, and phase identification of the produced nanomaterials [418]. Figure 36 shows the XRD patterns of Mil101(Fe), TiO_2, CQD, and Mil101(Fe)-CQD-TiO_2. XRD patterns of synthesized Mil101(Fe) revealed peaks at 2θ values of 25.5°, 18.57°, 16.65°, and 9.42°. The displayed XRD patterns correlate to the crystal planes of (852), (511), (111), and (311) [419]. The measured peaks corroborated the strong crystallinity of Mil101(Fe), and the results are consistent with prior investigations.

The XRD patterns of the synthesized titanium dioxide (TiO_2) exhibited sharp, narrow, and intense peaks, indicating a crystalline structure. The TiO_2 patterns displayed firm peaks at 2θ values of 25.3°, 37.8°, 40.0°, 54.6°, 62.9°, and 75.3°, which correspond to the crystal planes (101), (004), (200), (105), (211), (204), and (107). These results confirm that TiO_2 is in the anatase phase, which is consistent with findings from the Raman analysis [420,421]. CQD does not have a periodic crystal structure [422] and cannot scatter electrons [423] It exhibits an unstructured ring with X-ray diffraction peaks at 20.4° and 24.6° [424]. The prominent diffraction peak at 2θ = 22° to 25° corresponds to the (002) reflection plane of graphite [425]. The synthesised CQD in this investigation

showed peaks in the 2θ range of 9° - 90°. The prominent diffraction peak between 9 ° and 20 ° in 2θ indicates the amorphous nature of CQD [426]. The results are consistent with those obtained from Raman analysis. The shift in the broad diffraction peak is attributed to the type of precursor, synthesis process, and synthesis temperature [427]. These findings suggest that the carbon atoms in CQD are organised disorderedly. These results are consistent with Raman analysis. The presence of tiny and sharp diffractograms in CQD XRD patterns indicates the presence of leftover organic compounds within the amorphous carbon area. Thulasi et al. and Din et al. [427,428] investigated the synthesis of CQD using green chemistry and obtained results that are consistent with those found in our investigation. The ternary composite displayed significant peaks at 25.7°, 38.0°, 48.4°, 54.8°, 62.9°, and 75.5°, confirming the formation of the Mil101(Fe)-CQD-TiO_2 ternary composite.

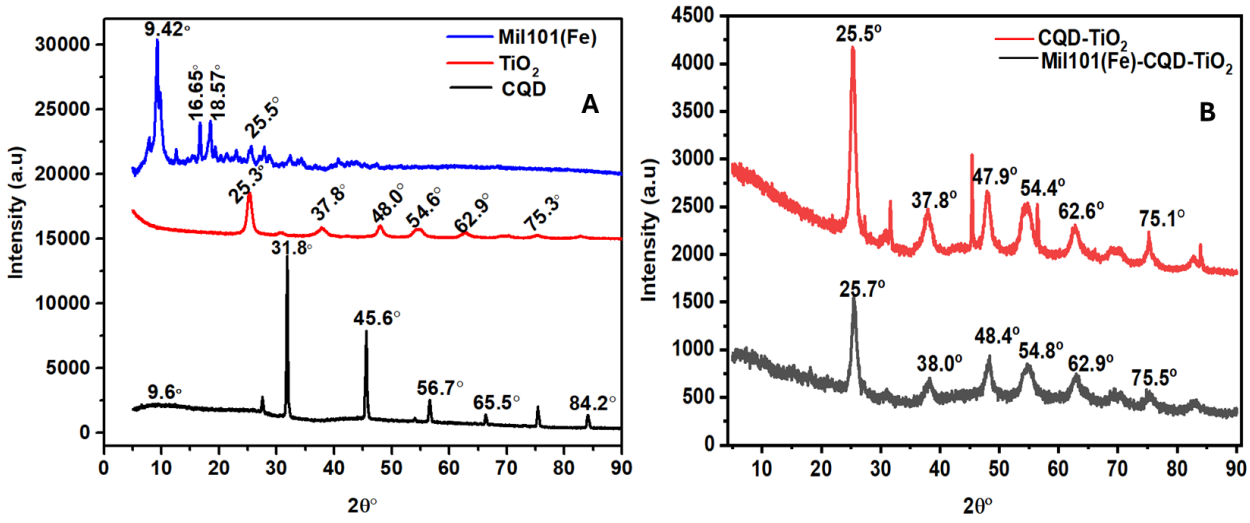

Figure 36: Shows the XRD of (A) Mil101(Fe), TiO_2 and CQD, and (B) depicts the XRD of CQD-TiO_2 and Mil101(Fe)-CQD-TiO_2.

The average particle size was calculated using the Scherrer equation applied to the apparent full width at half maximum intensity (FWHM) of the most prominent peak, as shown in the equation 6.

Where D represents the particle size, β is the full width at half maximum (FWHM), θ is the Bragg's angle of the intense peak, and λ denotes the wavelength of the x-ray beam (0.15405 nm). The constant K is equal to 0.9. Table 9 presents the calculated d-spacing and crystallite size for the synthesized nanomaterials. The d-spacing is the

distance between two parallel atomic planes that produce diffraction peaks. In contrast, crystallite size refers to the coherent volume within the material corresponding to these diffraction peaks. The composite exhibited a crystallite size of 7.72 nm, which is smaller than the sizes of both TiO_2 (8.10 nm) and CQD (30.8 nm). These findings suggest that integrating Mil101(Fe), CQD, and TiO_2 into a ternary composite yields a smaller crystallite size than the individual components.

Table 9: Shows the calculated crystallite sizes and d spacing of Mil101(Fe), CQD, TiO_2, Mil101(Fe)-CQD-TiO_2.

Material	Crystallite size (nm)	d-spacing (nm)	2θ
Mil101(Fe)	4.33	0.94	9.44°
CQD	30.8	0.28	31.1°
TiO_2	8.10	0.35	25.8°
Mil101(Fe)-CQD-TiO_2	7.71	0.34	25.7°

The functional groups on the surface of TiO_2, CQD, Mi101 (Fe) and Mi101(Fe)-CQD-TiO_2 were evaluated using FTIR techniques. Fourier transform infrared (FTIR) spectroscopy is a valuable technique for analysing the characteristics of various nanomaterials. It helps identify chemical bonds, molecular structures, and functional groups within a material [429]. To confirm the presence of these functional groups, FTIR analysis was conducted at wavelengths ranging from 4000 cm^{-1} - 400 cm^{-1}.

5.3.1.2 FTIR analysis of TiO_2, CQD, Mil101(Fe) and Mil101(Fe)-CQD-TiO_2

Figure 37(A-B) presents the FTIR spectrum of TiO_2, CQD, Mil101(Fe), and the Mil101(Fe)-CQD-TiO_2 ternary composite. The FTIR spectra of TiO_2 exhibit an absorption band at 3361 cm^{-1}, attributed to the presence of hydroxyl (OH) groups. A peak around 1608 cm^{-1} corresponds to carbonyl (C=O) groups, while the peak at 1244

cm^{-1} refers to O-H groups on the surface of TiO_2 [430]. These findings are generally consistent with the existing literature [431,432]. The FTIR spectrum of CQD shows that the adsorption peak at 1379 cm^{-1} belongs to the production of O-H groups, while the peak at 1601 cm^{-1} refers to the C=O from the carbonyl groups [433,434]. The peak seen at 2913 cm^{-1} is attributable to the symmetric stretch of C-H, and the band observed at 3406 cm^{-1} relates to the hydroxyl bond on the surface of CQD [435].

The FTIR spectrum of Mil101(Fe) exhibits a high absorption peak at 584 cm^{-1}, which is attributable to Fe-O vibration. In contrast, peaks detected between 700 cm^{-1} and 1095 cm^{-1} relate to C-H bonding, indicating the presence of an organic linker in the Mil101(Fe) structures [436,437]. The peaks at 1385 cm^{-1} and 1666 cm^{-1} are due to asymmetric and symmetric carboxylic group vibrations [438,439]. The large adsorption band at 3415 cm^{-1} is attributed to the stretching of the hydroxyl group [440]. The findings are consistent with the existing literature [441,442]. The FTIR spectra of the ternary composite showed a blue shift in the absorption peaks when compared to the individual components. The signal at 3415 cm^{-1} corresponds to the presence of hydroxyl groups. Additionally, a peak associated with carbonyl groups was observed at a lower wavelength than that of MIl101(Fe), CQD, and TiO_2, specifically at 1696 cm^{-1} [443]. The FTIR spectra of the composite retained characteristics similar to those of MIl101 (Fe). This observation suggests the presence of coordination bonding or hydrogen bonding among Mil101(Fe), CQD, and TiO_2. No additional peaks were detected, indicating that the ternary composite had been successfully synthesised.

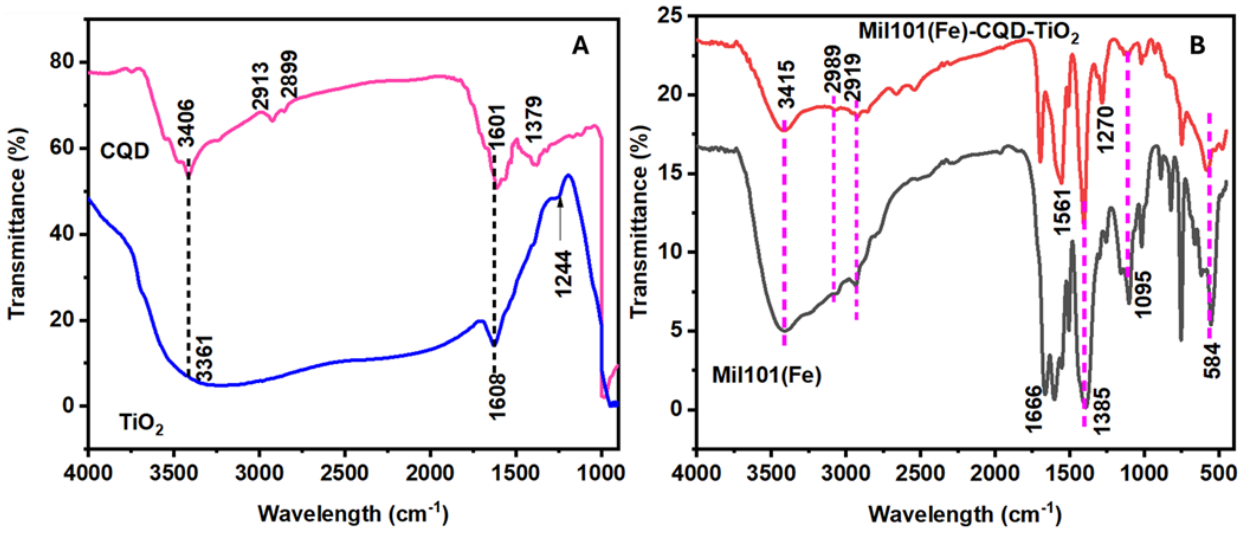

Figure 37: Shows the FTIR spectra of TiO_2 and CQD, (B) depicts the FTIR spectra of Mil101(Fe) and Mil101(Fe)-CQD-TiO_2.

The crystal phases, interplanar spaces between the molecules in the synthesised CQD, TiO_2, Mil101(Fe) and Mil101(Fe)-CQD-TiO_2 were examined using the HR-TEM technique. High-resolution transmission microscopy (HR-TEM) is a phase-contrast imaging technique that allows for image capture at nearly atomic resolution. This method is particularly helpful for examining crystallinity, lattice planes, crystal phases, and defects in nanomaterials. HR-TEM effectively analyses the elemental distribution and morphological structure of nanomaterials at the nanoscale [444,445].

5.3.1.3 HR-TEM analysis of CQD, TiO_2, Mil101(Fe) and Mil101(Fe)-CQD-TiO_2

HR-TEM was utilized to study the crystallinity, lattice planes, and morphological structures of Mil101(Fe), CQD, TiO_2, and the Mil101(Fe)-CQD-TiO_2 ternary composite. Figures 38(A-E) show HR-TEM images of CQD, TiO_2, Mil101(Fe), and Mil101(Fe)-CQD-TiO_2. Figure 38A depicts monodispersed CQD particles with a spherical shape. These findings were consistent with the reports of Amira et al. and Sanfranko et al. [446,447]. Figure 38B presents an HR-TEM image of the produced TiO_2. The results indicate that the TiO_2 are agglomerated and exhibits irregular shapes [446]. Agglomeration occurs when particles become unstable at the nanoscale and tend to

cluster until they reach a stable configuration. These observations align with the existing literature [448]. The TiO_2 exhibit a circular shape with a consistent structure. Additionally, the round shape of the TiO_2 promotes good dispersion in various solutions, resulting in a large surface area that enhances interactions with other materials [449,450]. Uneven and agglomerated TiO_2 can decrease the number of active sites on their surface, thereby limiting the effective surface area and impairing the composite's performance [451]. Additionally, TiO_2 exhibits lattice fringes with an interlayer spacing of 0.36 nm. This interspacing corresponds to the (101) crystal plane of anatase, indicating that TiO_2 has a crystalline structure [420]. This observation is consistent with the XRD results. Figure 38D depicts the HR-TEM of Mil101(Fe), which showed a big rod-like or needle-shaped morphology with a smooth surface. Some of the rod-like formations overlapped, indicating an aggregation of Mil101(Fe) particles. The measured features of Mil101(Fe) indicate anisotropic development during hydrothermal synthesis, which is temperature-dependent [275,452]. Figure 38E shows an HR-TEM image of the Mil101(Fe)-CQD-TiO_2 ternary composite material. The image reveals a well-distributed CQD and TiO_2 on the surface of Mil101(Fe). The ternary composite exhibits lattice fringes with interplanar spacings of 0.30 nm and 0.36 nm, indicating its crystallinity. These interplanar spacings indicate the presence of TiO_2 in the composite, corresponding to the anatase (101) crystal phase of TiO_2. These findings are consistent with the XRD analysis.

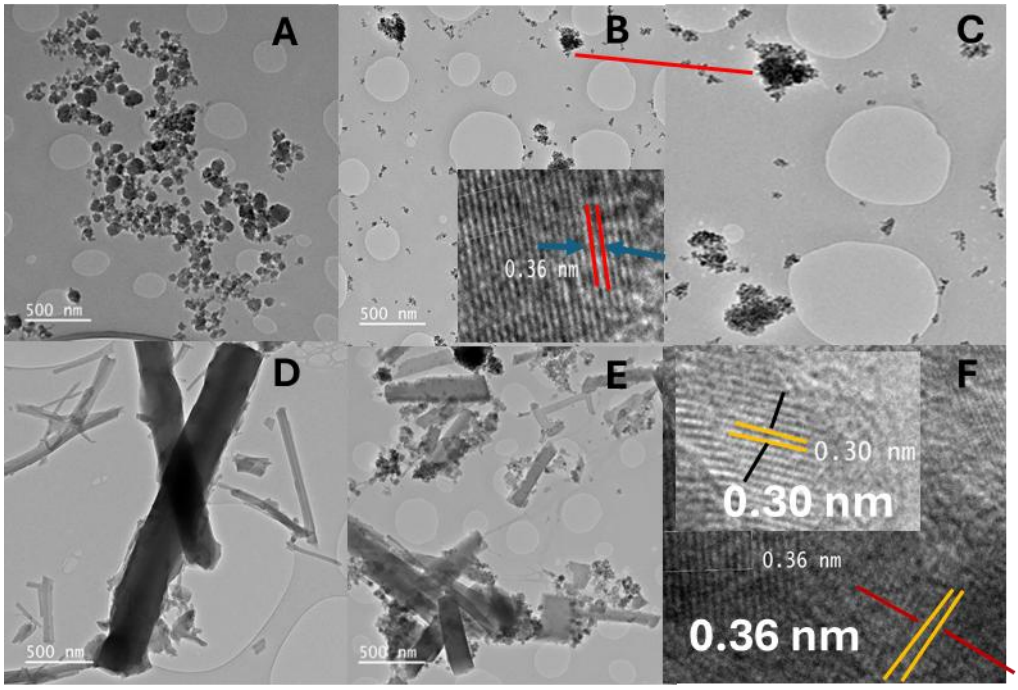

Figure 38: Depicts (A) the HR-TEM image of CQD, (B) TiO_2, (C) enhanced image of (B), (D) Mil101(Fe),(E) Mil101(Fe)-CQD-TiO_2 and (F) the interplanar spacing of Mil101(Fe)-CQD-TiO_2 ternary composite.

Raman analysis was also employed to analyze the vibrational frequencies, and chemical bonds present in the produced materials. Raman spectroscopy is a non-contact vibrational spectroscopic technique that can be used for both qualitative and quantitative analyses. Quantitative analysis involves measuring the intensity of scattered radiation, while qualitative analysis focuses on determining the frequencies of the scattered radiation [453]. This technique has become an essential tool for material characterisation, enabling the investigation of vibrational modes and the nature of chemical bonding within a sample [454].

5.3.2.4 Raman analysis of TiO_2, CQD, Mil101(Fe) and Mil101(Fe)-CQD-TiO_2 ternary composite

Figure 39 (A-B) depicts the Raman spectra of Mil101(Fe), CQD, TiO_2, and the Mil101(Fe)-CQD-TiO_2 ternary composite. The TiO_2 Raman spectrum revealed four unique Raman bands. The peak at 644 cm^{-1} is associated with Eg, while the band at 520 cm^{-1} corresponds to A1g. Additionally, the bands at 405 cm^{-1} and 145 cm^{-1}

correspond to B1g and Eg [455]. The vibrational frequencies corroborated the anatase phase of TiO_2 [328]. These findings are compatible with the XRD and HR-TEM analyses. The Raman spectra of CQD exhibited three Raman bands. The D and G of CQD emerged at 1363 cm^{-1} and 1588 cm^{-1}, and the peak at 2793 cm^{-1} validates the synthesized CQD's amorphous nature [329]. These results are compatible with the XRD analysis of CQD. The D band relates to the vibration of sp^2 carbon atoms, whereas the G band relates to a disordered carbon structure [80]. The Raman spectra of Mil101(Fe) showed four Raman bands that corresponded to the organic ligands in the structure. The band seen at 860 cm^{-1} corresponds to C-H vibrations, whereas the band seen at 1138 cm^{-1} is related to the C-C bond in the benzene ring [456]. The bands at 1429 cm^{-1} and 1606 cm^{-1} are due to C=O stretching vibrations in the carboxylic group [457]. The ternary composite's Raman spectra revealed enhanced intensity bands, confirming the successful integration of Mil101(Fe), CQD, and TiO_2. For example, a band identified at 149 cm^{-1} in the TiO_2 spectrum increased in intensity to 154 cm^{-1} in the ternary spectrum. Furthermore, the peak at 1584 cm^{-1} in the ternary composite was found at 1588 cm^{-1} in the CQD Raman spectrum. The distortion of the Mil101(Fe) bands in the ternary composite suggests a strong electronic interaction between Fe centres and oxygen-containing groups from CQD and TiO_2. These findings are aligned with those obtained in the HR-TEM examination of the ternary composite.

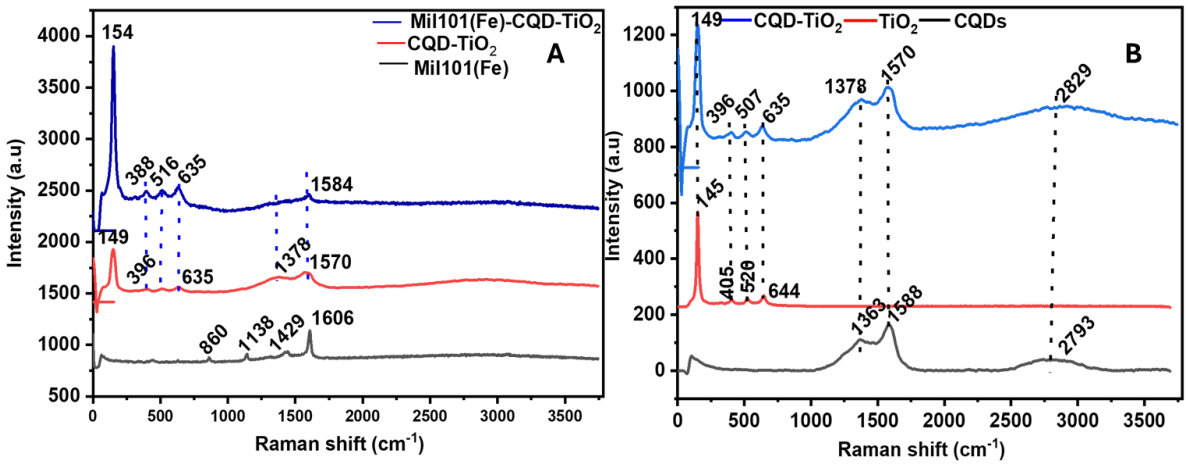

Figure 39: Shows the Raman spectra of (A) Mil101(Fe), Mil101(Fe)-CQD-TiO_2 and (B) depicts the Raman spectra of CQD, TiO_2 and CQD-TiO_2.

To further confirm the formation of Mil101(Fe)-CQD-TiO_2 ternary composite, the elemental composition in the synthesised CQD, TiO_2, and Mil101(Fe) was determined using the EDS technique. Energy-dispersive spectroscopy is an analytical technique used to measure and identify the elements present in a material. EDS detects the intensity or energy of X-rays generated by a sample when subjected to an electron beam [458]. It is also used in conjunction with scanning or transmission electron microscopy to produce an elemental map of the material. Element mapping enables scientists to visualise the arrangement of elements within a sample.

5.3.1.5 EDS analysis of Mil101(Fe), CQD, TiO_2 and Mil101(Fe)-CQD-TiO_2

EDS was employed to determine the elements found in Mil101(Fe), CQD, and TiO_2 and to confirm the synthesis of the Mil101(Fe)-CQD-TiO_2 ternary composite. Figure 40(A–D) depicts the EDS spectra of various samples. Figure 40A depicts the EDS spectrum of Mil101(Fe), which is largely composed of iron (Fe), oxygen (O), and carbon. This composition is consistent with FTIR results, which confirm the presence of carbonyl, hydroxyl, and Fe metal groups on the surface of Mil101(Fe). Furthermore, the presence of copper, silicon, and chlorine is owing to contaminants in the sample. Figure 40B depicts the EDS spectrum of CQD, which is composed of carbon and oxygen, demonstrating the presence of oxygen-containing groups on the carbon quantum dot surface. The peaks for copper (Cu), calcium (Ca), and chlorine in CQD are due to contaminants. In Figure 40C, the chemical composition of TiO_2 is presented. The TiO_2 spectrum primarily shows peaks for titanium and oxygen, with a peak for copper likely resulting from impurities in the titanium sample. The EDS spectra exhibit peaks for oxygen, iron, and titanium, indicating the successful synthesis of the ternary composite. The peaks for aluminium and copper are associated with contaminants in the sample. The EDS spectra of the Mil101(Fe)-CQD-TiO_2 ternary composite show peaks for Fe, Ti, and O, confirming the integration of the composite as shown in Figure 40D.

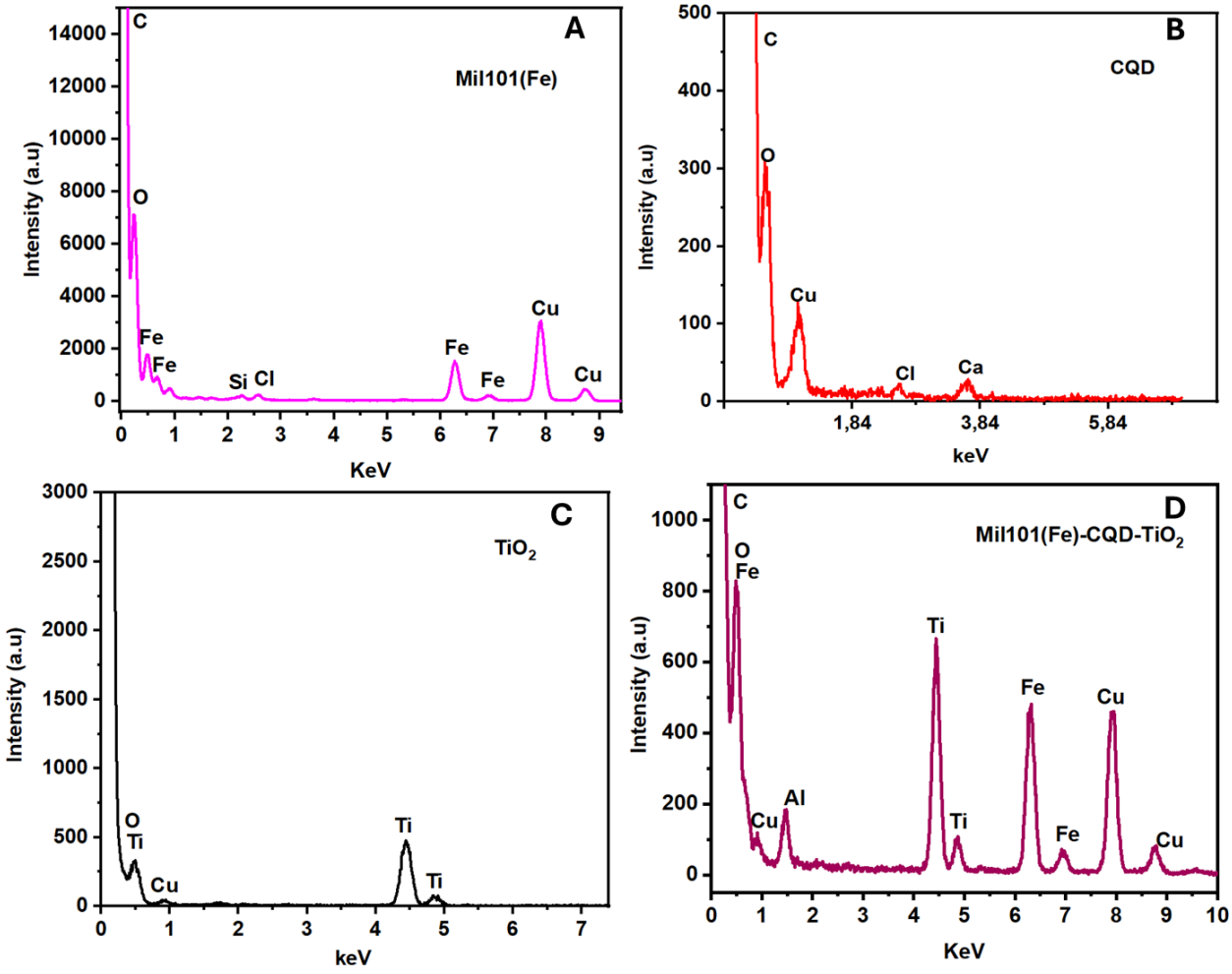

Figure 40: Shows the EDS spectra of (A) CQD, (B) Mil101(Fe), (C) TiO_2, and (D) Mil101(Fe)-CQD-TiO_2.

Figure 41(A-D) shows the elemental mapping of the materials. Elemental mapping facilitates an understanding of the distribution of different elements within synthetic materials. Figures 41(A-D) show elemental maps of carbon, titanium, oxygen, and iron. The mapping results are compatible with the EDS spectra of the synthesized materials, demonstrating the existence of all the elements identified by the various spectra.

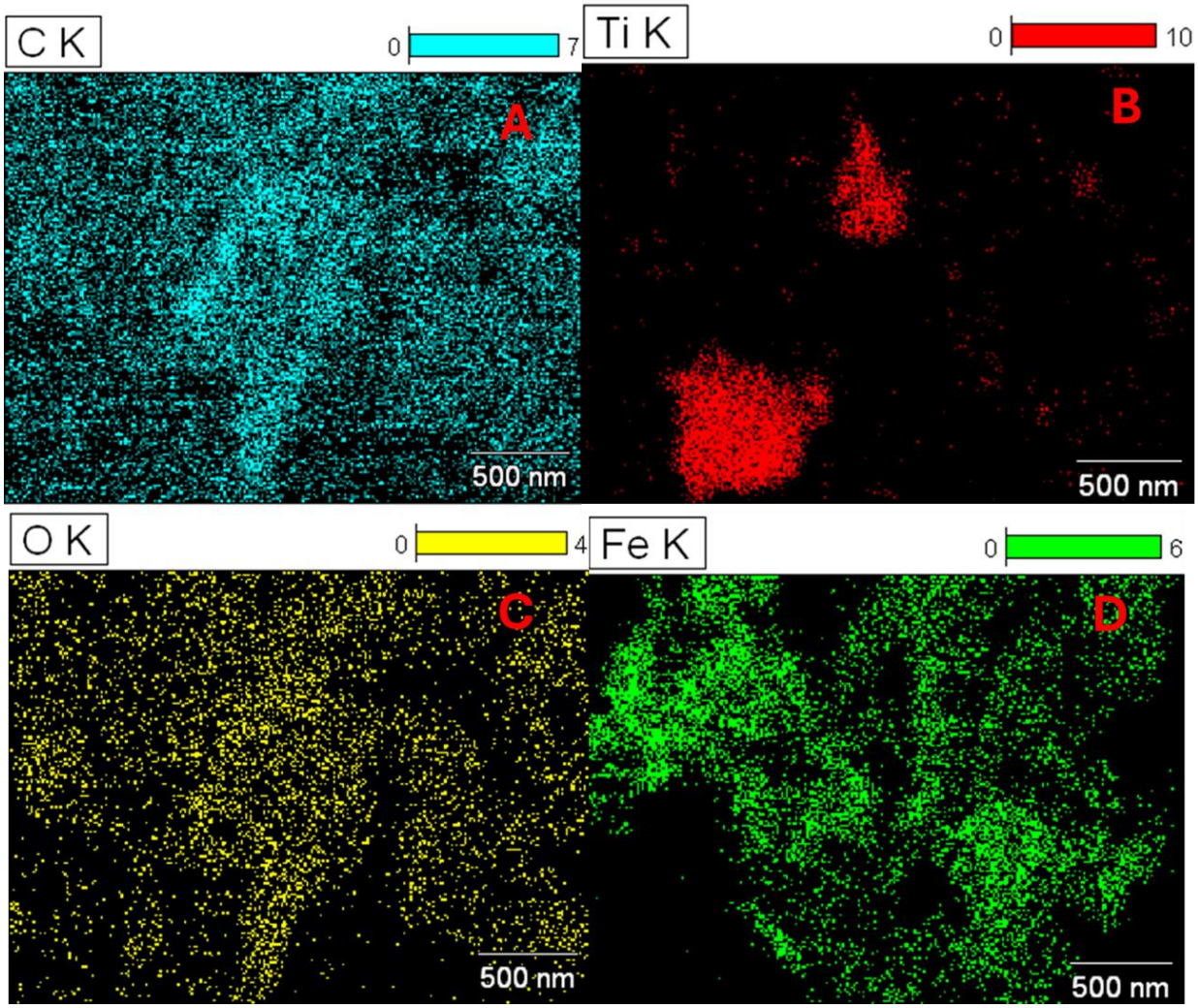

Figure 41: Illustrates the elemental mapping of (A) carbon, (B) titanium, (C) oxygen and (D) iron.

The redox properties of the modified electrodes GCE-CQD, GCE-TiO_2, GCE-Mil101(Fe), and GCE-Mil101(Fe)-CQD-TiO_2 were investigated using CV. The EIS technique was employed to further study the reaction kinetics on the electrode surface.

5.4. Electrochemical analysis

5.4.1 Cyclic voltammetry analysis of GCE, GCE-Mil101(Fe)

Cyclic voltammetry is a powerful electrochemical technique for studying oxidation-reduction processes of molecular species. CV also investigates the kinetics of reactions at the electrode-electrolyte interface, electron transport, absorption

processes, and diffusion-controlled processes [459]. Figure 42(A-B) shows the cyclic voltammograms of GCE and GCE-Mil101(Fe) electrodes in a 0.1M phosphate buffer (pH 6.8). The bare electrode exhibited no redox activity; thus, it was utilised for comparison. The GCE-Mil101(Fe) demonstrated a pair of redox characteristics after being modified with Mil101(Fe). At a peak potential of 0.143 V, GCE-Mil101(Fe) had an oxidation peak current (I_{pa}), and at a peak potential of -0.69 V, it had an anodic peak current (I_{pb}). These data are attributed to the surface redox interaction between Fe^{3+} and Fe^{2+}, signifying its faradaic behaviour.

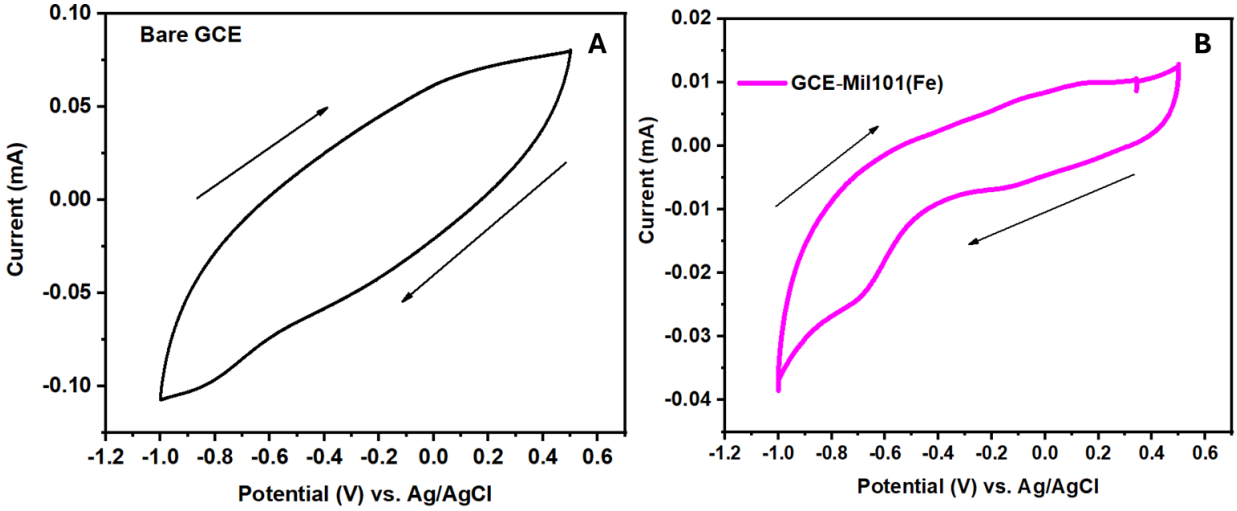

Figure 42: Shows the (A) cyclic voltammogram of a bare electrode, and (B) depicts the cyclic voltammogram of GCE-Mil101(Fe), a scan rate of 50 mVs^{-1}, in 0.1M (pH 6.8).

5.4.2 Comparative studies of GCE-CQD-TiO_2, GCE-Mil101(Fe)-CQD-TiO_2 and GCE-Mil101(Fe)-TiO_2

The electrochemical performance of the modified electrodes GCE-Mil101(Fe)-TiO_2, GCE-CQD-TiO_2, and GCE-Mil101(Fe)-CQD-TiO_2 was investigated in a phosphate buffer solution at pH 6.8, applying cyclic voltammetry using a sweep rate of 50 mV s^{-1}, as depicted in Figure 43. The GCE-CQD-TiO_2 exhibited an oxidation peak at -0.0161 V and a reduction peak at -0.62 V, resulting in a peak-to-peak separation (ΔE_P) of 0.559 V. In contrast, the GCE-Mil101(Fe)-TiO_2 showed a greater current response

compared to GCE-CQD-TiO_2, with oxidation and reduction peaks at 0.029 V and 0.488 V, resulting in a peak separation of 0.517 V. The modified GCE with Mil101(Fe)-CQD-TiO_2 ternary composite exhibited greater current responsiveness compared to GCE-CQD-TiO_2 and GCE-Mil101(Fe)-TiO_2, accompanied by a decrease in ΔE_p. The strong current responsiveness and decrease in ΔE_p indicate that GCE-CQD-TiO_2-Mil101(Fe) promotes fast electron transport at the electrode-electrolyte interface. This observation is attributed to the ternary composite's characteristics, including increased surface area and enhanced electrical conductivity. The Mil101(Fe)-CQD-TiO_2 ternary composite was then utilized as an electrode modification in further experiments.

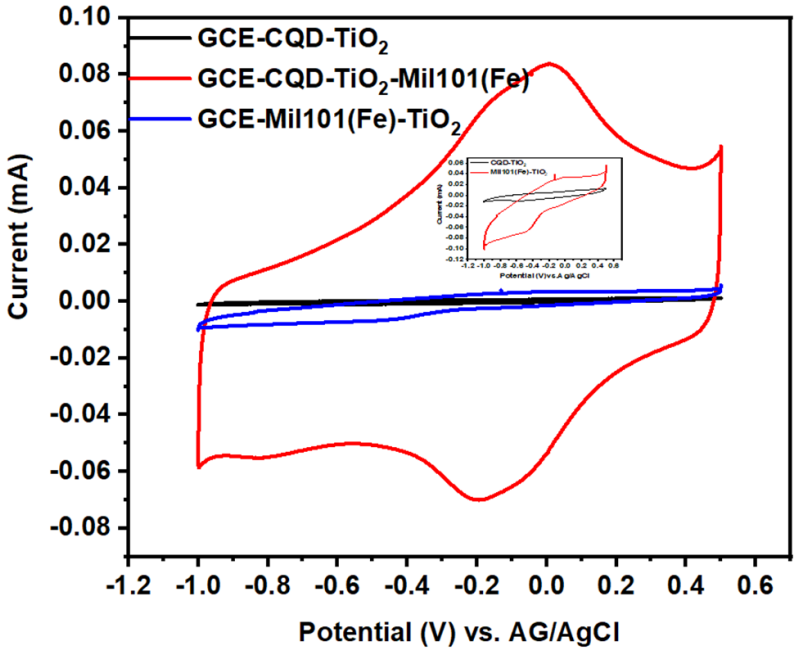

Figure 43: Illustrates the cyclic voltammograms of GCE-CQD-TiO_2, GCE-Mil101(Fe)-CQD-TiO_2 and GCE-Mil101(Fe)-TiO_2 at a sweep rate of 50 mV s^{-1}, in 0.1 M PBS (pH 6.8).

5.4.3 Scan rate dependence studies

Scan-rate dependence studies were conducted using cyclic voltammetry to assess reaction kinetics across different scan rates. This approach quantifies electron mobility, diffusion coefficients, surface coverages, electroactive surface area and adsorption-desorption processes. Figure 44(A-D) illustrates the cyclic voltammograms recorded

at different sweep rates, the linear plot of $(mV\ s^{-1})^{1/2}$ versus peak current, the shift potential versus peak current, and log v versus peak potential. The GCE-CQD-TiO_2-Mil101(Fe) demonstrated an oxidation peak current (I_{pa}) at a peak potential of 0.0174 V and a reduction peak current (I_{pb}) at a peak potential of -0.213 V. The observed appearance of the redox peaks is attributed to interactions among Mil101(Fe), CQD, and TiO_2. The TiO_2 interacts with Mil101(Fe) via OH groups, forming hydrogen bonds with the organic linkers of Mil101(Fe), thereby stabilising the bond. The ΔEp for the GCE-Mil101(Fe)-CQD-TiO_2 system was determined to be 0.230 V, indicating quasi-reversibility. A linear curve shown in Figure 44B indicates that the current response is directly proportional to $(mV\ s^{-1})^{1/2}$, with correlation coefficients r^2 = 0.98 and 0.99. A rise in the current response with $(mV\ s^{-1})^{1/2}$ indicated diffusion-controlled electrocatalytic activity at the GCE-Mil101(Fe)-CQD-TiO_2 interface. However, as shown in Figure 44C, a minor shift in peak potential was observed as the scan rate increased, indicating an irreversible electrochemical reaction, with correlation coefficients (r^2) of 0.99 and 0.98. Figure 44D presents a linear plot of log scan rate versus potential, with a slope of 0.062 and r^2 = 0.98. For quasi-reversible systems, the Randles-Sevcik and Laviron equations (7 and 8) are used to determine the surface coverage and diffusion coefficient

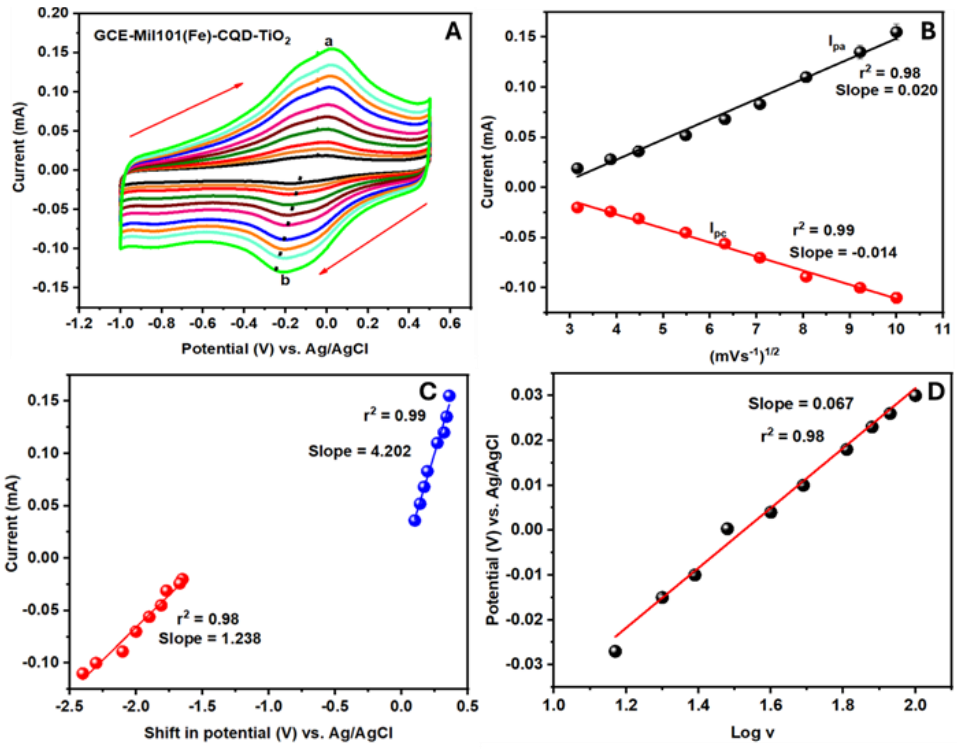

Figure 44: Shows (A) cyclic voltammograms at different scan rates in 0.1M PBS (pH,7.2), (B) linear curve of the $(mV\ s^{-1})^{1/2}$ against peak current, (C) shift potential against peak current and (D) Log v vs. peak potential.

Where D is the diffusion coefficient measured in $cm^2\ s^{-1}$, C is the concentration of the electrolyte in mol cm^{-3}, R is the universal gas constant measured in 8.3145 J mol^{-1}, F represents Faraday's constant, 96485 measured in C mol^{-1}. Additionally, A is the area of the electrode measured in cm^2, V represents the sweep scan in mV s^{-1}, α is the transfer coefficient, Γ is the surface coverage in mol cm^{-2}, T represents the temperature 298K and α is the transfer coefficient. The diffusion coefficient was determined to assess electron mobility at the GCE-Mil101(Fe)-CQD-TiO_2 surface-electrolyte interface. The calculated diffusion coefficient is 2.576×10^{-11} $cm^2\ s^{-1}$, which is comparable to values reported in the literature. The relationship between the current response and the absorbed species on the electrode surface was assessed by determining the surface coverage. The surface coverage was determined to be 2.0609 x 10^{-9} mol cm^2.

5.4.3 Electrochemical impedance spectroscopy analysis of GCE-CQD, GCE-TiO_2, GCE-CQD-TiO_2, GCE-Mil101(Fe)-TiO_2 and GCE-Mil101(Fe)-CQD-TiO_2

Electrochemical impedance spectroscopy is an electrochemical technique for measuring the impedance of an electrochemical system at various frequencies using a direct current voltage [460]. EIS operates by perturbing a system in steady state or equilibrium. This method enables investigation of electrode interactions, including charge transfer, concentrations of electroactive species, and mass transfer from the bulk solution to the electrode surface [461]. The EIS technique was used to explore the diffusion mechanisms and electron mobility at the electrode-electrolyte interface. Figure 45 illustrates the Nyquist plots for GCE-TiO_2, GCE-Mil101(Fe)-TiO_2, GCE-CQD, and GCE-CQD-TiO_2-Mil101(Fe). EIS experiments were conducted in phosphate-buffered saline at pH 6.8 to investigate the electron-transfer kinetics of the modified electrodes. All modified electrodes underwent EIS analysis over a frequency range of 200 kHz to 100 mHz. The diameter of the semicircle in the Nyquist plot represents the electron transfer resistance (R_{ct}) at the electrode-electrolyte interface, which is crucial

for assessing the electrochemical performance of the system, while solution resistance (R_s) refers to the electrolyte resistance [462]. A lower R_{ct} value indicates rapid electron transport, while a lower R_s value signifies high ionic conductivity in the system. Rundle's equivalent circuit was utilized to evaluate parameters such as charge transfer resistance. The Mil101(Fe)-CQD-TiO_2 modified electrode exhibits a lower practical charge transfer resistance compared to several other modified electrodes, including GCE-CQD, GCE-TiO_2, GCE-CQD-TiO_2, and GCE-Mil101(Fe)-TiO_2. The CQD-TiO_2-Mil101(Fe) electrode demonstrated a smaller impedance arc diameter and an R_{ct} of 36.87 Ω. In contrast, the GCE-TiO_2 has an R_{ct} of 54.05 Ω, the GCE-CQD has an R_{ct} of 82.83 Ω, the GCE-CQD-TiO_2 has an R_{ct} of 45.91 Ω, and the GCE-Mil101(Fe)-TiO_2 has an R_{ct} of 39.49 Ω. These findings suggest that the GCE-CQD-TiO_2-Mil101(Fe) electrode facilitates faster electron transfer kinetics. Table 10 summarizes the electrochemical characteristics of the modified electrodes.

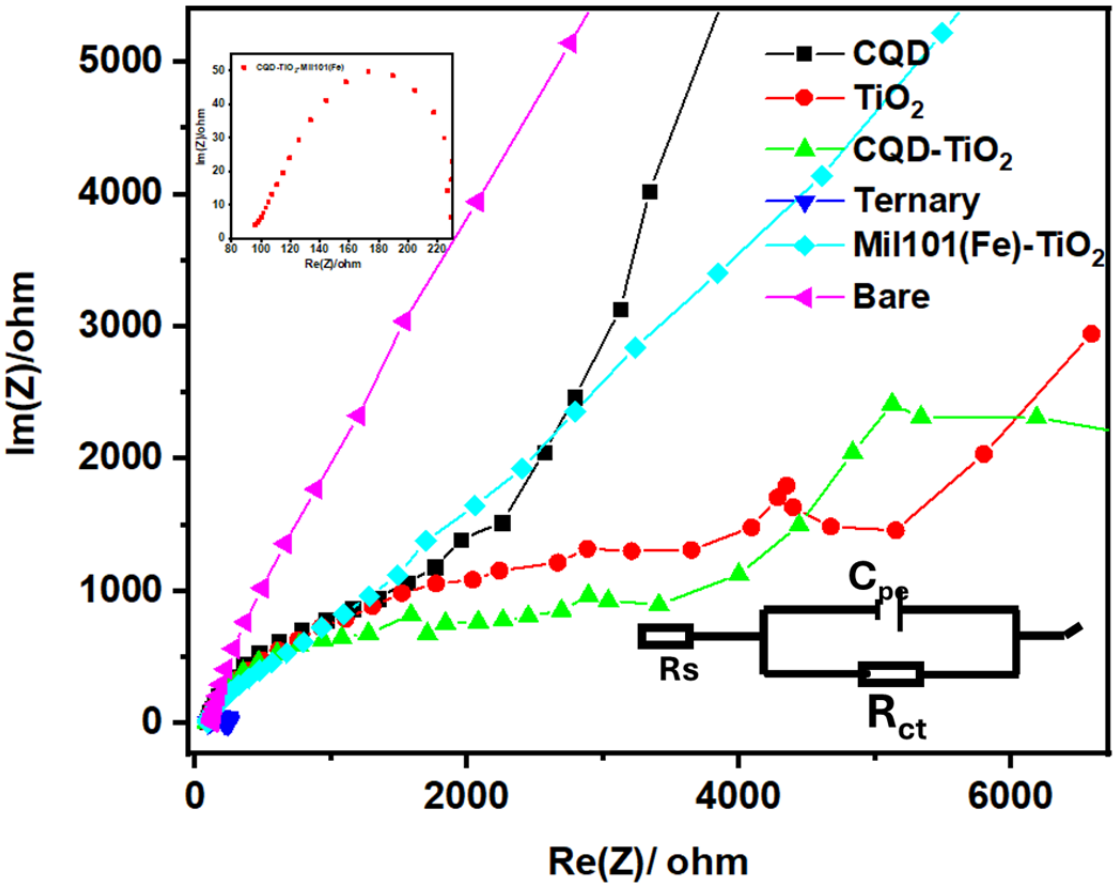

Figure 45: Depicts the Nyquist curves of GCE-CQD, GCE-TiO_2, GCE-CQD-TiO_2, GCE-Mil101(Fe)-TiO_2 and GCE-Mil101(Fe)-CQD-TiO_2 in 0.1M PBS (pH,6.8).

Table 10: Summary of the electrochemical parameters obtained from the GCE-TiO_2, GCE-CQD, GCE-CQD-TiO_2, GCE-Mil101(Fe)-TiO_2 and GCE-Mil101(Fe)-CQD-TiO_2.

Electrode	R_{ct} (Ω)	ΔEp	Diffusion controlled	R_s (Ω)	Synergy observed
GCE-TiO_2	54.05	0.81	No	69.45	NO
GCE-CQD	82.83	0.61	No	81.88	NO
GCE-CQD-TiO_2	45.91	0.559	Yes	94.59	Limited
GCE-Mof-TiO_2	39.49	0.517	Yes	95.55	Moderate
GCE-Mil101(Fe)-CQD-TiO_2	**36.87**	**0.230**	Yes	**96.08**	Strong synergistic effect

5.5 Electrochemical response of the aptasensor

5.5.1. Optimization of the aptasensor

The GCE-CQD-TiO_2-Apt-BSA sensor was optimized using cyclic voltammetry by testing various incubation times of the self-assembled aptamer layer on the working electrode and study the changes in peak current. To enhance the response of the aptasensor, the working electrode was incubated for 1 h, 2 h, 3 h, 4 h, 5 h, and overnight in a solution containing the catalyst (Mil101(Fe)-CQD-TiO_2 cross-linkers with EDC and NHS), a binding buffer (tris buffer), an aptamer solution, and a blocking agent. As shown in Figure 46A, increasing the incubation duration from 1 hour to 3 hours significantly raised the reduction peak (I_{pb}) current of the GCE-Mil101(Fe)-CQD-TiO_2-Apta-BSA sensor. Extending the incubation time to overnight reduced the aptasensor response. These findings suggest that a 3 h incubation period is sufficient to saturate all accessible active sites on the working electrode surface. Figure 46B illustrates the current response of the aptasensor at various incubation times.

Additionally, the stability of the constructed aptasensor was evaluated over time by performing 100 cycles at a scan rate of 50 mV s^{-1}, as shown in Figure 46C. This parameter is significant in electrochemical biosensors because it determines the platform's long-term stability and reliability. During the stability test, the aptasensor performed consistently, exhibiting stable current responses for both I_{pa} and I_{pb} redox peaks.

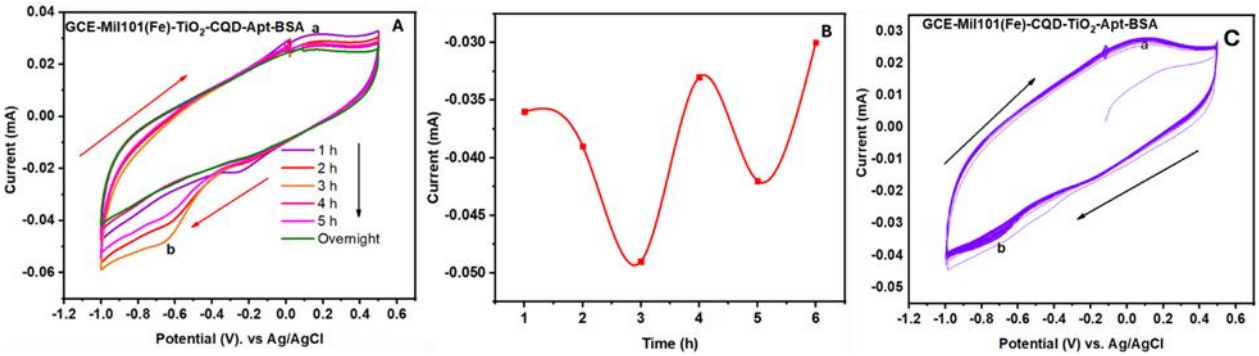

Figure 46: Shows (A) CV plots of electrode incubation at different incubation periods in 0.1M PBS (pH,7.2), (B) bar graph of time vs. current obtained at different incubation periods, and (C) CV plots of GCE-Mil101(Fe)-CQD-TiO_2-Apt-BSA.

5.5.2 Electrochemical characterization of the aptasensor

5.5.2.1 Scan rate dependence studies

Cyclic voltammetry experiments were carried out at various scan rates within a potential range of -1 V - 0.5 V. This analysis enabled the calculation of surface coverage, the electroactive surface at the interface of the developed aptasensor and diffusion coefficients. The electrochemical properties, as well as the diffusion coefficients and adsorption-desorption processes. Figure 47 (A-D) displays the cyclic voltammograms conducted at various scan rates, 49B the linear curve of (mV s^{-1})$^{1/2}$ versus peak current, 47C the linear curve of potential vs log current, and 47D the shift potential versus peak current, and log v versus peak potential. The results revealed an oxidation-reduction redox pair with a potential difference of 1.3 V, indicating that the

aptasensor exhibits quasi-irreversible behaviour, as demonstrated in Figure 47A [383]. The aptasensor demonstrated an oxidation peak current (I_{pa})at a peak potential of 0.092 V and a reduction peak (I_{pb}) current at a peak potential of -0.79 V. This behaviour suggests a possible electrostatic interaction between the composite's active sites, notably the carboxyl (-COOH) groups, and the amine bonds from the aptamer sequence. This interaction most likely promotes the formation of stable amide bonds [384]. The scan rate increased with peak current. These findings reveal that both cathodic and anodic peak currents increased linearly with $(mV\ s^{-1})^{1/2}$, with correlation coefficients r^2 of 0.99, as illustrated in Figure 47B. This finding indicates that the system is undergoing a diffusion-controlled charge-transfer electrocatalytic reaction. Figure 47C depicts the Tafel plot of log current vs. potential. Tafel slope evaluates an electrode's ability to generate current in response to a potential [463]. Furthermore, the Tafel slope is utilized to determine the rates and processes of electrocatalytic reactions. To establish the aptasensor's quasi-reversibility, the transfer coefficient (α) was determined using the slope obtained from Figure 47D. The current and potential values utilized in this plot were derived from oxidation peaks of Figure 47A [464]. The slope of this plot was used to calculate the transfer coefficient using Equation 12.

$$Slope = \frac{\alpha F}{2.303 \times RT} \quad \textit{equation 12}$$

Where R represents the universal gas constant (8.314 J mol^{-1}), F is Faraday's constant 96485 C mol^{-1}), and T is the temperature (298 K). The determined α value of 0.40 falls within the quasi-reversible zone [465]. The kinetic constant was calculated using the following equation. The determined K° value of 6.72×10^{-5} cm^{-1} indicates slow electron transport between the electrode-electrolyte interface and electroactive species. This number is consistent with the literature and confirms that the system is quasi-reversible. Equation 13 was used to calculate the K constant.

$$ln(k^o) = \frac{\alpha nF}{RT}\left(E_p - E^o\right) - ln\ \left(\frac{RT}{\alpha nF}\right) \text{ equation 13}$$

Figure 47D displays a Tafel plot of log scan rate vs potential. The Tafel slope was calculated by graphing the oxidation peak potential against the log of the scan rate. The slope of this Figure was used in equation 14. Where b represents the Tafel slope and K denotes the kinetic constant. Tafel slopes of 60 to 120 mV $decade^{-1}$ are

particularly beneficial as they imply a single-electron transfer during the rate-determining phase. The calculated Tafel slope was 49 mV decade $^{-1}$.

$E_p = \frac{b}{2} logv + k$ equation 14

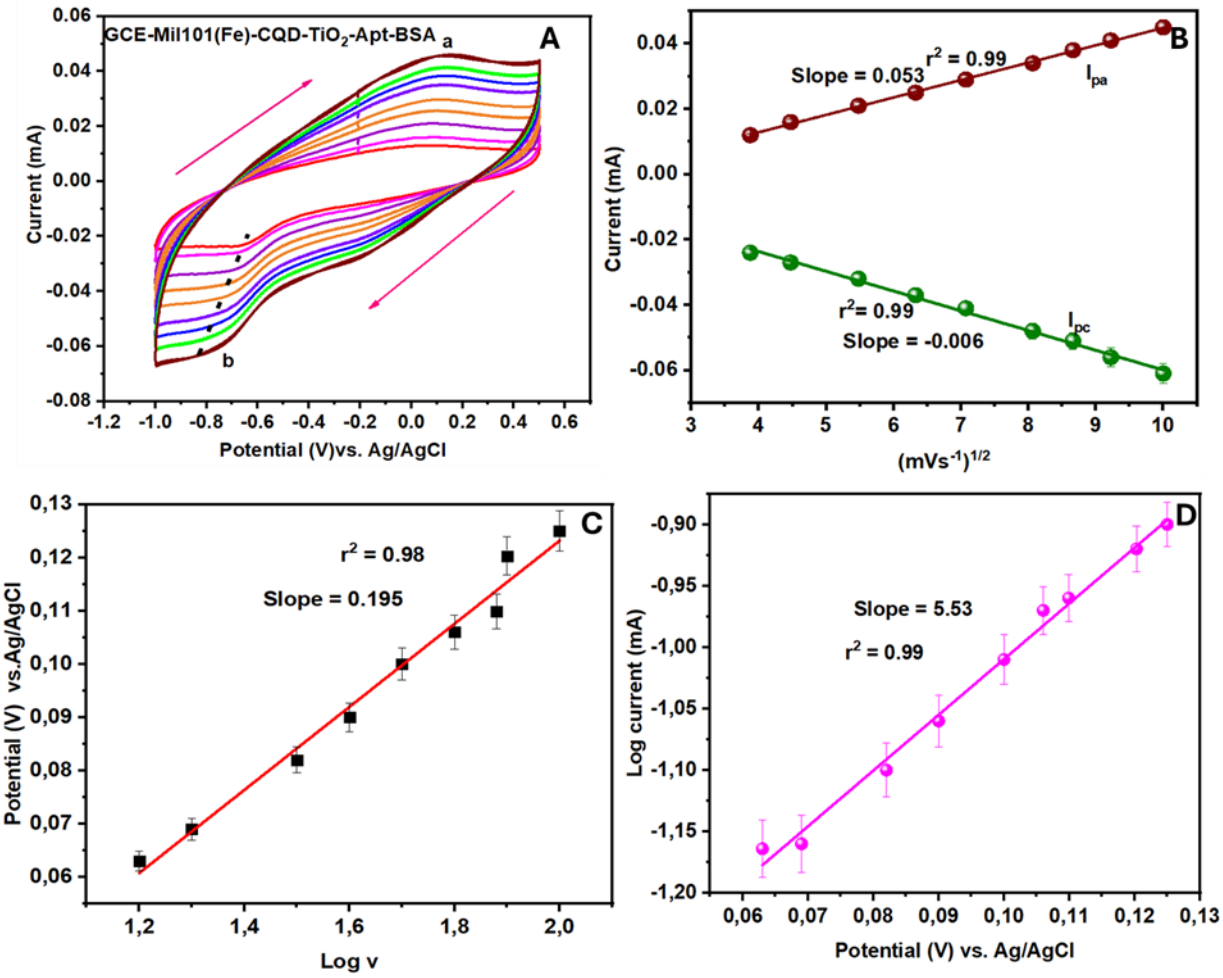

Figure 47: Shows (A) CV plots of GCE- Mil101(Fe)-CQD-TiO_2- Apt-BSA in 0.1M PBS (pH, 7.2), (B) linear plot of $(mV\ s^{-1})^{1/2}$ vs current, (C) potential vs. log current and (D) log v vs. potential.

To establish electron kinetics, the surface coverage and the diffusion coefficient were calculated using equations (7 and 8). The determined diffusion coefficient (D) is 5.994 × 10^{-11}cm² s^{-1}, and the surface coverage (Γ) is 6.747 ×10^{-9} mol cm^{-2}. The aptasensor surface coverage increased from 2.0609 × 10^{-9} mol cm^{-2} for the Mil101(Fe)-CQD-TiO_2 to 6.747 × 10^{-9} mol cm^{-2}. To assess the aptamer's contribution, a control experiment

was carried out using a glassy carbon electrode modified with bovine serum albumin (GCE-BSA). The surface coverage obtained for this electrode was 1.199×10^{-9} mol cm^{-2}. Subtracting GCE-BSA's surface coverage from that of GCE-Mil101(Fe)-CQD-TiO_2-Apt-BSA yields an adjusted Γ value of 5.557×10^{-9} mol cm^{-2}. The electroactive surface area (EASA) of the GCE- Mil101(Fe)-CQD-TiO_2 Apt-BSA was determined using Equation 9, which was utilised to compute based on the slope value of $(mV\ s^{-1})^{1/2}$ against the current response plot (Figure 47B).

Where A represents the area of the electrode (cm^2), n refers to the number of electron transfers, m represents the slope value, A is the area of the electrode (in cm^2), D represent the diffusion coefficient (in $cm^2\ s^{-1}$), and C is the concentration (in mol cm^{-3}). The calculated EASA was 3.224 cm². This indicates that the GCE-Mil101(Fe)-CQD-TiO_2-Apt-BSA has more active sites for analyte detection.

5.6 Application of GCE-Mil101(Fe)-CQD-TiO_2-Apt-BSA

5.6.1 Electrochemical detection of cadmium

The behaviour of the designed aptasensor was examined using square-wave voltammetry to detect Cd^{2+} in buffer solutions. The experiments were conducted at room temperature, utilizing a potential window of -1 V - 0.5 V and a scan rate of 50 mV s^{-1} in a phosphate buffer solution with a pH of 7.2. The reduction peak was selected for the Cd^{2+} SWV studies because it exhibited a more defined peak and a larger current response compared to the oxidation peaks. This observation is attributed to the quasi-reversible nature of the redox couple. Figure 48(A-D) illustrates the SWV measurements of different spiked Cd^{2+} concentrations. In Figure 48B, the binding curve of spiked Cd^{2+} concentrations vs peak current. Figure 48C shows the relationship between spiked cadmium ions and peak current, while Figure 48D presents the change in potential versus peak current.

Figure 48A presents the results of SWV scans conducted in different spiked Cd^{2+} concentrations. The SWV reverse scan revealed an increase in peak current that was directly proportional to the concentration of cadmium ions. This finding suggests that Cd^{2+} have a strong binding affinity for the surface of the developed aptasensor. The

aptasensor effectively detected cadmium ions at concentrations up to 9 µM, at a peak potential of -0.68 V (I_{pa}). It was observed that after spiking with 10 µM, the saturation point was reached, resulting in a linear range of 10-16 µM. The binding inhibition curve of cadmium ions on the GCE-Mil101(Fe)-CQD-TiO_2-Apt-BSA surface is illustrated in Figure 48B. Figure 48C illustrates a correlation coefficient of $r^2 = 0.97$ and a slope of 0.217 between the spiked Cd^{2+} concentrations and the current responses. As the concentration of Cd^{2+} increased, a minor shift in the peak potential was observed, indicating rapid electron transfer at the aptasensor surface. Figure 48D illustrates a linear relationship between shift potential and current responsiveness, with a correlation coefficient of $r^2 = 0.99$. The findings indicate that the designed GCE-Mil101(Fe)-CQD-TiO_2-Apt-BSA is a multifunctional system capable of detecting a wide range of contaminants. The LOD was calculated using equation 10. Where m is the slope of the linear curve of spiking concentration vs current response, and 3 (ð) is the standard deviation (n = 10).

The aptasensor demonstrated a sensitivity of 0.127 mA μM^{-1} and an LOD of 0.005 ng L^{-1}. Table 11 compares the electrochemical sensors used to detect Cd^{2+} with the developed aptasensor.

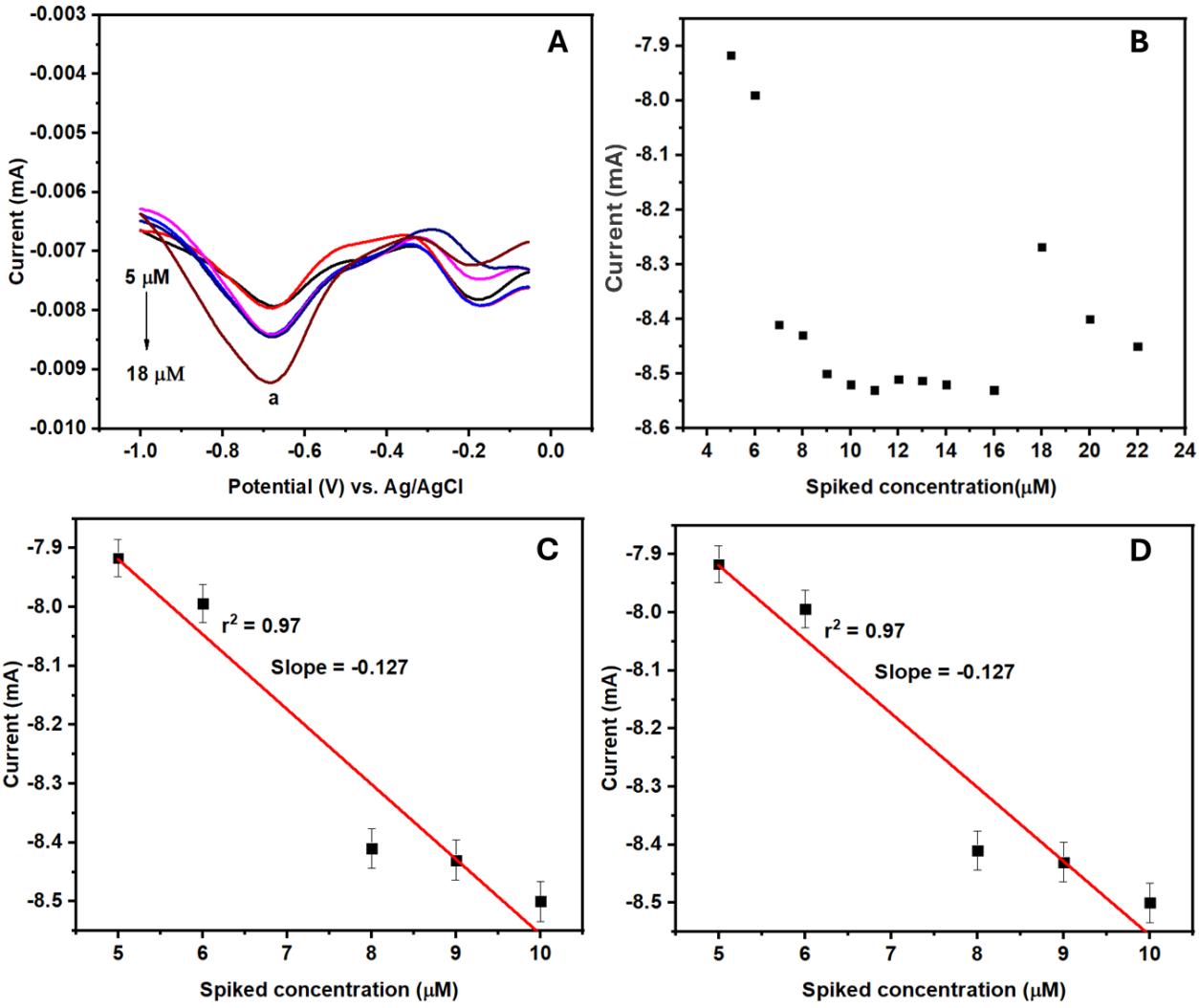

Figure 48: Depicts (A) the SWV measurements of spiked Cd^{2+} concentrations in 0.1 M PBS (pH,7.2), (B) the binding curve, (C) the spiked Cd^{2+} concentrations vs current response, and (D) the shift in potential vs spiked concentrations.

Table 11: Compares the electrochemical techniques used for detecting Cd^{2+} with the one developed in this study.

Modified electrode	**Technique**	**Limit of detection (LOD) (ng L^{-1})**	**Linear range (ng L^{-1})**	**References**
GCE-SO	SWV	3.3 x10^{-11}	1.0 ×10^{-8}- 5.0 ×$^{-8}$	[466]
GCE-APTE-Mono@	DPV	7.37	4 - 80	[467]
$NiWO_4$-MWCNTs-GCE	SWV	0.12	50 - 450	[468]
GCE-SWCNT	SWV	9.44	12–100	[194]
GCE-ZIF-rGO	SWASV	10.11	12–100	[59]
GCE-Apt-MSH	SWV	0.12	50 - 450	[469]
GCE-AuNP-CD	*DPV*	0.99	1-100	[470]
GCEN-NC	SWV	10.84	1.46 - 73	[471]
GCE-Mil101(Fe)-CQD-TiO_2-Apt-BSA	**SWV**	**0.005**	**7-11**	**This work**

5.6.2 Electrochemical detection of arsenic

The developed aptasensor was evaluated for the electrochemical detection of arsenic in phosphate buffer solutions. The experiment utilised square wave voltammetry within a potential window of -0.6 V - 0.5 V. Various working concentrations ranging from 4 to 12 µM were prepared. Figure 49(A-D) presents the SWV measurements at varying arsenic concentrations. Figure 49B illustrates the binding inhibition curve correlating spiked concentrations with current, while Figure 49C shows the linear relationship between spiked arsenic concentration and current. Additionally, Figure 49D shows a linear plot of spiked arsenic concentration versus the shift in potential.

As shown in Figure 49A, the peak current increased with increasing arsenic concentration, yielding a linear binding inhibition curve shown in Figure 49B. This increase in peak current in response to spiked concentrations is attributed to arsenic binding to active sites on the electrode surface. Two distinct peaks were identified during arsenic detection: one at -0.16 V, corresponding to As^{5+}, and another at 0.069 V, corresponding to As^{3+}. This observation is consistent with the reported literature [472]. Figure 49C illustrates the linear correlation between spiked concentration and current, with a correlation coefficient of $r^2 = 0.95$ and a slope of 0.0065. A slight negative shift in potential was also observed as spiked concentrations increased, as shown in Figure 49D. The limit of detection was calculated using equation 10. The sensor demonstrated an LOD of 0.092 ng L^{-1}, and a sensitivity of 0.0065 µM mA^{-1}.

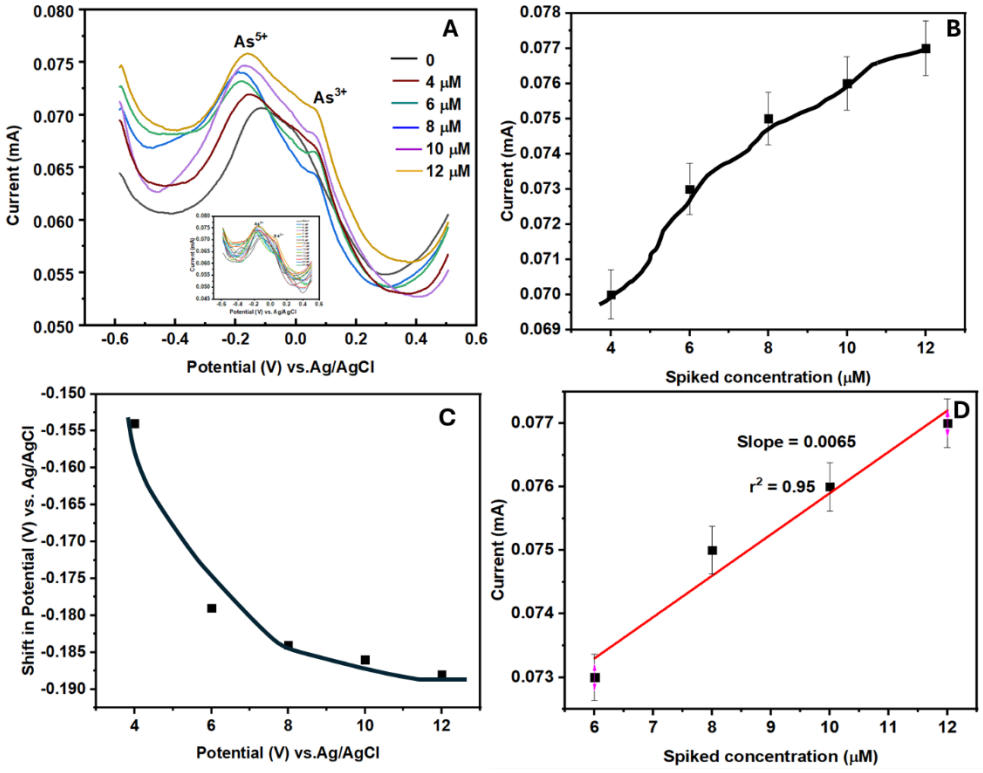

Figure 49: Displays the (A) SWV measurements in the presence of different spiked arsenic concentrations in 0.1 M PBS (pH,7.2), (B) binding inhibition curve, (C) linear curve of spiked concentrations vs. current and (D) shows the plot of shift in potential vs. spiked concentration.

5.6.3. Selectivity studies

The selectivity of the developed aptasensor for Cd^{2+} was evaluated by assessing the effects of various foreign ions on its detection performance. A range of potential cations, including $Cu^{2+,}$ Pb^{2+}, Zn^{2+}, and As^{3+}, was used in this test. A digestion method was employed to prepare working concentrations containing all interfering ions, along with Cd^{2+}. Three working concentrations, ranging from 2 to 8 µM, were prepared, and SWV was employed for this experiment in a potential window of -1.2 V - 0.6 V. As illustrated in Figure 50, the aptasensor exhibited the strongest signal for Cd^{2+} in all the spiked concentrations, demonstrating its ability to accurately identify Cd^{2+} in the presence of other metal ions. As observed in Figure 50, no peaks overlapped with that of Cd^{2+}. This was due to a strong interaction between Cd^{2+} and the -COOH groups, which enhanced binding and improved the electrochemical response.

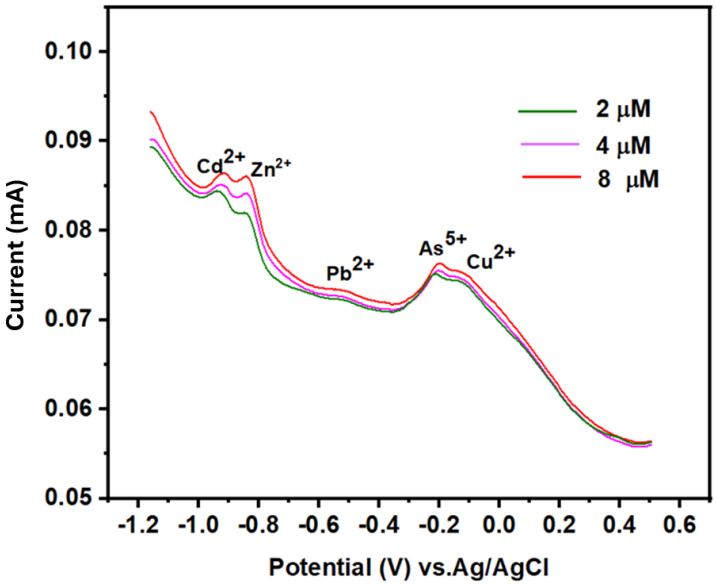

Figure 50: Shows the SWV measurements in 0.1 M PBS (pH,7.2) in the presence of Cd^{2+}, Cu^{2+}, Zn^{2+}, As^{3+}, Pb^{2+}.

5.6.4 Electrochemical detection of *Crypto*

The efficiency of the proposed aptasensor was evaluated by detecting *Crypto* in a phosphate buffer solution. The correlation between spiked *Crypto* concentrations (ranging from 3 to 22 µM) and the oxidation peak currents was examined using the SWV technique at a sweep rate of 50 mV s^{-1}. Figures 51(A-C) display the SWV response to varying concentrations of spiked Crypto, the binding inhibition curve relating spiked *Crypto* concentration to current density, and a linear plot of spiked *Crypto* concentration versus current density. In Figure 51A, the SWV response to different spike concentrations of *Crypto* is shown. As the concentration of *Crypto* increased, the oxidation peak current also correspondingly increased. This finding highlights the binding affinity of *Crypto* to the surface of GCE-Mil101(Fe)-CQD-TiO_2-Apt-BSA. In Figure 51B, the inhibitory curve shows the relationship between spiked *Crypto* concentrations and current density. The spike at a concentration of 9 µM resulted in saturation of the platform. Figure 51C illustrates a linear relationship between the concentration of *Crypto* and current density, displaying a correlation

coefficient of r^2 = 0.96 and a slope of 0.528. The detection limit of the aptasensor was calculated using Equation 10.

The aptasensor demonstrated a linear range of 0.0015 - 0.004 µM, a sensitivity of 0.529 mA μM^{-1}, and a limit of detection of 0.001 ng L^{-1}.

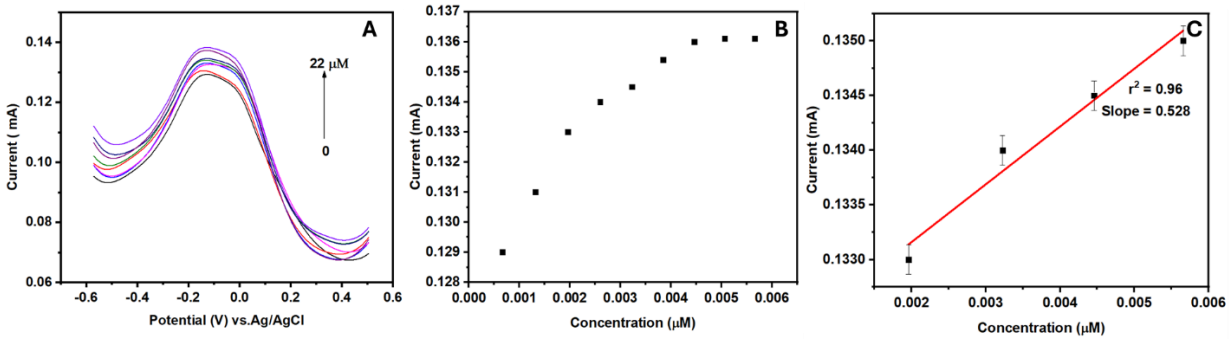

Figure 51: Illustrates (A) SWV measurements of spiked *Crypto* concentration in 0.1 M PBS (pH 7.2), (B) binding curve, (C) linear curve of spiked *Crypto* concentration vs current density.

Cyclic voltammetry was employed to investigate the oxidation-reduction behaviour of GCE-Mil101(Fe)-CQD-TiO_2-Apt-BSA in the presence of spiked concentrations of *Crypto*, ranging from 3 to 22 µM. This analysis utilized a sweep scan rate of 50 mV s^{-1} and was conducted in phosphate-buffered saline at pH 7.2. Figures 52(A-D) illustrate the cyclic voltammogram results. Figure 52B presents an inhibition curve depicting the relationship between the spiked *Crypto* concentration and current density. Figure 52C displays a linear plot of spiked *Crypto* concentrations versus current density, while Figure 52D shows the relationship between spiked *Crypto* concentrations and the shift in potential.

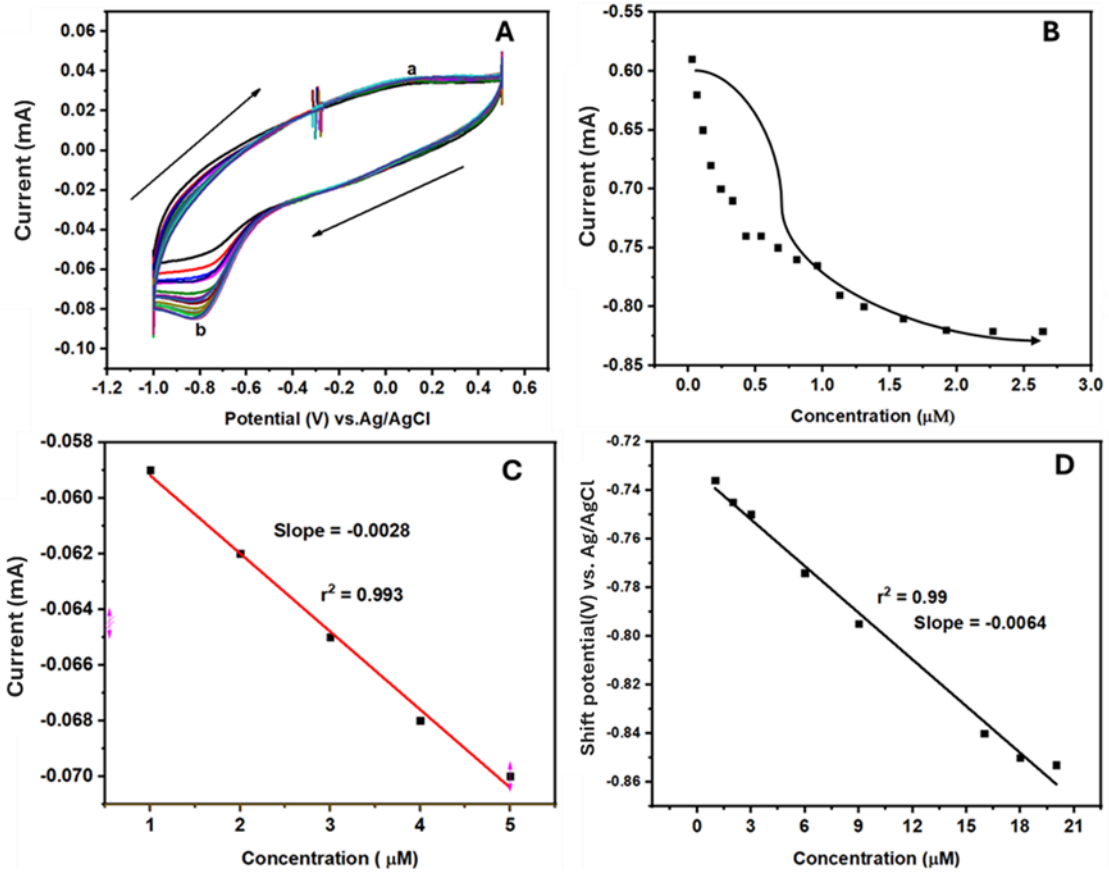

Figure 52: Displays (A) the CV measurements of spiked *Crypto* concentration in 0.1 M PBS (pH,7.2), (B) the binding curve (C) spiked *Crypto* concentration vs. current, and (D) the linear curve of shift in potential vs spiked *Crypto* concentrations.

Figure 52A illustrates the cyclic voltammetry response at different spiked concentrations of *Crypto*. Notably, the interaction between the aptasensor and increasing concentrations of *Crypto* resulted in an enhancement of the peak current (I_{pb}) of GCE-Mil101(Fe)-CQD-TiO_2-Apt-BSA, as illustrated in Figure 52B. Figure 52C shows a linear curve with a slope of -0.0028 and a correlation coefficient $r^2 = 0.993$, representing the relationship between the current reaction and the concentrations of spiked *Crypto.* As the concentrations of spiked *Crypto* increased, the reduction peak of the GCE-Mil101(Fe)-CQD-TiO_2-Apt-BSA shifted slightly, indicating rapid electron transfer kinetics at the electrode-electrolyte interface. This is further demonstrated in Figure 52D, which has a correlation coefficient of $r^2 = 0.99$. There has been little research on the detection of *Crypto* utilizing electrochemical sensors. Table 12 compares the aptasensor developed in this study with other electrochemical sensors designed to detect *Crypto* in water and buffer samples.

Table 12: Compares the electrochemical sensors used to detect *Crypto* with those used in this work.

Modified electrodes	**Technique**	**Limit of detection (LOD)(ng L^{-1})**	**Linear range (ng L^{-1})**	**References**
SPCE-Au	EIS	0.003	0.005 - 0.02	[185]
SPCE-GNPs	SWV	0.01	0.015 - 0.08	[400]
ITO-AuNPs	DPV	0.003	0.003 – 0.005	[401]
SPCE-AuNPs-Apt	EIS	0.010	0.05 – 0.02	[473]
GCE-Mil101(Fe)-CQD-TiO_2 -Apt-BSA	**SWV**	**0.001**	**0.001 – 0.004**	**This work**

5.6.5 Interaction between the Mil101(Fe)-CQD-TiO_2 and aptamer

The enhanced electrochemical response observed in the Mil101(Fe)-CQD-TiO_2-Apt-BSA is attributed to a synergistic mechanism that facilitates electron transfer, thereby improving the electrochemical signal. In this process, electrons flow from the iron in Mil101 to the conductive CQD and ultimately reach the TiO_2 structure, as shown in Scheme 21. Mil101(Fe) serves as the electron donor due to mixed ionic states on its surface, while the CQD acts as an electron mediator owing to its oxygen-containing surface groups. This property enhances charge transfer in the poorly conductive TiO_2 and Mil101(Fe), promoting rapid electron movement to the working electrode surface.

Additionally, the active carboxylic groups on the ternary composite surface bind to the aptamer, enabling its attachment to the electrode via EDC/NHS crosslinkers, thereby forming strong covalent bonds. The stable attachment of the aptamer on the modified electrode surface is demonstrated by high values of the diffusion coefficient, electroactive surface area, surface coverage, and a low charge transfer rate. These factors indicate efficient electron transfer between the electrolyte and the sensor, thereby increasing the number of binding sites at the electrode interface for analyte attachment. The mechanism of interaction between the ternary composite and the aptamer is shown in Scheme 21.

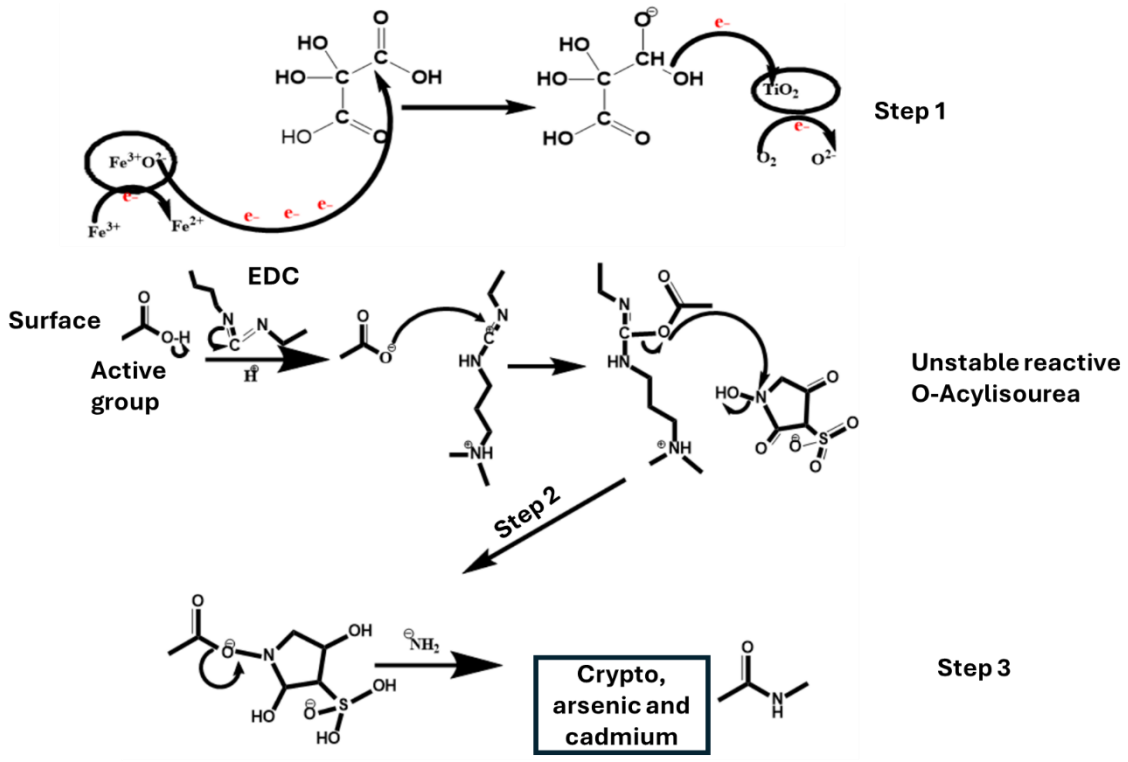

Scheme 21:Mechanisms between the Mil101(Fe)-CQD-TiO_2 ternary composite and the aptamer.

5.6.6 Selectivity studies

Selectivity is an essential parameter for biosensors, as it determines their capability to detect a target analyte in complex biological and environmental samples. In this study, we assessed the selectivity of the developed aptasensor by detecting a mismatched analyte. The experiment was conducted within a voltage range of -1 V - 0.5 V, using a phosphate buffer solution (pH 7.2) as the electrolyte and a scan rate of 50 mV s^{-1}. The concentrations of the prepared analyte varied from 1 to 11 µM. Figures 53(A-D) illustrate the square wave voltammetry (SWV) response of the GCE-Mil101(Fe)-CQD-TiO_2-Apt-BSA sensor for the detection of *Crypto*, compared to the response to the mismatched analyte. Figure 53B specifically shows the SWV response of GCE-Mil101(Fe)-CQD-TiO_2-Apt-BSA at different spiked concentrations of *Crypto*. Figure 53C shows the SWV response of GCE-Mil101(Fe)-CQD-TiO_2-Apt-BSA to various spiking mismatched analytes, whereas Figure 53D shows the two straight curves derived from *Crypto* detection and mismatched analyte detection. As illustrated in Figure 53A, the SWV response for the *Crypto* detection had a higher peak current response than that of the mismatched analyte. Figure 53B illustrates the SWV response to an increased concentration of *Crypto*. The peak current response increased with increasing Crypto concentrations. This suggests a strong correlation between the platform and the detection of *Crypto*. Figure 53C depicts the SWV response at different analyte concentrations with mismatch. The designed aptasensor showed no binding affinity with the spiking concentrations.

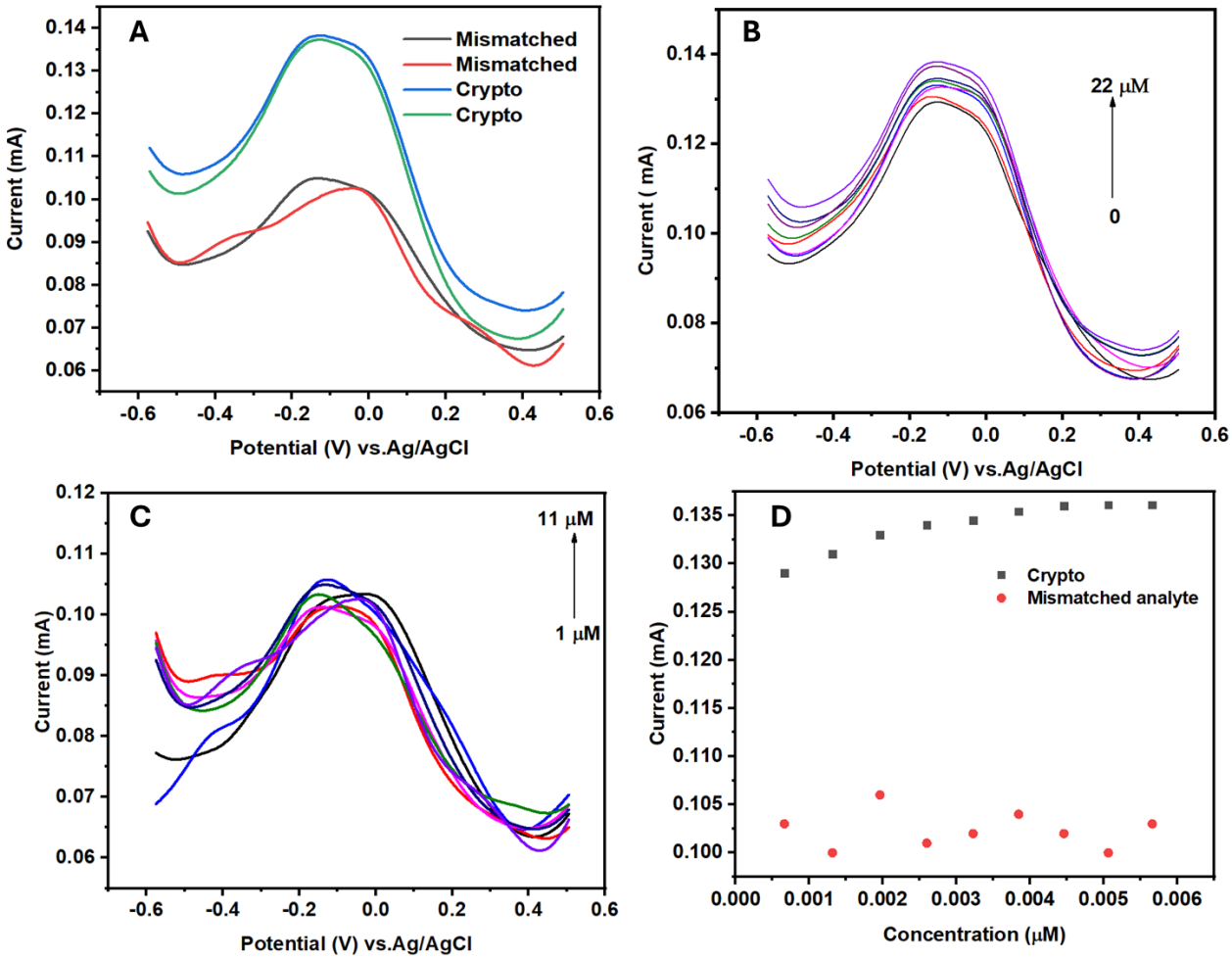

Figure 53: Depicts the SWV response obtained from *Crypto* detection and mismatched detection in 0.1 M PBS (pH, 7.2), (B) SWV response of GCE-Mil101(Fe)-CQD-TiO_2-Apt-BSA at different spiked *Crypto* concentrations, (C) the SWV response of GCE-Mil101(Fe)-CQD-TiO_2-Apt-BSA at various mismatched concentrations.

The performance of the developed aptasensor was further evaluated in water samples for the detection of *Crypto*, Cd^{2+}, and arsenic using the SWV technique, with acceptable recoveries.

5.7 Real water applications

SWV studies were conducted to evaluate the performance of the developed GCE-Mil101(Fe)-CQD-TiO_2-Apt-BSA in both wastewater and tap water. These investigations were conducted over a potential range of -1 - 0.5 V at a scan rate of 50

mV s^{-1}. Before the analysis, the wastewater was filtered, and the pH of both the wastewater and tap water was adjusted to 7.2. During the SWV studies, a blank measurement was taken using the water samples. The working concentrations of Crypto and Cd^{2+} introduced into the water samples (both wastewater and tap water) were determined from the aptasensor response.

Figure 54(A-D) illustrates the detection of Cd^{2+} in real water samples. Figure 54A shows the results of the square wave voltammetry experiment conducted with Cd^{2+} spiked concentrations on wastewater and tap water samples. It was observed that as the concentrations of the spiked Cd^{2+} increased, the peak current also increased. Figure 54B illustrates the relationship between peak current and spiked concentrations, yielding an r^2 value of 0.92. In Figure 54C, the SWV response to varying spiked Cd^{2+} concentrations are shown, with a linear increase in current with higher Cd^{2} concentrations, yielding an r^2 value of 0.93. The aptasensor displayed a similar response for Cd^{2+} in both wastewater and tap water samples, with recoveries ranging from 72% to 89.2%. The findings from Figure 54(A-D) are summarized in Table 13.

Figure 55(A-D) shows the detection of arsenic in real water samples. Figure 55A displays the SWV measurements in the presence of spiked arsenic concentrations in wastewater. 55B shows the linear plot of spiked concentration vs. peak current, 55C shows the SWV experiment in spiked tap water samples, and 55D shows the linear plot of spiked concentration against peak current. As shown in Figure 55A, the spiked concentration increased linearly with the peak current, resulting in a high correlation coefficient of 0.98, as illustrated in Figure 55B. Similarly, Figure 55C shows that spiked concentrations increased with peak current, yielding a correlation coefficient of 0.79 (Figure 55D). It was observed that the wastewater samples contained As^{3+}, while the tap water samples contained As^{5+}. The aptasensor exhibited a stronger electrochemical response in wastewater samples than in tap water, suggesting that wastewater has a higher arsenic concentration. The recoveries from the wastewater samples ranged from 87% to 93%, whereas the recoveries from the tap water samples ranged from 68% to 74%. The data obtained from the experiment are summarised in Table 14. The sensor demonstrated high precision in detecting cadmium and arsenic in wastewater and tap water. This was assessed by calculating the mean and standard

deviation of the recovery rates, which were incorporated into equation 11. The F-test results were 67% and 72% for cadmium, and 70% and 76% for arsenic.

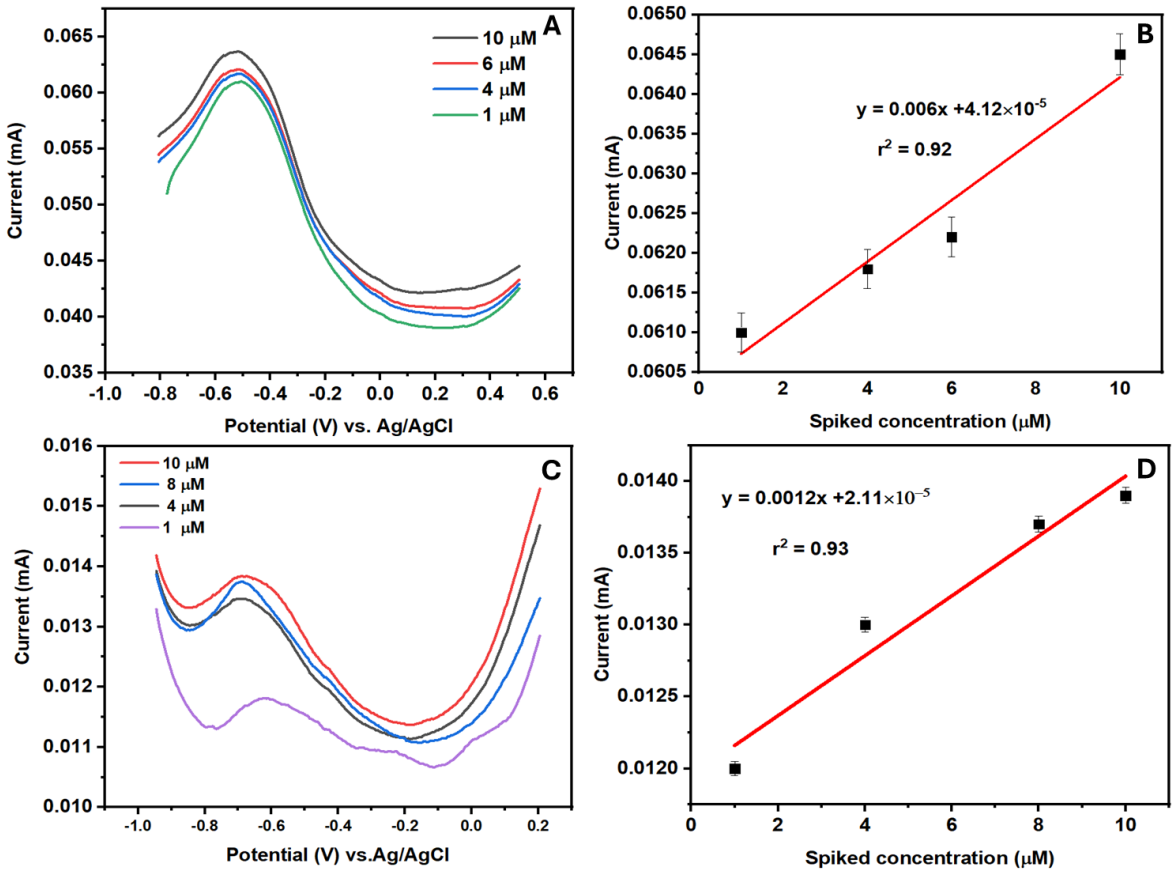

Figure 54: Illustrates (A) the SWV reaction to changing spiked Cd^{2+} concentrations in wastewater, (B) a linear curve of spiked concentration vs peak current, (C) represents the SWV experiment to different Cd^{2+} spiked concentrations, and (D) a linear curve of current vs spiked concentrations.

Table 13: Shows the summarised results obtained for the detection of Cd^{2+} in real water samples.

Sample	Added (µM)	Found (µM)	Recovery (%)
Wastewater			
	4	1.203	74.77
	6	1.03	82.20
	10	1.068	89.6

Tap water	4	1.083	72.92
	8	1.058	86.77
	10	1.15	88.54

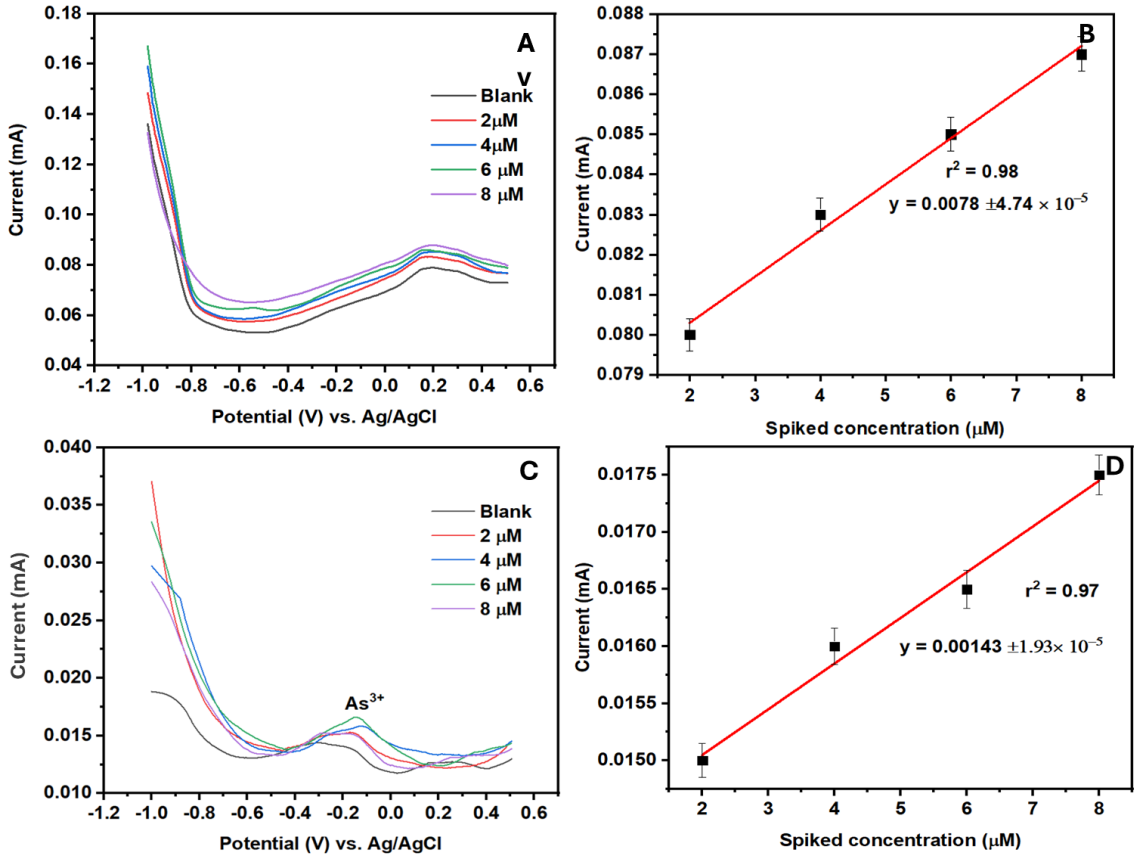

Figure 55: Display the SWV measurements in the presence of spiked arsenic concentrations in wastewater samples, (B) a linear plot of spiked arsenic concentration vs current, (C) illustrates the SWV experiment to different spiked concentrations in tap water, and (D) shows the linear curve of spiked arsenic concentrations vs current.

Table 14: Shows the summarised results obtained from the detection of arsenic in real water samples.

Sample	Added (µM)	Found (µM)	Recovery (%)

Wastewater	2	1.01	87.01
	4	1.04	90.23
	6	1.08	92.65
	8	1.1	93.56
Tap water	4	0.67	68.05
	6	0.86	70.12
	8	0.94	74.23

The data presented in Figures 56(A-D) shows the detection of *Crypto* in spiked wastewater and tap water. Figure 56A illustrates the SWV response to various spiked concentrations of *Crypto* in wastewater. The current response and spiking concentrations show a linear relationship, yielding a correlation coefficient $r^2 = 0.99$, as illustrated in Figure 56B. Figure 56C displays the SVW response to various concentrations of *Crypto* in tap water. It was noted that the aptasensor response in wastewater was significantly higher than that in tap water. Additionally, Figure 56D shows that as spiking concentrations increased, the current also increased. Table 15 summarizes the recoveries for detecting *Crypto* in both water samples, which ranged from 87% to 98%. For tap water, the recovery rates varied from 67% to 80%. Overall, the aptasensor exhibited better performance in wastewater samples compared to tap water. Equation 11 was used to perform the F-test, which assessed the aptasensor's precision. The determined mean and δ for wastewater were (8.23 and 85), while for tap water they were (12.9 and 55.1). Findings indicated the practical observations achieved high accuracy, with 90% and 85% for wastewater and tap water, respectively, demonstrating adequate reproducibility.

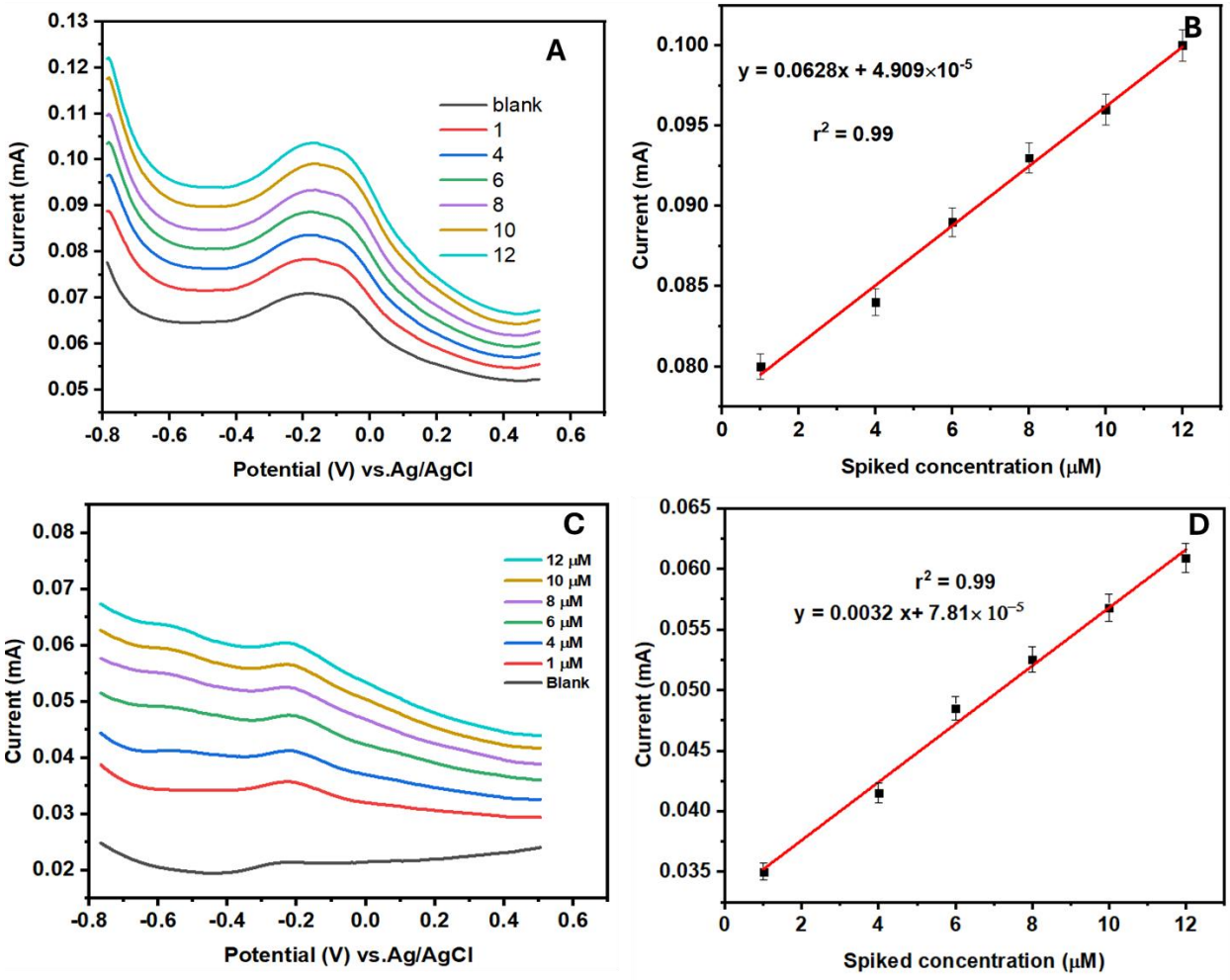

Figure 56: Displays the SWV measurements of spiked *Crypto* concentrations in wastewater, (B) linear plot of spiked concentration vs. peak current, (C) illustrates the SWV experiment to different spiked concentrations in tap water, and (D) shows the linear curve of current vs. spiked concentrations.

Table 15: Shows the summary of the detection of *Crypto* in real water samples with recoveries.

Sample	Added (μM)	Found (μM)	Recovery (%)
Wastewater	1	0.127	87.3
	4	0.140	96.5
	6	0.147	97.55
	8	0.152	98.1
Tap water	4	1.31	67.30
	6	1.5	75 .77
	8	1.75	82.28

5.8 Summary and Sub-conclusion

In this chapter, the hydrothermal method was effectively utilized to develop a ternary composite composed of Mil101(Fe)-CQD-TiO_2. This ternary composite was thoroughly analysed using various techniques. The structural and morphological analyses confirmed the successful integration of CQD, TiO_2 within the Mil101(Fe) framework, resulting in a high-surface-area composite with excellent conductivity. Electrochemical tests indicated that the ternary composite exhibited strong immobilisation of monolayer aptamers ($r = 6.747 \times 10^{-9}$ mol cm^{-2}), a larger electroactive surface area (3.22 cm^2), and significantly enhanced electron transfer kinetics, leading to improved sensor performance. The composite-enabled technology showcased excellent analytical performance in a label-free aptasensor for Cd^{2+}, arsenic, and *Crypto*. It demonstrated a high sensitivity of 0.528 mA μM^{-1} for *Crypto* and a low detection limit of 0.001 ng L^{-1}, whereas the obtained limits of detection for cadmium were 0.05 ng L^{-1} with a sensitivity of 0.127 mA μM^{-1} and 0.092 ng L^{-1} with a sensitivity of 0.0065 mA μM^{-1} for

arsenic. The aptasensor platform also performed well when tested with real water samples, with recovery rates ranging from 67% to 98% for *Crypto*, 72% to 89% for Cd^{2+} and 68 % to 93% for arsenic. Selectivity experiments indicated that the aptasensor exhibited minimal reactivity to mismatched analytes, highlighting its specificity. The findings establish the platform as a versatile tool for biological and environmental sensing, indicating its potential for detecting other heavy metals and microbial diseases.

CHAPTER SIX:

Comparative Evaluation of CQD-TiO_2 and Mil101(Fe)-CQD-TiO_2 Electrocatalysts: Performance, selectivity and Mechanism

6.1 Overview

This chapter summarizes the comparison between the Mil101(Fe)-carbon quantum-dot-titanium composite and the CQD-TiO_2 composite. Both nanocomposites were used for detecting *Crypto* in phosphate buffer and real water samples. Electrochemical techniques, including cyclic voltammetry, electrochemical impedance spectroscopy, and square wave voltammetry, were utilised to assess the electrochemical performance and mechanism at the modified electrode interface.

6.2 Comparative Electrochemical properties of CQD-TiO_2, Mil101(Fe)-CQD-TiO_2

This study compares the surface area, electron-transfer capability, stability, and sensitivity of Mil101(Fe)-CQD-TiO_2 vs. CQD-TiO_2 electrocatalysts. Carbon quantum dot (CQD) are proposed as a carbon-based material due to their high surface area-to-volume ratio, stability, and biocompatibility. Their surface contains oxygen-related functional groups, making them electron-rich. Initially, CQD were doped with titanium dioxide to form a CQD-TiO_2 nanocomposite, which was utilised as an electrode modifier for the detection of *Crypto* in buffer solutions and water samples. However, it did not demonstrate an improved electrochemical response. This lack of enhancement can be attributed to titanium dioxide being a semiconductor, which means it cannot donate more electrons. In contrast, carbon quantum dot are electron-rich and can donate electrons to the TiO_2 crystal structures. When TiO_2 receives enough energy, it can reduce oxygen and produce an enhanced electrochemical signal. The mechanism for electron transfer between TiO_2 and CQD is shown in Scheme 22.

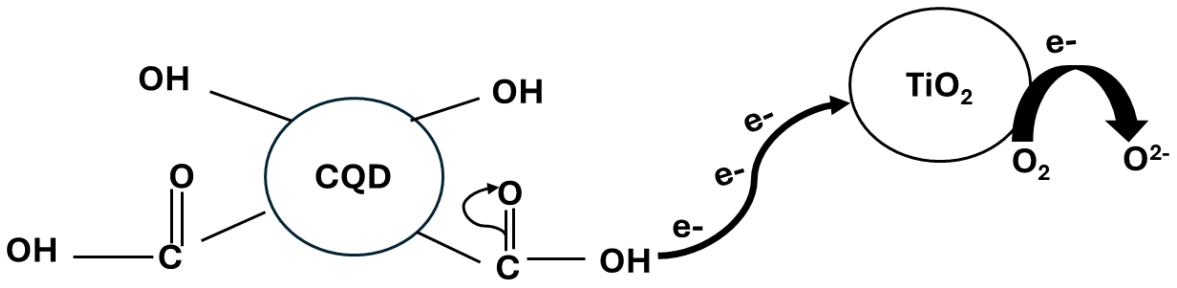

Scheme 22: Depicts the schematic mechanism of CQD-TiO_2.

Mil101(Fe) was embedded onto the surface of CQD-TiO_2 to form ternary composites. The effect of these materials on the CQD-TiO_2 surface was investigated using cyclic voltammetry to analyze the reaction kinetics occurring at the electrode interface. It was observed that all the modified electrodes compared in this work showed different peak-to-peak separations (ΔE_p). A lower ΔE_p is highly preferred in electrochemistry, as it signifies efficient electron transfer capabilities at the electrode interface. The cyclic voltammetry analysis indicated that the Mil101(Fe)-CQD-TiO_2 composite exhibited a peak-to-peak separation value of 0.88 V, which is lower in comparison to 0.90 V exhibited by GCE-CQD-TiO_2-Apt-BSA. A lower ΔEp indicates that electrons move more rapidly at the electrode interface, thereby enhancing the biosensor response.

The diffusion coefficients (D) for the modified electrodes were evaluated. A higher diffusion coefficient indicates that electrons are diffusing rapidly on the electrode surface. GCE-Mil101(Fe)-CQD-TiO_2-Apt-BSA exhibited a higher diffusion coefficient value of 5.994×10^{-11} cm^2 s^{-1} compared to the GCE-CQD-TiO_2-Apt-BSA, denoting a rapid movement of electrons. The surface coverages (Γ) were also determined to understand the electrode's electrocatalytic efficiency [474]. A higher Γ value indicates a more active electrode surface. GCE-Mil101(Fe)-CQD-TiO_2-Apt-BSA exhibited a higher surface coverage value, indicating a more active electrode compared to GCE-CQD-TiO_2-Apt-BSA. To further understand the potential active sites for analyte detection, the electrochemically active surface areas (EASA) were evaluated [475]. Notably, GCE-Mil101(Fe)-CQD-TiO_2-Apt-BSA exhibited a relatively higher EASA value of 3.224 cm^2, compared to GCE-CQD-TiO_2-Apt-BSA. A higher EASA value indicates that there are more active sites on the electrode available to bind the analyte. The observation is attributed to the greater porosity of Mil101(Fe)-CQD-TiO_2 than that of CQD-TiO_2

electrocatalysts. The porosity of the Mil101(Fe)-CQD-TiO_2 is beneficial for analyte detection.

Furthermore, Tafel slopes were assessed to quantify the efficiency of the modified electrodes [476]. Figure 57(A-B) shows the Tafel plot of Log v vs. potential for GCE-Mil101(Fe)-CQD-TiO_2-Apt-BSA, and Figure 57B shows the Tafel plot of Log v vs. potential for GCE-CQD-TiO_2-Apt-BSA. Tafel slopes with values between 60 $decade^{-1}$ and 120 $decade^{-1}$ are advantageous, as they imply a one-electron transfer process during the rate-determining step [477,478]. GCE-Mil101(Fe)-CQD-TiO_2-Apt-BSA exhibited a higher Tafel slope compared to GCE-CQD-TiO_2-Apt-BSA, indicating a higher reaction rate at the electrode surface. All the obtained parameters are summarised in Table 16.

Table 16: Summarises the parameters obtained from cyclic voltammetry experiments.

Electrode	**Diffusion coefficient ($cm^2\ s^{-1}$)**	**ΔE_p (V)**	**EASA (cm^2)**	**Surface coverage (mol cm^{-2})**	**Tafel slope**
GCE-Mil101(Fe)-CQD-TiO_2-Apt-BSA	5.994×10^{-11}	0.88	3.224	5.557×10^{-9}	60.5
GCE-CQD-TiO_2- Apt-BSA	4.54×10^{-14}	0.90	0.548	2.40×10^{-10}	49

The peak-to-peak separation of the modified electrodes was calculated by subtracting the cathodic peak potential from the anodic peak potential, while Diffusion coefficients were calculated using the Randles-Sevick equation. Surface coverages were determined using the Laviron equation. Additionally, the electrochemically active surface area was calculated using the slope of the linear plot of the square root of the scan rate and was fitted to the Randles-Sevick equation. Tafel slopes were determined by using the slope of the Tafel plot, which is the relationship between the log of the scan rate and the potential

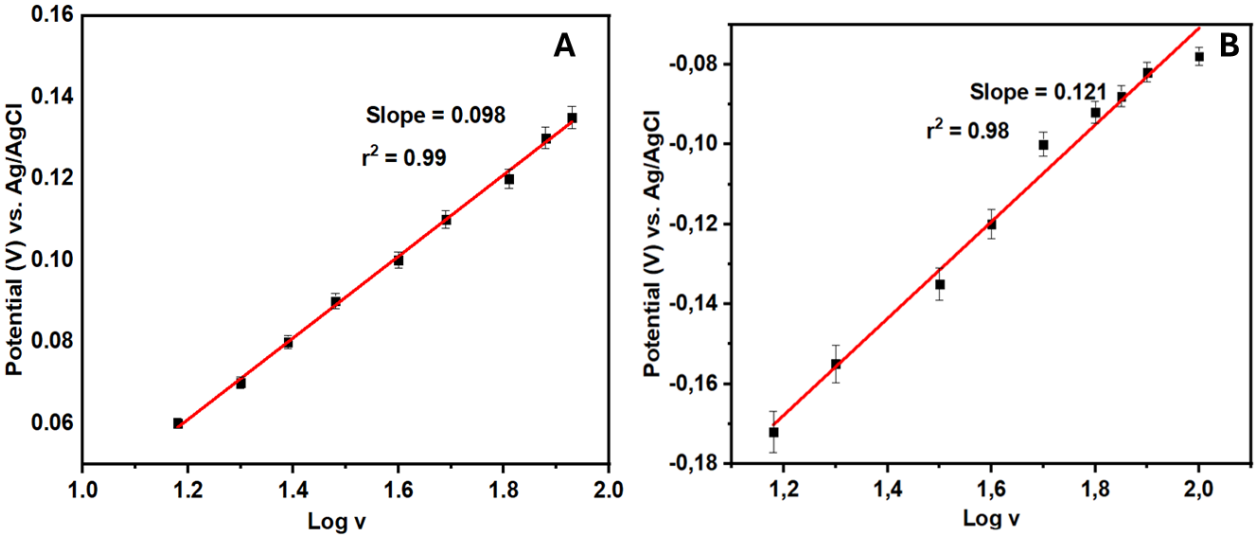

Figure 57: Shows the Tafel plots of Log V vs. potential obtained from (A) GCE-Mil101(Fe)-CQD-TiO_2-Apt-BSA and (B) GCE-CQD-TiO_2-Apt-BSA in 0.1M PBS (pH,7.2).

6.3 Electrochemical detection of *Crypto*

The performance of the aptasensors was evaluated by examining the relationship between spiked *Crypto* concentrations and the corresponding peak currents. The results are summarized in Table 17. Both aptasensors showed a linear increase in current with increasing concentrations of *Crypto*. This behaviour can be attributed to the aptamer's conformation, which facilitates enhanced electron movement between the electrode and the electrolyte. The GCE-Mil101(Fe)-CQD-TiO_2-Apt-BSA exhibited a low detection limit and higher sensitivity across a wide linear range. This superior performance is due to the increased number of active sites for analyte binding on the GCE-Mil101(Fe)-CQD-TiO_2-Apt-BSA electrode surface. Additionally, the greater porosity and conductivity of Mil101(Fe)-CQD-TiO_2, compared to the CQD-TiO_2 electrocatalyst, improve electron transfer, resulting in enhanced detection performance [479].

Table 17: Summary of the parameters obtained from Crypto detection using GCE-CQD-TiO_2 and GCE-Mil101(Fe)-CQD-TiO_2-Apt-BSA.

Electrode	Method	LOD (ng L^{-1})	LOQ (ng L^{-1})	Linear range (µM)	Sensitivity (mA $µM^{-1}$)
GCE-Mil101(Fe)-CQD-TiO_2-Apt-BSA	SWV	0.001	0.004	0.0015 – 0.004	0.529
GCE-CQD-TiO_2- Apt-BSA	SWV	0.0024	0.008	0.0025 - 0.0045	0.27

Notably, GCE-Mil101(Fe)-CQD-TiO_2-Apt-BSA exhibited more active sites, faster electron-transfer kinetics, and enhanced selectivity for Crypto, highlighting its superior performance in dynamic sensing environments. Scheme 23 shows the schematic mechanisms of Mil101(Fe)-CQD-TiO_2, illustrating the transfer of electrons from Fe in Mil101(Fe) through the CQD surface to TiO_2. Once a sufficient number of electrons enter the TiO_2 structure, it becomes capable of reducing oxygen, as shown in the reaction mechanism.

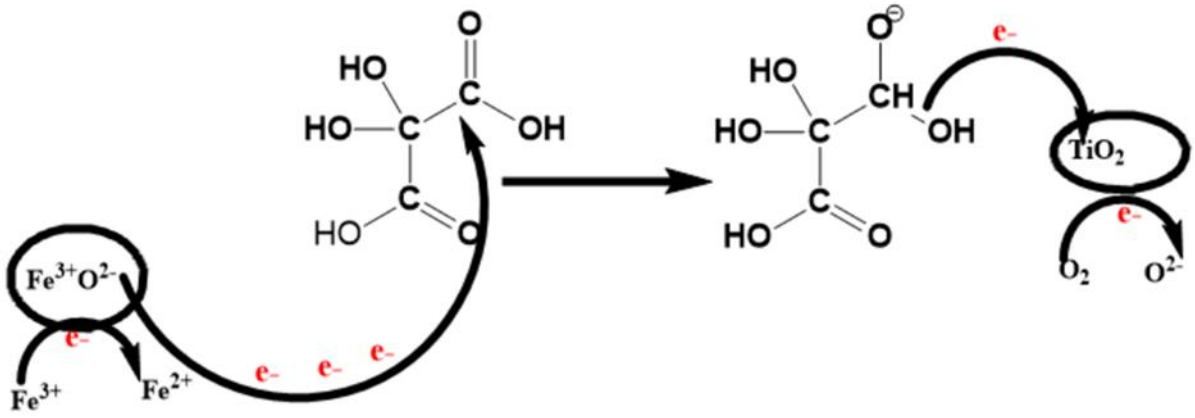

Scheme 23 :Shows a schematic mechanism of Mil101(Fe)-CQD-TiO_2.

6.4 Selectivity studies

Selectivity is a key factor in biosensor performance, ensuring that the sensor accurately detects the target analyte in the presence of potentially interfering species [480]. The investigation was conducted to examine the electrochemical response of GCE-Mil101(Fe)-CQD-TiO_2-Apt-BSA and GCE-CQD-TiO_2-Apt-BSA in the presence of interfering species. *Giardia and Escherichia coli* (E. coli) were chosen for this experiment. Figure 58 (A-B) shows the interference study for GCE-Mil101(Fe)-CQD-TiO_2-Apt-BSA, and Figure 58B shows the GCE-Mil101(Fe)-CQD-TiO_2-Apt-BSA.The electrochemical responses of both aptasensors were monitored in the presence of interfering species. As shown in Figures 58A and 58B, the detection of *Crypto* resulted in a high peak current response. However, when Giardia was added, the peak current response decreased. The addition of E. coli further decreased the current response. This observation suggests that the sensing platforms are selective towards Crypto, with GCE-Mil101(Fe)-CQD-TiO_2-Apt-BSA exhibiting better electrochemical performance than GCE-CQD-TiO_2-Apt-BSA.

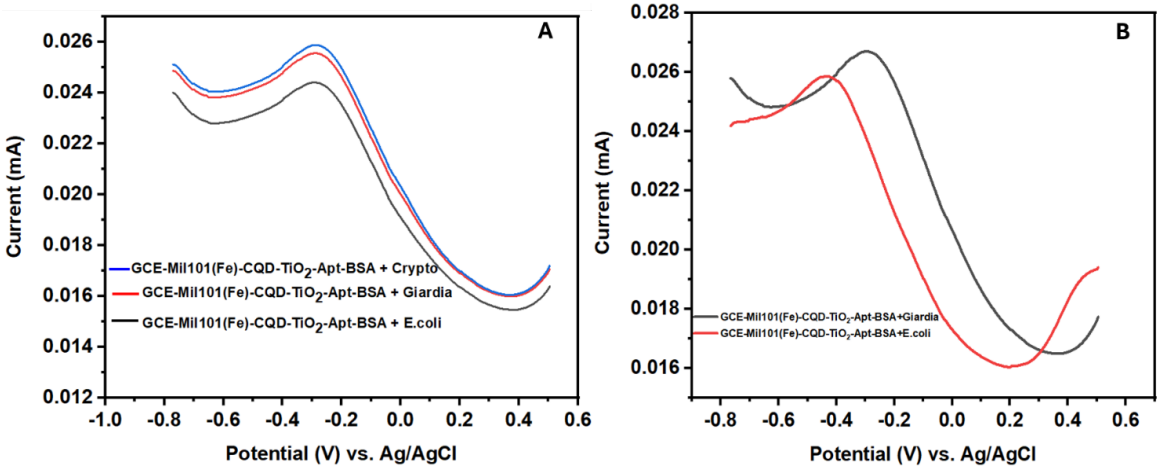

Figure 58 : Shows the SWV experiment in the presence of *Crypto*, E. coli and Giardia for GCE-Mil101(Fe)-CQD-TiO_2-Apt-BSA in 0.1 M PBS (pH,7.2) (B) SWV response of spiked concentrations of *Crypto*, E. coli and Giardia for GCE-Mil101(Fe)-CQD-TiO_2.

6.5 Summary and Sub-conclusion

In this chapter, the two electrocatalysts, Mil101(Fe)-CQD-TiO_2 and CQD-TiO_2, are evaluated for their sensitivity and performance in detecting *Crypto* in buffer solutions. The results indicate that Mil101(Fe)-CQD-TiO_2 exhibits faster electron-transfer rates, leading to improved electrochemical performance and selectivity. This highlights the platform's potential for identifying various analytes in both environmental and biological applications. Mil101(Fe)-CQD-TiO_2 also exhibited lower limits of detection, making it a strong candidate for the trace detection of heavy metals, pharmaceuticals, and clinical diagnostics. In contrast, CQD-TiO_2 exhibited a higher limit of detection, posing challenges for sensing applications. Furthermore, Mil101(Fe)-CQD-TiO_2 did not exhibit enhanced stability, which limits the reproducibility of the results. To achieve lower limits of detection, faster reaction kinetics, and greater stability, it is essential to explore more conductive electrocatalyst materials.

CHAPTER SEVEN:

Conclusion and Future Outlooks

7.1 Conclusion

In this work, we aimed to develop a nano-engineered electrochemical aptasensors for the label-free detection of *Crypto* and potential heavy metals in water. The aim was achieved by focusing on the objectives implemented. All the nanomaterials (CQD, TiO_2, Mil101(Fe), CQD-TiO_2, CQD-TiO_2-Mil101(Fe), were synthesised. Various characterisation techniques, such as HR-TEM, HR-SEM, FTIR, XPS, TGA, and XRD, confirmed the successful synthesis of the materials. The as-synthesised materials were then used to develop electrodes. All modified electrodes were characterised using CV, EIS, and Cp to investigate the electrochemical properties. The combination of carbon-based nanomaterials with metal oxide has been shown to improve electrochemical properties. The synergistic effects of these composites enhance electron transfer kinetics, creating more active sites for analyte detection and significantly boosting sensor performance. Among these, the Mil101(Fe)-CQD-TiO_2 ternary composite stands out as the most effective, with lower detection limits, higher sensitivities, and rapid kinetics. This combination facilitates fast electron movement and enhances the overall electrochemical response. The GCE-Mil101(Fe)-CQD-TiO_2-Apt-BSA aptasensor platform demonstrated superior performance in detecting *Crypto*, Cd^{2+}, and arsenic in both buffer solutions and real water samples. In conclusion, all the aptasensor platforms developed in this work were selective for *Crypto* and successfully detected it in both phosphate buffer and real water samples. However, only the GCE-Mil101(Fe)-CQD-TiO_2-Apt-BSA could detect Cd^{2+} in both buffer solutions and real water samples, as well as arsenic in phosphate buffer solutions.

The limits of detection achieved in this thesis were comparable to those reported in the literature and outperformed conventional techniques. For instance, Andria and her team conducted a study on the detection of Cd^{2+} in water samples using ICP-MS, obtaining an LOD of 2.2 ng L^{-1} [481]. In another study by Atasoy et al. [482]. used atomic absorption spectroscopy to detect arsenic in drinking water samples, achieving an LOD of 4.8 ng L^{-1}. Additionally, Sara et al. [483] reported the development of an electrochemical aptasensor for arsenic detection in water, which achieved an LOD of 0.12 ng L^{-1}.

In this work, *Crypto* was detected by UV-Vis spectroscopy, yielding an LOD of 0.083 ng L^{-1}. Kapel et al. [131] employed the ELISA method for detecting *Crypto*, yielding an LOD of 88 ng L^{-1}. Furthermore, Luka et al. [185] developed an electrochemical immunosensor for the label-free detection of *Crypto* in water samples, which achieved an LOD of 20 µg L^{-1}.

The developed GCE-Mil101(Fe)-CQD-TiO_2-Apt-BSA achieved LODs of 0.05 ng L^{-1} for Cd^{2+}, 0.092 ng L^{-1} for arsenic, and 0.001 ng L^{-1} for *Crypto*, all of which are below the WHO concentration limits. This study demonstrates that the developed aptasensor platform achieved lower limits of detection than conventional techniques and other electrochemical sensors, positioning it as a viable platform for dual detection of microbial pathogens and trace metals in water samples. The F-test results for the developed aptasensors for detecting *Cryptosporidium*, cadmium, and arsenic showed high precision in real water samples. The results provide a strong basis for expanding this approach to encompass multi-analyte detection and portable sensing systems focused on environmental and public health protection.

The Mil101(Fe)-CQD-TiO_2 electrocatalyst can be successfully scaled up using environmentally friendly synthesis methods, such as green synthesis. This approach is cost-effective, energy-efficient, and environmentally sustainable. Implementing a real-time monitoring and control system, possibly enhanced by machine learning, can further improve the electrocatalyst's scaling process. Machine learning can optimize synthesis pathways, help interpret data, and predict future trends for electrocatalysts. Additionally, strengthening collaborations between academia and industry can help scale up the Mil101(Fe)-CQD-TiO_2 electrocatalyst.

7.2 Future outlooks

1. The sensing platforms developed in this work can be integrated with microfluidics and on-chip-based technology for autonomous sample processing and detection.
2. Electrocatalysts can be utilised in the production of conductive screen-printed electrodes for pathogen, heavy metal detection and healthcare applications.

3. Electrocatalysts can also be used in the development of portable electrochemical devices, such as smartphone-based readouts for point-of-care applications.
4. The development of miniaturized paper-based platforms offers a cost-effective approach to environmental diagnostics.
5. Aptamers can be used for the multiple detection of pathogens, bacteria, and heavy metals.

This integration will enable the creation of portable, cost-effective, flexible, and reliable sensing devices for the early detection of pathogens, heavy metals, and microbial diseases in biological and environmental samples.

References

(1) Li.P, Wu, L., Drinking Water Quality and Public Health. *Expo. Health* **2019**, *2*, 73–79.hhps:// dio 10.3390/ijerph16040631.

(2) Fatemeh,P. E., Hajar-Alsadat, M.T, Asieh, S, Ze-Xian. L, Mohsen A., Asghar T.K., Biosensors for Wastewater Monitoring: A Review. *Biosens Bioelectron*. **2018**, 118, 66–79. doi: 10.1016/j.bios.2018.07.019.

(3) Kumar, V., Sharma, M., Sondhi, S., Kaur, K., Sharma, D., Sharma, S., Utreja, D., Removal of Inorganic Pollutants from Wastewater: Innovative Technologies and Toxicity Assessment. *Sustainability (Switzerland)*. MDPI , **2023**, 23, 16376. https://doi.org/10.3390/su152316376.

(4) Qiao, D., Wang, G., Li, X., Wang, S., Zhao, Y., Pollution, Sources and Environmental Risk Assessment of Heavy Metals in the Surface AMD Water, Sediments and Surface Soils around Unexploited Rona Cu Deposit, Tibet, China. *Chemosph*. **2020**, *248 125988*. https://doi.org/10.1016/j.125988.

(5) Sharma, A. K., Sharma, M., Sharma, A. K., Sharma, M., Mapping the Impact of Environmental Pollutants on Human Health and Environment: A Systematic Review and Meta-Analysis. *J Geochem Explor,* **2023**, *255*, 107325. https://doi.org/10.1016/j.gexplo.2023.107325.

(6) Joseph, L., Jun, B. M., Flora, J. R. V., Park, C. M., Yoon, Y. , Removal of Heavy Metals from Water Sources in the Developing World Using Low-Cost Materials: A Review. *Chemosphere*. Elsevier Ltd. **2019**, 229, 142–159. https://doi.org/10.1016/j.

(7) Vardhan, K. H., Kumar, P. S., Panda, R. C. A Review on Heavy Metal Pollution, Toxicity and Remedial Measures: Current Trends and Future Perspectives. *Journal of Molecular Liquids*. Elsevier B.V., **2019**, 290, 111197. https://doi.org/10.1016/j.molliq.2019.

(8) Luo, Y., Guo, W., Ngo, H. H., Nghiem, L. D., Hai, F. I., Zhang, J., Liang, S., Wang, X. C. A Review on the Occurrence of Micropollutants in the Aquatic Environment and Their Fate and Removal during Wastewater Treatment. *Science of the Total Environment*. Elsevier B.V., **2014**, 65, 619–641, https://doi.org/10.1016/j.scitotenv.2013.

(9) Sher, A. A., Ashraf, M. A.,Mustafa, B. E.,Raza, M. M. Epidemiological Trends of Foodborne Campylobacter Outbreaks in the United States of America, 1998–2016. *Food Microbiol.* **2021**, *9,* 103751. https://doi.org/10.1016/j.fm.2021..

(10) Ali, N. M., Khan, M. K., Mazhar, B., Mustafa, M. Impact of Water Pollution on Waterborne Infections: Emphasizing Microbial Contamination and Associated Health Hazards in Humans. *Discover Water* **2025**, *5* , 19. https://doi.org/10.1007/s43832-025-00198-x.

(11) Paul B. Tchounwou, C., Heavy Metal Toxicity and the Environment. *Molecular, Clinical and Environm.,* **2012**, *101*, 133–164. doi: 10.1007/978/3—76438340-4-6.

(12) Khulbe, K. C.; Matsuura, T. , Removal of Heavy Metals and Pollutants by Membrane Adsorption Techniques. *Applied Water Scie.,* **2018**, 8, 19. https://doi.org/10.1007/s13201-018-0661-6.

(13) Nime, J. D., Burek, D. L., Page, M. A., Holscher, Y., Acute Enterocolitis in a Human Being Infected with the Protozoan Cryptosporidium, *Gastroente.,* **1976**, 70, 592–598. Doi: 10.1051/parasite.

(14) Bestidas, G., Cryptosporidiosis-an Overview. *Journal Biomed. Res.,* **2012**, *25* 1–16. doi .org/10.5772/intechopwn.82990.

(15) Bones, A. J. Jossé, L.; More, C.; Miller, C. N. Michaelis, M.; Tsaousis, A. D. Past and Future Trends of Cryptosporidium in Vitro Research. *Exp Parasitol* **2019**, *196*, 28–37. https://doi.org/10.1016/j.exppara.2018.12.001.

(16). Luka, G., Ahmad, S., Falcone, N., Kraatz, H.-B. & Kraatz, B. Advances in Enzyme-Based Electrochemical Sensors: Current Trends, Benefts, and Constraints. In Bioelectronics and Medical Devices. *Woodhead Publishing* **2019**, 68, 555–590. https://doi.org/10.1016/j.vetpar.2007.09.001.

(17) Bouzid, M.; Hunter, P.R.; Chalmers, R.M.; Tyler, K. M. Cryptosporidium Pathogenicity and Virulence. *Clin. Microbiol. Rev.* **2013**, 26, 115–134.

(18) Efstratiou, A.; Ongerth, J. E.; Karanis, P. Waterborne Transmission of Protozoan Parasites: Review of Worldwide Outbreaks - An Update 2011–2016. *Water Res.* **2017**, *114*, 14–22. https://doi.org/10.1016/j.watres.2017.01.036.

(19) Deivayanai, V. C., Thamarai, P., Karishma, S., Saravanan, A., Vickram, A. S., Yaashikaa, P. R., Sonali, S. A Comprehensive Review on Impregnated Magnetic Nanoparticle in Advanced Wastewater Treatment: An in-Depth Technical Review and Future Directions. *Sustainable Chemistry for the Environment* **2025**, *9*, 100220. https://doi.org/10.1016/j.scenv.2025..https://doi.org/10.1016/j.watres.2017.01.036 .

(20) Jaishankar, M., Tseten, T., Anbalagan, N., Mathew, B. B., Beeregowda, K. N. Toxicity, Mechanism and Health Effects of Some Heavy Metals. *Interdisciplinary Toxicology*. Slovak Toxicology Society **2014**, 12, 60–72. https://doi.org/10.2478/intox-2014-0009.

(21) Cui, L., Wu, J., Ju, H. Label-Free Signal-on Aptasensor for Sensitive Electrochemical Detection of Arsenite. *Biosens. Bioelectron.* **2016**, *79*, 861–865. https://doi.org/10.1016/j.bios.2016.01.010.

(22) Cirovic, A., Satarug, S. Toxicity Tolerance in the Carcinogenesis of Environmental Cadmium. *International Journal of Molecular Sciences*. Multidisciplinary Digital Publishing Institute (MDPI) **2024**, 12, 1851. https://doi.org/10.3390/ijms25031851.

(23) Zhang, W., Miao, A. J., Wang, N. X., Li, C., Sha, J. Arsenic Bioaccumulation and Biotransformation in Aquatic Organisms. *Environment International*. Elsevier **2022**, 78, 107221. https://doi.org/10.1016/j.envint.2022..

(24) Patel, K. S., Pandey, P. K., Martín-Ramos, P., Corns, A Review on Arsenic in the Environment: Bio-Accumulation, Remediation, and Disposal. *RSC Advances*. Royal Society of Chemistry **2023**, 18, 14914–14929. https://doi.org/10.1039/d3ra02018e.

(25) *National Primary Drinking Water Regulations Contaminant MCL or TT 1 (Mg/L) 2 Potential Health Effects from Long-Term 3 Exposure above the MCL Common Sources of Contaminant in Drinking Water Public Health Goal (Mg/L) 2*.**2019**. https://doi.org/10.1007/978-981-10-7284-0.

(26) By Yulia Yancheva. Removing Heavy Metal Pollutants in Water with Graphene Acid. **2021**, *12*, 11112. https://doi.org/10.3390/ijerph17113782.

(27) Attaallah, R., Amine, A. Highly Selective and Sensitive Detection of Cadmium Ions by Horseradish Peroxidase Enzyme Inhibition Using a Colorimetric Microplate Reader and Smartphone Paper-Based Analytical Device. *Microchemical Journal* **2022**, *172,*106940. https://doi.org/10.1016/j.microc.2021..

(28) Pumipuntu, N., Piratae, S. Cryptosporidiosis: A Zoonotic Disease Concern. *Vet. World* **2018**, 11, 681–686. https://doi.org/10.1016/j.microc.2021.106940.

(29) Jain, U.; Saxena, K.,Hooda, V. Emerging Vistas on Pesticides Detection Based on Electrochemical Biosensors—An Update. *Food Chem.* **2022**, 371, 106940. https://doi.org/10.1016/j.microc.2021..

(30) Attar, A., Cubillana-Aguilera, L., Naranjo-Rodríguez, I., de Cisneros, Amperometric Inhibition Biosensors Based on Horseradish Peroxidase and Gold Sononanoparticles Immobilized onto Different Electrodes for Cyanide Measurements. *Bioelectrochemistry* **2015**, *101*, 84–91. https://doi.org/10.1016/j.bioelechem.2014.08.003.

(31) Naresh, V., Lee, N. A Review on Biosensors and Recent Development of Nanostructured Materials-Enabled Biosensors. *Sensors (Switzerland)*. MDPI **2021**, 59, 1–35. https://doi.org/10.3390/s21041109.

(32) Qi, X., Zhang, L., Wang, X.; Chen, S., Wang, X. A Label-Free Colorimetric Aptasensor Based on an Engineered Chimeric Aptamer and Au@FeP Nanocomposites for the Detection of Kanamycin. *Food Control* **2023**, *149*, 109700. https://doi.org/10.1016/j.foodcont.2023.

(33) Constantinou, A., Chen, C., Deonarain, M. P. Modulating the Pharmacokinetics of Therapeutic Antibodies. *Biotechnology Letters* **2010**, 14, 609–622. https://doi.org/10.1007/s10529-010-0214-z.

(34) Yang, L. F., Ling, M., Kacherovsky, N., Pun, S. H. Aptamers 101: Aptamer Discovery and in Vitro Applications in Biosensors and Separations. *Chemical Science*. Royal Society of Chemistry **2023**, 45, 8990.. https://doi.org/10.1039/d3sc00439b.

(35) Liu, R., Zhang, F., Sang, Y., Katouzian, I., Screening, Identification, and Application of Nucleic Acid Aptamers Applied in Food Safety Biosensing. *Trends in Food Science and Technology*. Elsevier Ltd **2022**, 25, 355–375. https://doi.org/10.1016/j.tifs.2022.03.025.

(36) Qi, S., Duan, N., Sun, Y., Zhou, Y., Ma, P., Wu, S., Wang, Z. High-Affinity Aptamer of Allergen β-Lactoglobulin: Selection, Recognition Mechanism and Application. *Sens. Actuators B Chem.* **2021**, *340*, 129956. https://doi.org/10.1016/j.snb.2021.

(37) Holzinger, M.; Goff, A. Le; Cosnier, S. Nanomaterials for Biosensing Applications: A Review. *Frontiers in Chemistry*. Frontiers Media S. A **2014,** 112, 00063. https://doi.org/10.3389/fchem.2014.00063.

(38) Freeman, R., Girsh, J., Willner, I. Nucleic Acid/Quantum Dots (QDs) Hybrid Systems for Optical and Photoelectrochemical Sensing. *ACS Applied Materials and Interfaces*. **2013**, 4, 2815–2834. https://doi.org/10.1021/am303189h.

(39) Zhao .P. , Zhang, Q. Cao, J., Facile and Green Synthesis of Highly Fluorescent Carbon Quantum Dots from Water Hyacinth for the Detection of Ferric Iron and Cellular Imaging. *nanomaterials* **2022**, No. 12, 1528. https://doi.org/10.1021/am303189h.

(40) Jin, X., R. Chen, J. Y. Activated Carbon and Carbon Quantum Dots/Titanium Dioxide Composite Based on Waste Rice Noodles: Simultaneous Synthesis and Application in Water Pollution Control. *nanomaterials* **2022**, 472, 113–120. https://doi.org/10.3389/fchem.2014.00063.

(41) Khan, M. Q.; Ahmad, K.; Alsalme, A.; Kim, H. Hydrothermal Synthesis of Nanostructured NiO for Hydrazine Sensing Application. *Mater. Chem. Phys.* **2022**, *289*. https://doi.org/10.1016/j.matchemphys.2022.126463.

(42) Jung, H.; Wook, Y.; Lee, G.; Cho, S.; Kang, M.; Pyun, J. Analytica Chimica Acta A Capacitive Biosensor Based on an Interdigitated Electrode with Nanoislands. *Anal. Chim. Acta* **2014**, *844*, 27–34. https://doi.org/10.1016/j.aca.2014.07.006.

(43) Ali, M. E., Hashim, U., Nanobiosensor for Detection and Quantification of DNA Sequences in Degraded Mixed Meats. **2011**, *20, 1098*. https://doi.org/10.1155/2011/781098.

(44) Links, D. A. Synthesis, Characterization, and Electrochemical and Electrical Properties of Novel Mono and Ball-Type Metallophthalocyanines with Four 9,9-Bis(4-Hydroxyphenyl)Fluorene ¨. **2011.** 99, 157. https://doi.org/10.1039/c0dt01575j.

(45) Sayyad, P. W.; Ingle, N. N.; Al-Gahouari, T., Mahadik, M. M., Bodkhe, . Sensitive and Selective Detection of Cu2+ and Pb2+ Ions Using Field Effect Transistor (FET) Based on L-Cysteine Anchored PEDOT:PSS/RGO Composite. *Chem. Phys. Lett.* **2020**, *761,* 138056.https://doi.org/10.1016/j.cplett.2020.

(46) Lee, S., Oh, J., Kim, D.;,Piao, Y. A Sensitive Electrochemical Sensor Using an Iron Oxide/Graphene Composite for the Simultaneous Detection of Heavy Metal Ions. *Talanta* **2016**, *160*, 528–536. https://doi.org/10.1016/j.talanta.2016.07.034.

(47) Samie, A., Al-Qahtani, A., El Bakri, A., Ehdaie, B. Challenges and Innovative Strategies to Interrupt Cryptosporidium Transmission in Resource-Limited Settings. *Curr. Trop. Med. Rep.* **2015**, 2, 161–170. https://doi.org/10.1007/s40475-015-0057-8.

(48) Joshi, A., Prasad, S., Kasav, J. B. Water and Sanitation Hygiene Knowledge Attitude Practice in Urban Slum Settings. *Glob. J. Health Sci.* **2014**, *6*, 23–34. https://doi.org/10.5539/gjhs.v6n2p23.

(49) Kotloff, K.L., Nataro, J.P., Burden and Aetiology of Diarrhoeal Disease in Infants and Young Children in Developing Countries (the Global Enteric Multicenter Study, GEMS): A Prospective, Case-Control Study. *Lancet* **2013**, No. 382, 209–222.

(50) Utami, W. S., Murhandarwati, E. H., Artama, W. T.; Kusnanto, H. Cryptosporidium Infection Increases the Risk for Chronic Diarrhea among People Living with HIV in Southeast Asia. *A systematic review and meta-analysis. Asia Pac. J. Public Health* **2020**, 32, 8–18. https://doi.org/10.1016/j.matchemphys.2022.126463.

(51) Cunha, F. S., Peralta, R. H. S. & Peralta, J. M. New Insights into the Detection and Molecular Characterization of Cryptosporidium with Emphasis in Brazilian Studies: *A review. Rev. Inst. Med. Trop. Sao Paulo* **2019**, 61, 1–12. https://doi.org/10.1039/c0dt01575j.

(52) Gunasekera, S.; Zahedi, A.; Dea, M. O. Organoids and Bioengineered Intestinal Models : Potential Solutions to the Cryptosporidium Culturing. **2015**, 34, 5556. Dilemma.https://doi.org/10.1155/2011/781098.

(53) Destura, R. V.; Cena, R.B.; Galarion, M.J.H.; Pangilinan, C.M.; Arevalo, G. M. ; A.; R.O.C.; Petronio, J.A.G.; Salem, G.M.; Schwem, B.; Sevilleja, J. E. A. D. Advancing

Cryptosporidium Diagnostics from Bench to Bedside. *Curr. Trop. Med. Reports* **2015**, 2, 150–160.https://doi.org/10.5539/gjhs.v6n2p23.

(54) S. Balbinot, A.M. Srivastav, J. Vidic, I. Abdulhalim, M. M. Plasmonic Biosensors for Food Control. *Trends Food Sci Technol,* **2021**, 111, 128–140. https://doi.org/10.1016/j.crgsc.2022.100306.

(55) Chen, D.; Wang, X.; Luo, X.; Huang, G.; Tian, Z.; Li, W.; Liu, F. Delineating and Identifying Risk Zones of Soil Heavy Metal Pollution in an Industrialized Region Using Machine Learning. *Environmental Pollution* **2023**, *318*. 120932. https://doi.org/10.1016/j.envpol.2022.

(56) Briffa, J.; Sinagra, E.; Blundell, R. Heavy Metal Pollution in the 1Environment and Their Toxicological Effects on Humans. *Heliyon*. Elsevier Ltd, **2020**, 56, e0469. https://doi.org/10.1016/j.heliyon.2020..

(57) Collin, S.; Baskar, A.; Geevarghese, D. M.; Ali, M. N. V. S.; Bahubali, P.; Choudhary, R.; Lvov, V.; Tovar, G. I.; Senatov, F.; Koppala, S.; Swamiappan, S. Bioaccumulation of Lead (Pb) and Its Effects in Plants: A Review. *Journal of Hazardous Materials Letters* **2022**, *3*. 100064. https://doi.org/10.1016/j.hazl.2022.

(58) Pujol, L.; Evrard, D.; Groenen-Serrano, K.; Freyssinier, M.; Ruffien-Cizsak, A.; Gros, P. Electrochemical Sensors and Devices for Heavy Metals Assay in Water: The French Groups' Contribution. *Frontiers in Chemistry*. Frontiers Media S. A **2014**, 20, 00019, https://doi.org/10.3389/fchem.2014.

(59) Garg, N.; Deep, A.; Sharma, A. L. Sensitive Detection of Cadmium Using Amine-Functionalized Fe-MOF by Anodic Stripping Voltammetry. *Ind. Eng. Chem. Res.* **2023**, *62* , 9735–9746. https://doi.org/10.1021/acs.iecr.3c01385.

(60) Wang, H.; Cheng, H.; Wang, J.; Xu, L.; Chen, H.; Pei, R. Selection and Characterization of DNA Aptamers for the Development of Light-up Biosensor to Detect Cd(II). *Talanta* **2016**, *154*, 498–503. https://doi.org/10.1016/j.talanta.2016.04.005.

(61) Akramipour, R.; Golpayegani, M. R.; Gheini, S.; Fattahi, N. Speciation of Organic/Inorganic Mercury and Total Mercury in Blood Samples Using Vortex Assisted Dispersive Liquid-Liquid Microextraction Based on the Freezing of Deep Eutectic Solvent Followed by GFAAS. *Talanta* **2018**, *186*, 17–23. https://doi.org/10.1016/j.talanta.2018.04.042.

(62) Krata, A. A.; Wojciechowski, M.; Kalabun, M.; Bulska, E. Reference Measurements of Cadmium and Lead Contents in Candidates for New Environmental Certified Materials by Isotope Dilution Inductively Coupled Plasma Mass Spectrometry. *Microchemical Journal* **2018**, *142*, 36–42. https://doi.org/10.1016/j.microc.2018.06.013.

(63) Li, D.; Li, M. L.; Liu, W. R.; Qin, Z. Z.; Liu, S. A. Cadmium Isotope Ratios of Standard Solutions and Geological Reference Materials Measured by MC-ICP-MS. *Geostand. Geoanal. Res.* **2018**, *42*, 593–605. https://doi.org/10.1111/ggr.12236.

(64) Chen, X.; Xie, T.; Lu, C.; Chu, J.; Li, W.; Lin, R.; Wu, D.; Gu, Q. Highly Sensitive Detection of Lead Ions and Cadmium Ions Based on ZIF-8-NH2 Enhanced by Carbon Nanotubes and Bismuth Film. *J. Environ. Chem. Eng.* **2023**, *11*. 109515. https://doi.org/10.1016/j.jece.2023.109515.

(65) Squire, S.A.; Ryan, U. Cryptosporidium and Giardia in Africa: Current and Future Challenges. *Parasites and Vectors 2* **2017**, 10, 1–32. https://doi.org/10.1016/S0892-0362(02)00320-3.

(66) WHO. Guidelines for Drinking-Water Quality. *Geneva: World Health Organization* **2014**, 1–564. https://doi.org/10.1016/j.jece.2017.05.029

(67) Javanmard, E.; Rahimi, H. M.; Niyyati, M.; Aghdaei, H. A.; Sharifdini, M.; Mirjalali, H.; Zali, M. R.; Karanis, P. Molecular Analysis of Blastocystis Sp. And Its Subtypes from Treated Wastewater Routinely Used for Irrigation of Vegetable Farmlands in Iran. *J. Water Health* **2019**, *17*, 837–844. https://doi.org/10.2166/wh.2019.045.

(68) WHO. Preventing Diarrhoea Through Better Water Sanitation and Hygiene. Geneva, Switzerland: *Geneva, Switzerland* **2022**.

(69) Pratush, A.; Kumar, A.; Hu, Z. Adverse Effect of Heavy Metals (As, Pb, Hg, and Cr) on Health and Their Bioremediation Strategies: A Review. *International Microbiology*. Springer, **2018**, 56, 97–106. https://doi.org/10.1007/s10123-018-0012-3.

(70) Zhou, Q.; Yang, N.; Li, Y.; Ren, B.; Ding, X.; Bian, H.; Yao, X. Total Concentrations and Sources of Heavy Metal Pollution in Global River and Lake Water Bodies from 1972 to 2017. *Glob. Ecol. Conserv.* **2020**, *22*, e00925. https://doi.org/10.1016/j.gecco.2020.

(71) Ryan, U.; Hijjawi, N.; Xiao, L. Foodborne Cryptosporidiosis. *Int. J. Parasitol.* **2018**, *48*, 1–12. https://doi.org/10.1016/j.ijpara.2017.09.004.

(72) *Environmental Pollution Governance and Ecological Remediation Technology*; Zhang, J., Ruan, R., Bashir, M. J. K., Eds.; Environmental Science and Engineering; Springer International Publishing: Cham, **2023**, 34, 667. https://doi.org/10.1007/978-3-031-25284-6.

(73) Yu, X.; Zhang, S.; Guo, W.; Li, B.; Yang, Y.; Xie, B.; Li, K.; Zhang, L. Recent Advances on Functional Nucleic-Acid Biosensors. **2021**, 45, 118. https://doi.org/10.3390/app10207078

(74) Widmer, G.; Carmena, D.; Kvá, M.; Chalmers, R. M.; Kissinger, J. C.; Xiao, L. Update on Cryptosporidium Spp .: Highlights from the Seventh International Giardia and Cryptosporidium Conference. **2020**, *14*.

(75) C.V.Lyza Annamalai, N. Anna Jose, S. T. Biosynthesis and Characterization of Silver and Gold Nanoparticles Using Aqueous Leaf Extraction of Phyllanthus Amarus Schum and Thonn. *World Appl. Sci. J.,* **2011**, No. 13, 1833–1840.

(76) J. Sarkar, S. Ray, D. Chattopadhyay, A. Laskar, K. A. Mycogenesis of Gold Nanoparticles Using a Phytopathogen Alternaria Alternate. *Bioprocess. Biosyst. Eng.* **2012**, No. 35, 637–643.

(77) Houssin, T., Follet, J., Follet, A., Dei-Cas, E., Senez, V. Label-Free Analysis of Water-Polluting Parasite by Electrochemical Impedance Spectroscopy. *Biosens. Bioelectron* **2010**, 5, 1122–1129.https://doi.org/10.1021/acsomega.9b03333.

(78) Nugen, S. R., Asiello, P. J., Connelly, J. T. & Baeumner, A. J. PMMA Biosensor for Nucleic Acids with Integrated Mixer and Electrochemical Detection. *Biosens. Bioelectron* **2009**, 24, 2428–2433.https://doi.org/10.3390/toxins13120870.

(79) Low J, Cheng B, Y. J. Surface Modification and Enhanced Photocatalytic CO2 Reduction Performance of TiO2. *A review J. App. Surf science* **2022**, 392, 658–686.

(80) Chen, Y.N.; Cheng, H.X.; Wang, W.N.; Jin, Z.; Liu, Q.; Yang, H.Y.; Cao, Y.; Li, W.D.; Fakhri, A. Preparation of Carbon Dots-Hematite Quantum Dots-Loaded Hydroxypropyl Cellulose-Chitosan Nanocomposites for Drug Delivery, Sunlight Catalytic and Antimicrobial Application. *J. Photochem. Photobiol* **2021**, 219, 112201.https://doi.org/10.1007/s11356-020-10859-0

(81) Bhuvaneswari, K.; Radha, S.; Sreeja, B. S.; Senthil Kumar, P. Development of In-Situ Electrochemical Heavy Metal Ion Sensor Using Integrated 1D/0D/1D Hybrid by MWCNT and CQDs Supported MnO2 Nanomaterial. *Environ. Res.* **2023**, *225*. 115570. https://doi.org/10.1016/j.envres.2023..

(82) Kumar, D.; Bano, D.; Chandra, S.; Kumar, B.; Kumar, V.; Yadav, P. K.; Hasan, S. H. Highly Sensitive Electrochemical Sensing of Ascorbic Acid (Vitamin C) Using Pd-Doped MnO2 Supported on Carbon Quantum Dots (Pd-MnO2@CQD) in Water and Fruit Juices. *Analytical Sciences* **2025**, 89, 600. https://doi.org/10.1007/s44211-025-00787-9.

(83) Ishaq D. Sulaymon , Adamu Y. Ugya , Hong Cheng Wang, A. W. Environmental Pollution and Their Socioeconomic Impacts. *Woodhead Publishing Series in Food Science, Technology and Nutrition* **2021**, 321–355.https://doi.org/10.1039/d2va00218c.

(84) Pal, M.; Roba Bulcha, M.; Girma Lema, A.; Roba Bulcha, S. Cryptospordiosis: An Infectious Emerging Protozoan Zoonosis of Public Health Significance. *MOJ Biology and Medicine* **2021**, *6*, 161–163. https://doi.org/10.15406/mojbm.2021.06.00150.

(85) Webb, C.; Cabada, M. M. A Review on Prevention Interventions to Decrease Diarrheal Diseases' Burden in Children. *Current Tropical Medicine Reports*. Springer Verlag, **2018**, 88, 31–40. https://doi.org/10.1007/s40475-018-0134-x.

(86) Pal, M.; Shuramo, M. Y.; Gutama, K. P. Cryptosporidiosis: An Emerging Zoonotic Disease of Global Public Health Concern. *International Journal of Medical Parasitology and Epidemiology Sciences*. Aras Part Medical International Press **2021**,23, 73–77. https://doi.org/10.34172/ijmpes.2021.23.

(87) Mac Kenzie, W. R. A Massive Outbreak in Milwaukee of Cryptosporidium Infection Transmitted through the Public Water Supply. *N. Engl. J. Med* **1994**, 331, 161–167. https://doi.org/10.1002/tcr.202000073.

(88) Feng, Y.; Xiao, L. Molecular Epidemiology of Cryptosporidiosis in China. *Front. Microbiol.* **2017**, *8*, 1701. https://doi.org/10.3389/fmicb.2017.01701.

(89) Noaman, E. A.; Nayel, M.; Salama, A.; Mahmoud, M. A.; Adel, M.; El-Kattan; Dawood, A. S.; Abd El-Hamid, I. S.; Elsify, A.; Mousa, W.; Elkhtam, A.; Zaghawa, A. Enteric Protozoal Infections in Camels: Etiology, Epidemiology, and Future Perspectives. *German Journal of Veterinary Research*. German Multidisciplinary Publishing Center **2023**, 46, 1–17. https://doi.org/10.51585/gjvr.2023.1.0046.

(90) Rose, J. B.; Landeen, L. K.; Riley, K. R.; Gerba, C. P. Evaluation of Immunofluorescence Techniques for Detection of Cryptosporidium Oocysts and Giardia Cysts from Environmental Samples. *Appl. Environ. Microbiol.* **1989**, *55*, 3189–3196. https://doi.org/10.1128/aem.55.12.3189-3196.1989.

(91) Morgan-Ryan, A. Morphology Is Not a Reliable Tool for Delineating Species Within Cryptosporidium. *J Parasitol* **2003**, 399–402. https://doi.org/10.3390/ijerph17113782

(92) Brief Communication. **1981**, 7–9.https://doi.org/10.1007/s11356-020-10859-0.

(93) Liu, Z.; Gurlo, T.; von Grafenstein, H. Cell-ELISA Using β-Galactosidase Conjugated Antibodies. *J. Immunol. Methods* **2000**, *234*, 153–167. https://doi.org/10.1016/S0022-1759(99)00216-1.

(94) Regidi, S.; Ravindran, S.; Vijayan, A. L.; Maya, V.; Sreedharan, L.; Varghese, J.; Ramaswami, K.; Gopi, M. Effect of Lyophilization on HRP-Antibody Conjugation: An Enhanced Antibody Labeling Technology. *BMC Res. Notes* **2018**, *11* , 1–6. https://doi.org/10.1186/s13104-018-3688-8.

(95) Sakamoto, S.; Putalun, W.; Vimolmangkang, S.; Phoolcharoen, W.; Shoyama, Y.; Tanaka, H.; Morimoto, S. Enzyme-Linked Immunosorbent Assay for the Quantitative/Qualitative Analysis of Plant Secondary Metabolites. *J. Nat. Med.* **2018**, *72* , 32–42. https://doi.org/10.1007/s11418-017-1144-z.

(96) Grange, R. D.; Thompson, J. P.; Lambert, D. G.; Mahajan, R. P. Radioimmunoassay, Enzyme and Non-Enzyme-Based Immunoassays. *Br. J. Anaesth.* **2014**, *112*, 213–216. https://doi.org/10.1093/bja/aet293.

(97) Nydam, D. V.; Lindergard, G.; Guard, C. L.; Schaaf, S. L.; Wade, S. E.; Mohammed, H. O. Serological Detection of Exposure to Cryptosporidium Parvum in Cattle by ELISA and Its Evaluation in Relation to Coprological Tests. *Parasitol. Res.* **2002**, *88* , 797–803. https://doi.org/10.1007/s00436-002-0665-9.

(98) Razakandrainibe, R.; Mérat, C.; Kapel, N.; Sautour, M.; Guyot, K.; Gargala, G.; Ballet, J. J.; Pape, P. Le; Dalle, F.; Favennec, L. Multicenter Evaluation of an Elisa for the Detection of Cryptosporidium Spp. Antigen in Clinical Human Stool Samples. *Microorganisms* **2021**, *9* , 1–6. https://doi.org/10.3390/microorganisms9020209.

(99) Roellig, D. M.; Yoder, J. S.; Madison-Antenucci, S.; Robinson, T. J.; Van, T. T.; Collier, S. A.; Boxrud, D.; Monson, T.; Bates, L. A.; Blackstock, A. J.; Shea, S.; Larson, K.; Xiao, L.; Beach, M. Community Laboratory Testing for Cryptosporidium: Multicenter Study Retesting Public Health Surveillance Stool Samples Positive for Cryptosporidium by Rapid Cartridge Assay with Direct Fluorescent Antibody Testing. *PLoS One* **2017**, *12*, 1–12. https://doi.org/10.1371/journal.pone.0169915.

(100) van Lieshout, L.; Roestenberg, M. Clinical Consequences of New Diagnostic Tools for Intestinal Parasites. *Clinical Microbiology and Infection*. Elsevier B.V. **2015**, 520–528. https://doi.org/10.1016/j.cmi.2015.03.015.

(101) Destura, R. V.; Cena, R. B.; Galarion, M. J. H.; Pangilinan, C. M.; Arevalo, G. M.; Alba, R. O. C.; Petronio, J. A. G.; Salem, G. M.; Schwem, B.; Sevilleja, J. E. A. D. Advancing Cryptosporidium Diagnostics from Bench to Bedside. *Curr. Trop. Med. Rep.* **2015**, *2*, 150–160. https://doi.org/10.1007/s40475-015-0055-x.

(102) Laxer, M.A.; Timblin, B.K.; Patel, R. J. DNA Sequences for the Specific Detection of Cryptosporidium Parvum by the Polymerase Chain Reaction. *Am. J. Trop. Med. Hyg* **1991**, 45, 688–694.https://doi.org/10.1093/trstmh/trt042.

(103) Mesa, L.E.; Manrique, R.; Muskus, C.; Robledo, S. M. Test Accuracy of Polymerase Chain Reaction Methods against Conventional Diagnostic Techniques for Cutaneous Leishmaniasis (Cl) in Patients with Clinical or Epidemiological Suspicion of Cl. *Systematic review and metaanalysis. PLoS Negl. Trop. Dis.* **2020**, 14, 1–15.

(104) Jothikumar, N.; Da Silva, A. J.; Moura, I.; Qvarnstrom, Y.; Hill, V. R. Detection and Differentiation of Cryptosporidium Hominis and Cryptosporidium Parvum by Dual TaqMan Assays. *J. Med. Microbiol.* **2008**, *57*, 1099–1105. https://doi.org/10.1099/jmm.0.2008/001461-0.

(105) Jothikumar, N.; Da Silva, A.J.; Moura, I.; Qvarnstrom, Y.; Hill, V. R. Detection and Differentiation of Cryptosporidium Hominis and Cryptosporidium Parvum by Dual TaqMan Assays. *J. Med. Microbiol.* **2008**, 57, 109–1105. https://doi.org/10.1007/s40475-015-0055-x.

(106) Hadfield, S. J.; Robinson, G.; Elwin, K.; Chalmers, R. M. Detection and Differentiation of Cryptosporidium Spp. in Human Clinical Samples by Use of Real-Time PCR. *J. Clin. Microbiol.* **2011**, *49*, 918–924. https://doi.org/10.1128/JCM.01733-10.

(107) Liu, Y.; Xiang, J.; Gao, Y.; Wang, J.; Liu, L.; Li, R.; Wang, J. Rapid Detection of Cryptosporidium Spp. in Diarrheic Cattle Feces by Isothermal Recombinase Polymerase Amplification Assays. *Heliyon* **2023**, *9,* e20794. https://doi.org/10.1016/j.heliyon.2023..

(108) Karanis, P.; Thekisoe, O.; Kiouptsi, K.; Ongerth, J.; Igarashi, I.; Inoue, N. Development and Preliminary Evaluation of a Loop-Mediated Isothermal Amplification Procedure for Sensitive Detection of Cryptosporidium Oocysts in Fecal and Water Samples. *Appl. Environ. Microbiol.* **2007**, *73*, 5660–5662. https://doi.org/10.1128/AEM.01152-07.

(109) Mahmoudi, M. R.; Kazemi, B.; Mohammadiha, A.; Mirzaei, A.; Karanis, P. Detection of Cryptosporidium and Giardia (Oo)Cysts by IFA, PCR and LAMP in Surface Water from Rasht, Iran. *Trans. R. Soc. Trop. Med. Hyg.* **2013**, *107* , 511–517. https://doi.org/10.1093/trstmh/trt042.

(110) Karanis, P.; Ongerth, J. LAMP - a Powerful and Flexible Tool for Monitoring Microbial Pathogens. *Trends in Parasitology*. **2009**, 56, 498–499. https://doi.org/10.1016/j.pt.2009.07.010.

(111) Inomata, A.; Kishida, N.; Momoda, T.; Akiba, M.; Izumiyama, S.; Yagita, K.; Endo, T. Development and Evaluation of a Reverse Transcription-Loop-Mediated Isothermal Amplification Assay for Rapid and High-Sensitive Detection of Cryptosporidium in Water Samples. *Water Science and Technology* **2009**, *60*, 2167–2172. https://doi.org/10.2166/wst.2009.599.

(112) koloren, zeynep. LAMP DETECTION of Cryptosporidium SPECIES in SURFACE WATER SAMPLES COLLECTED from RIVER YESILIRMAK and STREAM TERSAKAN (Samsun-Amasya). *ANADOLU UNIVERSITY JOURNAL OF SCIENCE AND TECHNOLOGY –C Life Sciences and Biotechnology* **2017**, *6*, 778. https://doi.org/10.18036/aubtdc.269434.

(113) Mahmudunnabi, R. G.; Pannu, A. S.; Nguyen, N. T.; Stratton, H. M.; Shiddiky, M. J. A. Avoiding Commercial Kit-Based DNA Isolation and Purification Steps: A Rapid Method for Cryptosporidium Oocyst Detection. *Sensors and Diagnostics* **2025**, *4* , 229–238. https://doi.org/10.1039/d4sd00344f.

(114) Destura, R. V.; Cena, R. B.; Galarion, M. J. H.; Pangilinan, C. M.; Arevalo, G. M.; Alba, R. O. C.; Petronio, J. A. G.; Salem, G. M.; Schwem, B.; Sevilleja, J. E. A. D. Advancing Cryptosporidium Diagnostics from Bench to Bedside. *Current Tropical Medicine Reports*. Springer Verlag , **2015,** 67, 150–160. https://doi.org/10.1007/s40475-015-0055-x.

(115) Assessment of Some Heavy Metals in Selected Vegetables, Fruits and Their Respective Soil. *Journal of Applied and Emerging Sciences* **2020**, 70–74. https://doi.org/10.36785/buitems.jaes.376.

(116) Türkmen, M.; Türkmen, A.; Tepe, Y.; Töre, Y.; Ateş, A. Determination of Metals in Fish Species from Aegean and Mediterranean Seas. *Food Chem.* **2009**, *113*, 233–237. https://doi.org/10.1016/j.foodchem.2008.06.071.

(117) Türkmen, M.; Türkmen, A.; Tepe, Y.; Töre, Y.; Ateş, A. Determination of Metals in Fish Species from Aegean and Mediterranean Seas. *Food Chem.* **2009**, *113*, 233–237. https://doi.org/10.1016/j.foodchem.2008.06.071.

(118) Liang, S. Y.; Chan, Y. H.; Hsia, K. T.; Lee, J. L.; Kuo, M. C.; Hwa, K. Y.; Chan, C. W.; Chiang, T. Y.; Chen, J. S.; Wu, F. T.; Ji, D. Der. Development of Loop-Mediated Isothermal Amplification Assay for Detection of Entamoeba Histolytica. *J. Clin. Microbiol.* **2009**, *47*, 1892–1895. https://doi.org/10.1128/JCM.00105-09.

(119) Martinez-Finley, E. J.; Chakraborty, S.; Fretham, S. J. B.; Aschner, M. Cellular Transport and Homeostasis of Essential and Nonessential Metals. In *Metallomics*; Royal Society of Chemistry, **2012**; 4, 593–605. https://doi.org/10.1039/c2mt00185c.

(120) Türkmen, M.; Türkmen, A.; Tepe, Y.; Töre, Y.; Ateş, A. Determination of Metals in Fish Species from Aegean and Mediterranean Seas. *Food Chem.* **2009**, *113*, 233–237. https://doi.org/10.1016/j.foodchem.2008.06.071.

(121) Seleem, E. M.; Mostafa, A.; Mokhtar, M.; Salman, S. A. Risk Assessment of Heavy Metals in Drinking Water on the Human Health, Assiut City, and Its Environs, Egypt. **2022**, 89, 778-800. https://doi.org/10.1007/s12517-021-06784-2/Published.

(122) Orzoł, A.; Gołębiowski, A.; Szultka-Młyńska, M.; Głowacka, K.; Pomastowski, P.; Buszewski, B. ICP-MS Analysis of Cadmium Bioaccumulation and Its Effect on Pea Plants (Pisum Sativum L.). *Pol. J. Environ. Stud.* **2022**, *31*, 4779–4787. https://doi.org/10.15244/pjoes/149259.

(123) Radziemska, M.; Wyszkowski, M.; Bęś, A.; Mazur, Z.; Jeznach, J.; Brtnický, M. The Applicability of Compost, Zeolite and Calcium Oxide in Assisted Remediation of Acidic Soil Contaminated with Cr(III) and Cr(VI). *Environmental Science and Pollution Research* **2019**, *26*, 21351–21362. https://doi.org/10.1007/s11356-019-05221-y.

(124) Stewart, P. W.; Reihman, J.; Lonky, E. I.; Darvill, T. J.; Pagano, J. Cognitive Development in Preschool Children Prenatally Exposed to PCBs and MeHg. *Neurotoxicol. Teratol.* **2003**, *25*, 11–22. https://doi.org/10.1016/S0892-0362(02)00320-3.

(125) Budtz-Jørgensen, E.; Grandjean, P.; Jørgensen, P. J.; Weihe, P.; Keiding, N. Association between Mercury Concentrations in Blood and Hair in Methylmercury-Exposed

Subjects at Different Ages. In *Environmental Research*; **2004**; 95, 385–393. https://doi.org/10.1016/j.envres.2003.11.001.

(126) Patel, N. B.; Xu, Y.; McCandless, L. C.; Chen, A.; Yolton, K.; Braun, J.; Jones, R. L.; Dietrich, K. N.; Lanphear, B. P. Very Low-Level Prenatal Mercury Exposure and Behaviors in Children: The HOME Study. *Environ. Health* **2019**, *18*, 799. https://doi.org/10.1186/s12940-018-0443-5.

(127) Kumar, A.; Cabral-Pinto, M.; Kumar, A.; Kumar, M.; Dinis, P. A. Estimation of Risk to the Eco-Environment and Human Health of Using Heavy Metals in the Uttarakhand Himalaya, India. *Applied Sciences (Switzerland)* **2020**, *10*, 1–18. https://doi.org/10.3390/app10207078.

(128) Jabariyan, S.; Zanjanchi, M. A. Colorimetric Detection of Cadmium Ions Using Modified Silver Nanoparticles. *Appl. Phys. A Mater. Sci. Process.* **2019**, *125*, 1211. https://doi.org/10.1007/s00339-019-3167-7.

(129) Genchi, G.; Sinicropi, M. S.; Lauria, G.; Carocci, A.; Catalano, A. The Effects of Cadmium Toxicity. *International Journal of Environmental Research and Public Health*. MDPI AG June 1, 2020. https://doi.org/10.3390/ijerph17113782.

(130) Li, Y.; Zhou, M.; Waterhouse, G. I. N.; Sun, J.; Shi, W.; Ai, S. Efficient Removal of Cadmium Ions from Water by Adsorption on a Magnetic Carbon Aerogel. *Environmental Science and Pollution Research* **2021**, *28*, 5149–5157. https://doi.org/10.1007/s11356-020-10859-0.

(131) Dincer, C.; Bruch, R.; Costa-Rama, E.; Fernández-Abedul, M. T.; Merkoçi, A.; Manz, A.; Urban, G. A.; Güder, F. Disposable Sensors in Diagnostics, Food, and Environmental Monitoring. *Advanced Materials*. Wiley-VCH Verlag **2019**, 76, 998. https://doi.org/10.1002/adma.201806739.

(132) Razakandrainibe, R.; Mérat, C.; Kapel, N.; Sautour, M.; Guyot, K.; Gargala, G.; Ballet, J. J.; Pape, P. Le; Dalle, F.; Favennec, L. Multicenter Evaluation of an Elisa for the Detection of Cryptosporidium Spp. Antigen in Clinical Human Stool Samples. *Microorganisms* **2021**, *9* , 1–6. https://doi.org/10.3390/microorganisms9020209.

(133) Irvine, G. W.; Tan, S. N.; Stillman, M. J. A Simple Metallothionein-Based Biosensor for Enhanced Detection of Arsenic and Mercury. *Biosensors (Basel).* **2017**, *7*, 34546. https://doi.org/10.3390/bios7010014.

(134) Raril, C.; Manjunatha, J. G. Fabrication of Novel Polymer-Modified Graphene-Based Electrochemical Sensor for the Determination of Mercury and Lead Ions in Water and Biological Samples. *J. Anal. Sci. Technol.* **2020**, *11*, 889. https://doi.org/10.1186/s40543-019-0194-0.

(135) Obiora, S. C.; Chukwu, A.; Davies, T. C. Contamination of the Potable Water Supply in the Lead–Zinc Mining Communities of Enyigba, Southeastern Nigeria. *Mine Water Environ.* **2019**, *38*, 148–157. https://doi.org/10.1007/s10230-018-0550-0.

(136) Obiora, S. C.; Chukwu, A.; Davies, T. C. Contamination of the Potable Water Supply in the Lead–Zinc Mining Communities of Enyigba, Southeastern Nigeria. *Mine Water Environ.* **2019**, *38*, 148–157. https://doi.org/10.1007/s10230-018-0550-0.

(137) Zhang, D.; Crini, G.; Lichtfouse, E.; Rhimi, B.; Wang, C. Removal of Mercury Ions from Aqueous Solutions by Crosslinked Chitosan-Based Adsorbents: A Mini Review. *Chemical Record* **2020**, *20*, 1220–1234. https://doi.org/10.1002/tcr.202000073.

(138) Malik, L. A.; Bashir, A.; Qureashi, A.; Pandith, A. H. Detection and Removal of Heavy Metal Ions: A Review. *Environmental Chemistry Letters*. Springer Verlag **2019**, 67, 1495–1521. https://doi.org/10.1007/s10311-019-00891-z.

(139) Zamora-Ledezma, C.; Negrete-Bolagay, D.; Figueroa, F.; Zamora-Ledezma, E.; Ni, M.; Alexis, F.; Guerrero, V. H. Heavy Metal Water Pollution: A Fresh Look about Hazards, Novel and Conventional Remediation Methods. *Environmental Technology and Innovation*. Elsevier B.V. **2021**, 221, 101504. https://doi.org/10.1016/j.eti.2021..

(140) Singh, V.; Ahmed, G.; Vedika, S.; Kumar, P.; Chaturvedi, S. K.; Rai, S. N.; Vamanu, E.; Kumar, A. Toxic Heavy Metal Ions Contamination in Water and Their Sustainable Reduction by Eco-Friendly Methods: Isotherms, Thermodynamics and Kinetics Study. *Sci. Rep.* **2024**, *14* . https://doi.org/10.1038/s41598-024-58061-3.

(141) Alexander, D.; Rohman, A. Analytical Method Validation of Icp-Aes for Analysis of Cadmium, Chromium, Cuprum, Mangan and Nickel in Milk. *International Journal of Applied Pharmaceutics* **2019**, *11* (4), 341–344. https://doi.org/10.22159/ijap.2019v11i4.29503.

(142) Alice, K. S. *DETERMINATION OF ARSENIC CONCENTRATION AND CONTAMINATION FACTOR IN WATER FROM SELECTED BOREHOLES IN NAIROBI CITY COUNTY, KENYA*; 2022.

(143) Zamfir, L. G.; Puiu, M.; Bala, C. Advances in Electrochemical Impedance Spectroscopy Detection of Endocrine Disruptors. *Sensors (Switzerland)*. MDPI AG November 2, 2020, pp 1–21. https://doi.org/10.3390/s20226443.

(144) Picard-Lafond, A.; Larivière, D.; Boudreau, D. Revealing the Hydrolysis Mechanism of a Hg2+-Reactive Fluorescein Probe: Novel Insights on Thionocarbonated Dyes. *ACS Omega* **2020**, *5* (1), 701–711. https://doi.org/10.1021/acsomega.9b03333.

(145) *Environmental Pollution Governance and Ecological Remediation Technology*; Zhang, J., Ruan, R., Bashir, M. J. K., Eds.; Environmental Science and Engineering; Springer International Publishing: Cham, 2023. https://doi.org/10.1007/978-3-031-25284-6.

(146) Omeje, K. O.; Ezema, B. O.; Okonkwo, F.; Onyishi, N. C.; Ozioko, J.; Rasaq, W. A.; Sardo, G.; Okpala, C. O. R. Quantification of Heavy Metals and Pesticide Residues in Widely Consumed Nigerian Food Crops Using Atomic Absorption Spectroscopy (Aas) and Gas Chromatography (Gc). *Toxins (Basel).* **2021**, *13* (12). https://doi.org/10.3390/toxins13120870.

(147) Poudel, A.; Shyam Sunder, G. S.; Rohanifar, A.; Adhikari, S.; Kirchhoff, J. R. Electrochemical Determination of Pb2+ and Cd2+ with a Poly(Pyrrole-1-Carboxylic Acid) Modified Electrode. *Journal of Electroanalytical Chemistry* **2022**, *911*. https://doi.org/10.1016/j.jelechem.2022.116221.

(148) Nguyen et Al.

(149) Sargazi, S.; Fatima, I.; Hassan Kiani, M.; Mohammadzadeh, V.; Arshad, R.; Bilal, M.; Rahdar, A.; Díez-Pascual, A. M.; Behzadmehr, R. Fluorescent-Based Nanosensors for Selective Detection of a Wide Range of Biological Macromolecules: A Comprehensive Review. *International Journal of Biological Macromolecules*. Elsevier B.V. May 1, 2022, pp 115–147. https://doi.org/10.1016/j.ijbiomac.2022.02.137.

(150) Farnsworth, P. B.; Spencer, R. L. Ion Sampling and Transport in ICP-MS. *Spectrochimica Acta - Part B Atomic Spectroscopy*. Elsevier B.V. August 1, 2017, pp 105–122. https://doi.org/10.1016/j.sab.2017.06.009.

(151) Al-Hakkani, M. F. Guideline of Inductively Coupled Plasma Mass Spectrometry "ICP–MS": Fundamentals, Practices, Determination of the Limits, Quality Control, and Method Validation Parameters. *SN Applied Sciences*. Springer Nature July 1, 2019. https://doi.org/10.1007/s42452-019-0825-5.

(152) Wilschefski, S. C.; Baxter, M. R. Inductively Coupled Plasma Mass Spectrometry: Introduction to Analytical Aspects. *Clinical Biochemist Reviews* **2019**, *40* (3), 115–133. https://doi.org/10.33176/AACB-19-00024.

(153) Saravanan, P.; Saravanan, V.; Rajeshkannan, R.; Arnica, G.; Rajasimman, M.; Baskar, G.; Pugazhendhi, A. Comprehensive Review on Toxic Heavy Metals in the Aquatic System: Sources, Identification, Treatment Strategies, and Health Risk Assessment. *Environmental Research*. Academic Press Inc. October 1, 2024. https://doi.org/10.1016/j.envres.2024.119440.

(154) Ahmed, A.; Singh, A.; Padha, B.; Sundramoorthy, A. K.; Tomar, A.; Arya, S. UV–Vis Spectroscopic Method for Detection and Removal of Heavy Metal Ions in Water Using Ag Doped ZnO Nanoparticles. *Chemosphere* **2022**, *303*. https://doi.org/10.1016/j.chemosphere.2022.135208.

(155) O'Sullivan, J. E.; Watson, R. J.; Butler, E. C. V. An ICP-MS Procedure to Determine Cd, Co, Cu, Ni, Pb and Zn in Oceanic Waters Using in-Line Flow-Injection with Solid-Phase

Extraction for Preconcentration. *Talanta* **2013**, *115*, 999–1010. https://doi.org/10.1016/j.talanta.2013.06.054.

(156) PhD, A. A. E. Chapter 1 - An Introduction to Sensors and Biosensors. *Electrochemical Biosensors* **2019**, No. 7, 1–10.

(157) Ensafi, A. A.; Karimi-Maleh, H.; Ghiaci, M.; Arshadi, M. Characterization of Mn-Nanoparticles Decorated Organo-Functionalized SiO2-Al2O3 Mixed-Oxide as a Novel Electrochemical Sensor: Application for the Voltammetric Determination of Captopril. *J. Mater. Chem.* **2011**, *21* (38), 15022–15030. https://doi.org/10.1039/c1jm11909e.

(158) Dincer, C.; Bruch, R.; Costa-Rama, E.; Fernández-Abedul, M. T.; Merkoçi, A.; Manz, A.; Urban, G. A.; Güder, F. Disposable Sensors in Diagnostics, Food, and Environmental Monitoring. *Advanced Materials* **2019**, *31* (30). https://doi.org/10.1002/adma.201806739.

(159) Neeraj Dilbaghi, E. L. Nanosensors for Environmental Applications. *https://link.springer.com/oscar-static/images/darwin/header/img/logo-springer-nature-link-3149409f62.svg* **2020**.

(160) Zhai, Z.; Leng, B.; Yang, N.; Yang, B.; Liu, L.; Huang, N. Rational Construction of 3D-Networked Carbon Nanowalls / Diamond Supporting CuO Architecture for High-Performance Electrochemical Biosensors. **2019**, *1901527* (9), 1–11. https://doi.org/10.1002/smll.201901527.

(161) Yang, H. Enzyme-Based Ultrasensitive Electrochemical Biosensors. *Curr. Opin. Chem. Biol.* **2012**, *16* (3–4), 422–428. https://doi.org/10.1016/j.cbpa.2012.03.015.

(162) Xiang, C.; Li, R.; Adhikari, B.; She, Z.; Li, Y. Talanta Sensitive Electrochemical Detection of Salmonella with Chitosan – Gold Nanoparticles Composite Fi Lm. *Talanta* **2015**, *140*, 122–127. https://doi.org/10.1016/j.talanta.2015.03.033.

(163) Contreras Jiménez, G.; Eissa, S.; Ng, A.; Alhadrami, H.; Zourob, M.; Siaj, M. Aptamer-Based Label-Free Impedimetric Biosensor for Detection of Progesterone. *Anal. Chem.* **2015**, *87* (2), 1075–1082. https://doi.org/10.1021/ac503639s.

(164) Lin, L. P.; Tan, M. T. T. Biosensors for the Detection of Lung Cancer Biomarkers: A Review on Biomarkers, Transducing Techniques and Recent Graphene-Based Implementations. *Biosensors and Bioelectronics*. Elsevier Ltd October 1, 2023. https://doi.org/10.1016/j.bios.2023.115492.

(165) Ahmed, A.; Rushworth, J. V.; Hirst, N. A.; Millner, P. A. Biosensors for Whole-Cell Bacterial Detection. *Clin. Microbiol. Rev.* **2014**, *27* (3), 631–646. https://doi.org/10.1128/CMR.00120-13.

(166) Frías, I. A. M.; Avelino, K. Y. P. S.; Silva, R. R.; Andrade, C. A. S.; Oliveira, M. D. L. Trends in Biosensors for HPV: Identification and Diagnosis. *J. Sens.* **2015**, *2015*. https://doi.org/10.1155/2015/913640.

(167) Wu, J.; Fu, Z.; Yan, F.; Ju, H. Biomedical and Clinical Applications of Immunoassays and Immunosensors for Tumor Markers. *TrAC - Trends in Analytical Chemistry* **2007**, *26* (7), 679–688. https://doi.org/10.1016/j.trac.2007.05.007.

(168) Mattiasson, B.; Ertürk, G. Why Using Molecularly Imprinted Polymers in Connection to Biosensors? *Sensors (Switzerland)* **2017**, *17* (2), 1–5. https://doi.org/10.3390/s17020246.

(169) Rodriguez-Mozaz, S.; Lopez De Alda, M. J.; Barceló, D. Biosensors as Useful Tools for Environmental Analysis and Monitoring. *Anal. Bioanal. Chem.* **2006**, *386* (4), 1025–1041. https://doi.org/10.1007/s00216-006-0574-3.

(170) A.P.F, T. Biosensors–Sense and Sensitivity. *Science (1979).* **2021**, No. 290, 1315–1317.

(171) Gerion, Daniele, and G.-J. D. . "PROTEIN CHARACTERIZATION Label-Free and Labeled Technology for Protein Characterization and Localized Surface Plasmon Resonance (LSPR) Permits Label-Free Protein Quantitation at the Ng/ML Level, and with Labels, Can Achieve Sensitivities Greater than p. *Biopharm Int.* **2010**.

(172) Hong, Y.; Ku, M.; Lee, E.; Suh, J.-S.; Huh, Y.-M.; Yoon, D. S.; Yang, J. Localized Surface Plasmon Resonance Based Nanobiosensor for Biomarker Detection of Invasive Cancer Cells. *J. Biomed. Opt.* **2013**, *19* (5), 051202. https://doi.org/10.1117/1.jbo.19.5.051202.

(173) Chen, B.; Zhou, X.; Li, C.; Wang, Q.; Liu, D.; Lin, B. Rapid Screening of Phenylketonuria Using a CD Microfluidic Device. *J. Chromatogr. A* **2011**, *1218* (14), 1907–1912. https://doi.org/10.1016/j.chroma.2011.02.001.

(174) Yang, L.; Shi, P.; Huang, S.; Silva, D. DE; Fisher, R.; Radford, B.; Thompson, H.; Mcgree, J. THE ANNALS of APPLIED STATISTICS Articles A Copula Model for Marked Point Process with a Terminal Event: An Application in Dynamic Prediction of Insurance Claims Model-Robust Bayesian Design through Generalised Additive Models for Monitoring Submerged Shoals. *AN OFFICIAL JOURNAL OF THE INSTITUTE OF MATHEMATICAL STATISTICS* **2024**, *18* (4).

(175) Nigam, V. K.; Shukla, P. Enzyme Based Biosensors for Detection of Environmental Pollutants-A Review. *Journal of Microbiology and Biotechnology*. Korean Society for Microbiolog and Biotechnology **2015**, 1773–1781. https://doi.org/10.4014/jmb.1504.04010.

(176) Hara, T. O.; Singh, B. Electrochemical Biosensors for Detection of Pesticides and Heavy Metal Toxicants in Water: Recent Trends and Progress. *ACS Environmental Science and*

Technology Water. American Chemical Society **2021**, 78,462–478. https://doi.org/10.1021/acsestwater.0c00125.

(177) Rebollar-Pérez, G.; Campos-Terán, J.; Ornelas-Soto, N.; Méndez-Albores, A.; Torres, E. Biosensors Based on Oxidative Enzymes for Detection of Environmental Pollutants. *Biocatalysis* **2016**, *1*, 2010. https://doi.org/10.1515/boca-2015-0010.

(178) Chadha, U.; Bhardwaj, P.; Agarwal, R.; Rawat, P.; Agarwal, R.; Gupta, I.; Panjwani, M.; Singh, S.; Ahuja, C.; Selvaraj, S. K.; Banavoth, M.; Sonar, P.; Badoni, B.; Chakravorty, A. Recent Progress and Growth in Biosensors Technology: A Critical Review. *Journal of Industrial and Engineering Chemistry*. Korean Society of Industrial Engineering Chemistry **2022**, 10, 21–51. https://doi.org/10.1016/j.jiec.2022.02.010.

(179) Chinnasamy Thiruppathiraja 1, V. S. S. K. P. A. M. A. Development of Electrochemical Based Sandwich Enzyme Linked Immunosensor for Cryptosporidium Parvum Detection in Drinking Water. *J Environ Monit* **2011**, *13*, 83–90. https://doi.org/10.1016/j.cmi.2015.03.015.

(180) Felix, F. S.; Angnes, L. Electrochemical Immunosensors – A Powerful Tool for Analytical Applications. *Biosensors and Bioelectronics*. Elsevier **2018**,29, 470–478. https://doi.org/10.1016/j.bios.2017.11.029.

(181) Omidfar, K.; Khorsand, F.; Darziani Azizi, M. New Analytical Applications of Gold Nanoparticles as Label in Antibody Based Sensors. *Biosensors and Bioelectronics* **2013**, 5, 336–347. https://doi.org/10.1016/j.bios.2012.12.045.

(182) Saxena, K.; Kumar, A.; Chauhan, N.; Khanuja, M.; Malhotra, B. D.; Jain, U. Electrochemical Immunosensor for Detection of H. Pylori Secretory Protein VacA on g-C3N4/ZnO Nanocomposite-Modified Au Electrode. *ACS Omega* **2022**, *7* , 32292–32301. https://doi.org/10.1021/acsomega.2c03627.

(183) Tschmelak, J.; Proll, G.; Riedt, J.; Kaiser, JBiosensors for Unattended, Cost-Effective and Continuous Monitoring of Environmental Pollution: Automated Water Analyser Computer Supported System (AWACSS) and River Analyser (RIANA). *Int. J. Environ. Anal. Chem.* **2005**, *85*, 837–852. https://doi.org/10.1080/03067310500149619.

(184) Fang, L.; Liao, X.; Jia, B.; Shi, L.; Kang, L.; Zhou, L.; Kong, W. Recent Progress in Immunosensors for Pesticides. *Biosensors and Bioelectronics*. Elsevier Ltd September 15, 2020. https://doi.org/10.1016/j.bios.2020.112255.

(185) Yi Li, F. D. T. H. G. V. E. M. G. CRISPR/Cas12a-Powered Immunosensor Suitable for Ultra-Sensitive Whole Cryptosporidium Oocyst Detection from Water Samples Using a Plate Reader. *National center for biotechnology information* **2021**, 117–120.https://doi.org/10.1128/CMR.00120-13.

(186) Luka, G. S.; Najjaran, H.; Hoorfar, M. On-Chip-Based Electrochemical Biosensor for the Sensitive and Label-Free Detection of Cryptosporidium. *Sci. Rep.* **2022**, *12*, 69908. https://doi.org/10.1038/s41598-022-10765-0.

(187) Siwak, A. M.; Baker, P. G.; Dube, A. Biosensors as Early Warning Detection Systems for Waterborne Cryptosporidium. *Water Science and Technology* **2023**, *88*, 615–630. https://doi.org/10.2166/wst.2023.229.

(188) Hu, S.; Zhang, S.; Qin, J.; Cai, K.; Peng, C.; Luo, L.; Gu, Y.; Mei, Y. Simultaneous Determination of Lead and Cadmium in Water by Metal Oxide Framework Complex-Modified Glassy Carbon Electrodes. *Microchemical Journal* **2024**, *205*. 111154, https://doi.org/10.1016/j.microc.2024..

(189) Nodoushan, S. M.; Nasirizadeh, N.; Sedighian, H.; Kachuei, R.; Azimzadeh-Taft, M.; Fooladi, A. A. I. Detection of Staphylococcal Enterotoxin A (SEA) Using a Sensitive Nanomaterial-Based Electrochemical Aptasensor. *Diam. Relat. Mater.* **2022**, *127*. 109042. https://doi.org/10.1016/j.diamond.2022..

(190) Fallah, A.; Imani Fooladi, A. A.; Havaei, S. A.; Mahboobi, M.; Sedighian, H. Recent Advances in Aptamer Discovery, Modification and Improving Performance. *Biochemistry and Biophysics Reports*. Elsevier B.V. **2024**, 123, 101852. https://doi.org/10.1016/j.bbrep.2024..

(191) Tuerk, C.; Gold, L. *Systematic Evolution of Ligands by Exponential Enrichment: RNA Ligands to Bacteriophage T4 DNA Polymerase*. https://www.science.org.

(192) Orzoł, A.; Gołębiowski, A.; Szultka-Młyńska, M.; Głowacka, K.; Pomastowski, P.; Buszewski, B. ICP-MS Analysis of Cadmium Bioaccumulation and Its Effect on Pea Plants (Pisum Sativum L.). *Pol J Environ Stud* **2022**, *31*, 4779–4787. https://doi.org/10.15244/pjoes/149259.

(193) Angus, S. V.; Kwon, H. J.; Yoon, J. Y. Field-Deployable and near-Real-Time Optical Microfluidic Biosensors for Single-Oocyst-Level Detection of Cryptosporidium Parvum from Field Water Samples. *Journal of Environmental Monitoring* **2012**, *14*, 3295–3304. https://doi.org/10.1039/c2em30700f.

(194) Liu, Y.; Zhang, D.; Ding, J.; Hayat, K.; Yang, X.; Zhan, X.; Zhang, D.; Lu, Y.; Zhou, P. Label-Free and Sensitive Determination of Cadmium Ions Using a Ti-Modified Co3 O4-Based Electrochemical Aptasensor. *Biosensors (Basel).* **2020**, *10*, 195. https://doi.org/10.3390/BIOS10120195.

(195) Zaras, I.; Kralka, E.; Olszewski, M.; Jarczewska, M. A Label-Free Electrochemical Detection of Cadmium Ions Using Aptamer-Based Biosensor. *J. Electrochem. Soc.* **2024**, *171* , 117510. https://doi.org/10.1149/1945-7111/ad8d13.

(196) Li, M.; He, B.; Yan, H.; Xie, L.; Cao, X.; Jin, H.; Wei, M.; Ren, W.; Suo, Z.; Xu, Y. An Aptasensor for Cadmium Ions Detection Based on PEI-MoS2@Au NPs 3D Flower-like Nanocomposites and Thi-PtPd NPs Core-Shell Sphere. *Anal. Chim. Acta* **2022**, *1232*. https://doi.org/10.1016/j.aca.2022.340470.

(197) Mushiana, T.; Mabuba, N.; Idris, A. O.; Peleyeju, G. M.; Orimolade, B. O.; Nkosi, D.; Ajayi, R. F.; Arotiba, O. A. An Aptasensor for Arsenic on a Carbon-gold Bi-Nanoparticle Platform. *Sens. Biosensing Res.* **2019**, *24,* 100280. https://doi.org/10.1016/j.sbsr.2019..

(198) Saravanan, P.; Saravanan, V.; Rajeshkannan, R.; Arnica, G.; Rajasimman, M.; Baskar, G.; Pugazhendhi, A. Comprehensive Review on Toxic Heavy Metals in the Aquatic System: Sources, Identification, Treatment Strategies, and Health Risk Assessment. *Environmental Research*. Academic Press Inc. **2024**. 119440, https://doi.org/10.1016/j.envres.2024..

(199) Karimi-Maleh, H.; Zhang, Z.; Zare, N.; Karaman, O.; Wen, Y.; Wu, T.; Zhong, N.; Fu, L. A Novel Disposable Dual-Sensing Platform Based on DNA-Aptamer Amplified with Gold Nanoparticles/Nb4C3-MXene for Simultaneous Detection of Lead and Cadmium. *Adv. Compos. Hybrid Mater.* **2025**, *8*, 1116. https://doi.org/10.1007/s42114-025-01216-1.

(200) Malik, S.; Singh, J.; Goyat, R.; Saharan, Y.; Chaudhry, V.; Umar, A.; Ibrahim, A. A.; Akbar, S.; Ameen, S.; Baskoutas, S. Nanomaterials-Based Biosensor and Their Applications: A Review. *Heliyon* **2023**, *9* , e19929. https://doi.org/10.1016/j.heliyon.2023.e19929.

(201) Besha, A.T., Liu, Y., Fang, C., Bekele, D.N., Naidu, R. Assessing the Interactions between Micropollutants and Nanoparticles in Engineered and Natural Aquatic Environments. *Environ. Sci. Technol* **2020**, 50, 135–215. https://doi.org/10.1016/j.jhazmat.2011.12.033.

(202) Khan, I., Saeed, K., Khan, I. Nanoparticles: Properties, Applications and Toxicities. *Arabian J. Inside Chem.* **2019**, *7*, 908–931.https://doi.org/10.1007/s00128-020-03088-1.

(203) Mondal, S. Potential of Nanotechnology for Rural Applications. *Arab. J. Sci. Eng.* **2020**, *7* , 5011–5042. https://doi.org/10.1086/652140.

(204) Hernandez-Vargas , G. , Sosa-Hernández , J.E. , Saldarriaga-Hernandez, S. et al. Electrochemical Biosensors: A Solution to Pollution Detection with Reference to Environmental Contaminants. *Biosensors (Basel).* **2018**, No. 8, 29.

(205) Abdul G . *Nanomaterials in Environmental Sensors*; **2024**, 23, 667. https://doi.org/10.1016/j.teac.2021.e00139.

(206) T. Masciangioli, W. X. Z. Environmental Technologies at the Nanoscale, Environ. *Sci. Technol* **2020**, *37*, 102–108. https://doi.org/10.1038/s41598-024-64797-9.

(207) Kharey, P.; Dutta, S. B.; Sarkar, S.; Rao, B. N.; Satyanarayana, N. Research on Green Synthetic Iron Nanoparticles Research on Green Synthetic Iron Nanoparticles. **2020**, 34, 567. https://doi.org/10.1088/1757-899X/612/2/022025.

(208) P. Biswas, M.M. Hasan, D. Dey, A.C. Dos Santos Costa, S.A. Polash, S. B.; N. Ferdous, M.A. Kaium, M.D.H. Rahman, F.K. Jeet, et al. Amentoflavone Derivatives Significantly Act towards the Main Protease (3CLPRO/MPRO) of SARS-CoV-2: In Silico Admet Profiling, Molecular Docking, Molecular Dynamics Simulation, Network Pharmacology. *Candidate antiviral drugs for COVID-19 and their environmental implications: a comprehensive analysis* **2021**, 79, 668. https://doi.org/10.1016/j.checat.2022.09.005.

(209) Sourav Ghosh, K Martin Sagayam, Dibyajyoti Haldar, A Amir Anton Jone, Biswaranjan Acharya, V. C. G. and A. K. A Review on the Types of Nanomaterials and Methodologies Used for the Development of Biosensors. *Advances in Natural Sciences: Nanoscience and Nanotechnology* **2024**, *15* , 2043–6262. https://doi.org/10.1016/j.cej.2019.122111.

(210) Can, M. Green Gold Nanoparticles from Plant-Derived Materials : An Overview of the Reaction Synthesis Types , Conditions , and Applications. **2020**, *36*, 859–877. https://doi.org/10.1021/acsomega.0c00707.

(211) Islam, M. S.; Elahee, G. M. F.; Fang, Y.; Yu, X. (Bill); Advincula, R. C.; Cao, C. (Chase). Polylactic Acid (PLA)-Based Multifunctional and Biodegradable Nanocomposites and Their Applications. *Composites Part B: Engineering*. Elsevier **2025**,23, 567. https://doi.org/10.1016/j.compositesb.2025.112842.

(212) Liu, Z.; Zou, H.; Wang, N.; Yang, T.; Peng, Z.; Wang, J.; Li, N.; Huang, C. Photoluminescence of Carbon Quantum Dots : Coarsely Adjusted by Quantum Confinement Effects and Finely by Surface Trap States. **2018**, *61* , 490–496.https://doi.org/10.1016/j.vibspec.2016.02.004.

(213) Đorđević, L.; Arcudi, F.; Cacioppo, M.; Prato, M. Carbon Dots for Biomedical and Energy Applications ' C. **2022**, *17*, 456. https://doi.org/10.1038/s41565-021-01051-7.

(214) Debnath, R.; Ikbal, A. M. A.; Ravi, N. K.; Kargarzadeh, H.; Palit, P.; Thomas, S. Carbon Nanodots-Based Polymer Nanocomposite: A Potential Drug Delivery Armament of Phytopharmaceuticals. *Polymers*. Multidisciplinary Digital Publishing Institute (MDPI) **2025**, 56, 890. https://doi.org/10.3390/polym17030365.

(215) Sousa, H. B. A.; Martins, C. S. M.; Prior, J. A. V. You Don't Learn That in School: An Updated Practical Guide to Carbon Quantum Dots. *Nanomaterials* **2021**, *11*, 1–88. https://doi.org/10.3390/nano11030611.

(216) Boakye-Yiadom, K. O.; Kesse, S.; Opoku-Damoah, Y.; Filli, M. S.; Aquib, M.; Joelle, M. M. B.; Farooq, M. A.; Mavlyanova, R.; Raza, F.; Bavi, R.; Wang, B. Carbon Dots:

Applications in Bioimaging and Theranostics. *Int. J. Pharm.* **2019**, *564*, 308–317. https://doi.org/10.1016/j.ijpharm.2019.04.055.

(217) Yuan, F.; Li, S.; Fan, Z.; Meng, X.; Fan, L.; Yang, S. Shining Carbon Dots: Synthesis and Biomedical and Optoelectronic Applications. *Nano Today* **2016**, *11* , 565–586. https://doi.org/10.1016/j.nantod.2016.08.006.

(218) Shen, C. L.; Liu, H. R.; Lou, Q.; Wang, F.; Liu, K. K.; Dong, L.; Shan, C. X. Recent Progress of Carbon Dots in Targeted Bioimaging and Cancer Therapy. *Theranostics* **2022**, *12*, 2860–2893. https://doi.org/10.7150/thno.70721.

(219) Pourmadadi, M.; Rahmani, E.; Rajabzadeh-Khosroshahi, M.; Samadi, A.; Behzadmehr, R.; Rahdar, A.; Ferreira, L. F. R. Properties and Application of Carbon Quantum Dots (CQDs) in Biosensors for Disease Detection: A Comprehensive Review. *J. Drug Deliv. Sci. Technol.* **2023**, *80*, 104156. https://doi.org/10.1016/j.jddst.2023.104156.

(220) Papaioannou, N.; Titirici, M. M.; Sapelkin, A. Investigating the Effect of Reaction Time on Carbon Dot Formation, Structure, and Optical Properties. *ACS Omega* **2019**, *4*, 21658–21665. https://doi.org/10.1021/acsomega.9b01798.

(221) Wang, B.; Yu, J.; Sui, L.; Zhu, S.; Tang, Z.; Yang, B.; Lu, S. Rational Design of Multi-Color-Emissive Carbon Dots in a Single Reaction System by Hydrothermal. *Advanced Science* **2021**, *8*, 1–8. https://doi.org/10.1002/advs.202001453.

(222) Neeraj Tejwan , Subbroto Kumar Saha, J. Das. Multifaceted Applications of Green Carbon Dots Synthesized from Renewable Sources. *Science, Advances in Colloid and Interface* **2020**, 58, 102046. https://doi.org/10.1366/11-06455.

(223) Chandran, P.; Ghosh, A.; Ramaprabhu, S. High-Performance Platinum-Free Oxygen Reduction Reaction and Hydrogen Oxidation Reaction Catalyst in Polymer Electrolyte Membrane Fuel Cell. *Sci. Rep.* **2018**, *8*, 78. https://doi.org/10.1038/s41598-018-22001-9.

(224) Sangjan, A.; Boonsith, S.; Sansanaphongpricha, K.; Thinbanmai, T.; Ratchahat, S.; Laosiripojana, N.; Wu, K. C. W.; Shin, H. S.; Sakdaronnarong, C. Facile Preparation of Aqueous-Soluble Fluorescent Polyethylene Glycol Functionalized Carbon Dots from Palm Waste by One-Pot Hydrothermal Carbonization for Colon Cancer Nanotheranostics. *Sci. Rep.* **2022**, *12* , 1–18. https://doi.org/10.1038/s41598-022-14704-x.

(225) Kundelev, E. V.; Tepliakov, N. V.; Leonov, M. Y.; Maslov, V. G.; Baranov, A. V.; Fedorov, A. V.; Rukhlenko, I. D.; Rogach, A. L. Amino Functionalization of Carbon Dots Leads to Red Emission Enhancement. *Journal of Physical Chemistry Letters* **2019**, *10*, 5111–5116. https://doi.org/10.1021/acs.jpclett.9b01724.

(226) Huang, X.; Zhu, Y.; Kianfar, E. Nano Biosensors: Properties, Applications and Electrochemical Techniques. *Journal of Materials Research and Technology*. Elsevier Editora Ltda **2021**, 48, 1649–1672. https://doi.org/10.1016/j.jmrt.2021.03.048.

(227) Yuan, F.; Yuan, T.; Sui, L.; Wang, Z.; Xi, Z.; Li, Y.; Li, X.; Fan, L.; Tan, Z.; Chen, A.; Jin, M.; Yang, S. Engineering Triangular Carbon Quantum Dots with Unprecedented Narrow Bandwidth Emission for Multicolored LEDs. *Nat. Commun.* **2018**, *9*, 1–11. https://doi.org/10.1038/s41467-018-04635-5.

(228) Akhtar, N.; Syakir Ishak, M. I.; Bhawani, S. A.; Umar, K. Various Natural and Anthropogenic Factors Responsible for Water Quality Degradation: A Review. *Water (Switzerland)* **2021**, *13*, 2260. https://doi.org/10.3390/w13192660.

(229) Wang, X.; Zhou, J.; Wang, H. Bioreceptors as the Key Components for Electrochemical Biosensing in Medicine. *Cell Reports Physical Science*. Cell Press, **2024**, 45, 101801. https://doi.org/10.1016/j.xcrp.2024.101801.

(230) Mehrab P. An Electrochemical Aptasensor for Detection of Prostate-Specific Antigen-Based on Carbon Quantum Dots-Gold Nanoparticles. *National center for Biotechnology information* **2023**, *7*, 175–183. https://doi.org/10.3390/s21196578.

(231) Zhang, Y.; Li, K.; Ren, S.; Dang, Y.; Liu, G.; Zhang, R.; Zhang, K.; Long, X.; Jia, K. Coal-Derived Graphene Quantum Dots Produced by Ultrasonic Physical Tailoring and Their Capacity for Cu(II) Detection. *ACS Sustain. Chem. Eng.* **2019**, *7* , 9793–9799. https://doi.org/10.1021/acssuschemeng.8b06792.

(232) Jiao, L.; Wang, Y.; Jiang, H.; Xu, Q. Metal – Organic Frameworks as Platforms for Catalytic Applications. **2018**, *1703663*, 1–23. https://doi.org/10.1002/adma.201703663.

(233) Dandan, L.; Hai-qun, X.; Long, J.; Hai-long, J. Metal-Organic Frameworks for Catalysis: State of the Art, Challenges, and Opportunities. *EnergyChem* **2019**, *1*, 100005. https://doi.org/10.1016/j.enchem.2019.100005.

(234) Chuhadiya, S.; Suthar, D.; Patel, S. L.; Dhaka, M. S. Metal Organic Frameworks as Hybrid Porous Materials for Energy Storage and Conversion Devices : A Review. *Coord. Chem. Rev.* **2021**, *446*, 214115. https://doi.org/10.1016/j.ccr.2021.214115.

(235) Mohan, B.; Kumar, S.; Xi, H.; Ma, S.; Tao, Z.; Xing, T. Biosensors and Bioelectronics Fabricated Metal-Organic Frameworks (MOFs) as Luminescent and Electrochemical Biosensors for Cancer Biomarkers Detection. *Biosens. Bioelectron.* **2022**, *197* , 113738. https://doi.org/10.1016/j.bios.2021.113738.

(236) Ahmadijokani, F.; Mohammadkhani, R.; Ahmadipouya, S.; Shokrgozar, A.; Rezakazemi, M.; Molavi, H.; Aminabhavi, T. M.; Arjmand, M. Superior Chemical Stability of UiO-66

Metal-Organic Frameworks (MOFs) for Selective Dye Adsorption. *Chemical Engineering Journal* **2020**, *399* , 125346. https://doi.org/10.1016/j.cej.2020.125346.

(237) Wang, X.; Zhang, W.; Zhang, X.; Ran, L.; Zhao, Q.; Zou, B.; Zhou, L.; Ye, Z. A Novel Design of Self-Assembled Metal-Organic Frameworks MIL-53 (Fe) Modified Resin as a Catalyst for Catalytic Degradation of Tetracycline. *J. Clean. Prod.* **2022**, *348*, 131385. https://doi.org/10.1016/j.jclepro.2022.131385.

(238) Abdelhameed, R. M.; Darwesh, O. M.; El-shahat, M. Microporous and Mesoporous Materials Titanium-Based Metal-Organic Framework Capsulated with Magnetic Nanoparticles : Antimicrobial and Photocatalytic Degradation of Pesticides. *Microporous and Mesoporous Materials* **2023**, *354*, 112543. https://doi.org/10.1016/j.micromeso.2023.112543.

(239) Allahbakhshi, M.; Mohammad, N.; Mosaferi, M. Synthesis of Functionalized Metal-Organic Framework Metal-Organic Framework (MIL-53)/ Chitosan for Removing Dye and Pharmaceuticals. **2022**, *35*, 178. https://doi.org/10.1088/1757-899X/149/1/012178.

(240) Turabik, M.; Kalderis, D. Chemosphere A Dual Purpose Aluminum-Based Metal Organic Framework for the Removal of Chloramphenicol from Wastewater. **2022**, *308* 136411. https://doi.org/10.1016/j.chemosphere.2022..

(241) Abdelhameed, R. M.; Taha, M.; Abdel-gawad, H.; Hegazi, B. Amino-Functionalized Al-MIL-53 for Dimethoate Pesticide Removal from Wastewater and Their Intermolecular Interactions. *J. Mol. Liq.* **2021**, *327*, 114852. https://doi.org/10.1016/j.molliq.2020.114852.

(242) Wang, J.; Yi, X.; Xu, X.; Ji, H.; Alanazi, A. M.; Wang, C.; Zhao, C.; Valentino, Y.; Wang, P.; Liu, W. Eliminating Tetracycline Antibiotics Matrix via Photoactivated Sulfate Radical-Based Advanced Oxidation Process over the Immobilized MIL-88A : Batch and Continuous Experiments. *Chemical Engineering Journal* **2022**, *431*, 133213. https://doi.org/10.1016/j.cej.2021.133213.

(243) Zhang, Q.; Qileng, A.; Li, J.; Cao, Y.; Liu, W.; Liu, Y. Grafting a Porous Metal − Organic Framework [NH 2 - MIL-101 (Fe)] with AgCl Nanoparticles for the Efficient Removal of Congo Red. **2023**, *101*, 2c06300. https://doi.org/10.1021/acsomega..

(244) Tang, L.; Ji, R.; Cao, X.; Lin, J.; Jiang, H.; Li, X.; Teng, K. S.; Luk, C. M.; Zeng, S.; Hao, J.; Lau, S. P. Deep Ultraviolet Photoluminescence of Water-Soluble Self-Passivated Graphene Quantum Dots. *ACS Nano* **2012**, *6* , 5102–5110. https://doi.org/10.1021/nn300760g.

(245) Tian, P.; Tang, L.; Teng, K. S.; Lau, S. P. Graphene Quantum Dots from Chemistry to Applications. *Materials Today Chemistry*. Elsevier Ltd December 1, 2018, pp 221–258. https://doi.org/10.1016/j.mtchem.2018.09.007.

(246) Ullah, S.; Adeel, M.; Zain, M.; Rizwan, M.; Kashif, M.; Jilani, G.; Hameed, A.; Khan, A.; Arshad, M.; Raza, A.; Baluch, M. A.; Rui, Y. Physiological and Biochemical Response of Wheat (Triticum Aestivum) to TiO 2 Nanoparticles in Phosphorous Amended Soil : A Full Life Cycle Study. **2020**, *263, 755.* www.sciencedirect.comwww.materialstoday.com/proceedings.

(247) Abdul-Ghani, R.; Al-Mekhlafi, A.M.; Karanis, P. Loop-Mediated Isothermal Amplification (LAMP) for Malarial Parasites of Humans: Would It Come to Clinical Reality as a Point-of-Care Test? *Acta Trop.* **2012**, 122, 233–240. ps://doi.org/10.1021/acscatal.8b00456.

(248) Usman, M.; Farooq, M.; Wakeel, A.; Nawaz, A.; Alam, S.; Ashraf, I.; Sanaullah, M. Science of the Total Environment Nanotechnology in Agriculture : Current Status , Challenges and Future Opportunities. *Science of the Total Environment* **2020**, *721*, 137778. https://doi.org/10.1016/j.scitotenv.2020.137778.

(249) Venkataramanan, N. S.; Matsui, K.; Kawanami, H.; Ikushima, Y. Green Synthesis of Titania Nanowire Composites on Natural Cellulose Fibers, sensors **2007**, *1*0, 18–19. https://doi.org/10.1039/b609887h.

(250) Khalid K. Abbas; Al-Ghaban, A. M. H. A. Enhanced Solar Light Photoreduction of Innovative TiO2 Nanospherical Shell by Reduced Graphene Oxide for Removal Silver Ions from Aqueous Media. *J. Environ. Chem. Eng.* **2019**, 3, 103168. https://doi.org/10.1016/j.elecom.2021.106952.

(251) Ani, I. J.; Akpan, B. U. G.; Olutoye, M. A.; Hameed, B. H. Photocatalytic Degradation of Pollutants in Petroleum Refinery Wastewater by TiO2- and ZnO-Based Photocatalysts: Recent Development. *J. Clean. Prod.* **2018**, 20, 930–954. https://doi.org/10.1038/s41598-024-64797-9.

(252) Athanasekou, C. P.; Likodimos, V.; Falaras, P. Recent Developments of TiO2 Photocatalysis Involving Advanced Oxidation and Reduction Reactions in Water. *J. Environ. Chem. Eng.* **2018**, 6, 7386–7394. https://doi.org/10.1016/j.apsusc.2019.143836.

(253) Abeledo-Lameiro, M. J.; Ares-Mazás, E.; Gómez-Couso, H. Evaluation of Solar Photocatalysis Using TiO2 Slurry in the Inactivation of Cryptosporidium Parvum Oocysts in Water. *J. Photochem. Photobiol. B* **2016**, *163*, 92–99.https://doi.org/10.1016/j.cej.2018.07.034.

(254) Hayat, A.; Rhouati, A.; Mishra, R. K.; Alonso, G. A.; Nasir, M.; Istamboulie, G.; Marty, J. L. An Electrochemical Sensor Based on TiO2/Activated Carbon Nanocomposite Modified Screen Printed Electrode and Its Performance for Phenolic Compounds Detection in Water Samples. *Int. J. Environ. Anal. Chem.* **2016**, *96*, 237–246. https://doi.org/10.1080/03067319.2015.1137910.

(255) Samuel, Z.; Jokazi, M.; Nwahara, N.; Nyokong, T. Nitrite Electrochemical Sensing Using Cu Centred Porphyrin Functionalized TiO2 Nanoparticles Modified Glassy Carbon Electrode. *J. Appl. Electrochem.* **2025**, *55* , 1341–1356. https://doi.org/10.1007/s10800-024-02232-7.

(256) Henrique, P.; Camargo, C.; Satyanarayana, K. G.; Wypych, F. Nanocomposites : Synthesis , Structure , Properties and New Application Opportunities. **2009**, *12*, 1–39. https://doi.org/10.1016/j.electacta.2013.04.136.

(257) Saleh, T. A. Environmental Technology & Innovation Nanomaterials : Classification , Properties , and Environmental Toxicities. *Environ. Technol. Innov.* **2020**, *20*, 101067. https://doi.org/10.1016/j.eti.2020.101067.

(258) Omanovi, E.; Badnjevi, A.; Kazlagi, A.; Hajlovac, M. Nanocomposites : A Brief Review. **2020**, 51–59. https://doi.org/10.1021/acs.jpcc.5b04080.

(259) Amit Kumar Nayak; Mazumder, S.; Ara, T. J.; § M. T. A.; Hasnain, M. S. 2 - Calcium Fluoride-Based Dental Nanocomposites. *Applications of Nanocomposite Materials in Dentistry* **2019**, 27–45. https://doi.org/10.1007/s11814-021-0980-4.

(260) Braun, T.; Schubert, A.; Zsindely, S. Nanoscience and Nanotechnology on the Balance. **1997**, *38* , 321–325. https://doi.org/10.1016/j.ccr.2009.12.023.

(261) Rawtani , D. , Khatri , N. , Tyagi , S. , and Pandey, G. Nanotechnology-Based Recent Approaches for Sensing and Remediation of Pesticides . *J. Environ. Manag* **2018**, No. 206, 749–762.https://doi.org/10.1039/c3ay26476a.

(262) Zawani, N.; Azman, M.; Nur, P.; Zainal, S.; Alang, S. A. Enhancement the Electrochemical Conductivity of a Modified Reduced Graphene Oxide / Calixarene Screen-Printed Electrode Using Response Surface Methodology. **2020**,70, 1–14. https://doi.org/10.1371/journal.pone.0234148.

(263) Nourbakhsh, A.; Rahimnejad, M.; Asghary, M.; Younesi, H. Simultaneous Electro-Determination of Trace Copper, Lead, and Cadmium in Tap Water by Using Silver Nanoparticles and Graphene Nanoplates as Nanocomposite Modified Graphite Electrode. *Microchemical Journal* **2022**, *175*, 107137. https://doi.org/10.1016/j.microc.2021.107137.

(264) Bansod, B. K.; Kumar, T.; Thakur, R.; Rana, S.; Singh, I. A Review on Various Electrochemical Techniques for Heavy Metal Ions Detection with Different Sensing Platforms. *Biosensors and Bioelectronics*. Elsevier, **2017**, 40, 443–455. https://doi.org/10.1016/j.bios.2017.03.031.

(265) Yadav, M.; Dhanda, M.; Arora, R.; Singh, G.; Mohan, H.; Lata, S. A TiO2-Adenine Nanocomposite as Modification Material for Screen-Printed Gold Electrode to Detect

H1N1 (Swine Flu) Virus: A Disposable Genosensor. *Microchemical Journal* **2024**, *197*. 109831.https://doi.org/10.1016/j.microc.2023.

(266) Liu, S.; Xing, X.; Yu, J.; Lian, W.; Li, J.; Cui, M.; Huang, J. A Novel Label-Free Electrochemical Aptasensor Based on Graphene-Polyaniline Composite Film for Dopamine Determination. *Biosens. Bioelectron.* **2012**, *36* , 186–191. https://doi.org/10.1016/j.bios.2012.04.011.

(267) Zhang, X.; Shen, J.; Ma, H.; Jiang, Y.; Huang, C.; Han, E.; Yao, B.; He, Y. . . Optimized Dendrimer-Encapsulated Gold Nanoparticles and Enhanced Carbon Nanotube Nanoprobes for Amplified Electrochemical Immunoassay of E. Coli in Dairy Product Based on Enzymatically Induced Deposition of Polyaniline. *Biosens. Bioelectron.* **2018**, 80, 666–673. https://doi.org/10.1021/nn901221k.

(268) Quintero-Jaime, A. F.; Berenguer-Murcia, Á.; Cazorla-Amorós, D.; Morallón, E. Carbon Nanotubes Modified with Au for Electrochemical Detection of Prostate Specific Antigen: Effect of Au Nanoparticle Size Distribution. *Front. Chem.* **2019**, *7* , 547. https://doi.org/10.3389/fchem.2019.00147.

(269) Li, R.; Luan, J.; Zhang, Y.; Jiang, L.; Yan, H.; Chi, Q.; Yan, Z. A Review of Efficient Photocatalytic Water Splitting for Hydrogen Production. *Renewable and Sustainable Energy Reviews*. Elsevier **2024**, 67, 3939. https://doi.org/10.1016/j.rser.2024.114863.

(270) Yadav, M.; Dhanda, M.; Arora, R.; Jagdish, R.; Singh, G.; Lata, S. Titania (TiO2)/Silica (SiO2) Nanospheres or NSs Amalgamated on a Pencil Graphite Electrode to Sense l-Ascorbic Acid Electrochemically and Augmented NSs for Antimicrobial Behaviour. *New Journal of Chemistry* **2022**, *46*, 12783–12796. https://doi.org/10.1039/d2nj01892f.

(271) Mengyang Li. B. . An Aptasensor for Cadmium Ions Detection Based on PEI-MoS2@Au NPs 3D Flower-like Nanocomposites and Thi-PtPd NPs Core-Shell Sphere. *Analytical Chem Act* **2022**, *1*, 1113–1120. https://doi.org/10.1088/1757-899X/343/1/012003.

(272) Uda, M. N. A.; Gopinath, S. C. B.; Hashim, U.; Halim, N. H.; Parmin, N. A.; Uda, M. N. A.; Adam, T.; Anbu, P. Silica and Graphene Mediate Arsenic Detection in Mature Rice Grain by a Newly Patterned Current–Volt Aptasensor. *Sci. Rep.* **2021**, *11*, 189. https://doi.org/10.1038/s41598-021-94145-0.

(273) Xing, S.; Zheng, K.; Shi, L.; Kang, K.; Peng, Z.; Zhang, X.; Liu, B.; Yang, H.; Yue, G. Fluorescence Detection of Pb2+ in Environmental Water Using Biomass Carbon Quantum Dots Modified with Acetamide-Glycolic Acid Deep Eutectic Solvent. *Molecules* **2024**, *29*, 1662. https://doi.org/10.3390/molecules29071662.

(274) Viet, N. X.; Hoan, N. X.; Takamura, Y. Development of Highly Sensitive Electrochemical Immunosensor Based on Single-Walled Carbon Nanotube Modified Screen-Printed Carbon Electrode. *Mater. Chem. Phys.* **2019**, *227* , 123–129. https://doi.org/10.1016/j.matchemphys.2019.01.068.

(275) Tyagi, A.; Tripathi, K. M.; Singh, N.; Choudhary, S.; Gupta, R. K. Green Synthesis of Carbon Quantum Dots from Lemon Peel Waste: Applications in Sensing and Photocatalysis. *RSC Adv.* **2016**, *6,* 72423–72432. https://doi.org/10.1039/c6ra10488f.

(276) Chen, J.; Tang, M.; Nie, S.; Xiao, P.; Zhao, T.; Chen, Y. Synthesis Methods, Performance Optimization, and Application Progress of Metal–Organic Framework Material MIL-101(Cr). *Chemistry (Easton).* **2025**, *7* , 78. https://doi.org/10.3390/chemistry7030078.

(277) Yadav, M.; Singh, G.; Lata, S. Sol–Gel-Assisted Synthesis of PVPO-TiO2 Nanocomposites Extended to Bifunctionality as Efficient Electrode for Enzymeless D -(+)-Glucose Sensing and Antimicrobial Potential. *Journal of Solid State Electrochemistry* **2022**, *26* , 2153–2170. https://doi.org/10.1007/s10008-022-05216-9.

(278) Tawari, A.; Einicke, W. D.; Gläser, R. Photocatalytic Oxidation of NO over Composites of Titanium Dioxide and Zeolite ZSM-5. *Catalysts* **2016**, *6*131. https://doi.org/10.3390/catal6020031.

(279) Karnchanawong, S., Limpiteeprakan, P., Evaluation of Heavy Metal Leaching from Spent Household Batteries Disposed in Municipal Solid Waste. *Waste Manage.*, **2009**, *29* , 550–558. https://doi.org/10.1016/j.wasman.2008.03.018

(280) Edebali, S. Synthesis and Characterization of MIL-101 (Fe) as Efficient Catalyst for Tetracycline Degradation by Using NaBH4: Artificial Neural Network Modeling. *Applied Surface Science Advances* **2023**, *18,* 100496. https://doi.org/10.1016/j.apsadv.2023..

(281) Pajkossy. T. Electrochemistry Communications Analysis of Quasi-Reversible Cyclic Voltammograms. *Electrochem. Communication* **2018**, 69–72. 30100–30107. https://doi.org/10.1039/c4ra03720k.

(282) Vesztergom, S. , "Electrochimica Acta Analysis of Voltammograms of Quasi-Reversible Redox Systems : Transformation to Potential Program Invariant Form. *Electrochim. Acta* **2019**, No. 5, 1121–1129.

(283) V. Ag and L. Box. , "Chronoamperometric Investigations of the Electrode – Electrolyte Interface of a Commercial High Temperature PEM FuelFuelCell," Fuel Cells,. *Fuel Cells,* **2010**, No. 6, 983–992.

(284) Bardini, L. . , "an Introduction to Electrochemical Spectroscopy . Material Today **2018**. 7, 223–2260. https://doi.org/10.1038/s41427-019-0107-0.

(285) F. Hernandez and H. Baltruschat. , "Electrochemical Characterization of Gold Stepped Surfaces Modified with Pd," Langmuir. *Langmuir* **2006**, 25, 4877–4884.https://doi.org/10.1016/j.apcatb.2016.04.016.

(286) Allen L., L. R. *Electrochemical Methods***; 2001**.

(287) B. Rezaei. *, Chapter 2 - Electrochemical Detection Techniques in Biosensor Applications.*; **2019**.https://doi.org/10.1007/s40097-021-00431-8.

(288) Osteryoung J, O. J. *Square-Wave Voltammetry, **2020,*** 14 , 234. https://doi.org/10.1016/j.apsadv.2023.100534.

(289) Lovri~, M.; Osteryoung, J. *THEORY OF DIFFERENTIAL NORMAL PULSE VOLTAMMETRY*.

(290) Barker, G. C.; Gardner, A. W.; Applications, B. *Forty Years of Square-Wave Polarography Summary of Contents Introduction Early SW Polarographs Radiofrequency Polarography and Faradaic Rectification Low-f Req u Ency-H i g h-f Req u Ency I Nte Rmod u I at i o n Po La Rog Rap h y Multimode Polarograph Developments Connected with SWP/SWV Over the Last Two Decades Static Mercury Drop Electrode Micro Processors and Pola Rog Ra p h YNolta Mmetry Data Processing Commercial Instrumentation Abnormal Peak Shapes in SWP Light-Induced Electron Emission*; **1992**; 117, 290. https://doi.org/10.1016/j.stem.2024.12.011

(291) Kalousek; Ralek. *REVERSIBLE Figure 1. Ramp Voltage Functions and Illustrative Polarograms*; **2010**, 19. Dio: 10.1007/s10008-023-05770-2.

(292) Ruchets, A.; Donker, N.; Zosel, J.; Schönauer-Kamin, D.; Moos, R.; Guth, U.; Mertig, M. CO Gas Detection on Pt|YSZ|Pt Solid Electrolyte Sensors by Methods Based on Dynamic Voltage Variations. *J. Electrochem. Soc.* **2021**, *168* , 117506. https://doi.org/10.1149/1945-7111/ac2fc5.

(293) López-Tenés, M.; Laborda, E.; Martínez-Ortiz, F.; González, J.; Molina, Á. Square Wave Voltammetry as a Powerful Tool for Studying Multi-Electron Molecular Catalysts. *Journal of Electroanalytical Chemistry* **2022**, *927*. 116943. https://doi.org/10.1016/j.jelechem.2022.

(294) Yadav, V.; Raj, M.; Goyal, R. N. Comparison of Different Unmodified and Nano-Material Modified Sensors for the Ultrasensitive Determination of Serotonin. *J. Electrochem. Soc.* **2020**, *167*, 027539. https://doi.org/10.1149/1945-7111/ab6dd3.

(295) Olmos, J. M.; Pereira, C. M. Electrochemical Sensing and Characterization of Denatonium Ion by Ion Transfer at Polarized Liquid/Liquid Interfaces. *Journal of Electroanalytical Chemistry* **2020**, *859*. 113860. https://doi.org/10.1016/j.jelechem.2020.

(296) Foundation, F. S. Spectroscopy : Principles , Theory , Techniques and Applications Spectroscopy-An Introduction. *Spectroscopy: Principles, Theory, Techniques and Applications PDF* **2009**, 1–164. 5004. https://doi.org/10.1039/d0ra03591b

(297) Biology, M. *Author 12 Spectroscopic Techniques : I Spectrophotometric Techniques*; **2010**. https://doi.org/10.1088/1742-6596/257/1/012008.

(298) Lawson, G.; Ogwu, J.; Tanna, S. Quantitative Screening of the Pharmaceutical Ingredient for the Rapid Identification of Substandard and Falsified Medicines Using Reflectance Infrared Spectroscopy. **2018**, 1–17. https://doi.org/10.1088/1757-899X/149/1/012178.

(299) Imran Din, M., Ahmed, M., Ahmad, M., Saqib, S., Mubarak, W., Hussain, Z., Khalid, R., Raza, H., Hussain, T. Novel and Facile Synthesis of Carbon Quantum Dots from Chicken Feathers and Their Application as a Photocatalyst to Degrade Methylene Blue Dye. *J Chem.,* **2023**,1, 9956427. https://doi.org/10.1155/2023/9956427.

(300) Gaikwad, J.; Sharma, S.; Hatware, K. V; Gaikwad, J.; Sharma, S. Critical Reviews in Analytical Chemistry Review on Characteristics and Analytical Methods of Tazarotene : An Update Review on Characteristics and Analytical Methods of Tazarotene : An Update. *Crit. Rev. Anal. Chem.* **2020**, *50*, 90–96. https://doi.org/10.1080/10408347.2019.1586519.

(301) Yu, J.; Wang, H.; Zhan, J.; Huang, W. Review of Recent UV – Vis and Infrared Spectroscopy Researches on Wine Detection and Discrimination. **2018**, *4928*. 1352511. https://doi.org/10.1080/05704928.2017.

(302) WM Riggs, M. P. Surface Analysis by X-Ray Photoelectron Spectroscopy. In *Methods of Surface Analysis* **2015**, 197, 45. https://doi.org/10.1016/j.sab.2015.05.002.

(303) J. Vac. Procedure Which Allows the Performance and Calibration of an XPS Instrument to Be Checked Rapidly and Frequently. *.Sci. Technol.* **2020**, 38, 043206.

(304) Brundle, C. R.; Crist, B. V. X-Ray Photoelectron Spectroscopy: A Perspective on Quantitation Accuracy for Composition Analysis of Homogeneous Materials. *Journal of Vacuum Science & Technology A* **2020**, *38* . https://doi.org/10.1116/1.5143897.

(305) Baer, M. Gold/Silver Core-Shell 20 Nm Nanoparticles Extracted from Citrate Solution Examined by XPS. *Surface chemistry* **2016**, *23* , 29–39.

(306) Baer, D. R.; Karakoti, A. S.; Clifford, C. A.; Minelli, C.; Unger, W. E. S. Importance of Sample Preparation on Reliable Surface Characterisation of Nano-Objects: ISO Standard 20579-4. *Surface and Interface Analysis* **2018**, *50* (9), 902–906. https://doi.org/10.1002/sia.6490.

(307) Dablemont, C.; Lang, P.; Mangeney, C.; Piquemal, J. Y.; Petkov, V.; Herbst, F.; Viau, G. FTIR and XPS Study of Pt Nanoparticle Functionalization and Interaction with Alumina. *Langmuir* **2008**, *24* (11), 5832–5841. https://doi.org/10.1021/la7028643.

(308) Olmos, J. M.; Pereira, C. M. Electrochemical Sensing and Characterization of Denatonium Ion by Ion Transfer at Polarized Liquid/Liquid Interfaces. *Journal of*

Electroanalytical Chemistry **2020**, *859*, 113860. https://doi.org/10.1016/j.jelechem.2020..

(309) Willard, H. . Instrumental Methods of Analysis. In *ANALYTICA CHEMISTRY*; 1989; Vol. 61.

(310) Chalmers, J. M.; Edwards, H. G. M.; Hargreaves, M. D. Introduction and Scope. *Infrared and Raman Spectroscopy in Forensic Science*. John Wiley and Sons **2012**, 1–7. https://doi.org/10.1002/9781119962328.ch1.

(311) Facade, T.; Paul, S. Unit 1 Unit 1. *Heritage* **2006**, No. April, 1–9.

(312) Roane, T. M.; Pepper, I. L. *Microscopic Techniques*; Elsevier Inc., 2015. https://doi.org/10.1016/B978-0-12-394626-3.00009-0.

(313) N. Jalili and K. Laxminarayana. , "A Review of Atomic Force Microscopy Imaging Systems : Application to Molecular Metrology and Biological Sciences,." *Mechatronics* **2004**, 14, 907–945.

(314) Soxpollard, N.; Strauss, S.; Jungmann, R.; MacPherson, I. S. Selection of Antibody-Binding Covalent Aptamers. *Commun Chem* **2024**, *7* , 678. https://doi.org/10.1038/s42004-024-01255-7.

(315) Hanan, A. R. A.; de Meireles, D. A.; Sponchiado Júnior, E. C.; Hanan, S.; Kuga, M. C.; Filho, I. B. Surface Characteristics of Reciprocating Instruments before and after Use - A SEM Analysis. *Braz. Dent. J.* **2015**, *26*, 121–127. https://doi.org/10.1590/0103-6440201300208.

(316) Subha, N.; Sikri, V. K. Comparative Evaluation of Surface Changes in Four Ni-Ti Instruments with Successive Uses - An SEM Study. *Journal of Conservative Dentistry* **2011**, *14*, 282–286. https://doi.org/10.4103/0972-0707.85817.

(317) Moeini, B., Haack, H., Fairley, N., Fernandez, V., Gengenbach, T. R., Easton, C. D., Linford, M. R., Box Plots: A Simple Graphical Tool for Visualizing Overfitting in Peak Fitting as Demonstrated with X-Ray Photoelectron Spectroscopy Data. *J Electron Spectros Relat Phenomena.*, **2021**, *250, 147094*. https://doi.org/10.1016/j.elspec.2021.147094.

(318) Symonowicz, J.; Jan, A.; Yan, H.; Chhowalla, M.; Di Martino, G. Scanning Plasmon-Enhanced Microscopy for Simultaneous Optoelectrical Characterization. *ACS Nano* **2024**, *18* (31), 20412–20421. https://doi.org/10.1021/acsnano.4c04671.

(319) O. Marti; B. Drake; P. K. Hansma. Atomic Force Microscopy of Liquid-covered Surfaces: Atomic Resolution Images. *Appl. Phys. Lett.* **1987**, *51* (7), 484–486.

(320) Cíbiková, I. *ENGLISH SLOVAK SLOVAK ENGLISH STEM DICTIONARY*.

(321) Marti. *AFM Instrumentation and Tips.*; 1999.

(322) Marinangeli, L.; Pompilio, L.; Baliva, A.; Billotta, S.; Bonanno, G.; Domeneghetti, M. C.; Fioretti, A. M.; Menozzi, O.; Nestola, F.; Piluso, E.; Pondrelli, M.; La Salvia, V.; Somma, M. C.; Tateo, F.; Petrinca, P.; Di Giulio, C.; Tangari, A. C. Development of an Ultra-Miniaturised XRD/XRF Instrument for the in Situ Mineralogical and Chemical Analysis of Planetary Soils and Rocks: Implication for Archaeometry. *Rendiconti Lincei* **2015**, *26* , 529–537. https://doi.org/10.1007/s12210-015-0477-3.

(323) Bunaciu, A. A.; Udriştioiu, E. gabriela; Aboul-Enein, H. Y. X-Ray Diffraction: Instrumentation and Applications. *Crit. Rev. Anal. Chem.* **2015**, *45* , 289–299. https://doi.org/10.1080/10408347.2014.949616.

(324) Khan, H.; Yerramilli, A. S.; D'Oliveira, A.; Alford, T. L.; Boffito, D. C.; Patience, G. S. Experimental Methods in Chemical Engineering: X-Ray Diffraction Spectroscopy—XRD. *Canadian Journal of Chemical Engineering* **2020**, *98* , 1255–1266. https://doi.org/10.1002/cjce.23747.

(325) Zhao, F.; Li, X.; Zuo, M.; Liang, Y.; Qin, P. Journal of Environmental Chemical Engineering Preparation of Photocatalysts Decorated by Carbon Quantum Dots (CQDs) and Their Applications : A Review. *J. Environ. Chem. Eng.* **2023**, *11* , 109487. https://doi.org/10.1016/j.jece.2023.109487.

(326) Badihi-Mossberg, M.; Buchner, V.; Rishpon, J. Electrochemical Biosensors for Pollutants in the Environment. *Electroanalysis*. Wiley-VCH Verlag **2007**, 456, 2015–2028. https://doi.org/10.1002/elan.200703946.

(327) Muthusankar, G.; Sangili, A.; Chen, S.; Karkuzhali, R.; Sethupathi, M.; Gopu, G.; Karthick, S.; Keerthika, R.; Sengottuvelan, N. In Situ Assembly of Sulfur-Doped Carbon Quantum Dots Surrounded Iron (III) Oxide Nanocomposite ; a Novel Electrocatalyst for Highly Sensitive Detection of Antipsychotic Drug Olanzapine. *J. Mol. Liq.* **2018**, *268*, 471–480. https://doi.org/10.1016/j.molliq.2018.07.059.

(328) Yadav, M.; Singh, G.; Lata, S. Polyvinylpyrrolidone/TiO2 Composites' Preparation via Sol–Gel Procedure Furthered with Non-Enzymatic Glucose Sensing and Antibacterial Effectiveness. *Environmental Science and Pollution Research* **2023**, *30*, 98563–98580. https://doi.org/10.1007/s11356-022-21558-3.

(329) Su, W.; Zhang, J.; Feng, Z.; Chen, T.; Ying, P.; Li, C. Surface Phases of TiO2 Nanoparticles Studied by UV Raman Spectroscopy and FT-IR Spectroscopy. *Journal of Physical Chemistry C* **2008**, *112*, 7710–7716. https://doi.org/10.1021/jp7118422.

(330) Omary, M. A.; Patterson, H. H. Temperature-Dependent Photoluminescence Properties of T1[Ag(CN)2]: Formation of Luminescent Metal - Metal-Bonded Inorganic Exciplexes in the Solid State. *Inorg. Chem.* **1998**, *37*, 1060–1066. https://doi.org/10.1021/ic970823y.

(331) Shafique, M.; Mahr, M. S.; Yaseen, M.; Bhatti, H. N. CQD/TiO2 Nanocomposite Photocatalyst for Efficient Visible Light-Driven Purification of Wastewater Containing Methyl Orange Dye. *Mater. Chem. Phys.* **2022**, *278*. 125583. https://doi.org/10.1016/j.matchemphys.2021..

(332) Kumar, N.; Ghosh, S.; Thakur, D.; Lee, C. P.; Sahoo, P. K. Recent Advancements in Zero- to Three-Dimensional Carbon Networks with a Two-Dimensional Electrode Material for High-Performance Supercapacitors. *Nanoscale Advances*. Royal Society of Chemistry **2023**, 90, 3146–3176. https://doi.org/10.1039/d3na00094j.

(333) Kumar, R.; Youssry, S. M.; Soe, H. M.; Abdel-Galeil, M. M.; Kawamura, G.; Matsuda, A. Honeycomb-like Open-Edged Reduced-Graphene-Oxide-Enclosed Transition Metal Oxides (NiO/Co3O4) as Improved Electrode Materials for High-Performance Supercapacitor. *J. Energy Storage* **2020**, *30*. https://doi.org/10.1016/j.est.2020.101539.

(334) Kang, S.; Kang, T. H.; Kim, B. S.; Oh, J.; Park, S.; Choi, I. S.; Lee, J.; Son, J. G. 2D Reentrant Micro-Honeycomb Structure of Graphene-CNT in Polyurethane: High Stretchability, Superior Electrical/Thermal Conductivity, and Improved Shape Memory Properties. *Compos. B Eng.* **2019**, *162*, 580–588. https://doi.org/10.1016/j.compositesb.2019.01.004.

(335) Cheng, C.; Shi, Y.; Li, M.; Xing, M.; Wu, Q. Carbon Quantum Dots from Carbonized Walnut Shells: Structural Evolution, Fluorescence Characteristics, and Intracellular Bioimaging. *Materials Science and Engineering C* **2017**, *79*, 473–480. https://doi.org/10.1016/j.msec.2017.05.094.

(336) Yen, Y. C.; Lin, C. Chen, P. Y.; Ko, W. Y.; Tien, T. R.; Lin, K. J. Green Synthesis of Carbon Quantum Dots Embedded onto Titanium Dioxide Nanowires for Enhancing Photocurrent. *R. Soc. Open Sci.* **2017**, *4,*161051. https://doi.org/10.1098/rsos..

(337) Subha, P. P.; Jayaraj, M. K. Solar Photocatalytic Degradation of Methyl Orange Dye Using TiO2 Nanoparticles Synthesised by Sol–Gel Method in Neutral Medium. *J. Exp. Nanosci.* **2015**, *10,* 1106–1115. https://doi.org/10.1080/17458080.2014.969338.

(338) Hassid, A.; Klinger, M.; Krzack, S.; Cohen, H. TGA-DSC Combined Coal Analysis as a Tool for QC (Quality Control) and Reactivity Patterns of Coals. *ACS Omega* **2022**, *7*, 1893–1907. https://doi.org/10.1021/acsomega.1c05296.

(339) Al-Kandari, H.; Abdullah, A. M.; Ahmad, Y. H.; Al-Kandari, S.; Alqaradawi, S. Y.; Mohamed, A. M. An Efficient Eco Advanced Oxidation Process for Phenol Mineralization Using a 2D/3D Nanocomposite Photocatalyst and Visible Light Irradiations. *Sci. Rep.* **2017**, *7*, 1–12. https://doi.org/10.1038/s41598-017-09826-6.

(340) Zhang, Z.; Chen, J.; Duan, Y.; Liu, W.; Li, D.; Yan, Z.; Yang, K. Highly Luminescent Nitrogen-Doped Carbon Dots for Simultaneous Determination of Chlortetracycline

and Sulfasalazine. *Luminescence* **2018**, *33*, 318–325. https://doi.org/10.1002/bio.3416.

(341) Feng, H. Z. Generation of Nitrogen-Doped Photoluminescent Carbonaceous Nanodots via the Hydrothermal Treatment of Fish Scales for the Detection of Hypochlorite. *RSC Adv.* **2015**, *5*, 44636. https://doi.org/10.1016/j.jconrel.2023.07.011.

(342) Ramya, A. V.; Manoj, B.; Mohan, A. N. Extraction and Characterization of Wrinkled Graphene Nanolayers from Commercial Graphite. *Asian Journal of Chemistry* **2016**, *28*, 1031–1034. https://doi.org/10.14233/ajchem.2016.19577.

(343) Atchudan, R.; Jebakumar Immanuel Edison, T. N.; Shanmugam, M.; Perumal, S.; Somanathan, T.; Lee, Y. R. Sustainable Synthesis of Carbon Quantum Dots from Banana Peel Waste Using Hydrothermal Process for in Vivo Bioimaging. *Physica E Low. Dimens. Syst. Nanostruct.* **2021**, *126*, 114417. https://doi.org/10.1016/j.physe.2020..

(344) Kalaivani, T.; Anilkumar, P. Role of Temperature on the Phase Modification of TiO2 Nanoparticles Synthesized by the Precipitation Method. *Silicon* **2018**, *10*, 1679–1686. https://doi.org/10.1007/s12633-017-9652-8.

(345) Nagaraj, M.; Ramalingam, S.; Murugan, C.; Aldawood, S.; Jin, J.; Choi, I.; Kim, M. Detection of Fe 3 + Ions in Aqueous Environment Using Fluorescent Carbon Quantum Dots Synthesized from Endosperm of Borassus Flabellifer. *Environ. Res.* **2022**, *212*, 113273. https://doi.org/10.1016/j.envres.2022.113273.

(346) Shafique, M.; Mahr, M. S.; Yaseen, M.; Bhatti, H. N. CQD/TiO2 Nanocomposite Photocatalyst for Efficient Visible Light-Driven Purification of Wastewater Containing Methyl Orange Dye. *Mater Chem Phys* **2022**, *278*. 125583. https://doi.org/10.1016/j.matchemphys.2022.

(347) Bandi, R.; Gangapuram, B. R.; Dadigala, R.; Eslavath, R.; Singh, S. S.; Guttena, V. Facile and Green Synthesis of Fluorescent Carbon Dots from Onion Waste and Their Potential Applications as Sensor and Multicolour Imaging Agents. *RSC Adv* **2016**, *6*, 28633–28639. https://doi.org/10.1039/c6ra01669c.

(348) Dada, S. N.; Babanyinah, G. K.; Tetteh, M. T.; Palau, V. E.; Walls, Z. F.; Krishnan, K.; Croft, Z.; Khan, A. U.; Liu, G.; Wiese, T. E.; Glotser, E.; Mei, H. Covalent and Noncovalent Loading of Doxorubicin by Folic Acid-Carbon Dot Nanoparticles for Cancer Theranostics. *ACS Omega* **2022**, *7*, 23322–23331. https://doi.org/10.1021/acsomega.2c01482.

(349) Mewada, A.; Pandey, S.; Shinde, S.; Mishra, N.; Oza, G.; Thakur, M.; Sharon, M.; Sharon, M. Green Synthesis of Biocompatible Carbon Dots Using Aqueous Extract of Trapa Bispinosa Peel. *Materials Science and Engineering C* **2013**, *33*, 2914–2917. https://doi.org/10.1016/j.msec.2013.03.018.

(350) Fathizadeh, M.; Ngoc Tien, H.; Khivantsev, K.; Song, Z.; Zhou, F.; Yu, M. *Polyamide/Nitrogen-Doped Graphene Oxide Quantum Dots (N-GOQD) Thin Film Nanocomposite Reverse Osmosis Membranes for High Flux Desalination*; **2017**, 45, 667. https://www.elsevier.com/open-access/userlicense/1.0/.

(351) Al-Taweel, S. S.; Saud, H. R.; Kadhum, A. A. H.; Takriff, M. S. The Influence of Titanium Dioxide Nanofiller Ratio on Morphology and Surface Properties of TiO 2 /Chitosan Nanocomposite. *Results Phys.* **2019**, *13*, 102296. https://doi.org/10.1016/j.rinp.2019.

(352) Luo, T.; Xu, L.; Peng, J.; Zhang, L.; Xia, Y.; Ju, S.; Liu, J.; Gang, R.; Wang, Z. Efficient Preparation of Si3N4 by Microwave Treatment of Solar-Grade Waste Silicon Powder. *ACS Omega* **2020**, *5* , 5834–5843. https://doi.org/10.1021/acsomega.9b04027.

(353) Denisenko, Y. G.; Molokeev, M. S.; Oreshonkov, A. S.; Krylov, A. S.; Aleksandrovsky, A. S.; Azarapin, N. O.; Andreev, O. V.; Razumkova, I. A.; Atuchin, V. V. Crystal Structure, Vibrational, Spectroscopic and Thermochemical Properties of Double Sulfate Crystalline Hydrate [Cseu(H2o)3(So4)2]·h2o and Its Thermal Dehydration Product Cseu(So4)2. *Crystals (Basel).* **2021**, *11* , 989. https://doi.org/10.3390/cryst11091027.

(354) Al-Kandari, H.; Abdullah, A. M.; Ahmad, Y. H.; Al-Kandari, S.; Alqaradawi, S. Y.; Mohamed, A. M. An Efficient Eco Advanced Oxidation Process for Phenol Mineralization Using a 2D/3D Nanocomposite Photocatalyst and Visible Light Irradiations. *Sci Rep* **2017**, *7* , 1–12. https://doi.org/10.1038/s41598-017-09826-6.

(355) Nallayagari, A. R.; Sgreccia, E.; Pizzoferrato, R.; Cabibbo, M.; Kaciulis, S.; Bolli, E.; Pasquini, L.; Knauth, P.; Di Vona, M. L. Tuneable Properties of Carbon Quantum Dots by Different Synthetic Methods. *J. Nanostructure Chem.* **2022**, *12*, 565–580. https://doi.org/10.1007/s40097-021-00431-8.

(356) Singh, L.; Sharma, T.; Singh, V. Study of Structural and Functional Properties of Fluorescent EDTA@CQDs Synthesized from Peanut Shells via Pyrolysis Technique. *Mater. Today Proc.* **2021**, *44*, 192–198. https://doi.org/10.1016/j.matpr.2020.08.555.

(357) Mushtaq, K.; Saeed, M.; Gul, W.; Munir, M.; Firdous, A.; Yousaf, T.; Khan, K. B.; Sarwar, H. M. R.; Riaz, M. A.; Zahid, S. Synthesis and Characterization of TiO2 via Sol-Gel Method for Efficient Photocatalytic Degradation of Antibiotic Ofloxacin. *Inorganic and Nano-Metal Chemistry* **2020**, *50*, 580–586. https://doi.org/10.1080/24701556.2020.1722695.

(358) Irshad, M. A.; Nawaz, R.; Rehman, M. Z. ur; Adrees, M.; Rizwan, M.; Ali, S.; Ahmad, S.; Tasleem, S. Synthesis, Characterization and Advanced Sustainable Applications of Titanium Dioxide Nanoparticles: A Review. *Ecotoxicol. Environ. Saf.* **2021**, *212*, 111978. https://doi.org/10.1016/j.ecoenv.2021.111978.

(359) Moeini, B.; Haack, H.; Fairley, N.; Fernandez, V.; Gengenbach, T. R.; Easton, C. D.; Linford, M. R. Box Plots: A Simple Graphical Tool for Visualizing Overfitting in Peak

Fitting as Demonstrated with X-Ray Photoelectron Spectroscopy Data. *J. Electron Spectros. Relat. Phenomena* **2021**, *250*, 147094. https://doi.org/10.1016/j.elspec.2021.

(360) Pinder, J. W.; Major, G. H.; Baer, D. R.; Terry, J.; Whitten, J. E.; Čechal, J.; Crossman, J. D.; Lizarbe, A. J.; Jafari, S.; Easton, C. D.; Baltrusaitis, J.; van Spronsen, M. A.; Linford, M. R. Avoiding Common Errors in X-Ray Photoelectron Spectroscopy Data Collection and Analysis, and Properly Reporting Instrument Parameters. *Applied Surface Science Advances* **2024**, *19*, 100534.https://doi.org/10.1016/j.apsadv.2023.

(361) Zhu, L.; Lu, Q.; Lv, L.; Wang, Y.; Hu, Y.; Deng, Z.; Lou, Z.; Hou, Y.; Teng, F. Ligand-Free Rutile and Anatase TiO2 Nanocrystals as Electron Extraction Layers for High Performance Inverted Polymer Solar Cells. *RSC Adv.* **2017**,55 20084–20092. https://doi.org/10.1039/c7ra00134g.

(362) Ren, P.; Fu, X.; Zhang, Y. Carbon Quantum Dots-TiO2 Nanocomposites with Enhanced Catalytic Activities for Selective Liquid Phase Oxidation of Alcohols. *Catal. Letters* **2017**, *147* , 1679–1685. https://doi.org/10.1007/s10562-017-2065-x.

(363) Martins, N. C. T.; Ângelo, J.; Girão, A. V.; Trindade, T.; Andrade, L.; Mendes, A. N-Doped Carbon Quantum Dots/TiO2 Composite with Improved Photocatalytic Activity. *Appl. Catal. B* **2016**, *193*, 67–74. https://doi.org/10.1016/j.apcatb.2016.04.016.

(364) Adan-mas, A.; Alcaraz, L.; Arévalo-cid, P.; López-gómez, F. A.; Montemor, F. Coffee-Derived Activated Carbon from Second Biowaste for Supercapacitor Applications. *Waste Management* **2021**, *120*, 280–289. https://doi.org/10.1016/j.wasman.2020.11.043.

(365) Liao, W.; Yang, J.; Zhou, H.; Murugananthan, M.; Zhang, Y. Electrochimica Acta Electrochemically Self-Doped TiO 2 Nanotube Arrays for Efficient Visible Light Photoelectrocatalytic Degradation of Contaminants. *Electrochim. Acta* **2014**, *136*, 310–317. https://doi.org/10.1016/j.electacta.2014.05.091.

(366) Wang, Y. J.; Wilkinson, D. P.; Zhang, J. Noncarbon Support Materials for Polymer Electrolyte Membrane Fuel Cell Electrocatalysts. *Chem. Rev.* **2011**, *111*, 7625–7651. https://doi.org/10.1021/cr100060r.

(367) Moeini, B., Haack, H., Fairley, N., Fernandez, V., Gengenbach, T. R., Easton, C. D., Linford, M. R., Box Plots: A Simple Graphical Tool for Visualizing Overfitting in Peak Fitting as Demonstrated with X-Ray Photoelectron Spectroscopy Data. *J Electron Spectros Relat Phenomena.*, **2021**, *250, 147094*. https://doi.org/10.1016/j.elspec.2021.147094.

(368) Pelouchova, H.; Janda, P.; Weber, J.; Kavan, L. Charge Transfer Reductive Doping of Single Crystal TiO 2 Anatase. **2004**, *566*, 73–83. https://doi.org/10.1016/j.jelechem.2003.11.013.

(369) Gao, X.; He, L.; Yu, H.; Xie, F. ScienceDirect The Non-Precious Metal ORR Catalysts for the Anion Exchange Membrane Fuel Cells Application : A Numerical Simulation and Experimental Study. *Int. J. Hydrogen Energy* **2020**, *45*, 23353–23367. https://doi.org/10.1016/j.ijhydene.2020.06.066.

(370) Eckermann, A. L.; Feld, D. J.; Shaw, J. A.; Meade, T. J. Electrochemistry of Redox-Active Self-Assembled Monolayers. *Coordination Chemistry Reviews*. August 2010, 1769–1802. https://doi.org/10.1016/j.ccr.2009.12.023.

(371) Ren, P., Fu, X., Zhang, Y., Carbon Quantum Dots-TiO2 Nanocomposites with Enhanced Catalytic Activities for Selective Liquid Phase Oxidation of Alcohols. *Catal Letters* **2017**, *147*, 1679–1685. https://doi.org/10.1007/s10562-017-2065-x.

(372) Chandran, P.; Ghosh, A.; Ramaprabhu, S. High-Performance Platinum-Free Oxygen Reduction Reaction and Hydrogen Oxidation Reaction Catalyst in Polymer Electrolyte Membrane Fuel Cell. *Sci. Rep.* **2018**, *8* , 3990. https://doi.org/10.1038/s41598-018-22001-9.

(373) Alemu, H.; Abegaz, B. M.; Bezabih, M. ELECTROCHEMICAL BEHAVIOUR AND VOLTAMMETRIC DETERMINATION OF GESHOIDIN AND ITS SPECTROPHOTOMETRIC AND ANTIOXIDANT PROPERTIES IN AQUEOUS BUFFER SOLUTIONS. *Bull. Chem. Soc. Ethiop* **2007**, *21*, 189–204.https://doi.org/10.1016/j.wasman.2020.11.043.

(374) Arham, Z.; Kurniawan, K. Electrode Modifier Performance of TiO2 Incorporated Carbon Quantum Dots Nanocomposites on Fe(CN) 63− /Fe(CN) 64− Electrochemical System. *Korean Journal of Chemical Engineering* **2022**, *39*, 1333–1338. https://doi.org/10.1007/s11814-021-0980-4.

(375) Magar, H. S.; Hassan, R. Y. A.; Mulchandani, A. Electrochemical Impedance Spectroscopy (Eis): Principles, Construction, and Biosensing Applications. *Sensors*. MDPI **2021**, 56, 789 https://doi.org/10.3390/s21196578.

(376) Randviir, E. P.; Banks, C. E. Electrochemical Impedance Spectroscopy: An Overview of Bioanalytical Applications. *Analytical Methods* **2013**, 1098–1115. https://doi.org/10.1039/c3ay26476a.

(377) Omotayo A. Arotiba , Priscilla G. Baker, Bhekie B. Mamba, Emmanuel I. Iwuoha. The Application of Electrodeposited Poly(Propylene Imine) Dendrimer as an Immobilisation Layer in a Simple Electrochemical DNA Biosensor. *Int. J. Electrochem. Sci.,* **2011**, *6*, 673–683. https://doi.org/10.1039/c3ay26476a.

(378) Ikani, N.; Pu, J. H.; Cooke, K. Analytical Modelling and Electrochemical Impedance Spectroscopy (EIS) to Evaluate Influence of Corrosion Product on Solution Resistance. *Powder Technol.* **2024**, *433*, 119252. https://doi.org/10.1016/j.powtec.2023..

(379) Sergey Mamedov, T. M. T. N. N. N.-G. S. Y. & L. Y. Characterization of Nano-Crystalline Structure of TiO2 for Dye-Sensitized Solar Cells by Raman Spectroscopy and Spectroscopic Ellipsometry. *Springer nature link* **2013**, *1578*, 208. https://doi.org/10.1016/j.ecoenv.2021.111978.

(380) Wang, H.; Long, X.; Sun, Y.; Wang, D.; Wang, Z.; Meng, H.; Jiang, C.; Dong, W.; Lu, N. Electrochemical Impedance Spectroscopy Applied to Microbial Fuel Cells: A Review. *Frontiers in Microbiology*. Frontiers Media S.A.**2022**, 34, 97350. https://doi.org/10.3389/fmicb.2022..

(381) Shaban, M.; Ashraf, A. M.; Abukhadra, M. R. TiO2 Nanoribbons/Carbon Nanotubes Composite with Enhanced Photocatalytic Activity; Fabrication, Characterization, and Application. *Sci. Rep.* **2018**, *8*0, 787. https://doi.org/10.1038/s41598-018-19172-w.

(382) Shraim, A. S.; Abdel Majeed, B. A.; Al-Binni, M. A.; Hunaiti, A. Therapeutic Potential of Aptamer-Protein Interactions. *ACS Pharmacology and Translational Science*. American Chemical Society **2022**, 78, 1211–1227. https://doi.org/10.1021/acsptsci.2c00156.

(383) Zhang, T.; Chen, H.; Tan, C.; Li, L.; Liu, C.; Li, W.; Yan, C.; Li, J.; Lu, R. *Elucidating the Binding Mechanism between Bovine Serum Albumin and TiO 2 Nanoparticles with Diverse Properties: Insights from Spectroscopic Methods and Molecular Docking Simulation*. https://ssrn.com/abstract=4405922.

(384) Guziejewski, D.; Stojanov, L.; Gulaboski, R.; Mirceski, V. Reversible and Quasireversible Electron Transfer under Conditions of Differential Square-Wave Voltammetry. *Journal of Physical Chemistry C* **2022**, *126*, 5584–5591. https://doi.org/10.1021/acs.jpcc.2c01188.

(385) Soxpollard, N.; Strauss, S.; Jungmann, R.; MacPherson, I. S. Selection of Antibody-Binding Covalent Aptamers. *Commun. Chem.* **2024**, *7*, 678. https://doi.org/10.1038/s42004-024-01255-7.

(386) Dawadi, S.; Gupta, A.; Khatri, M.; Budhathoki, B.; Lamichhane, G.; Parajuli, N. Manganese Dioxide Nanoparticles: Synthesis, Application and Challenges. **2024**, 34, 556. https://doi.org/10.1007/s12034-020-02247-8S.

(387) Arham, Z.; Kurniawan, K. Electrode Modifier Performance of TiO2 Incorporated Carbon Quantum Dots Nanocomposites on Fe(CN) 63− /Fe(CN) 64− Electrochemical System. *Korean Journal of Chemical Engineering* **2022**, *3*, 1333–1338. https://doi.org/10.1007/s11814-021-0980-4.

(388) Rabiee, N.; Chen, S.; Ahmadi, S.; Veedu, R. N. Aptamer-Engineered (Nano)Materials for Theranostic Applications. *Theranostics*. Ivyspring International Publisher **2023**, 126, 5183–5206. https://doi.org/10.7150/thno.85419.

(389) Chen, Z.; Xie, M.; Zhao, F.; Han, S. Application of Nanomaterial Modified Aptamer-Based Electrochemical Sensor in Detection of Heavy Metal Ions. *Foods*. MDPI, **2022**, 234, 1404 https://doi.org/10.3390/foods11101404.

(390) Laschuk, N. O.; Easton, E. B.; Zenkina, O. V. Reducing the Resistance for the Use of Electrochemical Impedance Spectroscopy Analysis in Materials Chemistry. *RSC Advances*. Royal Society of Chemistry **2021**, 27925–27936. https://doi.org/10.1039/d1ra03785d.

(391) Padha, B.; Verma, S.; Mahajan, P.; Arya, S. Electrochemical Impedance Spectroscopy (EIS) Performance Analysis and Challenges in Fuel Cell Applications. *Journal of Electrochemical Science and Technology*. Korean Electrochemical Society **2022**, 45, 167–176. https://doi.org/10.33961/jecst.2021.01263.

(392) Gökçe, G.; Aissa, S. Ben; Nemčeková, K.; Catanante, G.; Raouafi, N.; Marty, J.-L. *Aptamer-Modified Pencil Graphite Electrodes for the Impedimetric Determination of Ochratoxin A*; **2020**, 67, 800. https://doi.org/10.1016/j.matchemphys.**2019**.01.068.

(393) Mkhohlakali, A.; Fuku, X.; Seo, M. H.; Modibedi, M.; Khotseng, L.; Mathe, M. Electro-Design of Bimetallic PdTe Electrocatalyst for Ethanol Oxidation: Combined Experimental Approach and Ab Initio Density Functional Theory (DFT)—Based Study. *Nanomaterials* **2022**, *12*, 3607. https://doi.org/10.3390/nano12203607.

(394) Rajendran, R. V. and V. Synthesis Andcharacterization of Nano-TiO2 via Different Methods. *Arch. Appl. Sci. Res.* **2012**, 11, 83–1190. https://doi.org/10.1016/j.rechem.2023.100801.

(395) Online, V. A. RSC Advances Network Structure Possessing Multipodal Junctions And. **2013**, 7306–7312. https://doi.org/10.1039/c3ra22933e.

(396) Liang, Y. M.; Yang, H.; Zhou, B.; Chen, Y.; Yang, M.; Wei, K. S.; Yan, X. F.; Kang, C. Waste Tobacco Leaves Derived Carbon Dots for Tetracycline Detection: Improving Quantitative Accuracy with the Aid of Chemometric Model. *Anal. Chim. Acta* **2022**, *1191*, 339269. https://doi.org/10.1016/j.aca.2021.339269.

(397) Sudolská, M.; Dubecký, M.; Sarkar, S.; Reckmeier, C. J.; Zbořil, R.; Rogach, A. L.; Otyepka, M. Nature of Absorption Bands in Oxygen-Functionalized Graphitic Carbon Dots. *Journal of Physical Chemistry C* **2015**, *119*, 13369–13373. https://doi.org/10.1021/acs.jpcc.5b04080.

(398) Lee, E.; Hong, J. Y.; Kang, H.; Jang, J. Synthesis of TiO 2 Nanorod-Decorated Graphene Sheets and Their Highly Efficient Photocatalytic Activities under Visible-Light Irradiation. *J. Hazard. Mater.* **2012**, *219–220*, 13–18. https://doi.org/10.1016/j.jhazmat.2011.12.033.

(399) Nompetsheni, I.; Hlongwa, N. W.; Palaniyandy, N.; Fuku, X. CQD–TiO2 Composite as a Potential Crypto-Electrode Modifier for High-Performance Aptasensing with Ultra-Low Detection Limits. *J. Appl. Electrochem.* **2025**, 67, 192. https://doi.org/10.1007/s10800-025-02328-8.

(400) Lee, E.; Hong, J. Y.; Kang, H.; Jang, J. Synthesis of TiO 2 Nanorod-Decorated Graphene Sheets and Their Highly Efficient Photocatalytic Activities under Visible-Light Irradiation. *J. Hazard. Mater.* **2012**, *219–220*, 13–18. https://doi.org/10.1016/j.jhazmat.2011.12.033.

(401) Iqbal, A.; Labib, M.; Muharemagic, D.; Sattar, S.; Dixon, B. R.; Berezovski, M. V. Detection of Cryptosporidium Parvum Oocysts on Fresh Produce Using DNA Aptamers. *PLoS One* **2015**, *10*, 0137455. https://doi.org/10.1371/journal.pone.

(402) Thiruppathiraja, C.; Kamatchiammal, S.; Adaikkappan, P.; Alagar, M. An Advanced Dual Labeled Gold Nanoparticles Probe to Detect Cryptosporidium Parvum Using Rapid Immuno-Dot Blot Assay. *Biosens. Bioelectron.* **2011**, *26*, 4624–4627. https://doi.org/10.1016/j.bios.2011.05.006.

(403) Hassan, E. M.; Dixon, B. R.; Sattar, S. A.; Stalker, A.; Örmeci, B.; DeRosa, M. C. Highly Sensitive Magnetic-Microparticle-Based Aptasensor for Cryptosporidium Parvum Oocyst Detection in River Water and Wastewater: Effect of Truncation on Aptamer Affinity. *Talanta* **2021**, *222*. 121618. https://doi.org/10.1016/j.talanta.2020.

(404) Yi, Y.; Zhao, Y.; Zhang, Z.; Wu, Y.; Zhu, G. Recent Developments in Electrochemical Detection of Cadmium. *Trends in Environmental Analytical Chemistry*. Elsevier B, **2022**, 78, e00152. https://doi.org/10.1016/j.teac.2021.

(405) Zheng, X.; Chen, S.; Chen, J.; Guo, Y.; Peng, J.; Zhou, X.; Lv, R.; Lin, J.; Lin, R. Highly Sensitive Determination of Lead(II) and Cadmium(II) by a Large Surface Area Mesoporous Alumina Modified Carbon Paste Electrode. *RSC Adv.* **2018**, *8* , 7883–7891. https://doi.org/10.1039/c8ra00041g.

(406) Gupta, V. K.; Yola, M. L.; Atar, N.; Solak, A. O.; Uzun, L.; Üstündağ, Z. Electrochemically Modified Sulfisoxazole Nanofilm on Glassy Carbon for Determination of Cadmium(II) in Water Samples. *Electrochim. Acta* **2013**, *105*, 149–156. https://doi.org/10.1016/j.electacta.2013.04.136.

(407) Wang, G.; Wu, M.; Chu, L. T.; Chen, T. H. Portable Microfluidic Device with Thermometer-like Display for Real-Time Visual Quantitation of Cadmium(II) Contamination in Drinking Water. *Anal. Chim. Acta* **2021**, *1160*. 338444. https://doi.org/10.1016/j.aca.2021.

(408) Wang, X.; Zhou, J.; Wang, H. Bioreceptors as the Key Components for Electrochemical Biosensing in Medicine. *Cell Reports Physical Science* **2024**, 49, 101801. https://doi.org/10.1016/j.xcrp.2024.

(409) Bhalla, N.; Jolly, P.; Formisano, N.; Estrela, P. Introduction to Biosensors. *Essays Biochem.* **2016**, *60*, 1–8. https://doi.org/10.1042/EBC20150001.

(410) Mor, S. M.; Tumwine, J. K.; Ndeezi, G.; Srinivasan, M. G.; Kaddu-Mulindwa, D. H.; Tzipori, S.; Griffiths, J. K. Respiratory Cryptosporidiosis in HIV-Seronegative Children in Uganda: Potential for Respiratory Transmission. *Clinical Infectious Diseases* **2010**, *50*, 1366–1372. https://doi.org/10.1086/652140.

(411) Sohrabi, H.; Khataee, A.; Ghasemzadeh, S.; Majidi, M. R.; Orooji, Y. Layer Double Hydroxides (LDHs)- Based Electrochemical and Optical Sensing Assessments for Quantification and Identification of Heavy Metals in Water and Environment Samples: A Review of Status and Prospects. *Trends in Environmental Analytical Chemistry*. Elsevier B.V. **2021**, 67, e00139https://doi.org/10.1016/j.teac.2021.

(412) Wang, X.; Gao, W.; Yan, W. A Novel Aptasensor Based on Graphene/Graphite Carbon Nitride Nanocomposites for Cadmium Detection with High Selectivity and Sensitivity. *ACS Appl. Nano Mater.* **2018**, *1*, 2341–2346. https://doi.org/10.1021/acsanm.8b00380.

(413) El-Shishtawy, R. M.; Al-Ghamdi, H. A.; Alam, M. M.; Al-amshany, Z. M.; Asiri, A. M.; Rahman, M. M. Development of Cd2+ Sensor Based on BZNA/Nafion/Glassy Carbon Electrode by Electrochemical Approach. *Chemical Engineering Journal* **2018**, *352*, 225–231. https://doi.org/10.1016/j.cej.2018.07.034.

(414) Rahimizadeh, K.; Zahra, Q. ul ain; Chen, S.; Le, B. T.; Ullah, I.; Veedu, R. N. Nanoparticles-Assisted Aptamer Biosensing for the Detection of Environmental Pathogens. *Environmental Research*. Academic Press Inc. **2023,** 12,117123. https://doi.org/10.1016/j.envres.

(415) Ahsani, M. K.; Ahour, F.; Asghari, E. Development of Isoniazid Electrochemical Sensor Using Nickel Ferrite - Nitrogen and Sulfur Co-Doped Graphene Quantum Dot Nanocomposite as a New Electrode Modifier. *Sci. Rep.* **2024**, *14* , 900. https://doi.org/10.1038/s41598-024-64797-9.

(416) Xing, Y.; Si, H.; Sun, D.; Hou, X. Magnetic Fe3O4@NH2-MIL-101(Fe) Nanocomposites with Peroxidase-like Activity for Colorimetric Detection of Glucose. *Microchemical Journal* **2020**, *156,* 104929. https://doi.org/10.1016/j.microc.2020.

(417) Sha, M.; Xu, W.; Fang, Q.; Wu, Y.; Gu, W.; Zhu, C.; Guo, S. Metal-Organic-Framework-Involved Nanobiocatalysis for Biomedical Applications. *Chem Catalysis*. **2022**, 20, 2552–2589. https://doi.org/10.1016/j.checat.2022.09.005.

(418) Lutomia, D.; Poria, R.; Kala, D.; Garg, P.; Nagraik, R.; Kaushal, A.; Gupta, S.; Kumar, D. 2D Nanomaterials in Biosensing: Synthesis, Characterization, Integration in Biosensors and Their Applications. *Biosensors and Bioelectronics: X*. Elsevier **2025**, 67, 10061, 5https://doi.org/10.1016/j.biosx.2025.

(419) Ali, A.; Chiang, Y. W.; Santos, R. M. X-Ray Diffraction Techniques for Mineral Characterization: A Review for Engineers of the Fundamentals, Applications, and Research Directions. *Minerals* **2022**, *12* , 300. https://doi.org/10.3390/min12020205.

(420) Holder, C. F.; Schaak, R. E. Tutorial on Powder X-Ray Diffraction for Characterizing Nanoscale Materials. *ACS Nano*. American Chemical Society **2019**, 157, 7359–7365. https://doi.org/10.1021/acsnano.9b05157.

(421) Ermrich, M.; Opper, D. *X-RAY POWDER DIFFRACTION Nλ = 2d Sin ϑ The Analytical X-Ray Company*.https://doi.org/10.1016/j.scitotenv.2020

(422) Liu, Z.; He, W.; Zhang, Q.; Shapour, H.; Bakhtari, M. F. Preparation of a GO/MIL-101(Fe) Composite for the Removal of Methyl Orange from Aqueous Solution. *ACS Omega* **2021**, 47, 4597–4608. https://doi.org/10.1021/acsomega.0c05091.

(423) Kalaivani, T.; Anilkumar, P. Role of Temperature on the Phase Modification of TiO2 Nanoparticles Synthesized by the Precipitation Method. *Silicon* **2018**, *10*, 1679–1686. https://doi.org/10.1007/s12633-017-9652-8.

(424) Al-Kandari, H.; Abdullah, A. M.; Ahmad, Y. H.; Al-Kandari, S.; Alqaradawi, S. Y.; Mohamed, A. M. An Efficient Eco Advanced Oxidation Process for Phenol Mineralization Using a 2D/3D Nanocomposite Photocatalyst and Visible Light Irradiations. *Sci. Rep.* **2017**, *7*, 234. https://doi.org/10.1038/s41598-017-09826-6.

(425) Jun Chen, C. Advances in Phthalocyanine Compounds and Their Photochemical and Electro-Chemical Properties. *Curr. Org. Chem.* **2018**, *22* , 485–504. https://doi.org/10.1016/j.eti.2018.

(426) Zhang, Z.; Chen, J.; Duan, Y.; Liu, W.; Li, D.; Yan, Z.; Yang, K. Highly Luminescent Nitrogen-Doped Carbon Dots for Simultaneous Determination of Chlortetracycline and Sulfasalazine. *Luminescence* **2018**, *33*, 318–325. https://doi.org/10.1002/bio.3416.

(427) Wu, G.; Feng, M.; Zhan, H. Generation of Nitrogen-Doped Photoluminescent Carbonaceous Nanodots via the Hydrothermal Treatment of Fish Scales for the Detection of Hypochlorite. *RSC Adv.* **2015**, *5*, 44636–44641. https://doi.org/10.1039/c5ra04989j.

(428) Dimitrakis, Panagiotis.; Valov, Ilia.; Tappertzhofen, Stefan. *Metal Oxides for Non-Volatile Memory : Materials, Technology and Applications*; Elsevier, **2022**,78, 100064. https://doi.org/10.1016/j.hazl.2022.

(429) Nagaraj, M.; Ramalingam, S.; Murugan, C.; Aldawood, S.; Jin, J. O.; Choi, I.; Kim, M. Detection of Fe3+ Ions in Aqueous Environment Using Fluorescent Carbon Quantum Dots Synthesized from Endosperm of Borassus Flabellifer. *Environ. Res.* **2022**, *212*. 113273. https://doi.org/10.1016/j.envres.2022.

(430) Thulasi, S.; Kathiravan, A.; Asha Jhonsi, M. Fluorescent Carbon Dots Derived from Vehicle Exhaust Soot and Sensing of Tartrazine in Soft Drinks. *ACS Omega* **2020**, *5*, 7025–7031. https://doi.org/10.1021/acsomega.0c00707.

(431) Imran Din, M.; Ahmed, M.; Ahmad, M.; Saqib, S.; Mubarak, W.; Hussain, Z.; Khalid, R.; Raza, H.; Hussain, T. Novel and Facile Synthesis of Carbon Quantum Dots from Chicken Feathers and Their Application as a Photocatalyst to Degrade Methylene Blue Dye. *J. Chem.* **2023**, *2023*. https://doi.org/10.1155/2023/9956427.

(432) Koczoń, P.; Hołaj-Krzak, J. T.; Palani, B. K.; Bolewski, T.; Dąbrowski, J.; Bartyzel, B. J.; Gruczyńska-Sękowska, E. The Analytical Possibilities of FT-IR Spectroscopy Powered by Vibrating Molecules. *International Journal of Molecular Sciences*. **2023**, 45,2113. https://doi.org/10.3390/ijms24021013.

(433) Chesalov, Y. A.; Andrushkevich, T. V.; Baltakhinov, V. P. FTIR Study of the Role of Surface Complexes in a Transformation of Picoline Isomers on Vanadium-Titanium Oxide Catalysts. *Vib. Spectrosc.* **2016**, *83*, 138–150. https://doi.org/10.1016/j.vibspec.2016.02.004.

(434) Zhang, H.; Lv, X.; Li, Y.; Wang, Y.; Li, J. P25-Graphene Composite as a High Performance Photocatalyst. *ACS Nano* **2010**, *4*, 380–386. https://doi.org/10.1021/nn901221k.

(435) Mugundan, S.; Rajamannan, B.; Viruthagiri, G.; Shanmugam, N.; Gobi, R.; Praveen, P. Synthesis and Characterization of Undoped and Cobalt-Doped TiO2 Nanoparticles via Sol–Gel Technique. *Applied Nanoscience (Switzerland)* **2015**, *5*, 449–456. https://doi.org/10.1007/s13204-014-0337-y.

(436) Chen, Y.; Hong, C.; Xu, Q.; Zheng, H.; Wang, C.; Lu, H.; Zhang, S.; Du, M.; Zeng, G. Visible Light Up-Conversion of Bio-Carbon Quantum-Dot-Decorated TiO2 for Naphthalene Removal. **2024**, 345, 45. https://doi.org/10.20944/preprints202404.1092.v1.

(437) Wang, J.; An, J.; Zhang, Z.; Zhu, H.; Liang, X.; Yang, S.; Sheng, K.; Chen, L.; Lu, H.; Wang, Y. High Fluorescent Nitrogen − Doped Carbon Dots Derived from Sanghuangporus Lonicericola for Detecting Tetracyclines in Aquaculture Water and Rat Serum Samples. *Microchemical Journal* **2023**, *189,* 108517. https://doi.org/10.1016/j.microc.2023.

(438) Kundu, A.; Basu, S.; Maity, B. Upcycling Waste: Citrus Limon Peel-Derived Carbon Quantum Dots for Sensitive Detection of Tetracycline in the Nanomolar Range. *ACS Omega* **2023**, *8*, 36449–36459. https://doi.org/10.1021/acsomega.3c05424.

(439) Liu, Z.; He, W.; Zhang, Q.; Shapour, H.; Bakhtari, M. F. Preparation of a GO/MIL-101(Fe) Composite for the Removal of Methyl Orange from Aqueous Solution. *ACS Omega* **2021**, *6* , 4597–4608. https://doi.org/10.1021/acsomega.0c05091.

(440) Eltaweil, A. S.; Abd El-Monaem, E. M.; Omer, A. M.; Khalifa, R. E.; Abd El-Latif, M. M.; El-Subruiti, G. M. Efficient Removal of Toxic Methylene Blue (Mb) Dye from Aqueous Solution Using a Metal-Organic Framework (Mof) Mil-101(Fe): Isotherms, Kinetics, and Thermodynamic Studies. *Desalination Water Treat.* **2020**, *189*, 395–407. https://doi.org/10.5004/dwt.2020.25599.

(441) Li, Z.; Liu, X.; Jin, W.; Hu, Q.; Zhao, Y. Adsorption Behavior of Arsenicals on MIL-101(Fe): The Role of Arsenic Chemical Structures. *J. Colloid Interface Sci.* **2019**, *554*, 692–704. https://doi.org/10.1016/j.jcis.2019.07.046.

(442) Chaturvedi, G.; Kaur, A.; Umar, A.; Khan, M. A.; Algarni, H.; Kansal, S. K. Removal of Fluoroquinolone Drug, Levofloxacin, from Aqueous Phase over Iron Based MOFs, MIL-100(Fe). *J. Solid State Chem.* **2020**, *281*, 121029. https://doi.org/10.1016/j.jssc.2019..

(443) Dutt, M., Suhasini, K., Ratan, A., Shah, J., Kotnala, R. K., Singh, V. Mesoporous Silica Mediated Synthesis of α-Fe2O3 Porous Structures and Their Application as Humidity Sensors. *Journal of Materials Science: Materials in Electronics* **2018**, *29*, 20506–20516. https://doi.org/10.1007/s10854-018-0186-7.

(444) Hajiali, M., Farhadian, M., Tangestaninejad, S. Novel ZnO Nanorods/Bi2MoO6/MIL-101(Fe) Heterostructure Immobilized on FTO with Boosting Photocatalytic Activity for Tetracycline Degradation: Reaction Mechanism and Toxicity Assessment. *Appl. Surf. Sci.* **2022**, *602*, 154389.https://doi.org/10.1016/j.apsusc.2022.

(445) Ma, L., Xu, J., Liu, Y., An, Y., Improved Degradation of Tetracycline by Cu-Doped MIL-101(Fe) in a Coupled Photocatalytic and Persulfate Oxidation System: Efficiency, Mechanism, and Degradation Pathway. *Sep. Purif. Technol.* **2023**, *305*, 122450. https://doi.org/10.1016/j.seppur.2022.

(446) Barbosa, A. D. S., Julião, D., Fernandes, D. M., Peixoto, A. F, Catalytic Performance and Electrochemical Behaviour of Metal–Organic Frameworks: MIL-101(Fe) versus NH2-MIL-101(Fe). *Polyhedron* **2017**, *127*, 464–470. https://doi.org/10.1016/j.poly.2016.10.032.

(447) Cantoni, M., Ti, P., *High-Resolution TEM Chapter 6 High Resolution TEM Pb Ti High-Resolution TEM*. Microscopy Scie., **2007**, 445-534. ttps://doi.org/10.1016/j.chphi.2023.100197.

(448) Magar, H. S., Hassan, R. Y. A., Mulchandani, A., Electrochemical Impedance Spectroscopy (Eis): Principles, Construction, and Biosensing Applications. *Sensors*. MDPI , **2021,** 39**,** 578. https://doi.org/10.3390/s21196578.

(449) Šafranko, S., Stanković, A. Hajra, S. Preparation of Multifunctional N-Doped Carbon Quantum Dots from Citrus Clementina Peel: Investigating Targeted Pharmacological Activities and the Potential Application for Fe3+ Sensing. *Pharmaceuticals* **2021**, *14,*4090857. https://doi.org/10.3390/ph14090857.

(450) Ateia, E. E, Rabie, O., Mohamed, A. T. Assessment of the Correlation between Optical Properties and CQD Preparation Approaches. *Eur. Phys. J. Plus* **2024**, *139,* 0481. https://doi.org/10.1140/epjp/s13360-023-04811-7.

(451) Rathi, V. H., Jeice, A. R. Green Fabrication of Titanium Dioxide Nanoparticles and Their Applications in Photocatalytic Dye Degradation and Microbial Activities. *Chemical Physics Impact* **2023**, *6,* 100197. https://doi.org/10.1016/j.chphi.2023.

(452) Singh, H., Ahlawat, A., Dhiman, T. K., Solanki, P. R. Photocatalytic Degradation of Gentamicin Using TiO2 Nanoparticle Driven by UV Light Irradiation. *Mater. Lett.* **2023**, *346,* 13450. 4https://doi.org/10.1016/j.matlet.2023.

(453) Ansari, M. S., Kim, H. Enhanced Electrocatalytic Oxygen Evolution Reaction Kinetics Using Dual-Phase Engineering of Self-Supported Hierarchical NiCoV(OH)x Nanowire Arrays. *Fuel* **2021**, *304*, 121309. https://doi.org/10.1016/j.fuel.2021.

(454) Gang Li Gang Li, L. L. H. F. J. Effect of the Agglomeration of TiO2 Nanoparticles on Their Photocatalytic Performance in the Aqueous Phase. *Journal of Colloid and Interface Science* **2010**, *7*, 342–348.https://doi.org/10.3390/app7010049.

(455) Xu, W.; Li, W., Lu, L., Zhang, W.; Kang, J., Li, B. Morphology-Control of Metal-Organic Framework Crystal for Effective Removal of Dyes from Water. *J. Solid State Chem.* **2019**, *279,* 120950. https://doi.org/10.1016/j.jssc.2019.

(456) Sikirzhytski, V., Sikirzhytskaya, A., Lednev, I. K. Multidimensional Raman Spectroscopic Signatures as a Tool for Forensic Identification of Body Fluid Traces: A Review. *Applied Spectroscopy*. **2011**, 55, 1223–1232. https://doi.org/10.1366/11-06455.

(457) Front Matter. In *Infrared and Raman Spectroscopy in Forensic Science*; Wiley, **2012**. https://doi.org/10.1002/9781119962328.fmatter.

(458) Tamilselvan, V., Yuvaraj, D., Rakesh Kumar, R., Narasimha Rao, K. Growth of Rutile TiO 2 Nanorods on TiO 2 Seed Layer Deposited by Electron Beam Evaporation. *Appl. Surf. Sci.* **2012**, *258,* 4283–4287. https://doi.org/10.1016/j.apsusc.2011.12.079.

(459) Li, X., Lachmanski, L., Safi, S.New Insights into the Degradation Mechanism of Metal-Organic Frameworks Drug Carriers. *Sci. Rep.* **2017**, *7*, 345. https://doi.org/10.1038/s41598-017-13323-1.

(460) Tittel, J., Knechtel, F., Ploetz, E. Conquering Metal–Organic Frameworks by Raman Scattering Techniques. *Advanced Functional Materials*. John Wiley and Sons Inc , **2023,** 202, 307518. https://doi.org/10.1002/adfm.202307518.

(461) Zawani, N.; Azman, M.; Nur, P.; Zainal, S.; Alang, S. A. Enhancement the Electrochemical Conductivity of a Modified Reduced Graphene Oxide / Calixarene Screen-Printed Electrode Using Response Surface Methodology. **2020**, 1–14. https://doi.org/10.1371/journal.pone.0234148.

(462) Yadav, M.; Dhanda, M.; Arora, R.; Singh, G.; Mohan, H.; Lata, S. A TiO2-Adenine Nanocomposite as Modification Material for Screen-Printed Gold Electrode to Detect H1N1 (Swine Flu) Virus: A Disposable Genosensor. *Microchemical Journal* **2024**, *197*,109831. https://doi.org/10.1016/j.microc.2023..

(463) Lazanas, A. C. Prodromidis, M. I. Electrochemical Impedance Spectroscopy–A Tutorial. *ACS Measurement Science Au*. American Chemical Society , **2023**, 162–193. https://doi.org/10.1021/acsmeasuresciau.2c00070.

(464) Magar, H. S.; Hassan, R. Y. A.; Mulchandani, A. Electrochemical Impedance Spectroscopy (Eis): Principles, Construction, and Biosensing Applications. *Sensors*. MDPI **2021,**678, 578. https://doi.org/10.3390/s21196578.

(465) Nurdin, M., Maulidiyah, M., Salim, L. O. A, Muzakkar, M. Z., Umar, A. A. High Performance Cypermethrin Pesticide Detection Using Anatase TiO2-Carbon Paste Nanocomposites Electrode. *Microchemical Journal* **2019**, *145*, 756–761. https://doi.org/10.1016/j.microc.2018.11.050.

(466) Shinagawa, T., Garcia-Esparza, A. T., Takanabe, K. Insight on Tafel Slopes from a Microkinetic Analysis of Aqueous Electrocatalysis for Energy Conversion. *Sci. Rep.* **2015**, *5, 13801*. https://doi.org/10.1038/srep13801.

(467) *Comments Comment on "Composite Films of Surfactants, Nafion, and Proteins with Electrochemical and Enzyme Activity";* **1998**. https://pubs.acs.org/sharingguidelines.

(468) Muhammad, H., Tahiri, I. A., Muhammad, M., Masood, Z.; Versiani, M. A., Comprehensive Heterogeneous Electron Transfer Rate Constant Evaluation of Dissolved Oxygen in DMSO at Glassy Carbon Electrode Measured by Different Electrochemical Methods. *Journal of Electroanalytical Chemistry* **2016**, *775*, 157–162. https://doi.org/10.1016/j.jelechem.2016.05.049.

(469) Ghrkhlari, S., Ahour, F., Keshipour, S. A Novel Electrochemical Sensor for the Determination of Cadmium Ions Based on Nitrogen-Enriched Carbon Modified Electrode. *Sci. Rep.* **2025**, *15* ,1 . https://doi.org/10.1038/s41598-024-84185-7.

(470) Levanen, G.; Dali, A.; Leroux, Y.; Lupoi, T.; Betelu, S.; Michel, K.; Ababou-Girard, S.; Hapiot, P.; Dahech, I.; Cristea, C.; Feier, B.; Razan, F.; Geneste, F. Specific Electrochemical Sensor for Cadmium Detection: Comparison between Monolayer and Multilayer Functionalization. *Electrochim. Acta* **2023**, *464*. https://doi.org/10.1016/j.electacta.2023.142962.

(471) Mohammed, R. H. R.; Hassan, R. Y. A.; Mahmoud, R.; Farghali, A. A.; Hassouna, M. E. M. Electrochemical Determination of Cadmium Ions in Biological and Environmental Samples Using a Newly Developed Sensing Platform Made of Nickel Tungstate-Doped Multi-Walled Carbon Nanotubes. *J. Appl. Electrochem.* **2024**, *54* (3), 657–668. https://doi.org/10.1007/s10800-023-01976-y.

(472) Garg, N., Deep, A., Sharma, A. L. Simultaneous Detection of Lead and Cadmium Using a Composite of Zeolite Imidazole Framework and Reduced Graphene Oxide (ZIF-67/RGO) via Electrochemical Approach. *Environmental Engineering Research* **2023**, *28,* 269. https://doi.org/10.4491/eer.2022.

(473) Lahari, S. A., Kumawat, N., Amreen, K., Ponnalagu, R. N., Goel, S. IoT Integrated and Deep Learning Assisted Electrochemical Sensor for Multiplexed Heavy Metal Sensing in Water Samples. *NPJ Clean Water* **2025**, *8* , 6999. https://doi.org/10.1038/s41545-025-00441-x.

(474) Celesti, C., Iannazzo, D., Gugliandolo, C., Bacteria Derived Bioactive Compounds: A Valuable Tool for the Electrochemical Detection of Arsenic (III) Ions in Contaminated Water. *Sensors and Actuators Reports* **2025**, *10*, 100349. https://doi.org/10.1016/j.snr.2025.

(475) Iqbal, A.; Labib, M.; Muharemagic, D.; Sattar, S.; Dixon, B. R.; Berezovski, M. V. Detection of Cryptosporidium Parvum Oocysts on Fresh Produce Using DNA Aptamers. *PLoS One* **2015**, *10* (9). https://doi.org/10.1371/journal.pone.0137455.

(476) Kronberg, R., Laasonen, K. Coupling Surface Coverage and Electrostatic Effects on the Interfacial Adlayer-Water Structure of Hydrogenated Single-Crystal Platinum Electrodes. *Journal of Physical Chemistry C* **2020**, *124*, 13706–13714. https://doi.org/10.1021/acs.jpcc.0c02323.

(477) Zhu, P., Zhao, Y., Cyclic Voltammetry Measurements of Electroactive Surface Area of Porous Nickel: Peak Current and Peak Charge Methods and Diffusion Layer Effect. *Mater Chem Phys.,* **2019**, *233*, 60–67. https://doi.org/10.1016/j.matchemphys.2019.05.034.

(478) Song, C., Hui, R., Zhang, J., *High-Temperature PEM Fuel Cell Catalysts and Catalyst Layers 18.1 Opportunities and Challenges for High-Temperature PEM Fuel Cells*., **2008,** 861-888. https://doi.org/10.3389/fmicb.2022.973501.

(479) Frank, S. N., Bard, A. J., *Semiconductor Electrodes. 11. Electrochemistry at n-Type Ti02 Electrodes in Acetonitrile Solutions*. ACS., **2023**, 97, 7427-7433. Dio: 10.1007/s10008-023-05770-2.

(480) Wang, J., Zhong, H., Estudillo-Wong, L. A., Li, H., Alonso-Vante, N., Li, D., Synthesis and Electrocatalytic Performance of N-Doped Graphene Embedded with Co/CoO Nanoparticles towards Oxygen Evolution and Reduction Reactions. *Catal. Commun.* **2022**, *164*, 106428. https://doi.org/10.1016/j.catcom.2022.

(481) Subhan, M. A., Neogi, N., Choudhury, K. P., Rahman, M. M. Advances in Biosensor Applications of Metal/Metal-Oxide Nanoscale Materials. *Chemosensors*.

Multidisciplinary Digital Publishing Institute (MDPI) **2025**, 5, 878. https://doi.org/10.3390/chemosensors13020049.

(482) Ciuba, K., Piotrowska, A., Chaudhury, D., Dehingia, B., Duński, E., Behr, R., Molecular Signature of Primate Astrocytes Reveals Pathways and Regulatory Changes Contributing to Human Brain Evolution. *Cell Stem Cell* **2025**, *32*, 426-444.e14. https://doi.org/10.1016/j.stem.2024.12.011.

(483) Orzoł, A., Gołębiowski, A., Szultka-Młyńska, M., Głowacka, K., Pomastowski, ICP-MS Analysis of Cadmium Bioaccumulation and Its Effect on Pea Plants (Pisum Sativum L.). *Pol. J. Environ. Stud.* **2022**, *31*, 4779–4787. https://doi.org/10.15244/pjoes/149259.

(484) Atasoy, M. Development of a New and Highly Sensitive Method for Arsenic Determination in Drinking Water Samples Using Au-Coated W-Coil Atom Trap Hydride Generation Atomic Absorption Spectrometry. *ChemistrySelect* **2023**, *8*, 370. https://doi.org/10.1002/slct.202302370.

(485) Hamid Kargari, S., Ahour, F., Mahmoudian, M. An Electrochemical Sensor for the Detection of Arsenic Using Nanocomposite-Modified Electrode. *Sci. Rep.* **2023**, *13* 890. https://doi.org/10.1038/s41598-023-36103-6.